

Characterization of Stator Winding Short-Circuit Faults in Interior Permanent-Magnet Motor-Drive Systems

Andrew Strandt
Marquette University

Recommended Citation

Strandt, Andrew, "Characterization of Stator Winding Short-Circuit Faults in Interior Permanent-Magnet Motor-Drive Systems" (2013). *Master's Theses (2009 -)*. Paper 235.
http://epublications.marquette.edu/theses_open/235

CHARACTERIZATION OF STATOR WINDING SHORT-CIRCUIT FAULTS IN
INTERIOR PERMANENT-MAGNET MOTOR-DRIVE SYSTEMS

by
Andrew Philip Strandt, B.S.

A Thesis Submitted to the Faculty of the
Graduate School, Marquette University,
in Partial Fulfillment of the Requirements for the
Degree of Master of Science

Milwaukee, Wisconsin

December 2013

© Copyright 2013 by Andrew Philip Strandt

PREFACE

CHARACTERIZATION OF STATOR WINDING SHORT-CIRCUIT FAULTS IN INTERIOR PERMANENT-MAGNET MOTOR-DRIVE SYSTEMS

Andrew Philip Strandt, B.S.

Under the supervision of Professor Nabeel Demerdash

Marquette University, 2013

to circulate and to have copied for non-commercial purposes, at its discretion, the above title upon the request of individuals or institutions.

To my wife and my family

ABSTRACT

CHARACTERIZATION OF STATOR WINDING SHORT-CIRCUIT FAULTS IN INTERIOR PERMANENT-MAGNET MOTOR-DRIVE SYSTEMS

Andrew Philip Strandt

Maquette University, 2013

This thesis contains a comprehensive analysis of experimental data collected from a case-study interior permanent-magnet electric machine experiencing winding short-circuit faults of varying severity. The experimental data collected from the faulted machine is from both motoring operation energized by a PWM sensorless ac drive as well as generating operation driven by the test bed dynamometer with a resistive winding load. For both modes of operation a complete set of three-phase voltage and current signals was recorded and analyzed. The three fault diagnosis techniques applied and compared regarding their ability to diagnose and prognosticate a winding fault in an interior permanent-magnet machine are motor current spectrum analysis (MCSA), negative sequence components analysis utilizing a symmetrical components transformation, and the space-vector pendulous oscillation method. The applicability of these diagnosis techniques to this case-study experimental interior permanent-magnet machine demonstrate that motor current spectrum analysis is inconclusive in diagnosing a winding fault when the machine is operated as a motor, but useful for diagnosing a winding fault when the machine is operated as a generator. Negative sequence components analysis successfully diagnoses the winding fault in both the motor operation and the generator operation cases. Finally, the space-vector pendulous oscillation method results are inconclusive for both the motor operation and the generator operation test cases.

ACKNOWLEDGEMENTS

Andrew Philip Strandt

I wish to sincerely thank my thesis advisor, Professor Nabeel Demerdash, for his guidance of my research activities and for all that I have learned from him in my graduate classes.

I must express my deepest gratitude to my wife, Alia Strandt, for her constant encouragement and support of me in this research endeavour.

Likewise, I wish to sincerely thank my committee, Professor Edwin Yaz, Dr. Dan Ionel, and Dr. Ahmed Sayed Ahmed for their advice and support.

Heartfelt thanks go to my parents, Carl and Linda Strandt, and to my siblings, Mary, Daniel, Timothy, Peter, Michael, and Therese, for their love and support. Similar thanks are extended to my in-laws, John and Margarita Manarik, and my wife's siblings Selina and Craig for their love and support as well. I have greatly enjoyed the engineering conversations I have had over the years with my father and with my father-in-law, both of whom received their M.S. in Electrical Engineering from Marquette University, and with my grandfather, Earl Strandt, who received his M.S. in Electrical Engineering from New York University. With my graduation as M.S. in Electrical Engineering I continue an unbroken, three-generation tradition of advanced electrical engineering education in the Strandt family.

Acknowledgement and thanks are also due to the entities that supported this research. I wish to thank The Greater Milwaukee Foundation's Frank Rogers Bacon Research Assistantship, NSF-GOALI Grant No. 1028348, and the Wisconsin Energy Research Consortium for their financial support of this work. Likewise, I wish to thank ANSYS, Inc. for the donation of ANSYS Simplorer and ANSYS Maxwell, and Dr. Marius Rosu and Mr. Mark Solveson at ANSYS, Inc. for their advice. Finally, I wish to thank A.O. Smith Corp. for their donation of the case-study experimental machine used through this work.

Last, but not least, I wish to gratefully thank my fellow graduate students in the Electric Machines and Drives Laboratory at Marquette University, especially Dr. Gennadi Sizov, Dr. Peng Zhang, and Mr. Jiangbiao He for their valuable advice and assistance over the years.

Table of Contents

List of Tables	iv
List of Figures	vi
1 Introduction	1
1.1 Background	1
1.2 Literature Review	3
1.2.1 Causes of Electric Machine Stator Winding Faults	3
1.2.2 Modeling and Simulation of Electric Machine Stator Winding Faults	5
1.2.3 Stator Winding Fault Detection Methods	7
1.3 Statement of the Problem	9
2 Stator Winding Short-Circuit Fault Detection Methods	11
2.1 Motor Current Spectrum Analysis	11
2.2 Negative Sequence Components Analysis	17
2.3 Space-Vector Pendulous Oscillation Method	19
3 Interior Permanent-Magnet Machine Experimental Setup	24
3.1 Specifications and Properties of the Experimental IPM Machine	24
3.2 Experimental Setup and Test Equipment	28
4 Experimental IPM Machine Results - Motoring Operation	32
4.1 Time-Domain Phase Voltages and Phase Currents	33

4.2	Results of Motor Current Spectrum Analysis	49
4.3	Results of Negative Sequence Components Analysis	63
4.4	Results of Space-Vector Pendulous Oscillation Method Analysis . . .	63
4.5	Analysis and Discussion of Results	73
5	Experimental IPM Machine Results - Generating Operation	77
5.1	Time-Domain Phase Voltages and Phase Currents	78
5.2	Results of Motor Current Spectrum Analysis	105
5.3	Results of Negative Sequence Components Analysis	132
5.4	Results of Space-Vector Pendulous Oscillation Method Analysis . . .	133
5.5	Analysis and Discussion of Results	152
6	Conclusions and Future Work	155
6.1	Conclusions	155
6.2	Future Work	158
	Bibliography	159

List of Tables

1.1	Percentages of faults in electric machines.	3
2.1	Magnitude of the symmetrical component phasors of the above waveforms.	19
3.1	Ratings of the 3.5 hp IPM machine for the three parallel path winding configuration.	25
3.2	Ratings of the 3.5 hp IPM machine for the single path winding configuration.	25
3.3	Key parameters of the 3.5 hp IPM machine for the three parallel path winding configuration.	26
3.4	Key parameters of the 3.5 hp IPM machine for the single path winding configuration.	26
3.5	EMF harmonic parameters of the 3.5 hp IPM motor.	27
4.1	3rd harmonic component of the IPM machine phase currents when operated at 86.25 Hz.	50
4.2	9th harmonic component of the IPM machine phase currents when operated at 86.25 Hz.	50
4.3	27th harmonic component of the IPM machine phase currents when operated at 86.25 Hz.	50
4.4	Magnitude of the symmetrical component phasors of the IPM machine when operated at 86.25 Hz.	63
4.5	Swing angle of the IPM machine when operated at 86.25 Hz.	64

5.1	3rd harmonic components of the IPM machine faulted phase current when operated at 20 Hz.	105
5.2	9rd harmonic components of the IPM machine faulted phase current when operated at 20 Hz.	106
5.3	27rd harmonic components of the IPM machine faulted phase current when operated at 20 Hz.	106
5.4	3rd harmonic components of the IPM machine faulted phase current when operated at 30 Hz.	106
5.5	9th harmonic components of the IPM machine faulted phase current when operated at 30 Hz.	107
5.6	27th harmonic components of the IPM machine faulted phase current when operated at 30 Hz.	107
5.7	3rd harmonic components of the IPM machine faulted phase current when operated at 40 Hz.	107
5.8	9th harmonic components of the IPM machine faulted phase current when operated at 40 Hz.	107
5.9	27th harmonic components of the IPM machine faulted phase current when operated at 40 Hz.	108
5.10	Magnitude of the symmetrical component phasors of the IPM machine when operated at 20 Hz.	133
5.11	Magnitude of the symmetrical component phasors of the IPM machine when operated at 30 Hz.	133
5.12	Magnitude of the symmetrical component phasors of the IPM machine when operated at 40 Hz.	133
5.13	Swing angle of the IPM machine when operated at 20 Hz.	134
5.14	Swing angle of the IPM machine when operated at 30 Hz.	134
5.15	Swing angle of the IPM machine when operated at 40 Hz.	135

List of Figures

2.1	Time-domain waveforms of Equation 2.6.	14
2.2	Rectangular window.	14
2.3	Triangular window.	15
2.4	Blackman-Harris window.	15
2.5	FFT of $y(t)$ using a rectangular window.	16
2.6	FFT of $y(t)$ using a triangular window.	16
2.7	FFT of $y(t)$ using a Blackman-Harris window.	17
2.8	Imbalanced cosinusoidal waveforms.	19
2.9	Voltage space-vector example.	23
2.10	Current space-vector example.	23
2.11	Pendulous oscillation signal example from the example voltage and current space-vectors.	23
3.1	Cross-section of the case-study experimental IPM machine.	25
3.2	Schematic of one phase with a 16.7% winding fault used for the motor tests.	29
3.3	Schematic of one phase with a 16.7% winding fault used for the generator tests.	29
3.4	Schematic of one phase with a 33.3% winding fault used for the generator tests.	29
3.5	Schematic of one phase with a 66.7% winding fault used for the generator tests.	30

3.6	Schematic of one phase with a 100% winding fault used for the generator tests.	30
3.7	Resistance board for providing the winding short-circuit fault.	30
3.8	Experimental machine with dynamometer test bed.	31
4.1	Line-to-neutral voltage of the IPM machine at 86.25 Hz, half-load, with no winding fault.	34
4.2	Smoothed line-to-neutral voltage of the IPM machine at 86.25 Hz, half-load, with no winding fault.	34
4.3	Phase current of the IPM machine at 86.25 Hz, half-load, with no winding fault.	35
4.4	Line-to-neutral voltage of the IPM machine at 86.25 Hz, three-quarter-load, with no winding fault.	35
4.5	Smoothed line-to-neutral voltage of the IPM machine at 86.25 Hz, three-quarter-load, with no winding fault.	36
4.6	Phase current of the IPM machine at 86.25 Hz, three-quarter-load, with no winding fault.	36
4.7	Line-to-neutral voltage of the IPM machine at 86.25 Hz, half-load, with a 9.66 Ω , 16.7% winding fault.	37
4.8	Smoothed line-to-neutral voltage of the IPM machine at 86.25 Hz, half-load, with a 9.66 Ω , 16.7% winding fault.	37
4.9	Phase current of the IPM machine at 86.25 Hz, half-load, with a 9.66 Ω , 16.7% winding fault.	38
4.10	Fault current of the IPM machine at 86.25 Hz, half-load, with a 9.66 Ω , 16.7% winding fault.	38
4.11	Line-to-neutral voltage of the IPM machine at 86.25 Hz, three-quarter-load, with a 9.66 Ω , 16.7% winding fault.	39
4.12	Smoothed line-to-neutral voltage of the IPM machine at 86.25 Hz, three-quarter-load, with a 9.66 Ω , 16.7% winding fault.	40

4.13	Phase current of the IPM machine at 86.25 Hz, three-quarter-load, with a 9.66 Ω , 16.7% winding fault.	40
4.14	Fault current of the IPM machine at 86.25 Hz, three-quarter-load, with a 9.66 Ω , 16.7% winding fault.	41
4.15	Line-to-neutral voltage of the IPM machine at 86.25 Hz, half-load, with a 7.25 Ω , 16.7% winding fault.	41
4.16	Smoothed line-to-neutral voltage of the IPM machine at 86.25 Hz, half-load, with a 7.25 Ω , 16.7% winding fault.	42
4.17	Phase current of the IPM machine at 86.25 Hz, half-load, with a 7.25 Ω , 16.7% winding fault.	42
4.18	Fault current of the IPM machine at 86.25 Hz, half-load, with a 7.25 Ω , 16.7% winding fault.	43
4.19	Line-to-neutral voltage of the IPM machine at 86.25 Hz, three-quarter-load, with a 7.25 Ω , 16.7% winding fault.	43
4.20	Smoothed line-line voltage of the IPM machine at 86.25 Hz, three-quarter-load, with a 7.25 Ω , 16.7% winding fault.	44
4.21	Phase current of the IPM machine at 86.25 Hz, three-quarter-load, with a 7.25 Ω , 16.7% winding fault.	44
4.22	Fault current of the IPM machine at 86.25 Hz, three-quarter-load, with a 7.25 Ω , 16.7% winding fault.	45
4.23	Line-to-neutral voltage of the IPM machine at 86.25 Hz, half-load, with a 4.85 Ω , 16.7% winding fault.	45
4.24	Smoothed line-to-neutral voltage of the IPM machine at 86.25 Hz, half-load, with a 4.85 Ω , 16.7% winding fault.	46
4.25	Phase current of the IPM machine at 86.25 Hz, half-load, with a 4.85 Ω , 16.7% winding fault.	46
4.26	Fault current of the IPM machine at 86.25 Hz, half-load, with a 4.85 Ω , 16.7% winding fault.	47

4.27	Line-to-neutral voltage of the IPM machine at 86.25 Hz, three-quarter-load, with a 4.85Ω , 16.7% winding fault.	47
4.28	Smoothed line-to-neutral voltage of the IPM machine at 86.25 Hz, three-quarter-load, with a 4.85Ω , 16.7% winding fault.	48
4.29	Phase current of the IPM machine at 86.25 Hz, three-quarter-load, with a 4.85Ω , 16.7% winding fault.	48
4.30	Fault current of the IPM machine at 86.25 Hz, three-quarter-load, with a 4.85Ω , 16.7% winding fault.	49
4.31	FFT of the IPM machine phase A current at 86.25 Hz, half-load, with no winding fault.	51
4.32	FFT of the IPM machine phase B current at 86.25 Hz, half-load, with no winding fault.	51
4.33	FFT of the IPM machine phase C current at 86.25 Hz, half-load, with no winding fault.	52
4.34	FFT of the IPM machine phase A current at 86.25 Hz, three-quarter-load, with no winding fault.	52
4.35	FFT of the IPM machine phase B current at 86.25 Hz, three-quarter-load, with no winding fault.	53
4.36	FFT of the IPM machine phase C current at 86.25 Hz, three-quarter-load, with no winding fault.	53
4.37	FFT of the IPM machine phase A current at 86.25 Hz, half-load, with a 9.66Ω , 16.7% winding fault.	54
4.38	FFT of the IPM machine phase B current at 86.25 Hz, half-load, with a 9.66Ω , 16.7% winding fault.	54
4.39	FFT of the IPM machine phase C current at 86.25 Hz, half-load, with a 9.66Ω , 16.7% winding fault.	55
4.40	FFT of the IPM machine phase A current at 86.25 Hz, three-quarter-load, with a 9.66Ω , 16.7% winding fault.	55

4.41	FFT of the IPM machine phase B current at 86.25 Hz, three-quarter-load, with a 9.66Ω , 16.7% winding fault.	56
4.42	FFT of the IPM machine phase C current at 86.25 Hz, three-quarter-load, with a 9.66Ω , 16.7% winding fault.	56
4.43	FFT of the IPM machine phase A current at 86.25 Hz, half-load, with a 7.25Ω , 16.7% winding fault.	57
4.44	FFT of the IPM machine phase B current at 86.25 Hz, half-load, with a 7.25Ω , 16.7% winding fault.	57
4.45	FFT of the IPM machine phase C current at 86.25 Hz, half-load, with a 7.25Ω , 16.7% winding fault.	58
4.46	FFT of the IPM machine phase A current at 86.25 Hz, three-quarter-load, with a 7.25Ω , 16.7% winding fault.	58
4.47	FFT of the IPM machine phase B current at 86.25 Hz, three-quarter-load, with a 7.25Ω , 16.7% winding fault.	59
4.48	FFT of the IPM machine phase C current at 86.25 Hz, three-quarter-load, with a 7.25Ω , 16.7% winding fault.	59
4.49	FFT of the IPM machine phase A current at 86.25 Hz, half-load, with a 4.85Ω , 16.7% winding fault.	60
4.50	FFT of the IPM machine phase B current at 86.25 Hz, half-load, with a 4.85Ω , 16.7% winding fault.	60
4.51	FFT of the IPM machine phase C current at 86.25 Hz, half-load, with a 4.85Ω , 16.7% winding fault.	61
4.52	FFT of the IPM machine phase A current at 86.25 Hz, three-quarter-load, with a 4.85Ω , 16.7% winding fault.	61
4.53	FFT of the IPM machine phase B current at 86.25 Hz, three-quarter-load, with a 4.85Ω , 16.7% winding fault.	62
4.54	FFT of the IPM machine phase C current at 86.25 Hz, three-quarter-load, with a 4.85Ω , 16.7% winding fault.	62

4.55	Voltage space-vector of the IPM machine at 86.25 Hz, half-load, with no winding fault.	65
4.56	Current space-vector of the IPM machine at 86.25 Hz, half-load, with no winding fault.	65
4.57	Pendulous oscillation signal of the IPM machine at 86.25 Hz, half-load, with no winding fault.	65
4.58	Voltage space-vector of the IPM machine at 86.25 Hz, three-quarter-load, with no winding fault.	66
4.59	Current space-vector of the IPM machine at 86.25 Hz, three-quarter-load, with no winding fault.	66
4.60	Pendulous oscillation signal of the IPM machine at 86.25 Hz, full-load, with no winding fault.	66
4.61	Voltage space-vector of the IPM machine at 86.25 Hz, half-load, with a 9.66 Ω , 16.7% winding fault.	67
4.62	Current space-vector of the IPM machine at 86.25 Hz, half-load, with a 9.66 Ω , 16.7% winding fault.	67
4.63	Pendulous oscillation signal of the IPM machine at 86.25 Hz, half-load, with a 9.66 Ω , 16.7% winding fault.	67
4.64	Voltage space-vector of the IPM machine at 86.25 Hz, three-quarter-load, with a 9.66 Ω , 16.7% winding fault.	68
4.65	Current space-vector of the IPM machine at 86.25 Hz, three-quarter-load, with a 9.66 Ω , 16.7% winding fault.	68
4.66	Pendulous oscillation signal of the IPM machine at 86.25 Hz, three-quarter-load, with a 9.66 Ω , 16.7% winding fault.	68
4.67	Voltage space-vector of the IPM machine at 86.25 Hz, half-load, with a 7.25 Ω , 16.7% winding fault.	69
4.68	Current space-vector of the IPM machine at 86.25 Hz, half-load, with a 7.25 Ω , 16.7% winding fault.	69

4.69	Pendulous oscillation signal of the IPM machine at 86.25 Hz, half-load, with a $7.25\ \Omega$, 16.7% winding fault.	69
4.70	Voltage space-vector of the IPM machine at 86.25 Hz, three-quarter-load, with a $7.25\ \Omega$, 16.7% winding fault.	70
4.71	Current space-vector of the IPM machine at 86.25 Hz, three-quarter-load, with a $7.25\ \Omega$, 16.7% winding fault.	70
4.72	Pendulous oscillation signal of the IPM machine at 86.25 Hz, three-quarter-load, with a $7.25\ \Omega$, 16.7% winding fault.	70
4.73	Voltage space-vector of the IPM machine at 86.25 Hz, half-load, with a $4.85\ \Omega$, 16.7% winding fault.	71
4.74	Current space-vector of the IPM machine at 86.25 Hz, half-load, with a $4.85\ \Omega$, 16.7% winding fault.	71
4.75	Pendulous oscillation signal of the IPM machine at 86.25 Hz, half-load, with a $4.85\ \Omega$, 16.7% winding fault.	71
4.76	Voltage space-vector of the IPM machine at 86.25 Hz, three-quarter-load, with a $4.85\ \Omega$, 16.7% winding fault.	72
4.77	Current space-vector of the IPM machine at 86.25 Hz, three-quarter-load, with a $4.85\ \Omega$, 16.7% winding fault.	72
4.78	Pendulous oscillation signal of the IPM machine at 86.25 Hz, three-quarter-load, with a $4.85\ \Omega$, 16.7% winding fault.	72
5.1	Line-to-neutral voltage of the IPM machine at 20 Hz with no winding fault.	78
5.2	Phase current of the IPM machine at 20 Hz with no winding fault.	79
5.3	Open-circuit line-to-neutral voltage of the IPM machine at 20 Hz with no winding fault.	79
5.4	Open-circuit line-to-neutral voltage of the IPM machine at 20 Hz with a $5\ \Omega$, 16.7% winding fault.	80
5.5	Circulating fault current of the IPM machine at 20 Hz with a $5\ \Omega$, 16.7% winding fault, with an open-circuit terminal configuration.	80

5.6	Open-circuit line-to-neutral voltage of the IPM machine at 20 Hz with a $5\ \Omega$, 33.3% winding fault.	81
5.7	Circulating fault current of the IPM machine at 20 Hz with a $5\ \Omega$, 33.3% winding fault, with an open-circuit terminal configuration. . .	81
5.8	Line-to-neutral voltage of the IPM machine at 20 Hz with a $9.7\ \Omega$, 33.3% winding fault.	82
5.9	Phase current of the IPM machine at 20 Hz with a $9.7\ \Omega$, 33.3% winding fault.	83
5.10	Fault current of the IPM machine at 20 Hz with a $9.7\ \Omega$, 33.3% winding fault.	83
5.11	Line-to-neutral voltage of the IPM machine at 20 Hz with a $6.6\ \Omega$, 33.3% winding fault.	84
5.12	Phase current of the IPM machine at 20 Hz with a $6.6\ \Omega$, 33.3% winding fault.	84
5.13	Fault current of the IPM machine at 20 Hz with a $6.6\ \Omega$, 33.3% winding fault.	85
5.14	Line-to-neutral voltage of the IPM machine at 20 Hz with a $4.9\ \Omega$, 33.3% winding fault.	85
5.15	Phase current of the IPM machine at 20 Hz with a $4.9\ \Omega$, 33.3% winding fault.	86
5.16	Fault current of the IPM machine at 20 Hz with a $4.9\ \Omega$, 33.3% winding fault.	86
5.17	Line-to-neutral voltage of the IPM machine at 20 Hz with a $3.3\ \Omega$, 33.3% winding fault.	87
5.18	Phase current of the IPM machine at 20 Hz with a $3.3\ \Omega$, 33.3% winding fault.	87
5.19	Fault current of the IPM machine at 20 Hz with a $3.3\ \Omega$, 33.3% winding fault.	88

5.20	Line-to-neutral voltage of the IPM machine at 20 Hz with a 9.6 Ω , 66.7% winding fault.	88
5.21	Phase current of the IPM machine at 20 Hz with a 9.6 Ω , 66.7% winding fault.	89
5.22	Fault current of the IPM machine at 20 Hz with a 9.6 Ω , 66.7% winding fault.	89
5.23	Line-to-neutral voltage of the IPM machine at 20 Hz with a 6.6 Ω , 66.7% winding fault.	90
5.24	Phase current of the IPM machine at 20 Hz with a 6.6 Ω , 66.7% winding fault.	90
5.25	Fault current of the IPM machine at 20 Hz with a 6.6 Ω , 66.7% winding fault.	91
5.26	Line-to-neutral voltage of the IPM machine at 20 Hz with a 10 Ω , 100% winding fault.	91
5.27	Phase current of the IPM machine at 20 Hz with a 10 Ω , 100% winding fault.	92
5.28	Fault current of the IPM machine at 20 Hz with a 10 Ω , 100% winding fault.	92
5.29	Line-to-neutral voltage of the IPM machine at 20 Hz with a 6.5 Ω , 100% winding fault.	93
5.30	Phase current of the IPM machine at 20 Hz with a 6.5 Ω , 100% winding fault.	93
5.31	Fault current of the IPM machine at 20 Hz with a 6.5 Ω , 100% winding fault.	94
5.32	Line-to-neutral voltage of the IPM machine at 30 Hz with a 5.0 Ω , 16.7% winding fault.	94
5.33	Phase current of the IPM machine at 30 Hz with a 5.0 Ω , 16.7% winding fault.	95

5.34	Fault current of the IPM machine at 30 Hz with a 5.0 Ω , 16.7% winding fault.	95
5.35	Line-to-neutral voltage of the IPM machine at 30 Hz with a 3.3 Ω , 16.7% winding fault.	96
5.36	Phase current of the IPM machine at 30 Hz with a 3.3 Ω , 16.7% winding fault.	96
5.37	Fault current of the IPM machine at 30 Hz with a 3.3 Ω , 16.7% winding fault.	97
5.38	Line-to-neutral voltage of the IPM machine at 30 Hz with a 5.0 Ω , 33.3% winding fault.	97
5.39	Phase current of the IPM machine at 30 Hz with a 5.0 Ω , 33.3% winding fault.	98
5.40	Fault current of the IPM machine at 30 Hz with a 5.0 Ω , 33.3% winding fault.	98
5.41	Line-to-neutral voltage of the IPM machine at 30 Hz with a 3.3 Ω , 33.3% winding fault.	99
5.42	Phase current of the IPM machine at 30 Hz with a 3.3 Ω , 33.3% winding fault.	99
5.43	Fault current of the IPM machine at 30 Hz with a 3.3 Ω , 33.3% winding fault.	100
5.44	Line-to-neutral voltage of the IPM machine at 40 Hz with a 5.0 Ω , 16.7% winding fault.	100
5.45	Phase current of the IPM machine at 40 Hz with a 5.0 Ω , 16.7% winding fault.	101
5.46	Fault current of the IPM machine at 40 Hz with a 5.0 Ω , 16.7% winding fault.	101
5.47	Line-to-neutral voltage of the IPM machine at 40 Hz with a 3.3 Ω , 16.7% winding fault.	102

5.48	Phase current of the IPM machine at 40 Hz with a 3.3 Ω , 16.7% winding fault.	102
5.49	Fault current of the IPM machine at 40 Hz with a 3.3 Ω , 16.7% winding fault.	103
5.50	Line-to-neutral voltage of the IPM machine at 40 Hz with a 5.0 Ω , 33.3% winding fault.	103
5.51	Phase current of the IPM machine at 40 Hz with a 5.0 Ω , 33.3% winding fault.	104
5.52	Fault current of the IPM machine at 40 Hz with a 5.0 Ω , 33.3% winding fault.	104
5.53	FFT of the IPM machine phase A current at 20 Hz with no winding fault.	108
5.54	FFT of the IPM machine phase B current at 20 Hz with no winding fault.	109
5.55	FFT of the IPM machine phase C current at 20 Hz with no winding fault.	109
5.56	FFT of the IPM machine faulted phase current at 20 Hz with a 9.7 Ω , 33.3% winding fault.	110
5.57	FFT of the IPM machine phase B current at 20 Hz with a 9.7 Ω , 33.3% winding fault.	110
5.58	FFT of the IPM machine phase C current at 20 Hz with a 9.7 Ω , 33.3% winding fault.	111
5.59	FFT of the IPM machine faulted phase current at 20 Hz with a 6.6 Ω , 33.3% winding fault.	111
5.60	FFT of the IPM machine phase B current at 20 Hz with a 6.6 Ω , 33.3% winding fault.	112
5.61	FFT of the IPM machine phase C current at 20 Hz with a 6.6 Ω , 33.3% winding fault.	112

5.62	FFT of the IPM machine faulted phase current at 20 Hz with a 4.9 Ω , 33.3% winding fault.	113
5.63	FFT of the IPM machine phase B current at 20 Hz with a 4.9 Ω , 33.3% winding fault.	113
5.64	FFT of the IPM machine phase C current at 20 Hz with a 4.9 Ω , 33.3% winding fault.	114
5.65	FFT of the IPM machine faulted phase current at 20 Hz with a 3.3 Ω , 33.3% winding fault.	114
5.66	FFT of the IPM machine phase B current at 20 Hz with a 3.3 Ω , 33.3% winding fault.	115
5.67	FFT of the IPM machine phase C current at 20 Hz with a 3.3 Ω , 33.3% winding fault.	115
5.68	FFT of the IPM machine faulted phase current at 20 Hz with a 9.6 Ω , 66.7% winding fault.	116
5.69	FFT of the IPM machine phase B current at 20 Hz with a 9.6 Ω , 66.7% winding fault.	116
5.70	FFT of the IPM machine phase C current at 20 Hz with a 9.6 Ω , 66.7% winding fault.	117
5.71	FFT of the IPM machine faulted phase current at 20 Hz with a 6.6 Ω , 66.7% winding fault.	117
5.72	FFT of the IPM machine phase B current at 20 Hz with a 6.6 Ω , 66.7% winding fault.	118
5.73	FFT of the IPM machine phase C current at 20 Hz with a 6.6 Ω , 66.7% winding fault.	118
5.74	FFT of the IPM machine faulted phase current at 20 Hz with a 10 Ω , 100% winding fault.	119
5.75	FFT of the IPM machine phase B current at 20 Hz with a 10 Ω , 100% winding fault.	119

5.76	FFT of the IPM machine phase C current at 20 Hz with a 10 Ω , 100% winding fault.	120
5.77	FFT of the IPM machine faulted phase current at 20 Hz with a 6.5 Ω , 100% winding fault.	120
5.78	FFT of the IPM machine phase B current at 20 Hz with a 6.5 Ω , 100% winding fault.	121
5.79	FFT of the IPM machine phase C current at 20 Hz with a 6.5 Ω , 100% winding fault.	121
5.80	FFT of the IPM machine faulted phase current at 30 Hz with a 5.0 Ω , 16.7% winding fault.	122
5.81	FFT of the IPM machine phase B current at 30 Hz with a 5.0 Ω , 16.7% winding fault.	122
5.82	FFT of the IPM machine phase C current at 30 Hz with a 5.0 Ω , 16.7% winding fault.	123
5.83	FFT of the IPM machine faulted phase current at 30 Hz with a 3.3 Ω , 16.7% winding fault.	123
5.84	FFT of the IPM machine phase B current at 30 Hz with a 3.3 Ω , 16.7% winding fault.	124
5.85	FFT of the IPM machine phase C current at 30 Hz with a 3.3 Ω , 16.7% winding fault.	124
5.86	FFT of the IPM machine faulted phase current at 30 Hz with a 5.0 Ω , 33.3% winding fault.	125
5.87	FFT of the IPM machine phase B current at 30 Hz with a 5.0 Ω , 33.3% winding fault.	125
5.88	FFT of the IPM machine phase C current at 30 Hz with a 5.0 Ω , 33.3% winding fault.	126
5.89	FFT of the IPM machine faulted phase current at 30 Hz with a 3.3 Ω , 33.3% winding fault.	126

5.90	FFT of the IPM machine phase B current at 30 Hz with a 3.3 Ω , 33.3% winding fault.	127
5.91	FFT of the IPM machine phase C current at 30 Hz with a 3.3 Ω , 33.3% winding fault.	127
5.92	FFT of the IPM machine faulted phase current at 40 Hz with a 5.0 Ω , 16.7% winding fault.	128
5.93	FFT of the IPM machine phase B current at 40 Hz with a 5.0 Ω , 16.7% winding fault.	128
5.94	FFT of the IPM machine phase C current at 40 Hz with a 5.0 Ω , 16.7% winding fault.	129
5.95	FFT of the IPM machine faulted phase current at 40 Hz with a 3.3 Ω , 16.7% winding fault.	129
5.96	FFT of the IPM machine phase B current at 40 Hz with a 3.3 Ω , 16.7% winding fault.	130
5.97	FFT of the IPM machine phase C current at 40 Hz with a 3.3 Ω , 16.7% winding fault.	130
5.98	FFT of the IPM machine faulted phase current at 40 Hz with a 5.0 Ω , 33.3% winding fault.	131
5.99	FFT of the IPM machine phase B current at 40 Hz with a 5.0 Ω , 33.3% winding fault.	131
5.100	FFT of the IPM machine phase C current at 40 Hz with a 5.0 Ω , 33.3% winding fault.	132
5.101	Voltage space-vector of the IPM machine at 20 Hz with no winding fault.	136
5.102	Current space-vector of the IPM machine at 20 Hz with no winding fault.	136
5.103	Pendulous oscillation signal of the IPM machine at 20 Hz with no winding fault.	136

5.104	Voltage space-vector of the IPM machine at 20 Hz with a 9.7 Ω , 33.3% winding fault.	137
5.105	Current space-vector of the IPM machine at 20 Hz with a 9.7 Ω , 33.3% winding fault.	137
5.106	Pendulous oscillation signal of the IPM machine at 20 Hz with a 9.7 Ω , 33.3% winding fault.	137
5.107	Voltage space-vector of the IPM machine at 20 Hz with a 6.6 Ω , 33.3% winding fault.	138
5.108	Current space-vector of the IPM machine at 20 Hz with a 6.6 Ω , 33.3% winding fault.	138
5.109	Pendulous oscillation signal of the IPM machine at 20 Hz with a 6.6 Ω , 33.3% winding fault.	138
5.110	Voltage space-vector of the IPM machine at 20 Hz with a 4.9 Ω , 33.3% winding fault.	139
5.111	Current space-vector of the IPM machine at 20 Hz with a 4.9 Ω , 33.3% winding fault.	139
5.112	Pendulous oscillation signal of the IPM machine at 20 Hz with a 4.9 Ω , 33.3% winding fault.	139
5.113	Voltage space-vector of the IPM machine at 20 Hz with a 3.3 Ω , 33.3% winding fault.	140
5.114	Current space-vector of the IPM machine at 20 Hz with a 3.3 Ω , 33.3% winding fault.	140
5.115	Pendulous oscillation signal of the IPM machine at 20 Hz with a 3.3 Ω , 33.3% winding fault.	140
5.116	Voltage space-vector of the IPM machine at 20 Hz with a 9.6 Ω , 66.7% winding fault.	141
5.117	Current space-vector of the IPM machine at 20 Hz with a 9.6 Ω , 66.7% winding fault.	141

5.118	Pendulous oscillation signal of the IPM machine at 20 Hz with a 9.6 Ω , 66.7% winding fault.	141
5.119	Voltage space-vector of the IPM machine at 20 Hz with a 6.6 Ω , 66.7% winding fault.	142
5.120	Current space-vector of the IPM machine at 20 Hz with a 6.6 Ω , 66.7% winding fault.	142
5.121	Pendulous oscillation signal of the IPM machine at 20 Hz with a 6.6 Ω , 66.7% winding fault.	142
5.122	Voltage space-vector of the IPM machine at 20 Hz with a 10 Ω , 100% winding fault.	143
5.123	Current space-vector of the IPM machine at 20 Hz with a 10 Ω , 100% winding fault.	143
5.124	Pendulous oscillation signal of the IPM machine at 20 Hz with a 10 Ω , 100% winding fault.	143
5.125	Voltage space-vector of the IPM machine at 20 Hz with a 6.5 Ω , 100% winding fault.	144
5.126	Current space-vector of the IPM machine at 20 Hz with a 6.5 Ω , 100% winding fault.	144
5.127	Pendulous oscillation signal of the IPM machine at 20 Hz with a 6.5 Ω , 100% winding fault.	144
5.128	Voltage space-vector of the IPM machine at 30 Hz with a 5.0 Ω , 16.7% winding fault.	145
5.129	Current space-vector of the IPM machine at 30 Hz with a 5.0 Ω , 16.7% winding fault.	145
5.130	Pendulous oscillation signal of the IPM machine at 30 Hz with a 5.0 Ω , 16.7% winding fault.	145
5.131	Voltage space-vector of the IPM machine at 30 Hz with a 3.3 Ω , 16.7% winding fault.	146

5.132	Current space-vector of the IPM machine at 30 Hz with a 3.3 Ω , 16.7% winding fault.	146
5.133	Pendulous oscillation signal of the IPM machine at 30 Hz with a 3.3 Ω , 16.7% winding fault.	146
5.134	Voltage space-vector of the IPM machine at 30 Hz with a 5.0 Ω , 33.3% winding fault.	147
5.135	Current space-vector of the IPM machine at 30 Hz with a 5.0 Ω , 33.3% winding fault.	147
5.136	Pendulous oscillation signal of the IPM machine at 30 Hz with a 5.0 Ω , 33.3% winding fault.	147
5.137	Voltage space-vector of the IPM machine at 30 Hz with a 3.3 Ω , 33.3% winding fault.	148
5.138	Current space-vector of the IPM machine at 30 Hz with a 3.3 Ω , 33.3% winding fault.	148
5.139	Pendulous oscillation signal of the IPM machine at 30 Hz with a 3.3 Ω , 33.3% winding fault.	148
5.140	Voltage space-vector of the IPM machine at 40 Hz with a 5.0 Ω , 16.7% winding fault.	149
5.141	Current space-vector of the IPM machine at 40 Hz with a 5.0 Ω , 16.7% winding fault.	149
5.142	Pendulous oscillation signal of the IPM machine at 40 Hz with a 5.0 Ω , 16.7% winding fault.	149
5.143	Voltage space-vector of the IPM machine at 40 Hz with a 3.3 Ω , 16.7% winding fault.	150
5.144	Current space-vector of the IPM machine at 40 Hz with a 3.3 Ω , 16.7% winding fault.	150
5.145	Pendulous oscillation signal of the IPM machine at 40 Hz with a 3.3 Ω , 16.7% winding fault.	150

5.146	Voltage space-vector of the IPM machine at 40 Hz with a 5.0 Ω , 33.3% winding fault.	151
5.147	Current space-vector of the IPM machine at 40 Hz with a 5.0 Ω , 33.3% winding fault.	151
5.148	Pendulous oscillation signal of the IPM machine at 40 Hz with a 5.0 Ω , 33.3% winding fault.	151

Chapter 1

Introduction

1.1 Background

Interior permanent-magnet (IPM) synchronous machines are complex electromechanical energy conversion devices used to convert electrical power into mechanical rotational motion in motoring applications, and used to convert mechanical rotational motion into electrical power in generating applications [1]. As with all electric machines, the operation of the IPM machine is based on the electrically induced, rotating magnetic field theory developed in the early 20th century by Nikola Tesla and his contemporaries [2, 3]. Like the field-wound synchronous machine, the rotor in the IPM synchronous machine rotates at the synchronous speed of the rotating magnetic field produced by the stator. Unlike the field-wound synchronous machine the IPM synchronous machine does not need slip rings, brushes, and field winding coils since the rotor magnetic fields are established by the permanent magnets embedded in the rotor. This leads to higher efficiency, greater durability, and reduced maintenance as compared to the field-wound synchronous machines. For this reason the IPM synchronous machine is widely used for industrial applications where the

machine characteristics of high power density, high power factor, and high efficiency are desired or required. Common industrial applications which require these electric machine characteristics are found in the manufacturing, aerospace, and transportation industries. In these industries, as well as others, fault-tolerance, robustness, fault detection, and fault mitigation during operation can be very important to avoid hazardous operating conditions, personal injury, or material and economic loss.

The breakdown by percentage of common faults in low-voltage induction machines can be seen in Table 1.1 [4–8]. In high-voltage ac motors the percentage of winding short-circuit faults as the result of stator insulation failure may be 66% or greater [9]. Similar extensive surveys are not available for permanent-magnet machines, therefore, the percentages in Table 1.1 may not be directly applicable to permanent-magnet machines. However, because these permanent-magnet machines have 3-phase windings, these percentages are at least a starting point for evaluating the worth of studying stator winding faults. Stator faults include various winding faults such as inter-turn faults, phase-to-phase faults, phase-to-neutral faults, and phase-to-ground faults. Specifically, phase-to-phase faults are short-circuit faults between windings energized as separate phases. Phase-to-ground faults are short-circuit faults between a winding and a ground connection, and inter-turn faults are short-circuit faults between adjacent or non-adjacent winding coils or even adjacent or non-adjacent winding turns [10]. Rotor faults include field winding short-circuit faults in synchronous machines and broken rotor bars in squirrel cage induction machines.

Table 1.1: Percentages of faults in electric machines.

<i>Category of fault</i>	<i>Percentage of occurrences</i>
Stator	38%
Rotor	10%
Bearing	40%
Other	12%

Bearing faults include failure of the rotor bearings through wear, contamination, or fluting from electrical discharge, and the category of “other” faults includes the faults of various machine components not included in the other categories, such as brushes, slip rings, etc. [11]. Because stator winding faults make up a very high percentage of electric machine faults, the characterization and mitigation of such stator faults are widely studied in both academia and industry. Furthermore, unlike the squirrel-cage rotor induction machines, IPM machines are incapable of experiencing broken rotor bar faults, and unlike the field-wound synchronous machines, IPM machines are incapable of experiencing rotor winding faults other than permanent-magnet defects or damage. Therefore, it is most useful to study bearing faults and winding faults in IPM machines since, like all electric machines, IPM machines are capable of experiencing bearing and stator-winding faults.

1.2 Literature Review

1.2.1 Causes of Electric Machine Stator Winding Faults

The foremost causes of stator winding short-circuit faults are insulation degradation and failure, caused by electrical, thermal, and mechanical stresses. Even

though the terminology used is “short-circuit” fault, this does not imply that the fault is necessarily a complete short-circuit between two conductors. Rather, the terminology “short-circuit” indicates a degradation or reduction in the insulation resistance between two conductors, permitting more current than the leakage current to flow between conductors through an unintended path. The most common electrical cause of stator winding failure is the degradation of insulation over time because of overvoltage stresses on the winding dielectric material. Overvoltage stresses can be caused by operating the machine above its rated nameplate voltage, or by additive reflected waves of PWM voltage pulses generating an overvoltage at the machine terminals. The constant stress of withstanding voltages above the rated value for the winding insulation causes it to “break down,” or lose its capability to serve as an insulator. As the winding insulation degrades a small current begins to pass through the portion of the winding insulation which is failing. This smaller current creates additional current loops in the winding which did not previously exist, leading to additional and undesirable heating in the machine winding [12]. This additional heating further degrades the dielectric properties of the insulation, also accelerating the progression of the fault. Once this process starts, it generally accelerates quickly. As the insulating value decreases the the severity of the winding fault increases until it turns into a full short-circuit fault between turns, coils, or phases. Electrical and thermal causes can generate winding insulation faults separately, but once a fault starts both electrical and thermal means quickly begin contributing to the progression of the fault.

Stator winding faults caused by overvoltage stresses on the winding generally occur within the first few turns of the machine winding because it is there that the voltage gradient across the winding insulation is highest [13, 14].

Stator winding faults are caused by mechanical means when mechanical and chemical contaminants make their way into the machine winding and end-turns. Machines which operate in polluted operating environments or in environments where maintenance is difficult are especially susceptible to mechanical or chemical contamination. Mechanical contamination in the machine can physically abrade the insulation or hold onto moisture in the machine, decreasing its insulation properties at the abraded or moist spots, causing a small current to begin to flow through the insulation from one conductor to another [11, 15]. Chemical contamination which breaks down the insulation by chemical processes will lead to the same failure characteristic [11, 12].

1.2.2 Modeling and Simulation of Electric Machine Stator Winding Faults

Because stator winding faults make up a high percentage of all electric machine faults the study of the causes, detection, prognostication, mitigation, and effects of stator winding faults receive significant attention in the technical literature. To aid in developing methods for fault detection and prognostication the study of accurate modeling and simulation of electric machines under various fault conditions also receives a great deal of attention.

The two most common methods of developing stator winding fault models for simulation are those which create a network model of the machine winding with additional current loops for modeling the fault current, and those which create a finite-element model of the machine geometry with modifications in the geometry to model the fault current loops in the machine excitation. Most network models rely on some combination of linear circuit components such as resistances, inductances, and voltage sources to model the electrical characteristics of the machine. Using a linear component network model of an electric machine permits the creation of a state-space model of the faulted machine [16]. Generally the fault current loops are modeled as a resistance between turns or coils in the network to simulate the degradation of the winding insulation. Very often these resistive current loops are modeled in such a way which permits the simple addition of a few terms to the state-space model of the machine, permitting the electrical machine model to be solved with numerical methods which work fast and efficiently on ordinary differential equations [17]. Winding network models have the advantages of being simple to develop and fast to simulate, but do not contain information about the effects of the fault on the magnetic circuit of the machine.

Finite-element analysis (FEA) models of electric machines experiencing stator winding faults have the advantage of accurately modeling all of the intricate interactions between the electrical and magnetic circuits of the machine during the fault, but have the disadvantage of being much more computationally expensive and

time-consuming as compared to solving network models. Not only is FEA of the machine computationally expensive, but many of the standard techniques to reduce computation time and complexity in healthy electric machine FEA modeling cannot be used. For instance, reducing the machine geometry over which the FEA solution is performed according to boundaries of electrical and magnetic symmetry can rarely be done when including a fault since the fault eliminates the electrical and magnetic symmetry of the machine. There are techniques to work around these issues in FEA, but careful analysis of the symmetry boundaries of the machine needs to be performed [18, 19]. However, if the extended time and computational expense of modeling the entire cross-section of the machine is acceptable, FEA analysis can give very accurate fault results [20], since the FEA solution includes all the effects of time and space harmonics in the machine and most FEA software supports the use of nonlinear BH curves and other common machine nonlinearities.

1.2.3 Stator Winding Fault Detection Methods

Stator winding fault detection methods can be subdivided into two categories, off-line fault detection methods and on-line fault detection methods. Off-line stator winding fault detection methods entail removing the electric machine from its application in order to apply specialized test equipment or test processes to the stator winding to check for insulation failures and other faults [12, 21]. On-line stator winding fault detection methods are applied through measurement or estimation of

the machine waveforms during operation followed by advanced signal processing to diagnose and prognosticate winding short-circuit faults [22, 23].

Common off-line stator winding fault detection methods remove the machine from its application and apply specialized electrical test equipment to test the condition of the machine winding. One test which detects turn-to-turn direct shorts in the winding is the dc resistance test of the winding. This test will diagnose a winding short-circuit, but does not provide any information about incipient winding faults [21, 24]. High potential (HiPot) tests check the condition of the copper-to-ground insulation and will diagnose an incipient winding-to-ground fault, but do not detect phase-to-phase and turn-to-turn faults [21, 24]. Partial discharge testing is generally only performed on high-voltage motors, and again will diagnose phase-to-ground faults but not phase-to-phase and turn-to-turn faults [21]. Impulse testing, also known as surge testing, applies a voltage waveform with a very steep wavefront to the machine winding and observes the decaying oscillation of the RLC circuit formed by the test equipment and the machine winding, and will diagnose incipient phase-to-phase and turn-to-turn faults [15, 21, 24].

Common on-line stator winding fault detection methods utilize real-time measurements of machine waveforms coupled with advanced signal processing techniques to diagnose a winding fault without interrupting the operation of the machine. Motor current spectrum analysis is one technique for diagnosing winding faults by observing

new harmonic components which arise in the current spectrum under faulty conditions [4]. Similarly, negative sequence components analysis is also used for winding fault diagnosis by decomposing imbalanced waveforms into positive, negative, and zero sequence components; however, this method is susceptible false diagnosis if the machine contains inherent imbalances or the machine excitation supply is slightly imbalanced [23]. One technique which was developed to minimize the effects of supply imbalances is the negative sequence impedance analysis, which uses the ratio of the the negative sequence voltage over the negative sequence current as a fault index since it is nearly constant over a wide range of operating conditions [23, 25]. Other on-line fault diagnosis methods include the instantaneous power spectrum analysis [26], the use of search coils [27], back EMF estimation [28], and the use of artificial intelligence techniques such as neural networks and fuzzy logic for automating the diagnosis process [29].

1.3 Statement of the Problem

With the great increase in the use of permanent-magnet electric machines in various applications, the need for accurate fault diagnostics has increased dramatically. Various methods for stator winding short-circuit fault diagnosis have been successfully applied and verified for induction motors, but the use of these methods for detecting and prognosticating stator winding short-circuit faults in interior permanent-magnet machines has not been studied as thoroughly. In this thesis, three

common stator winding short-circuit fault diagnosis methods will be applied to experimental short-circuit fault data acquired from a case-study experimental 3.5 hp IPM machine. These three fault diagnostics methods will be compared with regard to their ability to accurately diagnose the occurrence and prognosticate the deterioration of a winding short-circuit fault in this IPM machine. Experimental results from the IPM machine in both a motoring test setup as well as a generating test setup will be presented, as fault detection and prognostication is difficult and inconsistent under sensorless ac drive excitation. The use of the IPM machine in a generating application permits the analysis of the applicability of the fault diagnosis methods to the machine alone.

Chapter 2

Stator Winding Short-Circuit Fault Detection Methods

The theoretical development of three common stator winding short-circuit fault detection methods is presented in this chapter. First the well-known motor current spectrum analysis (MCSA) [4] method will be presented, followed by negative sequence components analysis [30], and lastly by the space-vector pendulous oscillation method [31].

2.1 Motor Current Spectrum Analysis

Motor current spectrum analysis (MCSA), as its title implies, uses the frequency spectrum of the electric machine phase current to diagnose and prognosticate a winding fault. The following equation has been empirically developed and verified for predicting the frequency components which may increase in the current frequency spectrum under fault conditions [4]:

$$f_{fault} = f_1 \left\{ \frac{n}{p} (1 - s) \pm k \right\} \quad (2.1)$$

where f_{fault} is the frequency component that appears for winding faults, f_1 is the fundamental operating frequency, n is an index of integer values 1, 2, 3, ...; k is an index of integer values 1, 2, 3, ...; p is the number of pole pairs in the machine, and s is the slip. For electric machines which rotate synchronously with zero slip Equation 2.1 simplifies to

$$f_{fault} = f_1 \left\{ \frac{n}{p} \pm k \right\} \quad (2.2)$$

Oftentimes under fault conditions the third harmonic of the fundamental frequency significantly increases in the current spectrum, as predicted by Equation 2.2 and presented in Equation 2.3 [32, 33]. The ninth and twenty-seventh harmonic of the fundamental frequency, as seen in Equation 2.4 through Equation 2.5 will also be observed in this work.

$$f_{fault3rd} = 3f_1 \quad (2.3)$$

$$f_{fault9th} = 9f_1 \quad (2.4)$$

$$f_{fault27th} = 27f_1 \quad (2.5)$$

Of significant importance in applying MCSA to a waveform is selecting an appropriate window to use in calculating the frequency spectrum from time-domain

data [34]. Poor selection of the windowing function may result in the masking of the fault-generated harmonic components if the sidebands do not roll-off from the significant frequency components at a sufficiently fast rate. Three common windowing functions used for FFT analysis of data include the rectangular window seen in Figure 2.2, the triangular window seen in Figure 2.3, and the Blackman-Harris window seen in Figure 2.4 [35]. The rectangular window is the most basic window but can mask small harmonic components because of the slow roll-off of the sidebands, while the Blackman-Harris window is a more complex sum of sinusoids but the sidebands generated from the Blackman-Harris window roll-off at the much faster rate. Given a sum of sinusoids with small 3rd and 9th harmonics as seen in Equation 2.6, the results of applying an FFT utilizing the three previously mentioned windows can be seen in Figure 2.5 through 2.7. Notice how much more strongly the small 3rd and 9th harmonic components of $y(t)$ appear in the frequency spectrum of Figure 2.7 as compared to Figure 2.5.

$$y(t) = \sin(2\pi ft) + \frac{1}{500} \sin(2\pi 3ft) + \frac{1}{1000} \sin(2\pi 9ft) \quad (2.6)$$

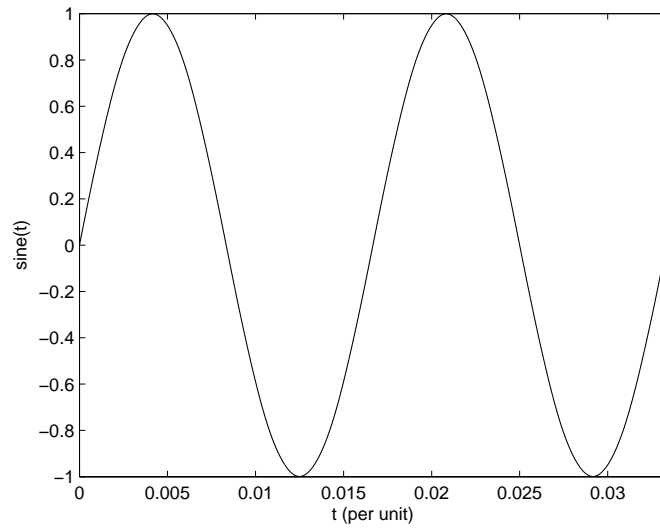


Figure 2.1: Time-domain waveforms of Equation 2.6.

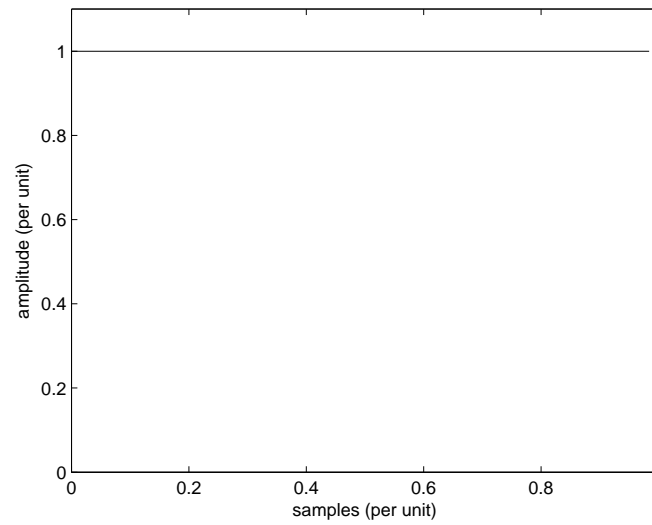


Figure 2.2: Rectangular window.

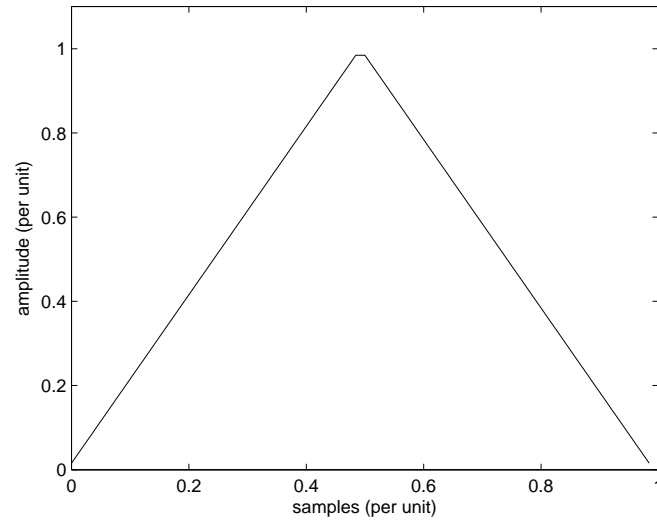


Figure 2.3: Triangular window.

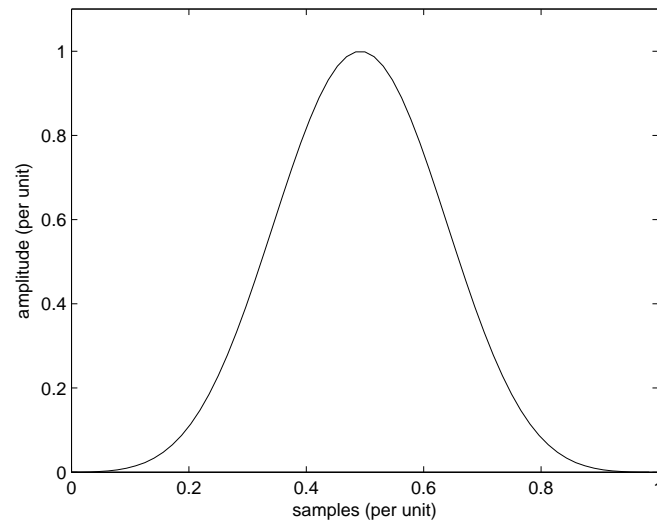


Figure 2.4: Blackman-Harris window.

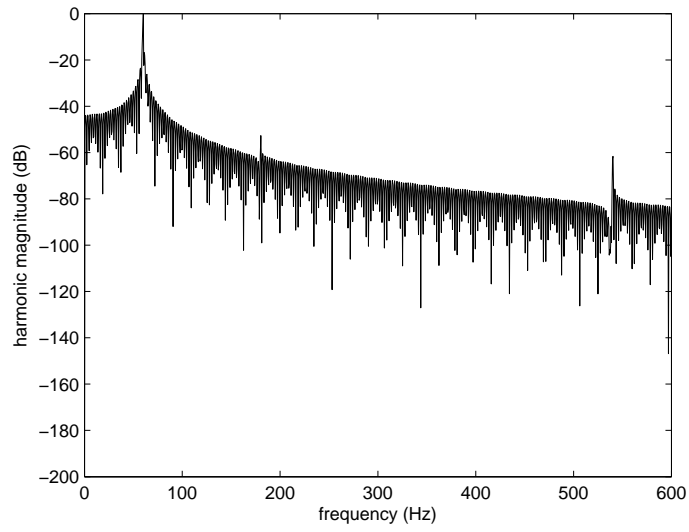


Figure 2.5: FFT of $y(t)$ using a rectangular window.

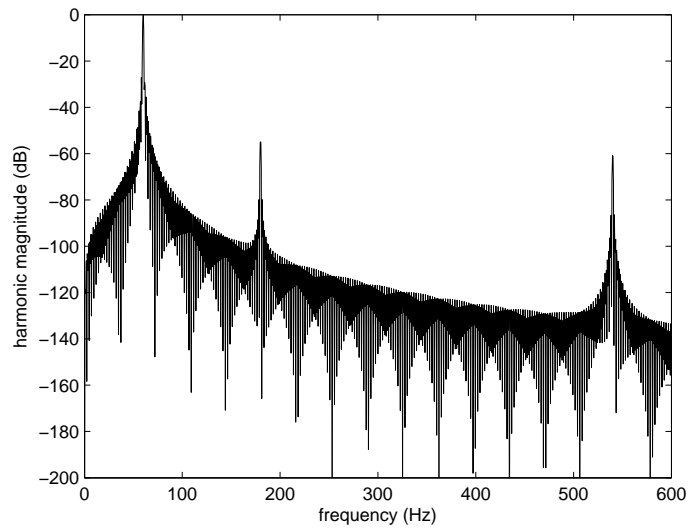


Figure 2.6: FFT of $y(t)$ using a triangular window.

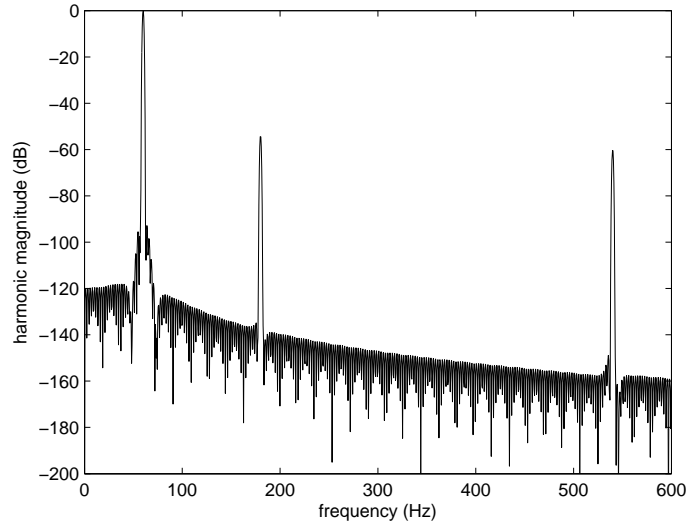


Figure 2.7: FFT of $y(t)$ using a Blackman-Harris window.

2.2 Negative Sequence Components Analysis

The negative sequence components analysis uses a symmetrical components transformation applied to the fundamental frequency components of the three-phase current waveforms to decompose the three phase current phasors into zero sequence, positive sequence, and negative sequence current phasors [36]. Perfectly balanced, forward-sequenced three-phase phasors will only generate a positive sequence phasor when transformed, but any imbalances in the waveforms will be decomposed into the zero sequence and negative sequence phasors resulting from the transform. The application of negative sequence components analysis to the study of electric machine faults is drawn from three-phase power systems fault analysis [30], where under healthy conditions the power system voltage and current phasors will transform solely

into positive sequence phasors. This analysis method works well [19] for balanced, well-designed machines with nearly perfectly balanced waveforms.

The symmetrical components transformation is given in Equation 2.7 [36]:

$$\begin{bmatrix} \mathbf{I}_0 \\ \mathbf{I}_1 \\ \mathbf{I}_2 \end{bmatrix} = \frac{1}{3} \begin{bmatrix} 1 & 1 & 1 \\ 1 & \alpha & \alpha^2 \\ 1 & \alpha^2 & \alpha \end{bmatrix} \begin{bmatrix} \mathbf{I}_{a1} \\ \mathbf{I}_{b1} \\ \mathbf{I}_{c1} \end{bmatrix} \quad (2.7)$$

where

$$\alpha = e^{j\frac{2\pi}{3}} \quad (2.8)$$

The phasor quantities \mathbf{I}_{a1} , \mathbf{I}_{b1} , and \mathbf{I}_{c1} are the fundamental components of the phase A, phase B, and phase C currents, respectively, while the output phasors \mathbf{I}_0 , \mathbf{I}_1 , and \mathbf{I}_2 are the zero-sequence component, the positive-sequence component, and the negative sequence component of the phase current, respectively.

For example, applying the symmetrical components transformation to the set of imbalanced cosinusoids given in Equations 2.9 through 2.11, which are graphed in Figure 2.8, gives phasors with magnitudes as shown in Table 2.1. Note that the magnitude imbalance in the time-domain waveforms is decomposed into non-zero negative and non-zero zero sequence phasors.

$$y_a(t) = \cos(2\pi ft) = 1\angle 0 \quad (2.9)$$

$$y_b(t) = 1.25 \cos\left(2\pi ft - \frac{2\pi}{3}\right) = 1.25\angle(-2\pi/3) \quad (2.10)$$

$$y_c(t) = 1.5 \cos\left(2\pi ft - \frac{4\pi}{3}\right) = 1.5 \angle(-4\pi/3) \quad (2.11)$$

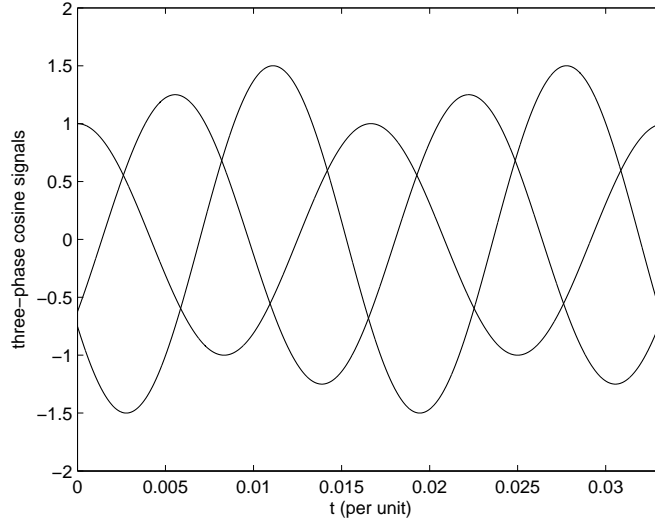


Figure 2.8: Imbalanced cosinusoidal waveforms.

Table 2.1: Magnitude of the symmetrical component phasors of the above waveforms.

<i>Positive</i>	<i>Negative</i>	<i>Zero</i>
1.212	0.139	0.140

2.3 Space-Vector Pendulous Oscillation Method

The space-vector pendulous oscillation method uses the magnitude of the time-varying oscillation between the rotating machine voltage and machine current space vectors to indicate and prognosticate a stator winding fault [31]. The voltage and current space-vectors are calculated from the time-domain voltage and current waveforms, as given in Equation 2.12 and Equation 2.13 respectively [31]. These time-varying

voltage and current space-vectors may be used to compute the “pendulous oscillation” signal of the machine as given Equation 2.15 [31]. The pendulous oscillation signal obtains its name from the fact that the angle between the voltage and current space-vectors rotating in the complex plane may be periodic, not constant. In a well balanced machine, the pendulous oscillation signal is composed of a fundamental frequency plus higher harmonics of small magnitudes. Under fault conditions, harmonics of larger magnitudes may begin to appear in the pendulous oscillation signal [31]. A fault index drawn from the pendulous oscillation signal, the “swing angle,” may be defined either as the peak-to-peak measurement of the fundamental frequency component of the pendulous oscillation signal [31, 37], or may be defined simply as the peak-to-peak measurement of the entire harmonic-rich waveform. Under fault conditions the swing angle may increase as compared to the healthy machine swing angle [31].

$$\bar{v}_s(t) = \frac{2}{3} (v_{an}(t) + \alpha v_{bn}(t) + \alpha^2 v_{cn}(t)) \quad (2.12)$$

$$\bar{i}_s(t) = \frac{2}{3} (i_a(t) + \alpha i_b(t) + \alpha^2 i_c(t)) \quad (2.13)$$

In Equation 2.12 and Equation 2.13, $\bar{v}_s(t)$ and $\bar{i}_s(t)$, are the time-domain voltage and current space-vectors, respectively, while v_{an} , v_{bn} , and v_{cn} are the phase voltages

and i_a , i_b , and i_c are the phase currents. The complex shift operator α is given as

$$\alpha = e^{j\frac{2\pi}{3}} \quad (2.14)$$

The pendulous oscillation of the angle between the voltage space-vector $\bar{v}_s(t)$ and the current space vector $\bar{i}_s(t)$ is given as:

$$\delta(t) = \angle \bar{v}_s(t) - \angle \bar{i}_s(t) \quad (2.15)$$

where $0 \leq \delta(t) < 2\pi \text{ e.rad}$. Hence the swing angle, $\Delta\delta_{sc}(t)$, can be defined as:

$$\Delta\delta_{sc}(t) = \max[\delta(t)] - \min[\delta(t)] \quad (2.16)$$

For a healthy and balanced three-phase electric machine, the pendulous oscillation angle for each instant of time is approximately constant. However, during inter-turn fault conditions, the voltage and current space-vectors experience distortions from their original healthy case, which could lead to variations in the pendulous oscillation angle, $\delta(t)$, with time and an increase in the swing angle, $\Delta\delta_{sc}(t)$. According to previous work done in [31], for induction machines the swing angle is proportional to the ratio between the magnitude of the circulating current in the shorted turns and the phase current, namely, the shorted-circuit current ratio in the winding.

Consider the three imbalanced three-phase voltage waveforms and three-phase current waveforms as expressed in Equation 2.17 through Equation 2.22:

$$v_a(t) = \cos(2\pi ft) \quad (2.17)$$

$$v_b(t) = 1.25 \cos\left(2\pi ft - \frac{2\pi}{3}\right) \quad (2.18)$$

$$v_c(t) = 1.5 \cos\left(2\pi ft - \frac{4\pi}{3}\right) \quad (2.19)$$

$$i_a(t) = 1.5 \cos\left(2\pi ft - \frac{\pi}{3}\right) \quad (2.20)$$

$$i_b(t) = 1.25 \cos\left(2\pi ft - \frac{2\pi}{3} - \frac{\pi}{3}\right) \quad (2.21)$$

$$i_c(t) = \cos\left(2\pi ft - \frac{4\pi}{3} - \frac{\pi}{3}\right) \quad (2.22)$$

From these time-domain waveforms the voltage space-vector and the current-space vector can be calculated using Equation 2.12 and Equation 2.13, as shown in Figure 2.9 and Figure 2.10. From the voltage and current space-vectors the the pendulous oscillation signal can be calculated using Equation 2.15 and can be seen in Figure 2.11. The peak-to-peak value of the pendulous oscillation signal, the swing angle, may be used as a fault index.

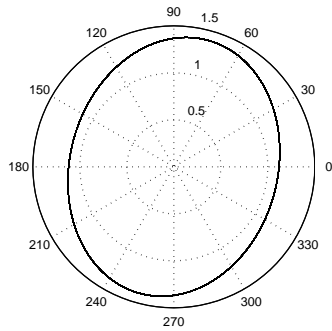


Figure 2.9: Voltage space-vector example.

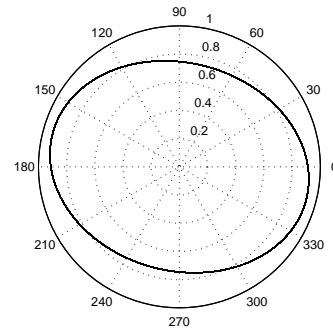


Figure 2.10: Current space-vector example.

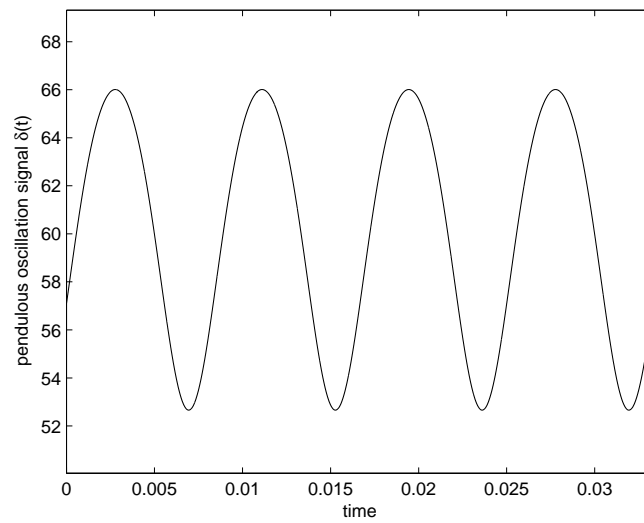


Figure 2.11: Pendulous oscillation signal example from the example voltage and current space-vectors.

Chapter 3

Interior Permanent-Magnet Machine Experimental Setup

In this chapter the specifications and properties of the experimental IPM machine are presented, as well as the experimental setup for both motoring operation and generating operation. Included in this chapter is the machine geometry cross-section, the rated machine specifications, and the Fourier series for the induced electromotive forces (emfs) and self and mutual winding inductances. The Fourier series for the induced electromotive forces and winding inductances were obtained from finite-element analysis of the machine performed in previous work. The experimental section describes the test setup and the winding configurations for the various short-circuit tests.

3.1 Specifications and Properties of the Experimental IPM Machine

The cross-section of the experimental case-study IPM machine is given in Figure 3.1. The rated operating conditions of this experimental IPM machine are presented in Table 3.1 and Table 3.2, and the key parameters of this machine are presented in Table 3.3 and Table 3.4.

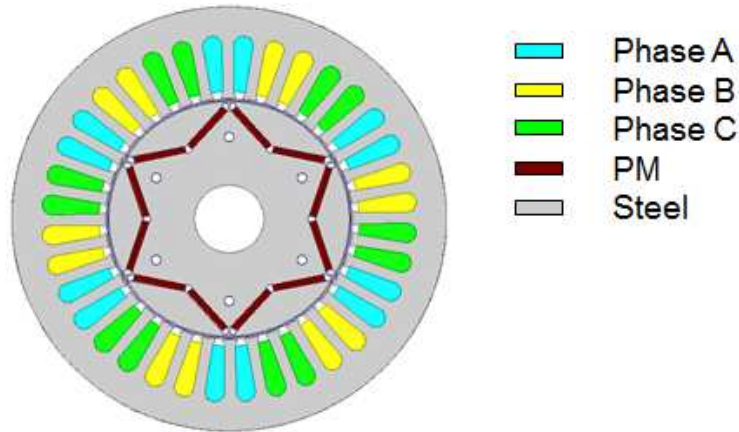


Figure 3.1: Cross-section of the case-study experimental IPM machine.

Table 3.1: Ratings of the 3.5 hp IPM machine for the three parallel path winding configuration.

<i>Quantity</i>	<i>Rating</i>
Rated power	3.5 hp = 2611 Watts
Rated speed	3450 rev/min
Rated torque	7.25 Newton-meters
Rated current	10 Amperes
Rated voltage	230 Volts
Stator winding	Single layer

Table 3.2: Ratings of the 3.5 hp IPM machine for the single path winding configuration.

<i>Quantity</i>	<i>Rating</i>
Rated power	3.5 hp = 2611 Watts
Rated speed	3450 rev/min
Rated torque	7.25 Newton-meters
Rated current	3.33 Amperes
Rated voltage	690 Volts
Stator winding	Single layer

Table 3.3: Key parameters of the 3.5 hp IPM machine for the three parallel path winding configuration.

<i>Parameter</i>	<i>Value</i>
No. of paths/phase	3
No. of coils/path	2
No. of turns per coil	60
No. of stator slots	36
No. of poles	6

Table 3.4: Key parameters of the 3.5 hp IPM machine for the single path winding configuration.

<i>Parameter</i>	<i>Value</i>
No. of paths/phase	1
No. of coils/path	6
No. of turns per coil	60
No. of stator slots	36
No. of poles	6

The Fourier series for the induced electromotive forces e_a , e_b , and e_c of the IPM machine are given as follows:

$$e_a(\sigma) = \omega_m \sum_{n=1}^{13} A_n \cos[n(\sigma) - \psi_n] \text{ Volts} \quad (3.1)$$

$$e_b(\sigma) = \omega_m \sum_{n=1}^{13} A_n \cos \left[n \left(\sigma - \frac{2\pi}{3} \right) - \psi_n \right] \text{ Volts} \quad (3.2)$$

$$e_c(\sigma) = \omega_m \sum_{n=1}^{13} A_n \cos \left[n \left(\sigma - \frac{4\pi}{3} \right) - \psi_n \right] \text{ Volts} \quad (3.3)$$

In the expressions for e_a , e_b , and e_c , ω_m is the rotor speed in mechanical radians per second (mech. rad/s) and the harmonic parameters are given in Table 3.5.

Table 3.5: EMF harmonic parameters of the 3.5 hp IPM motor.

n	A_n (Volts/mech.rad/s)	ψ_n (rad)
1	0.446408183760739	1.5702
3	0.101322835502239	1.5717
5	0.01889179563213	1.5854
7	0.0108144313274237	-1.5765
9	0.0138030048540252	-1.5583
11	0.018994264706141	1.5667
13	0.00887310386433631	1.5787

The values of the phase resistances and the expressions for the winding inductances of this experimental IPM machine are given in Equation 3.4 through Equation 3.10.

$$r_a = r_b = r_c = r_s = 0.49 \Omega \quad (3.4)$$

$$L_{aa} = [6.008607 + 1.981518 \cos(2\sigma) + 0.274595 \cos(4\sigma)] \cdot 10^{-3} H \quad (3.5)$$

$$L_{bb} = \left[6.008607 + 1.981518 \cos\left(2\sigma - \frac{4\pi}{3}\right) + 0.274595 \cos\left(4\sigma - \frac{2\pi}{3}\right) \right] \cdot 10^{-3} H \quad (3.6)$$

$$L_{cc} = \left[6.008607 + 1.981518 \cos\left(2\sigma - \frac{2\pi}{3}\right) + 0.274595 \cos\left(4\sigma - \frac{4\pi}{3}\right) \right] \cdot 10^{-3} H \quad (3.7)$$

$$L_{ab} = L_{ba} = \left[-1.940512 - 1.529431 \sin\left(2\sigma - \frac{\pi}{3}\right) - 0.08451 \sin\left(4\sigma - \frac{2\pi}{3}\right) \right] \cdot 10^{-3} H \quad (3.8)$$

$$L_{bc} = L_{cb} = \left[-1.940512 - 1.529431 \sin\left(2\sigma - \frac{5\pi}{3}\right) - 0.08451 \sin\left(4\sigma - \frac{4\pi}{3}\right) \right] \cdot 10^{-3} H \quad (3.9)$$

$$L_{ca} = L_{ac} = \left[-1.940512 - 1.529431 \sin(2\sigma - \pi) - 0.08451 \sin(4\sigma) \right] \cdot 10^{-3} H \quad (3.10)$$

3.2 Experimental Setup and Test Equipment

The phase winding configurations used for the various short-circuit tests of this IPM machine are shown in Figure 3.2 through Figure 3.6. Figure 3.7 and Figure 3.8 show the actual resistance board used for the short-circuit tests as well as the terminal block providing access to all eighteen coils in this experimental machine. This access to all eighteen machine winding coils permitted testing with various percentages of the winding short-circuited, as well as permitted reconfiguring the winding between three parallel paths per phase and one path per phase. For the motoring tests the drive used was a Yaskawa V1000 sensorless ac electric drive with a PWM carrier frequency of 5 kHz.

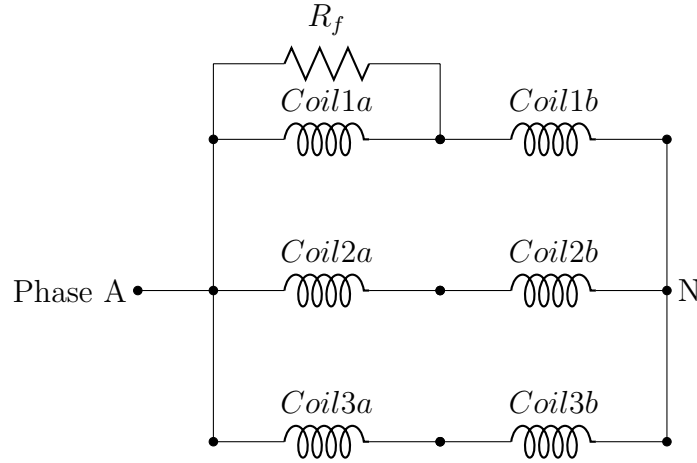


Figure 3.2: Schematic of one phase with a 16.7% winding fault used for the motor tests.

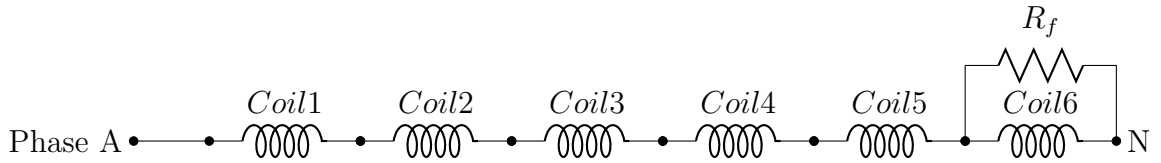


Figure 3.3: Schematic of one phase with a 16.7% winding fault used for the generator tests.

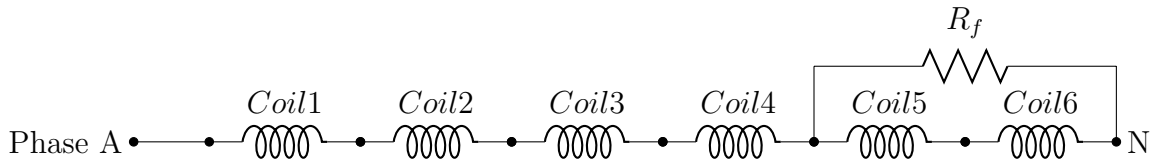


Figure 3.4: Schematic of one phase with a 33.3% winding fault used for the generator tests.

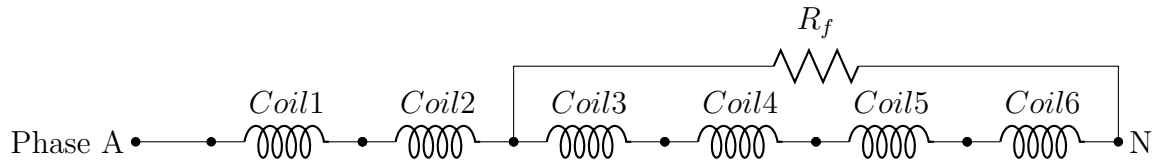


Figure 3.5: Schematic of one phase with a 66.7% winding fault used for the generator tests.

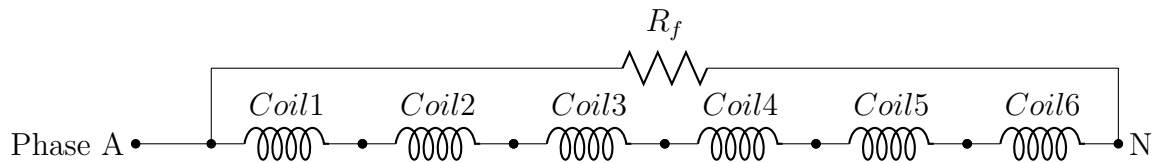


Figure 3.6: Schematic of one phase with a 100% winding fault used for the generator tests.

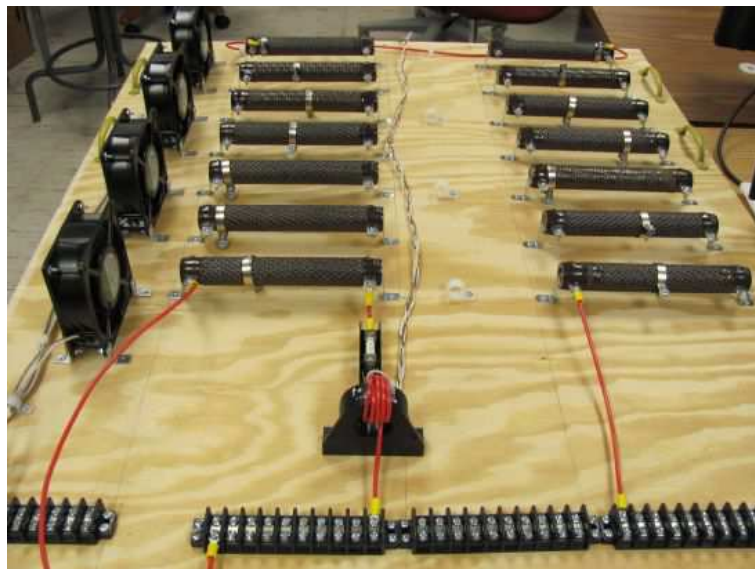


Figure 3.7: Resistance board for providing the winding short-circuit fault.



Figure 3.8: Experimental machine with dynamometer test bed.

Chapter 4

Experimental IPM Machine Results - Motoring Operation

In this chapter the experimental results from various winding short-circuit tests performed with the IPM machine energized as a motor are presented. Furthermore, the application of the three winding short-circuit fault diagnosis methods to the experimental data and the analysis of the results is also presented.

The following experimental results demonstrate the effect of various short-circuit winding fault resistances across one coil of the machine phase winding as shown in Figure 3.2 for half-speed, half-load operation and half-speed, three-quarters-load operation, where half-speed is 86.25 Hz. The experiments were performed at one-half the rated speed of the IPM machine because of the speed limitations of the available dynamometer load. However, the dynamometer did not have a similar constraint on the operating torque, permitting testing at both the one-half and three-quarter-load torque of the IPM machine.

4.1 Time-Domain Phase Voltages and Phase Currents

The various experimental voltage and current time-domain results for the IPM machine at different speed and torque test points and for increasing fault severity/decreasing fault resistances are shown in Figure 4.1 through Figure 4.30. As seen in Figure 4.1 through Figure 4.6, the current sensors contain a slight bias illustrated by the slight distortion and imbalance in the healthy phase currents. The line-to-neutral voltage was “smoothed” using a localized weighted linear least squares regression with a first degree polynomial model as seen in Figure 4.2. The inclusions of the “smoothed” Line-to-neutral voltage as seen in Figure 4.2 and Figure 4.5 is for convenience of calculating the voltage space-vector in the last section of this chapter. Because of the bandwidth limitations of the data acquisition system, the switching of the PWM voltage waveform was severely aliased, leading to poor space-vector transform results when including the aliased PWM switching.

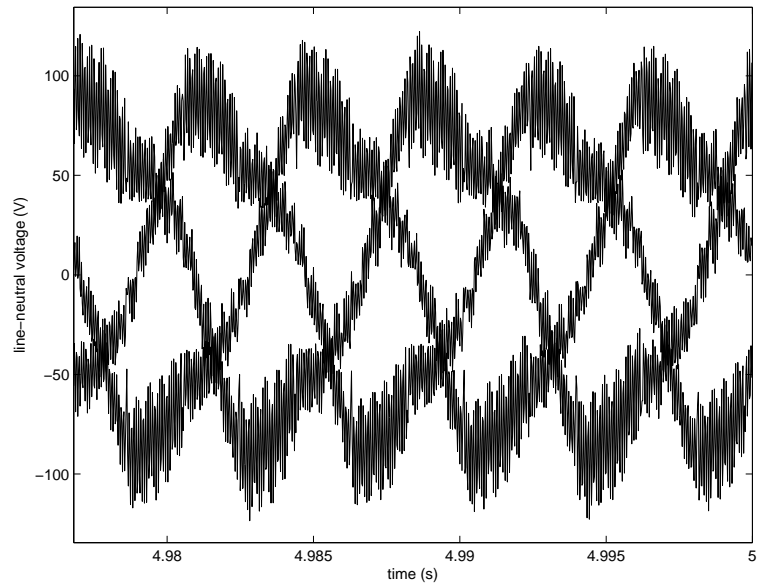


Figure 4.1: Line-to-neutral voltage of the IPM machine at 86.25 Hz, half-load, with no winding fault.

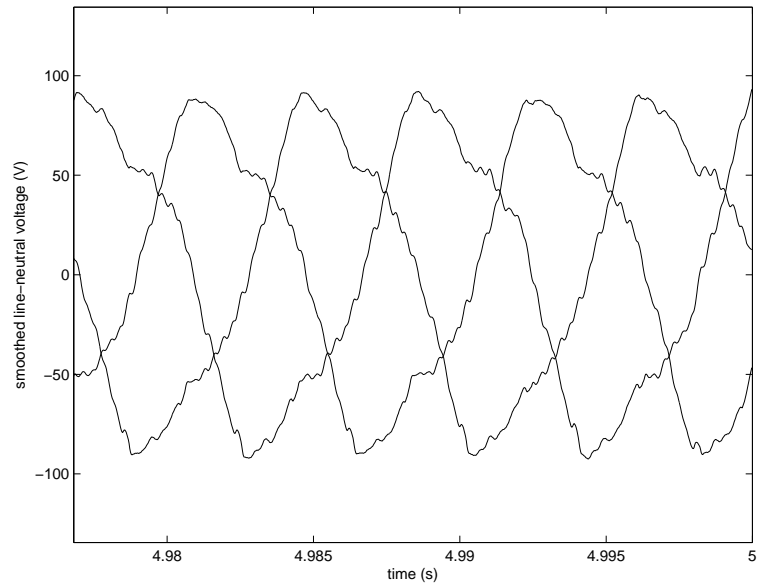


Figure 4.2: Smoothed line-to-neutral voltage of the IPM machine at 86.25 Hz, half-load, with no winding fault.

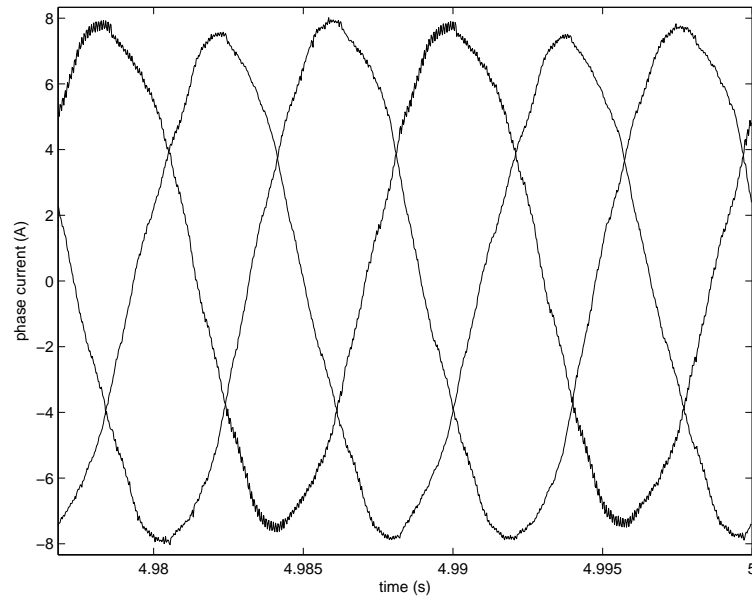


Figure 4.3: Phase current of the IPM machine at 86.25 Hz, half-load, with no winding fault.

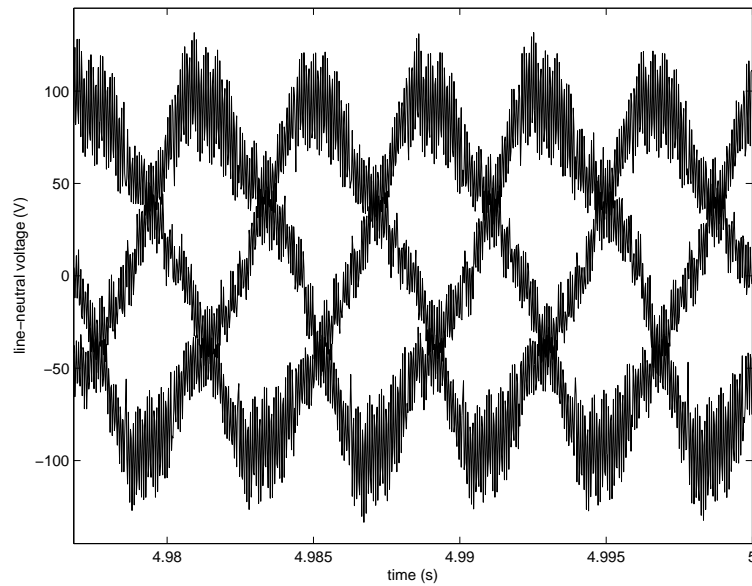


Figure 4.4: Line-to-neutral voltage of the IPM machine at 86.25 Hz, three-quarter-load, with no winding fault.

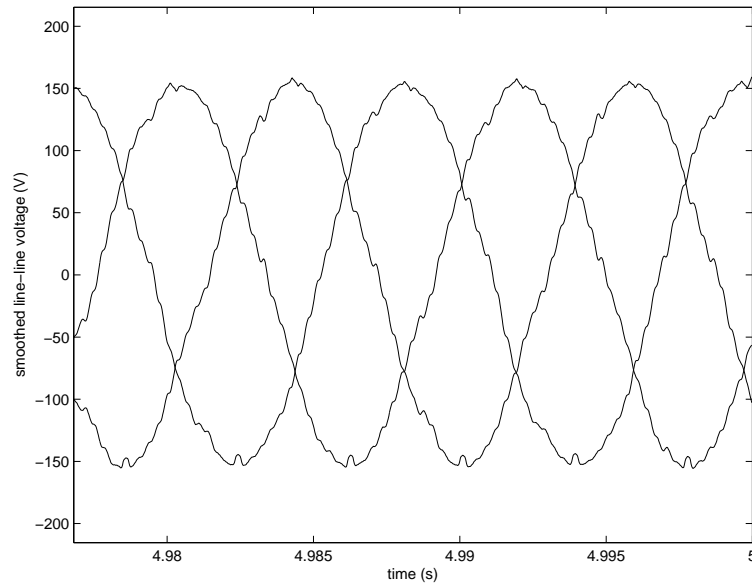


Figure 4.5: Smoothed line-to-neutral voltage of the IPM machine at 86.25 Hz, three-quarter-load, with no winding fault.

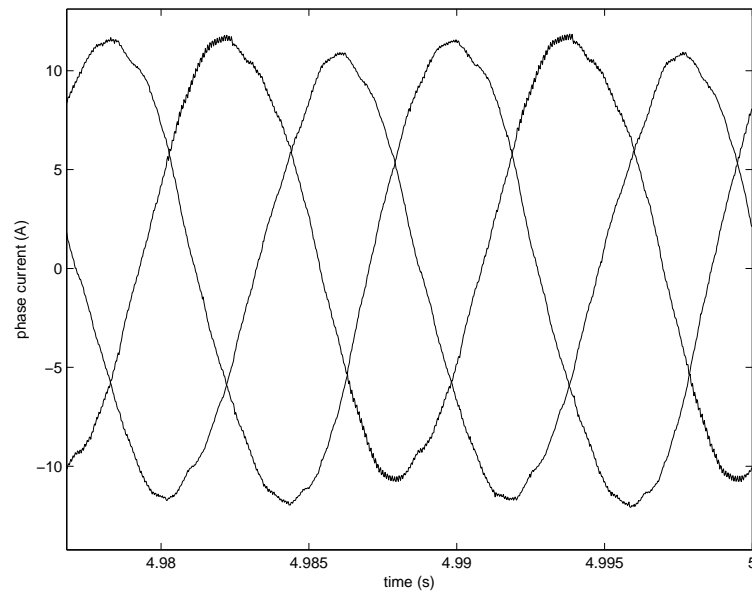


Figure 4.6: Phase current of the IPM machine at 86.25 Hz, three-quarter-load, with no winding fault.

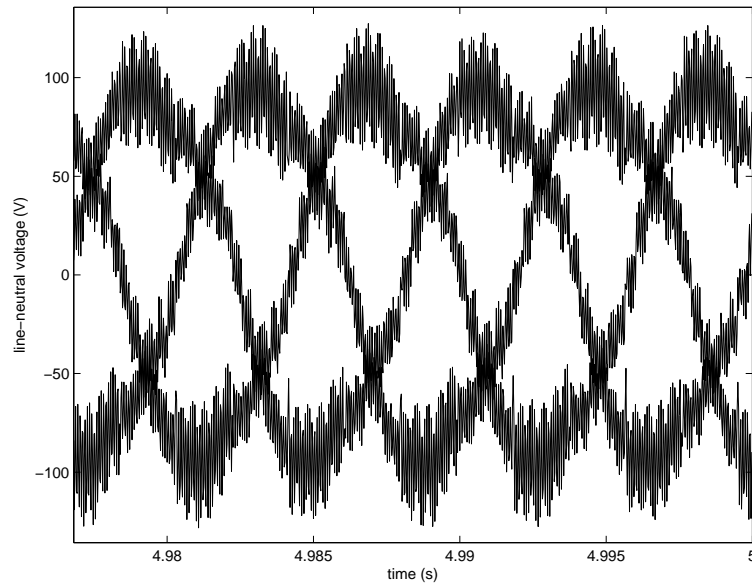


Figure 4.7: Line-to-neutral voltage of the IPM machine at 86.25 Hz, half-load, with a 9.66Ω , 16.7% winding fault.

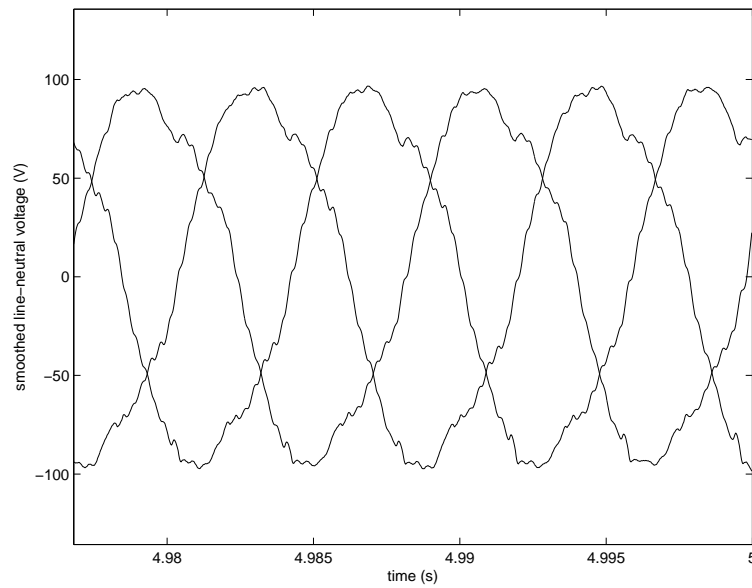


Figure 4.8: Smoothed line-to-neutral voltage of the IPM machine at 86.25 Hz, half-load, with a 9.66Ω , 16.7% winding fault.

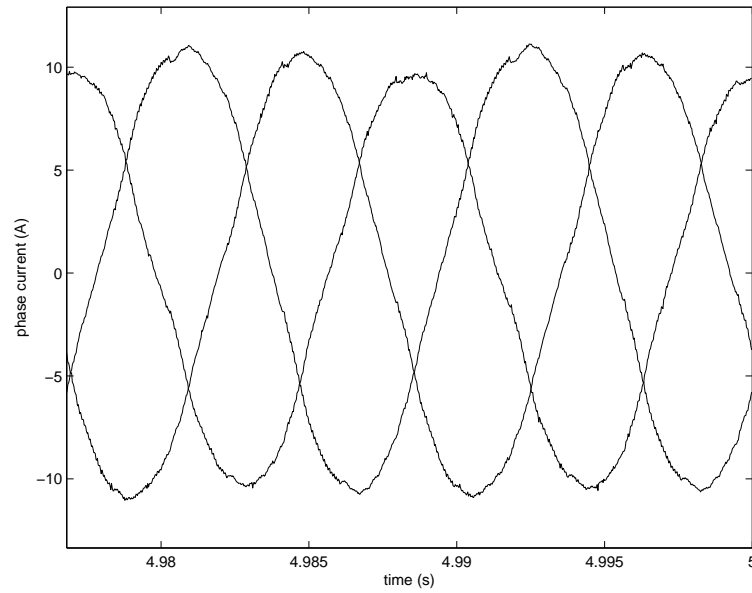


Figure 4.9: Phase current of the IPM machine at 86.25 Hz, half-load, with a 9.66Ω , 16.7% winding fault.

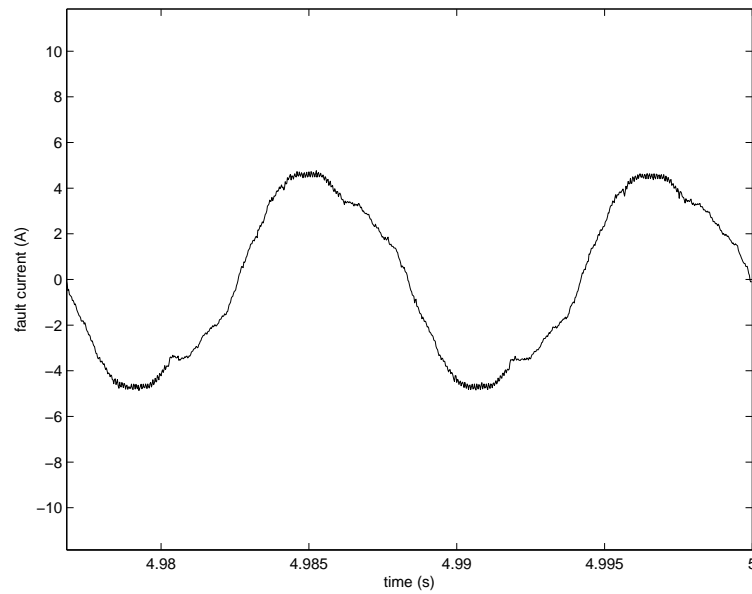


Figure 4.10: Fault current of the IPM machine at 86.25 Hz, half-load, with a 9.66Ω , 16.7% winding fault.

The experimental results for increasing fault severity/decreasing fault resistance are shown in Figure 4.11 through Figure 4.30. As the fault becomes more severe, the magnitude of the time-domain currents becomes increasingly imbalanced yet the currents do not become significantly distorted. This is likely because of the current control in the ac drive.

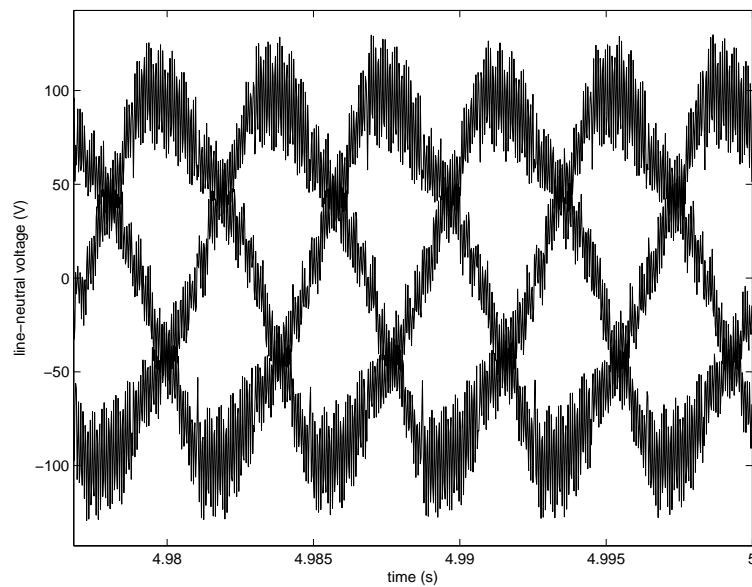


Figure 4.11: Line-to-neutral voltage of the IPM machine at 86.25 Hz, three-quarter-load, with a 9.66Ω , 16.7% winding fault.

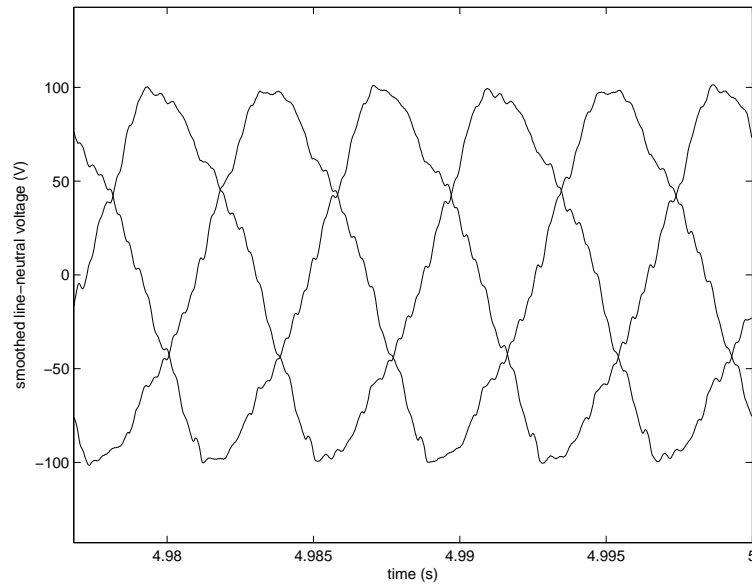


Figure 4.12: Smoothed line-to-neutral voltage of the IPM machine at 86.25 Hz, three-quarter-load, with a 9.66Ω , 16.7% winding fault.

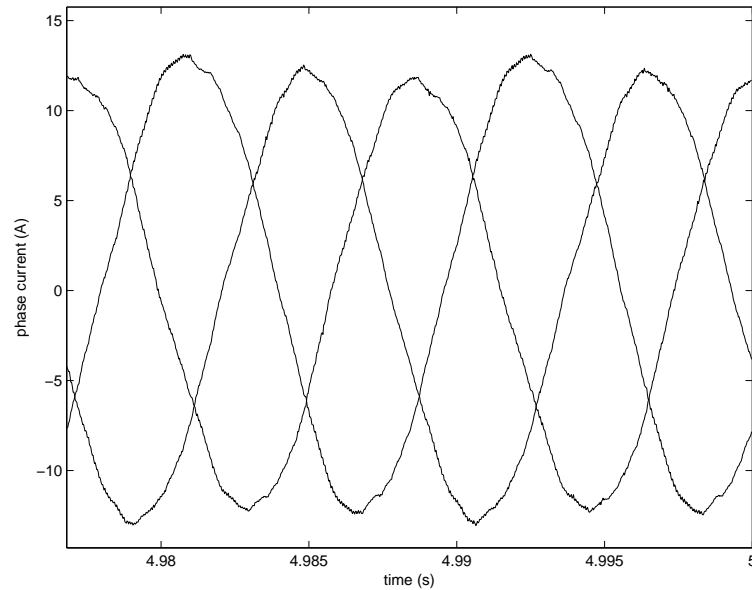


Figure 4.13: Phase current of the IPM machine at 86.25 Hz, three-quarter-load, with a 9.66Ω , 16.7% winding fault.

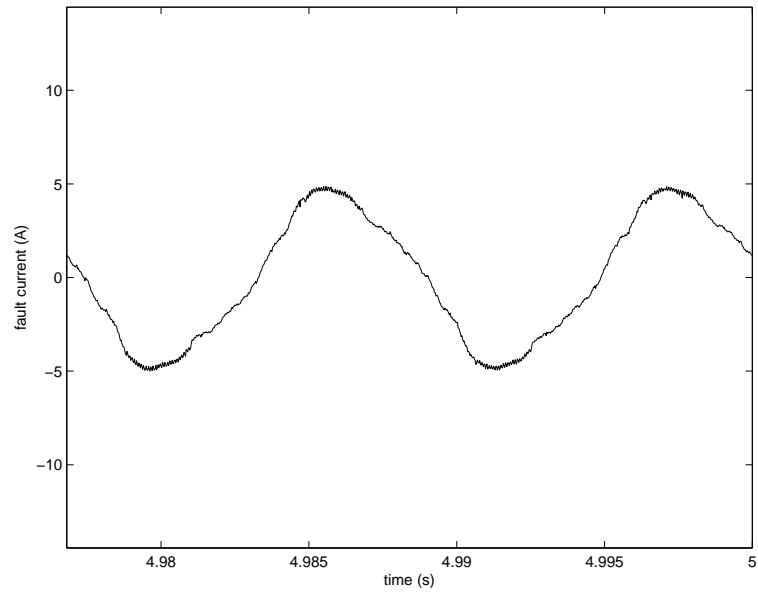


Figure 4.14: Fault current of the IPM machine at 86.25 Hz, three-quarter-load, with a 9.66Ω , 16.7% winding fault.

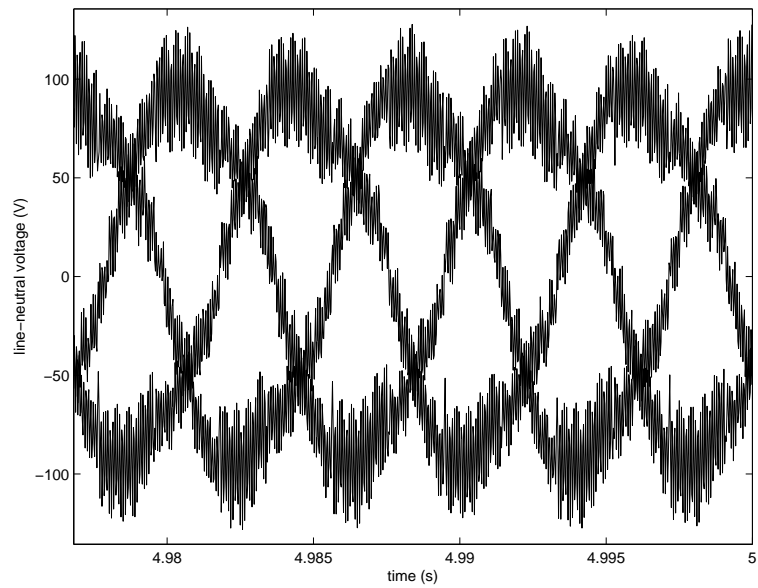


Figure 4.15: Line-to-neutral voltage of the IPM machine at 86.25 Hz, half-load, with a 7.25Ω , 16.7% winding fault.

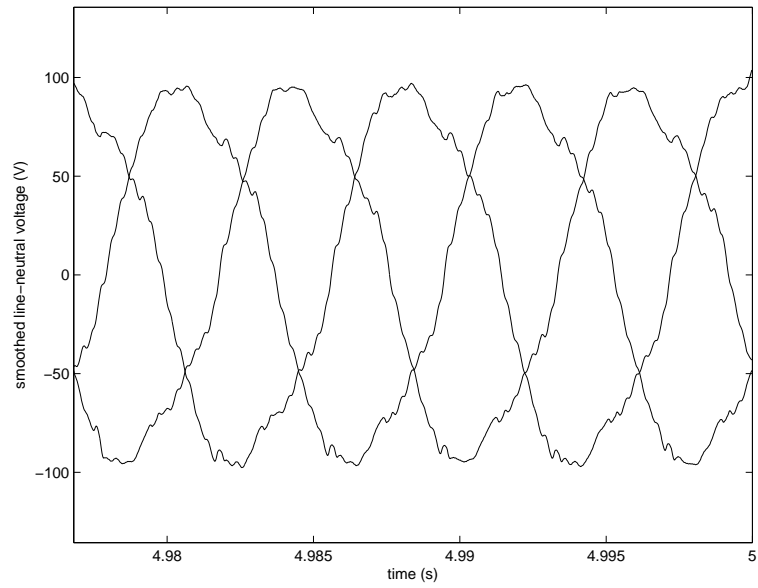


Figure 4.16: Smoothed line-to-neutral voltage of the IPM machine at 86.25 Hz, half-load, with a 7.25Ω , 16.7% winding fault.

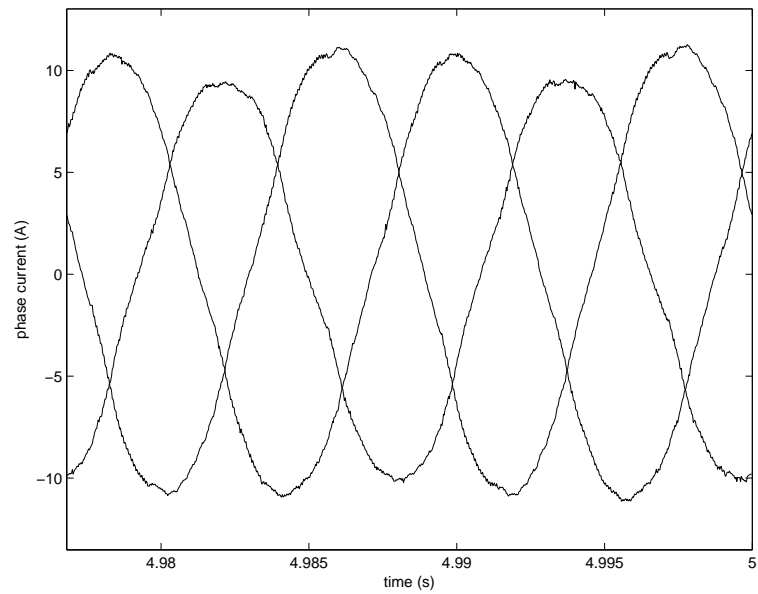


Figure 4.17: Phase current of the IPM machine at 86.25 Hz, half-load, with a 7.25Ω , 16.7% winding fault.

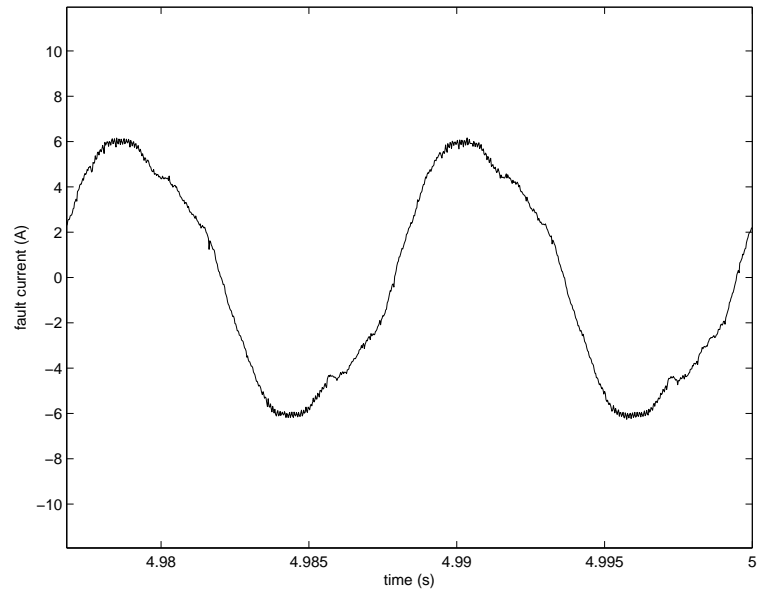


Figure 4.18: Fault current of the IPM machine at 86.25 Hz, half-load, with a 7.25Ω , 16.7% winding fault.

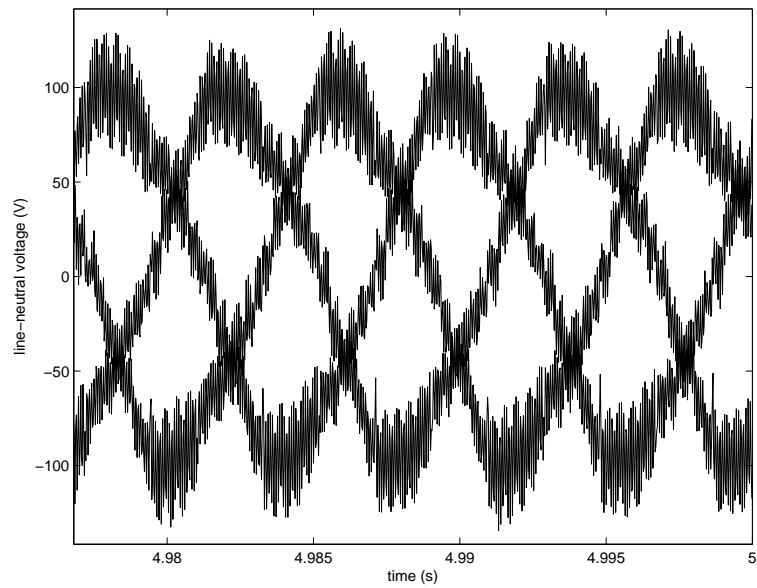


Figure 4.19: Line-to-neutral voltage of the IPM machine at 86.25 Hz, three-quarter-load, with a 7.25Ω , 16.7% winding fault.

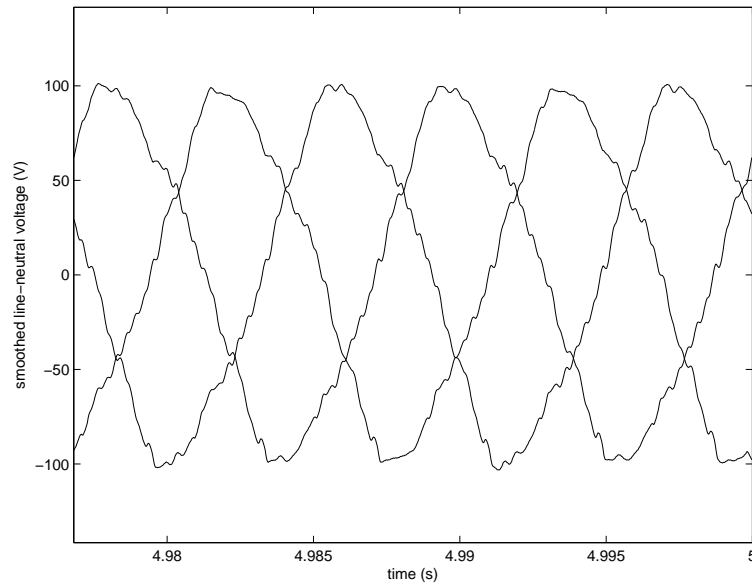


Figure 4.20: Smoothed line-line voltage of the IPM machine at 86.25 Hz, three-quarter-load, with a 7.25Ω , 16.7% winding fault.

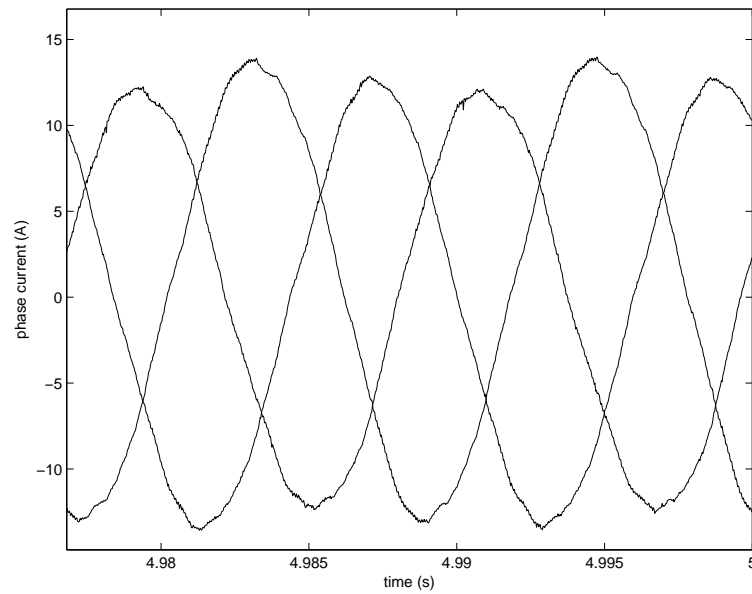


Figure 4.21: Phase current of the IPM machine at 86.25 Hz, three-quarter-load, with a 7.25Ω , 16.7% winding fault.

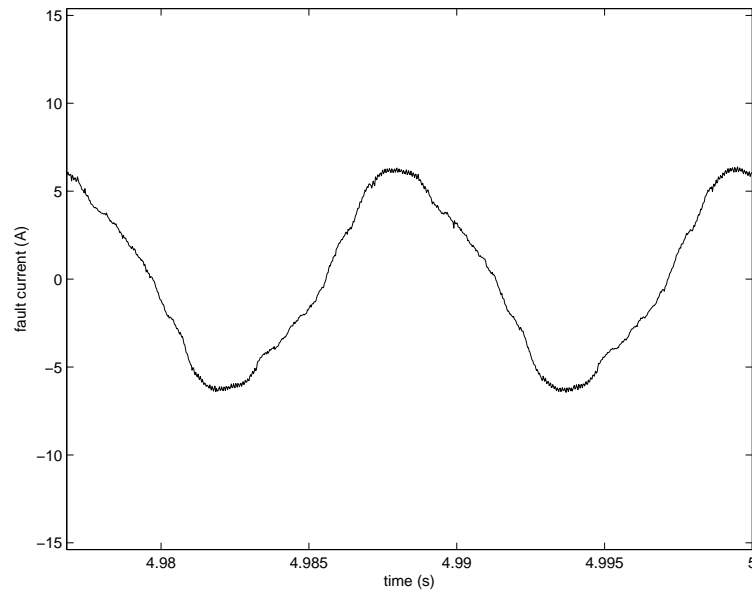


Figure 4.22: Fault current of the IPM machine at 86.25 Hz, three-quarter-load, with a 7.25Ω , 16.7% winding fault.

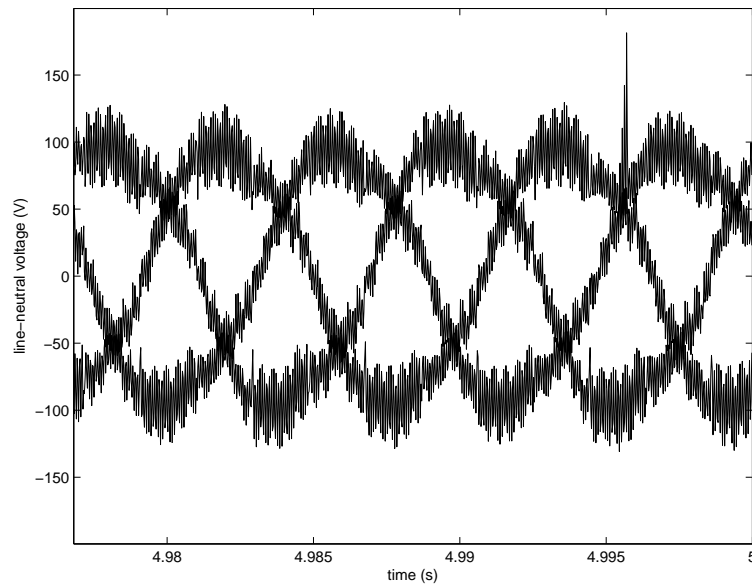


Figure 4.23: Line-to-neutral voltage of the IPM machine at 86.25 Hz, half-load, with a 4.85Ω , 16.7% winding fault.

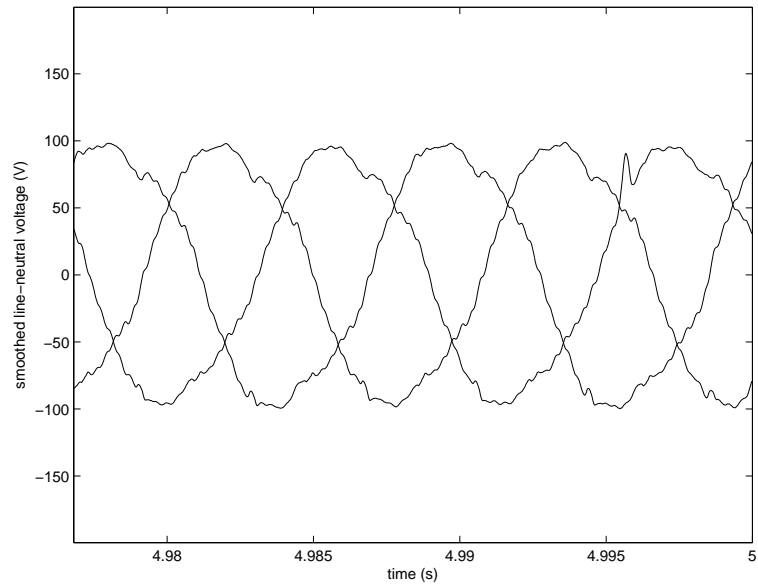


Figure 4.24: Smoothed line-to-neutral voltage of the IPM machine at 86.25 Hz, half-load, with a 4.85Ω , 16.7% winding fault.

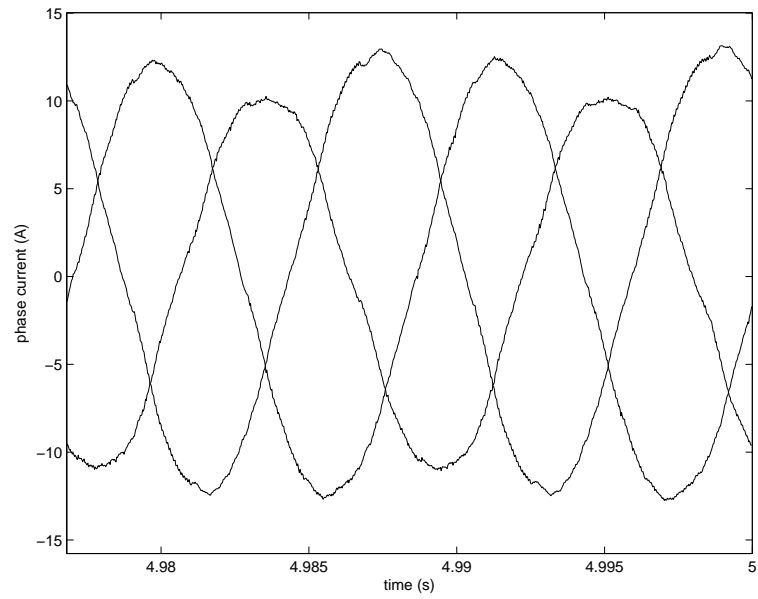


Figure 4.25: Phase current of the IPM machine at 86.25 Hz, half-load, with a 4.85Ω , 16.7% winding fault.

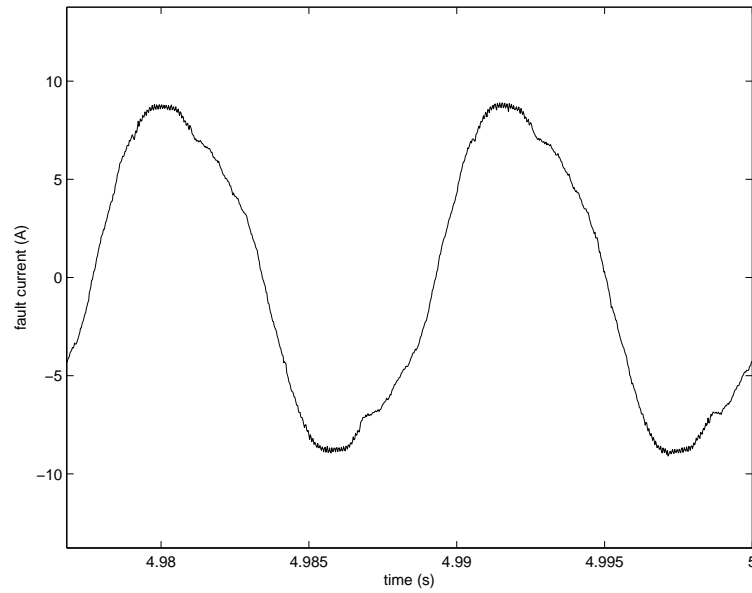


Figure 4.26: Fault current of the IPM machine at 86.25 Hz, half-load, with a 4.85Ω , 16.7% winding fault.

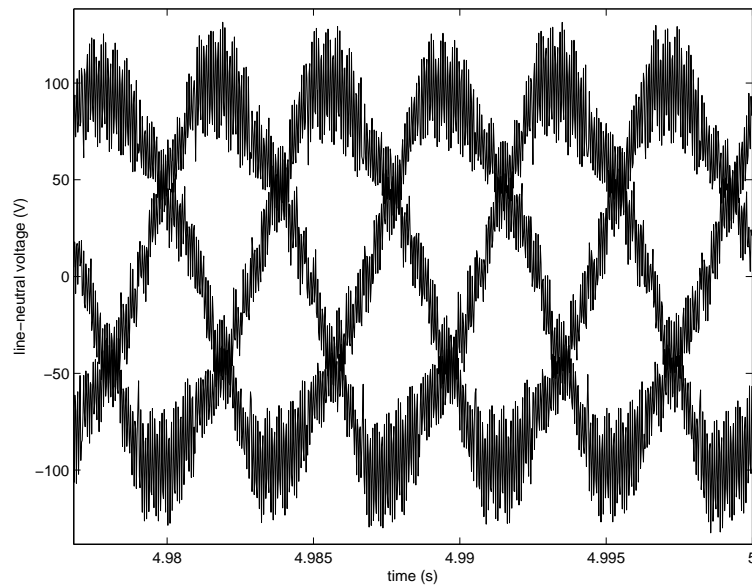


Figure 4.27: Line-to-neutral voltage of the IPM machine at 86.25 Hz, three-quarter-load, with a 4.85Ω , 16.7% winding fault.

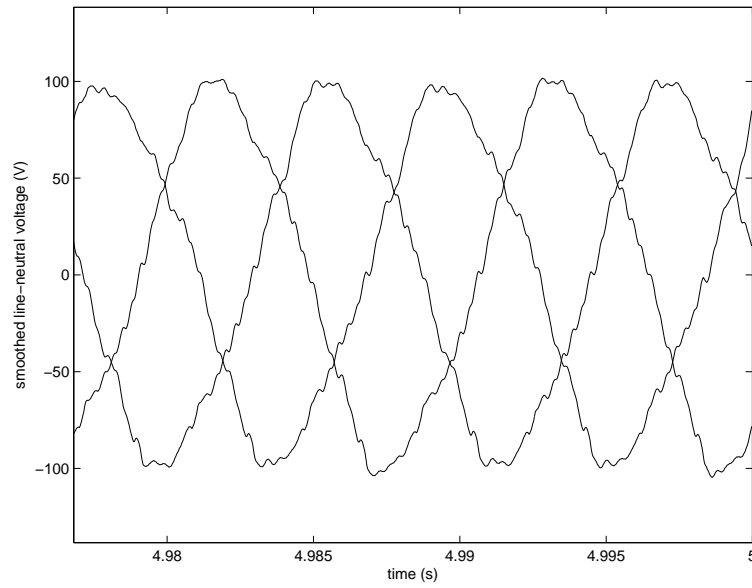


Figure 4.28: Smoothed line-to-neutral voltage of the IPM machine at 86.25 Hz, three-quarter-load, with a 4.85Ω , 16.7% winding fault.

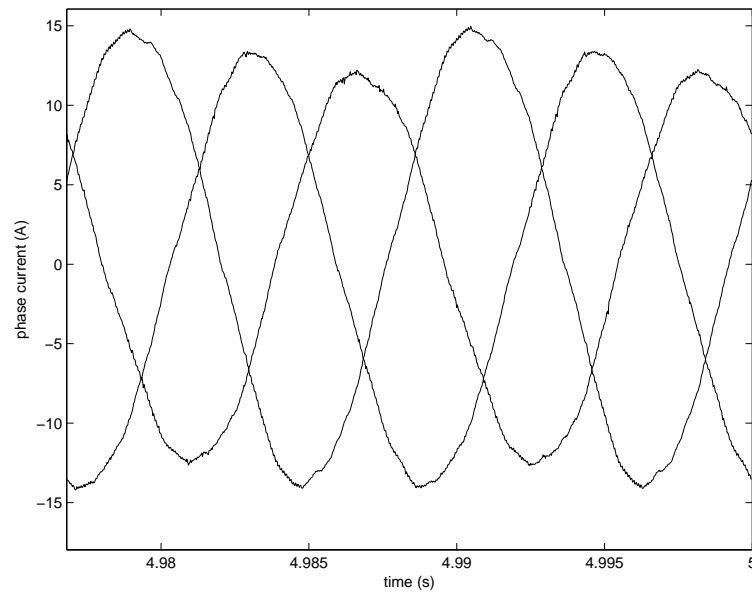


Figure 4.29: Phase current of the IPM machine at 86.25 Hz, three-quarter-load, with a 4.85Ω , 16.7% winding fault.

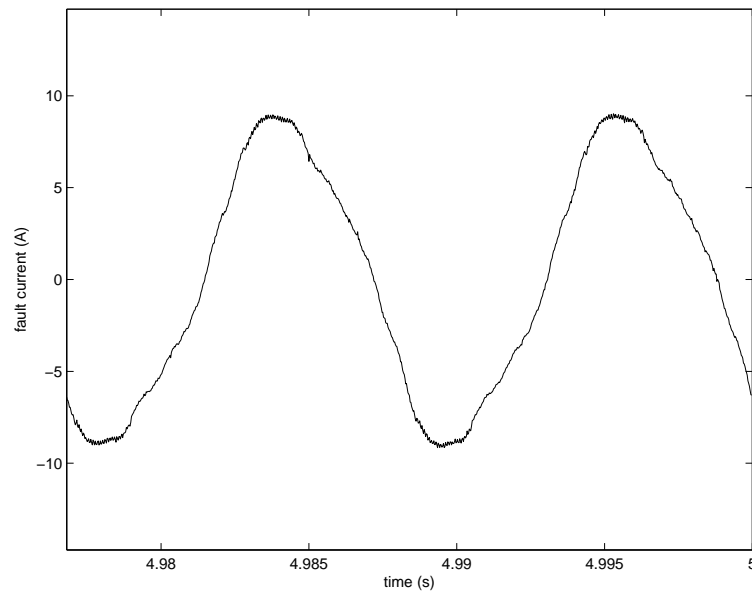


Figure 4.30: Fault current of the IPM machine at 86.25 Hz, three-quarter-load, with a 4.85Ω , 16.7% winding fault.

4.2 Results of Motor Current Spectrum Analysis

The frequency spectra for the experimental phase currents of the IPM machine at different speed and torque test points and for increasing fault severity/decreasing fault resistances are shown in Figure 4.31 through Figure 4.54. As seen in Figure 4.31 through Figure 4.36, this IPM machine's phase currents contain many small magnitude harmonics even for healthy operation. Introducing a short-circuit fault to the winding does not significantly change the harmonic content of the phase currents, as seen in Figure 4.37 through Figure 4.54.

Table 4.1: 3rd harmonic component of the IPM machine phase currents when operated at 86.25 Hz.

<i>Shaft load</i>	<i>Fault resistance</i>	<i>Phase A (dB)</i>	<i>Phase B (dB)</i>	<i>Phase C (dB)</i>
50 %	Inf.	-37.0	-34.6	-33.1
50 %	9.66 Ω	-39.1	-37.3	-41.2
50 %	7.25 Ω	-40.1	-38.6	-44.5
50 %	4.85 Ω	-39.8	-36.0	-48.7
75 %	Inf.	-34.1	-32.6	-31.0
75 %	9.66 Ω	-35.8	-39.8	-37.8
75 %	7.25 Ω	-36.0	-40.2	-38.2
75 %	4.85 Ω	-40.8	-39.6	-37.5

Table 4.2: 9th harmonic component of the IPM machine phase currents when operated at 86.25 Hz.

<i>Shaft load</i>	<i>Fault resistance</i>	<i>Phase A (dB)</i>	<i>Phase B (dB)</i>	<i>Phase C (dB)</i>
50 %	Inf.	-55.0	-67.8	-51.6
50 %	9.66 Ω	-56.8	-53.0	-50.5
50 %	7.25 Ω	-54.7	-52.2	-50.1
50 %	4.85 Ω	-57.0	-47.6	-50.4
75 %	Inf.	-58.4	-62.2	-54.9
75 %	9.66 Ω	-50.4	-50.2	-60.5
75 %	7.25 Ω	-47.4	-47.4	-60.2
75 %	4.85 Ω	-46.5	-60.7	-45.7

Table 4.3: 27th harmonic component of the IPM machine phase currents when operated at 86.25 Hz.

<i>Shaft load</i>	<i>Fault resistance</i>	<i>Phase A (dB)</i>	<i>Phase B (dB)</i>	<i>Phase C (dB)</i>
50 %	Inf.	-81.2	-72.1	-70.0
50 %	9.66 Ω	-67.1	-72.2	-74.8
50 %	7.25 Ω	-69.3	-68.0	-71.3
50 %	4.85 Ω	-69.1	-67.4	-86.2
75 %	Inf.	-76.2	-75.5	-73.2
75 %	9.66 Ω	-76.8	-83.2	-70.1
75 %	7.25 Ω	-76.0	-78.9	-71.3
75 %	4.85 Ω	-79.5	-80.8	-75.8

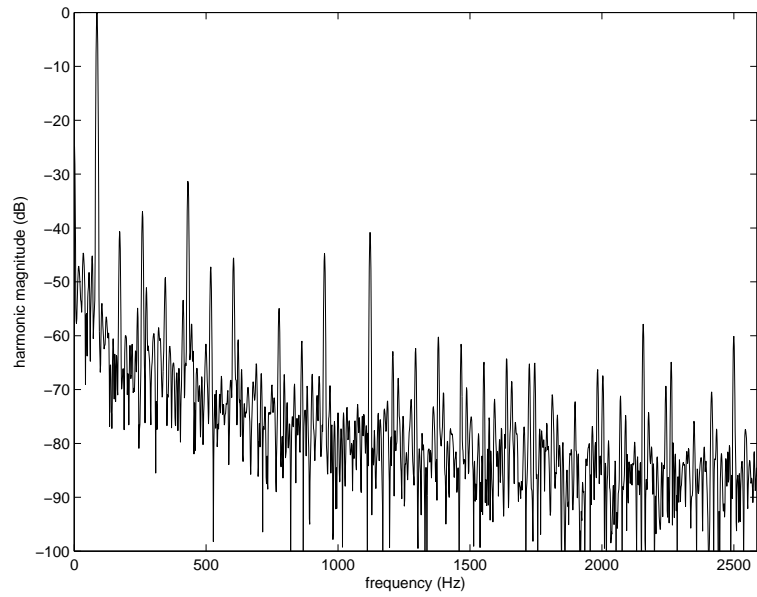


Figure 4.31: FFT of the IPM machine phase A current at 86.25 Hz, half-load, with no winding fault.

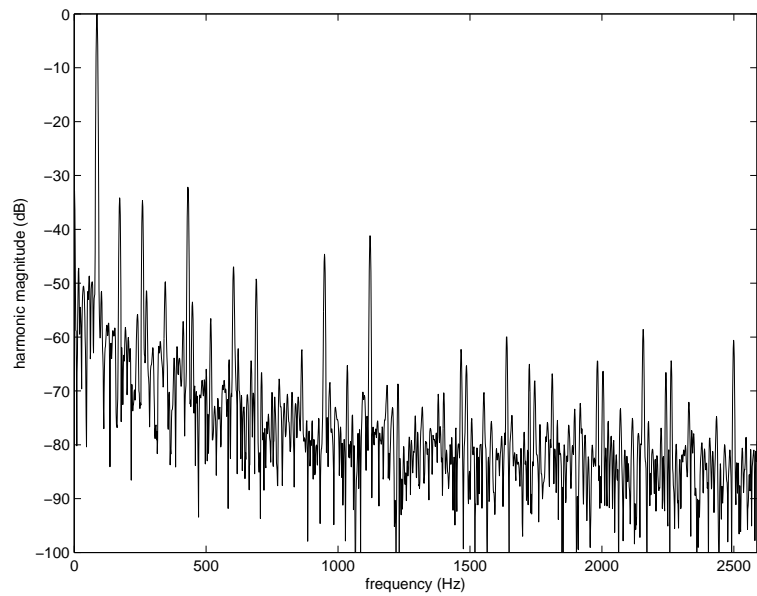


Figure 4.32: FFT of the IPM machine phase B current at 86.25 Hz, half-load, with no winding fault.

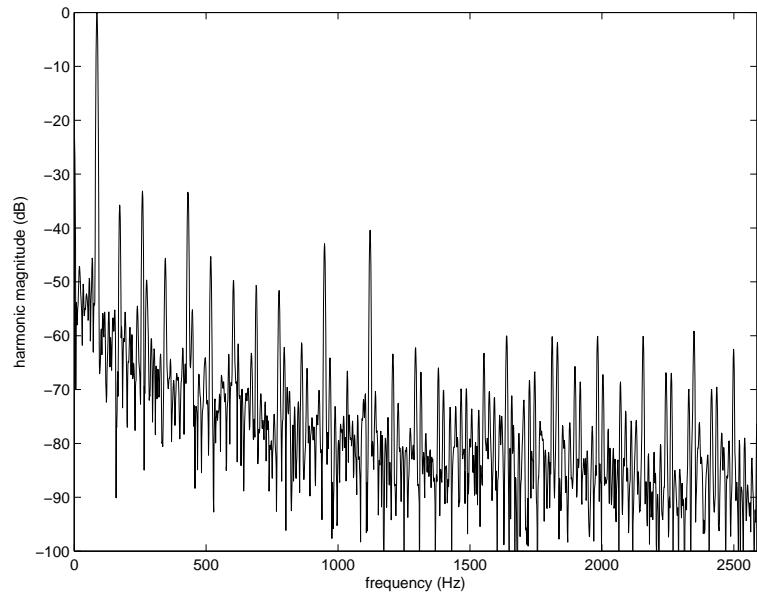


Figure 4.33: FFT of the IPM machine phase C current at 86.25 Hz, half-load, with no winding fault.

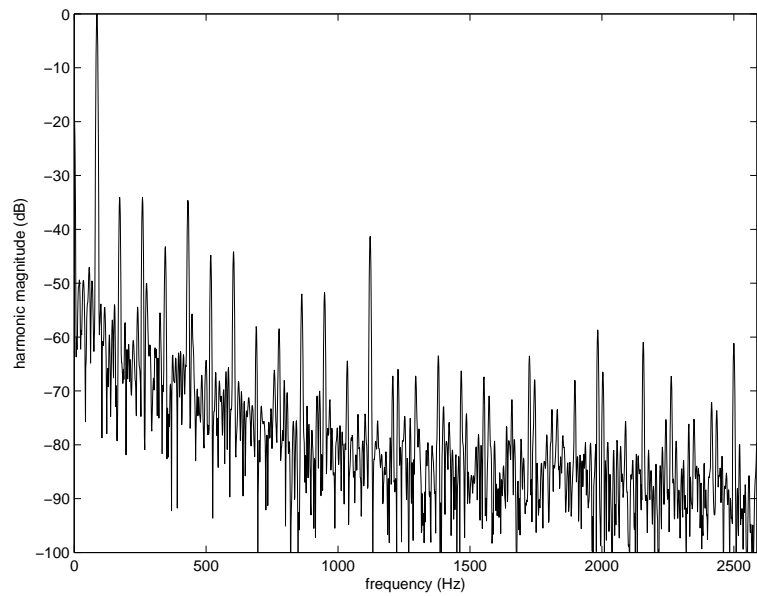


Figure 4.34: FFT of the IPM machine phase A current at 86.25 Hz, three-quarter-load, with no winding fault.

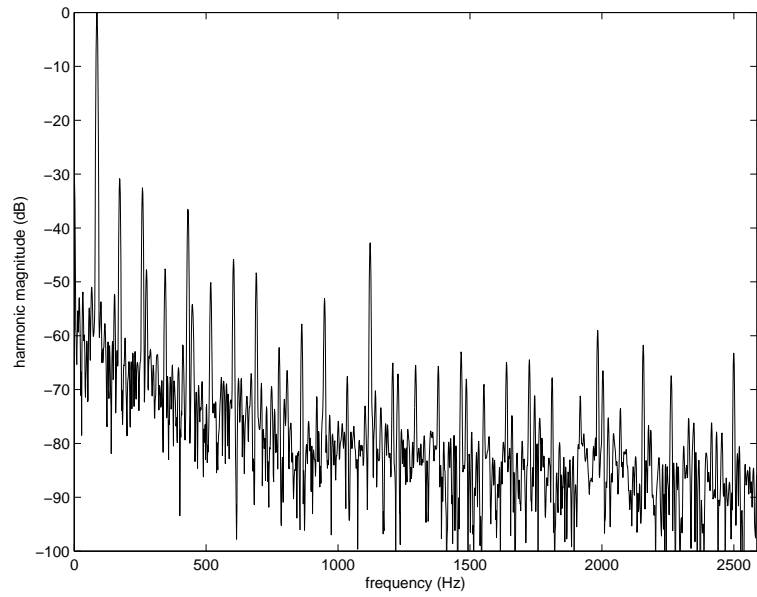


Figure 4.35: FFT of the IPM machine phase B current at 86.25 Hz, three-quarter-load, with no winding fault.

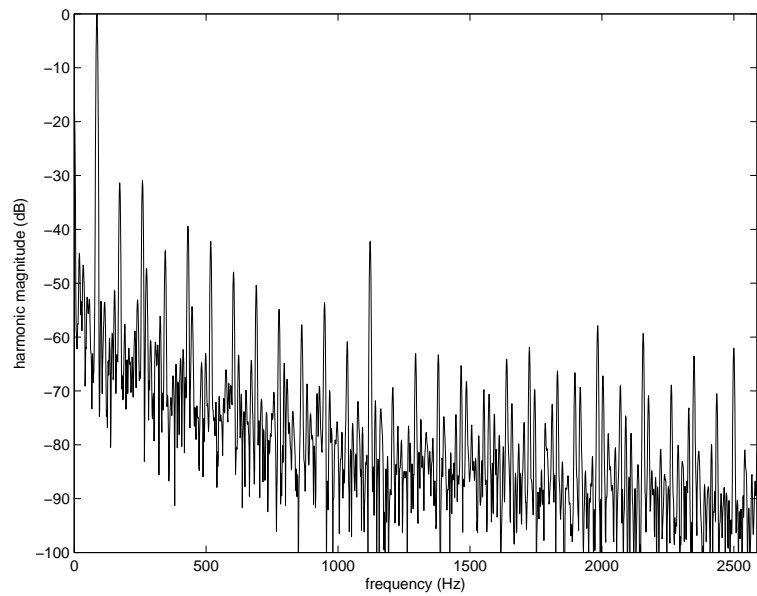


Figure 4.36: FFT of the IPM machine phase C current at 86.25 Hz, three-quarter-load, with no winding fault.

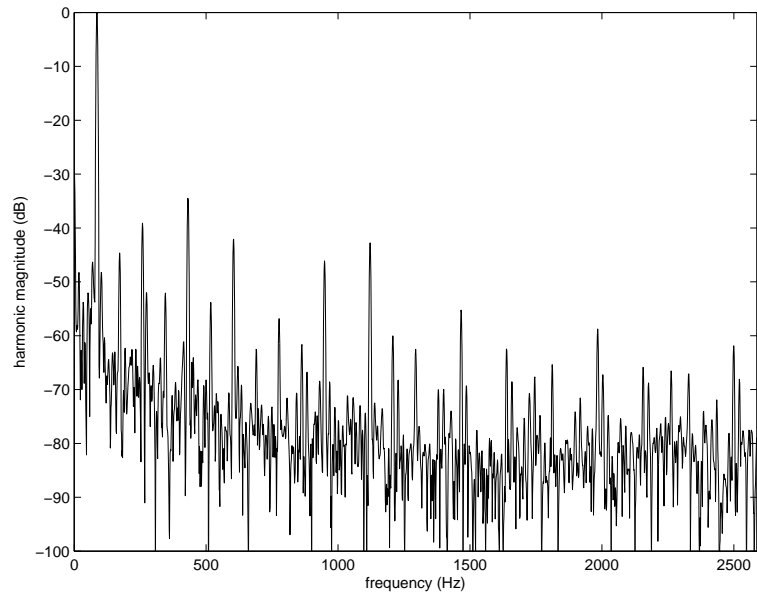


Figure 4.37: FFT of the IPM machine phase A current at 86.25 Hz, half-load, with a 9.66Ω , 16.7% winding fault.

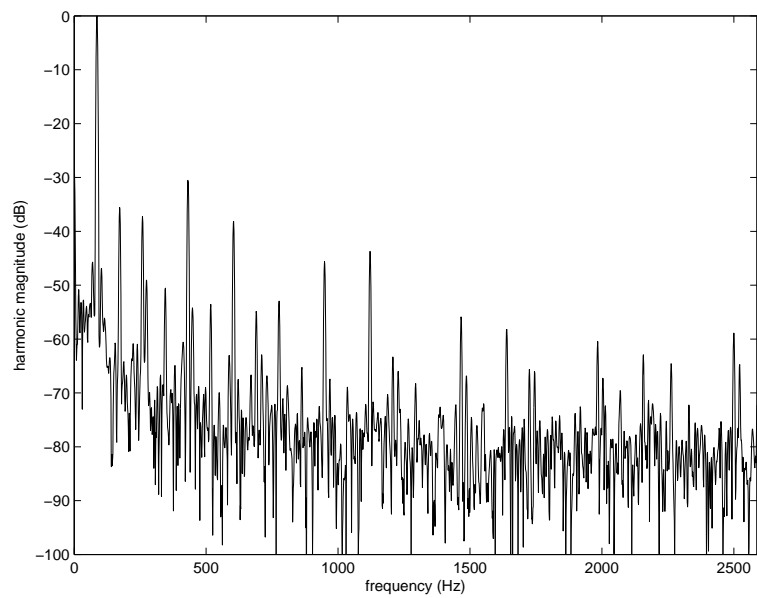


Figure 4.38: FFT of the IPM machine phase B current at 86.25 Hz, half-load, with a 9.66Ω , 16.7% winding fault.

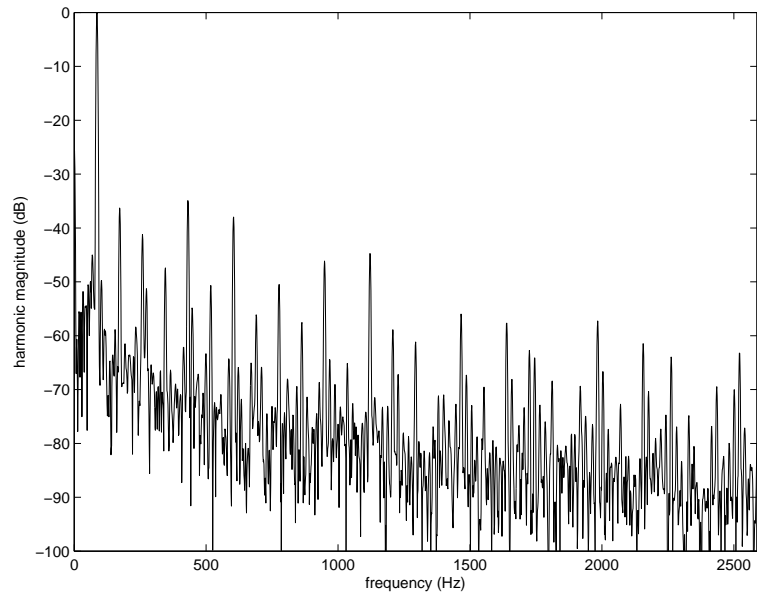


Figure 4.39: FFT of the IPM machine phase C current at 86.25 Hz, half-load, with a 9.66Ω , 16.7% winding fault.

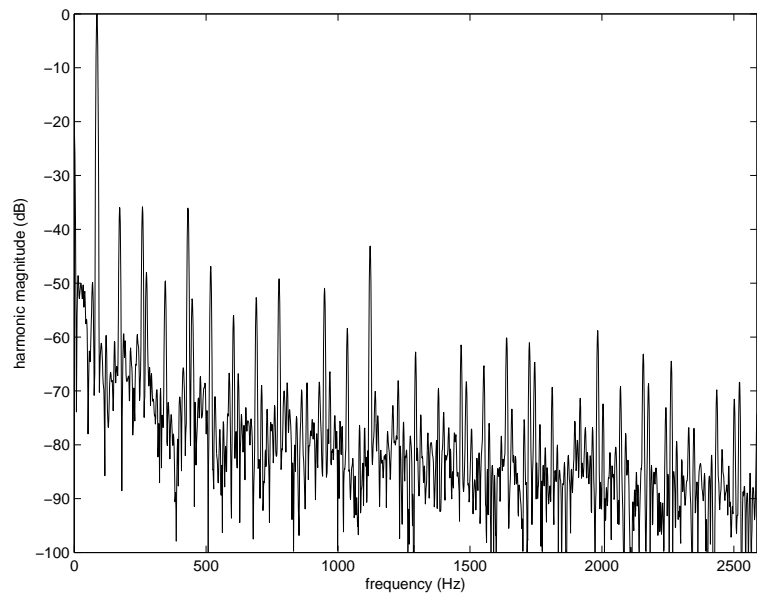


Figure 4.40: FFT of the IPM machine phase A current at 86.25 Hz, three-quarter-load, with a 9.66Ω , 16.7% winding fault.

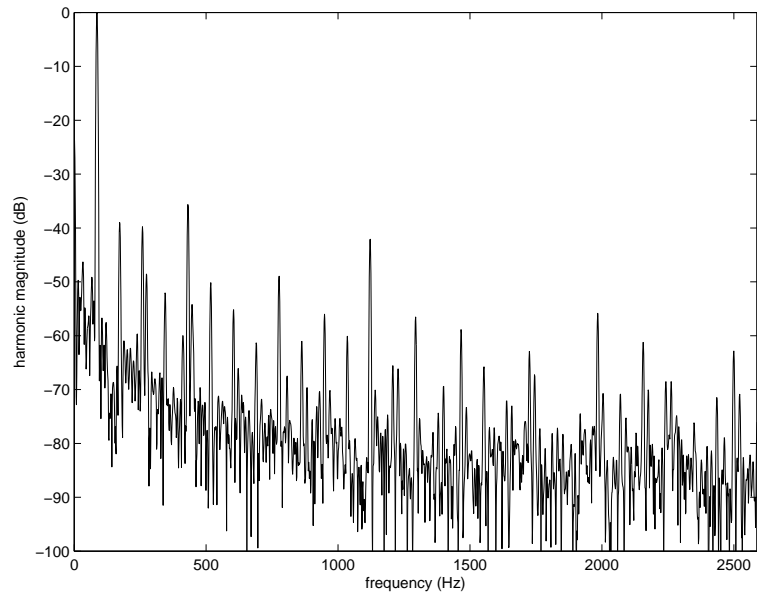


Figure 4.41: FFT of the IPM machine phase B current at 86.25 Hz, three-quarter-load, with a 9.66Ω , 16.7% winding fault.

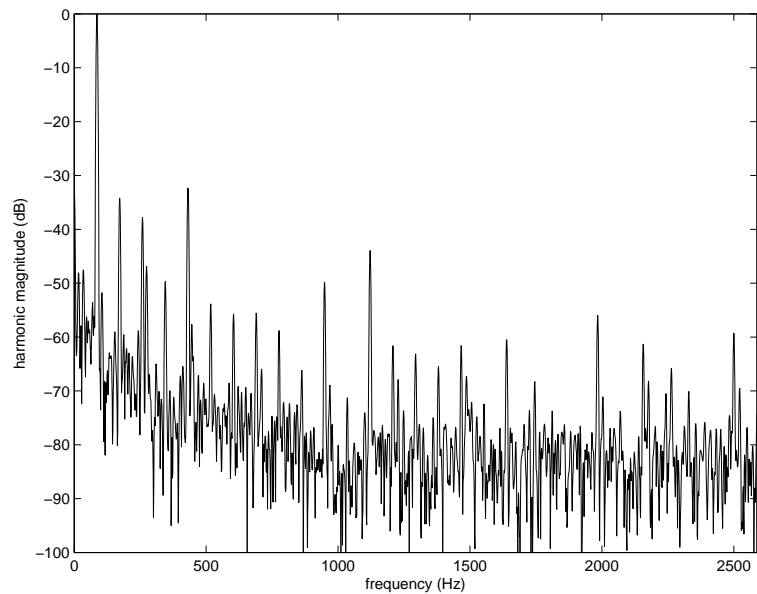


Figure 4.42: FFT of the IPM machine phase C current at 86.25 Hz, three-quarter-load, with a 9.66Ω , 16.7% winding fault.

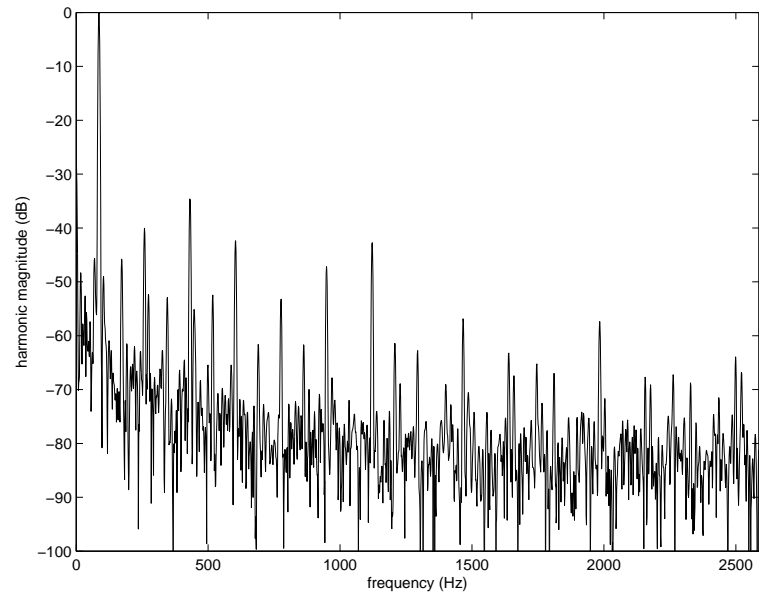


Figure 4.43: FFT of the IPM machine phase A current at 86.25 Hz, half-load, with a $7.25\ \Omega$, 16.7% winding fault.

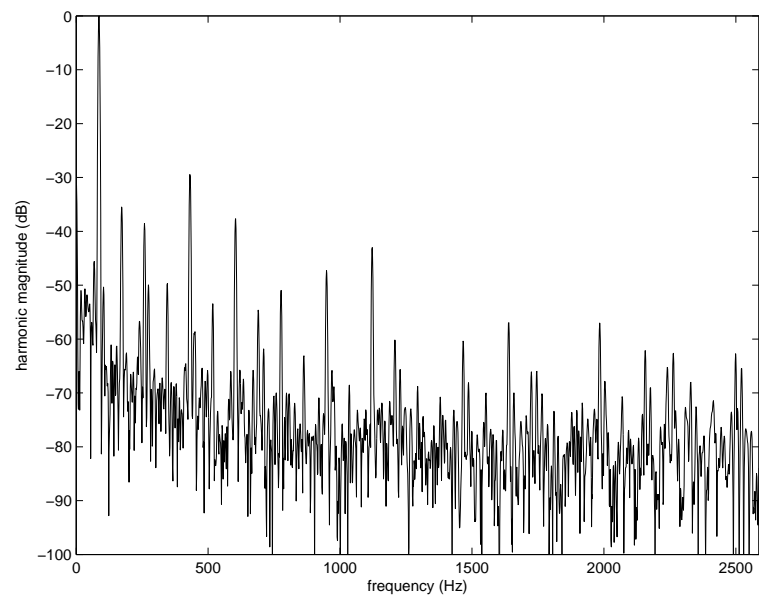


Figure 4.44: FFT of the IPM machine phase B current at 86.25 Hz, half-load, with a $7.25\ \Omega$, 16.7% winding fault.

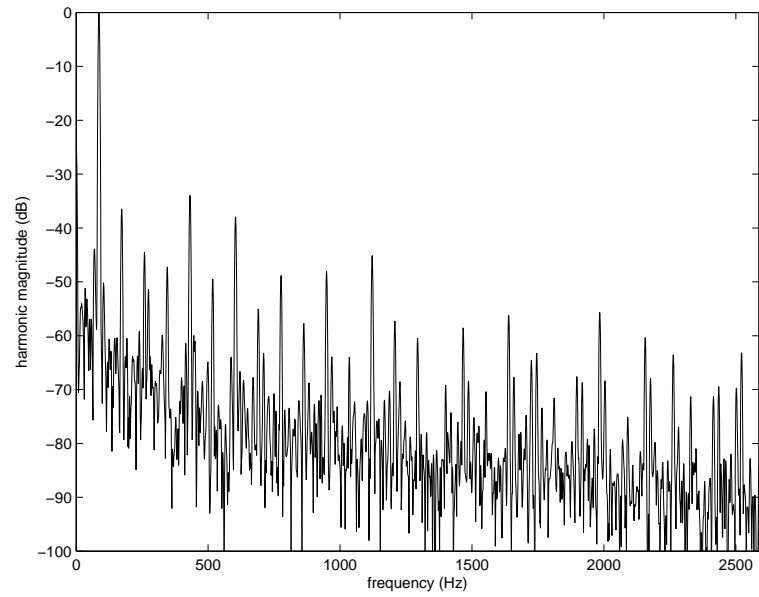


Figure 4.45: FFT of the IPM machine phase C current at 86.25 Hz, half-load, with a 7.25Ω , 16.7% winding fault.

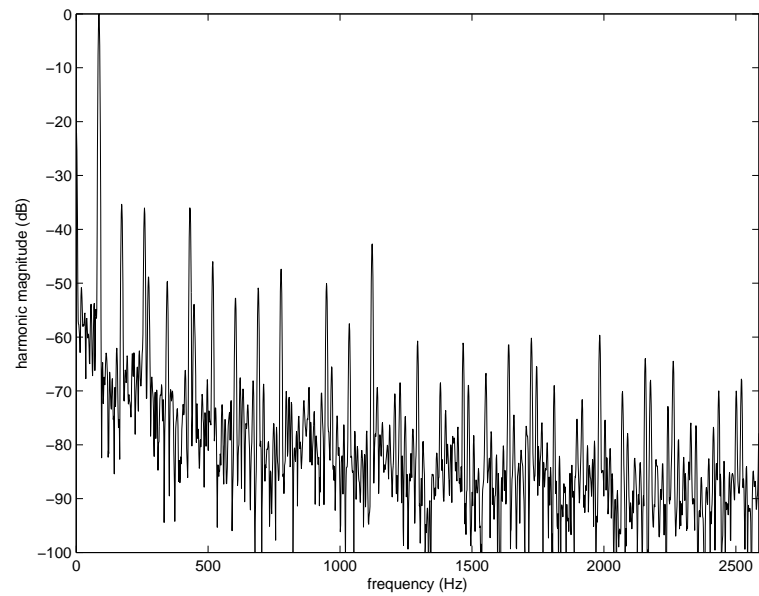


Figure 4.46: FFT of the IPM machine phase A current at 86.25 Hz, three-quarter-load, with a 7.25Ω , 16.7% winding fault.

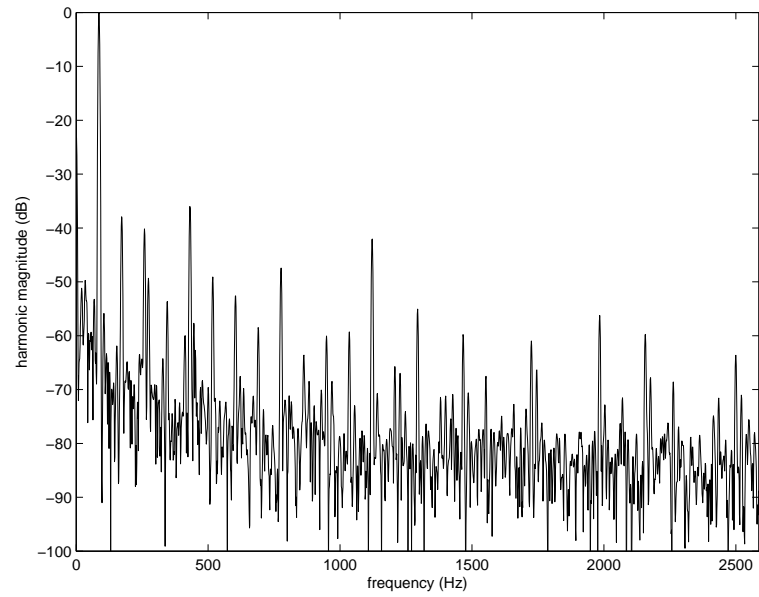


Figure 4.47: FFT of the IPM machine phase B current at 86.25 Hz, three-quarter-load, with a 7.25Ω , 16.7% winding fault.

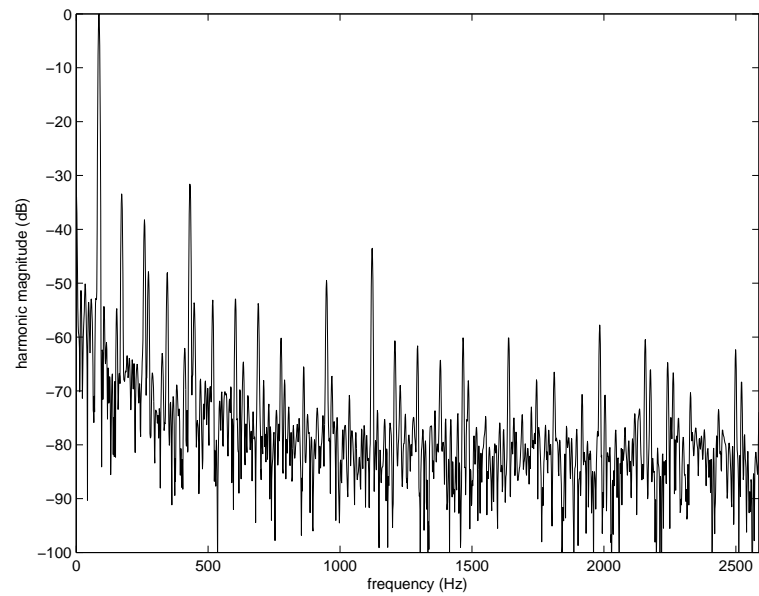


Figure 4.48: FFT of the IPM machine phase C current at 86.25 Hz, three-quarter-load, with a 7.25Ω , 16.7% winding fault.

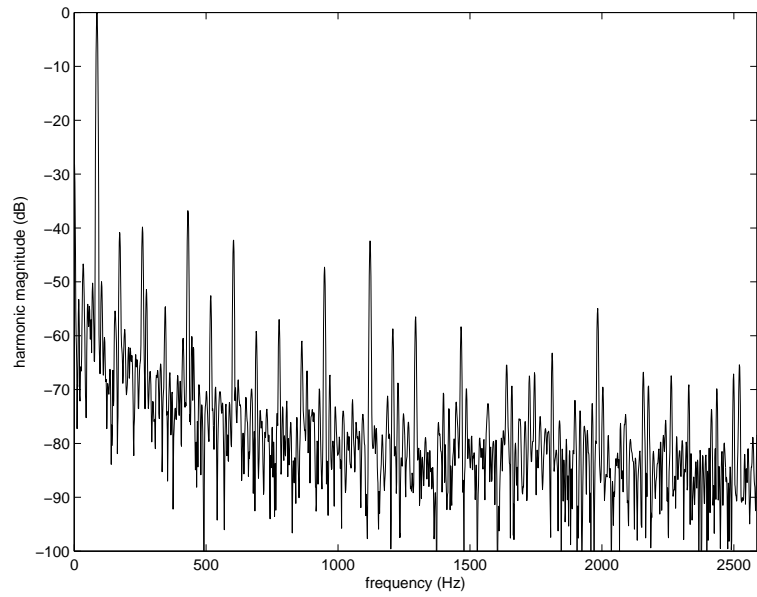


Figure 4.49: FFT of the IPM machine phase A current at 86.25 Hz, half-load, with a $4.85\ \Omega$, 16.7% winding fault.

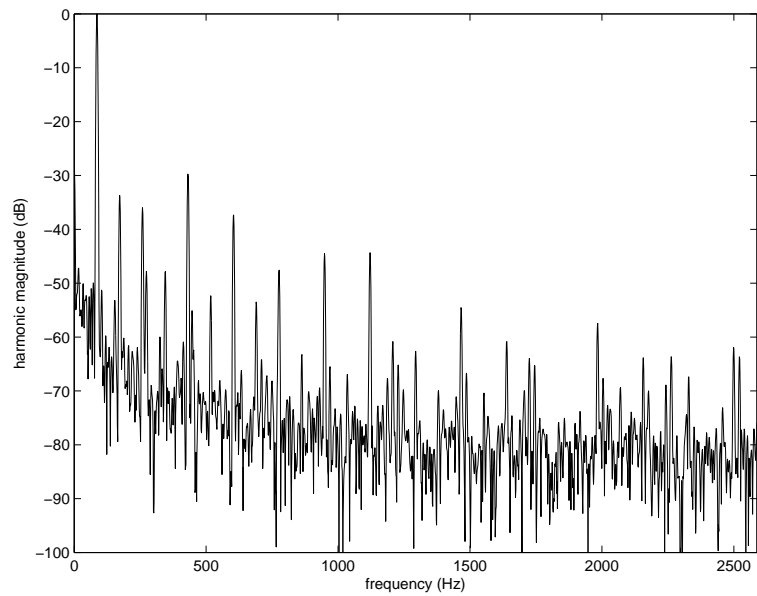


Figure 4.50: FFT of the IPM machine phase B current at 86.25 Hz, half-load, with a $4.85\ \Omega$, 16.7% winding fault.

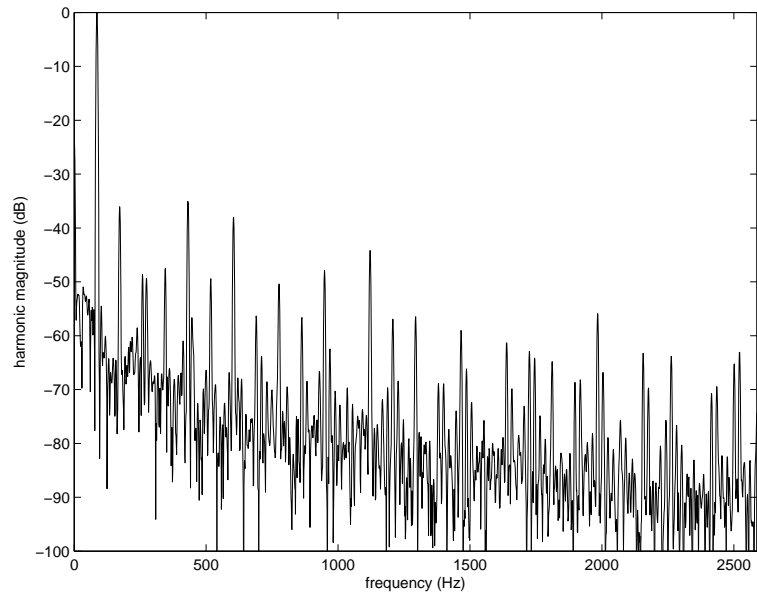


Figure 4.51: FFT of the IPM machine phase C current at 86.25 Hz, half-load, with a 4.85Ω , 16.7% winding fault.

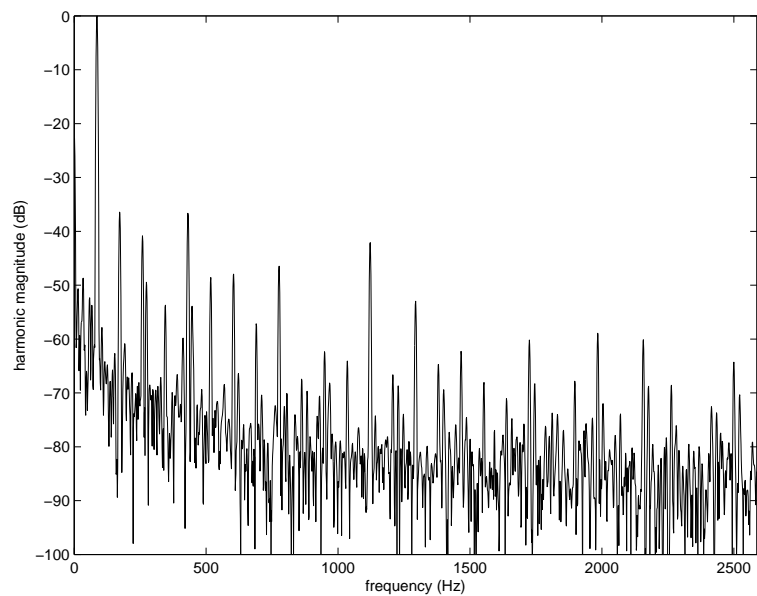


Figure 4.52: FFT of the IPM machine phase A current at 86.25 Hz, three-quarter-load, with a 4.85Ω , 16.7% winding fault.

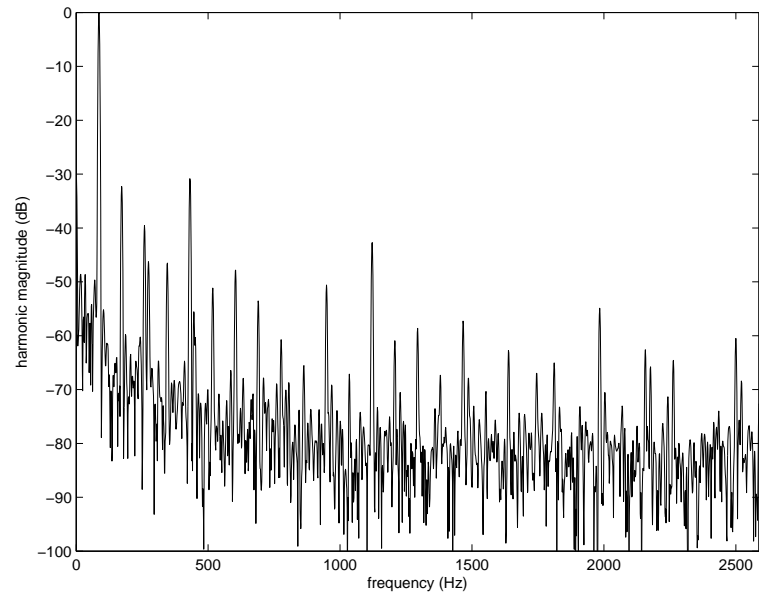


Figure 4.53: FFT of the IPM machine phase B current at 86.25 Hz, three-quarter-load, with a 4.85Ω , 16.7% winding fault.

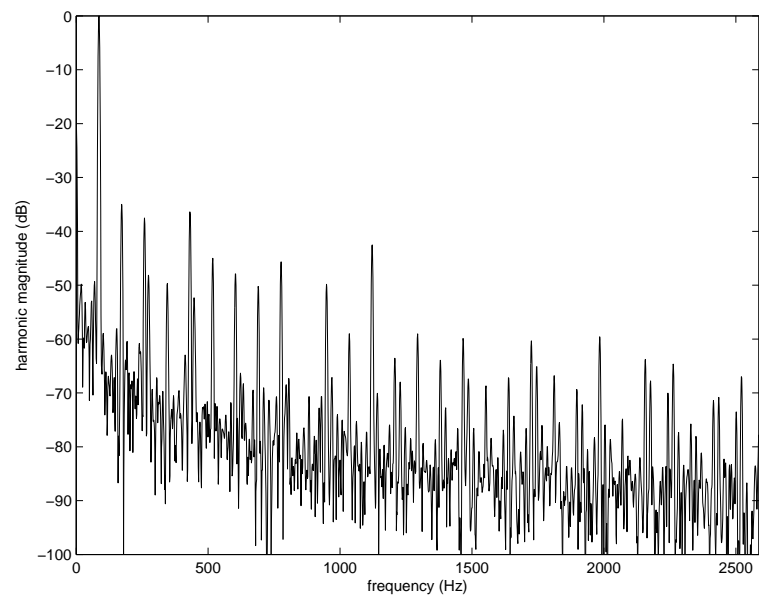


Figure 4.54: FFT of the IPM machine phase C current at 86.25 Hz, three-quarter-load, with a 4.85Ω , 16.7% winding fault.

4.3 Results of Negative Sequence Components Analysis

The results of the negative sequence components method applied to the experimental phase currents of the IPM machine at different speed and torque test points and for increasing fault severity/decreasing fault resistances are shown in Table 4.4. For increasing fault severity/decreasing fault resistance there is a noticeable, monotonic change in the magnitude of the negative sequence component of the phase current.

Table 4.4: Magnitude of the symmetrical component phasors of the IPM machine when operated at 86.25 Hz.

<i>Shaft load</i>	<i>Fault resistance</i>	<i>Positive</i>	<i>Negative</i>	<i>Zero</i>
50 %	Inf.	7.161	0.228	0.020
50 %	9.66 Ω	9.947	0.406	0.025
50 %	7.25 Ω	10.023	0.624	0.025
50 %	4.85 Ω	11.084	1.061	0.029
75 %	Inf.	10.528	0.480	0.027
75 %	9.66 Ω	11.639	0.412	0.028
75 %	7.25 Ω	11.969	0.680	0.029
75 %	4.85 Ω	12.568	1.069	0.032

4.4 Results of Space-Vector Pendulous Oscillation Method Analysis

The results from applying the space-vector pendulous oscillation method to the experimental phase currents of the IPM machine at different speed and torque test points and for increasing fault severity/decreasing fault resistances are shown in Figure 4.55 through Figure 4.78. The slightly distorted circle of the current space-vectors for the healthy machine operation shown in Figure 4.56 and Figure 4.59 again

indicate a slight bias in the current sensors.

The voltage space-vectors, current space-vectors, and pendulous oscillation signals for the various fault conditions are shown in Figure 4.61 through Figure 4.78. The tabulation of the swing angle of the pendulous oscillation signal for the various test conditions is shown in Table 4.5. For this IPM machine the swing angle is not a reliable indicator of the fault, as indicated by the non-monotonic nature of the progression of the swing angle versus the fault severity.

Table 4.5: Swing angle of the IPM machine when operated at 86.25 Hz.

<i>Shaft load</i>	<i>Fault resistance</i>	<i>Swing angle</i>
50 %	Inf.	18.51 deg.
50 %	9.66 Ω	14.64 deg.
50 %	7.25 Ω	16.53 deg.
50 %	4.85 Ω	19.52 deg.
75 %	Inf.	25.02 deg.
75 %	9.66 Ω	16.42 deg.
75 %	7.25 Ω	18.03 deg.
75 %	4.85 Ω	20.79 deg.

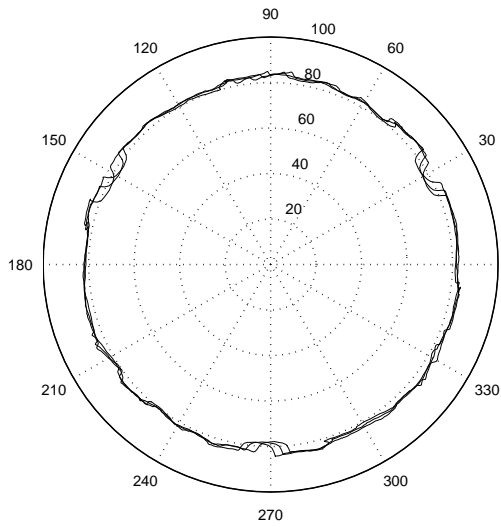


Figure 4.55: Voltage space-vector of the IPM machine at 86.25 Hz, half-load, with no winding fault.

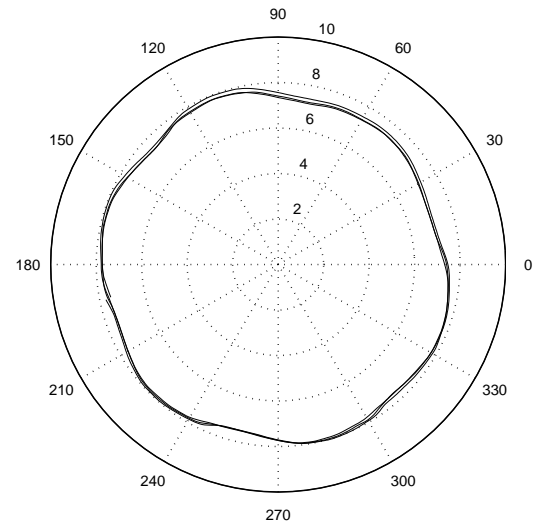


Figure 4.56: Current space-vector of the IPM machine at 86.25 Hz, half-load, with no winding fault.

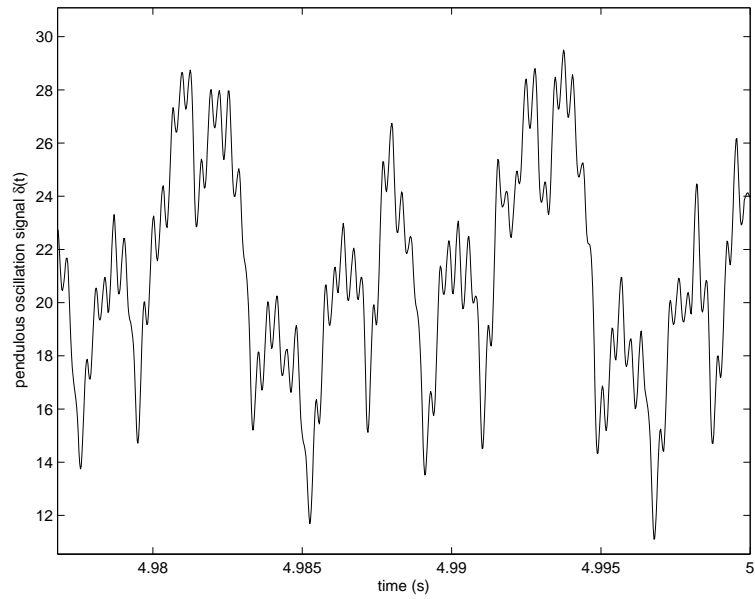


Figure 4.57: Pendulous oscillation signal of the IPM machine at 86.25 Hz, half-load, with no winding fault.

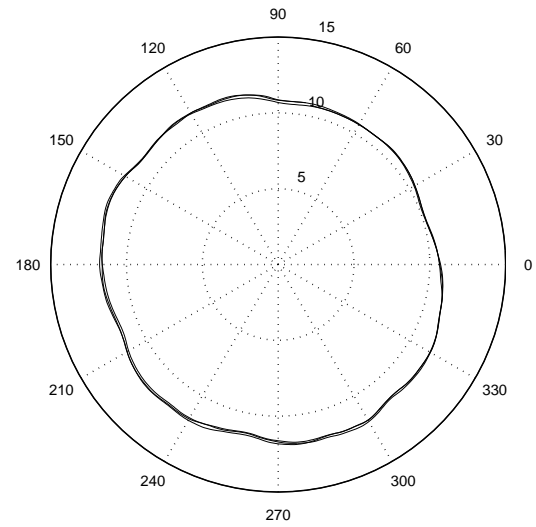
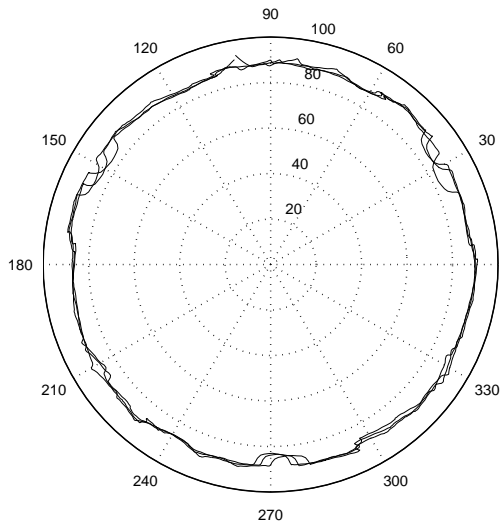


Figure 4.58: Voltage space-vector of the IPM machine at 86.25 Hz, three-quarter-load, with no winding fault.

Figure 4.59: Current space-vector of the IPM machine at 86.25 Hz, three-quarter-load, with no winding fault.

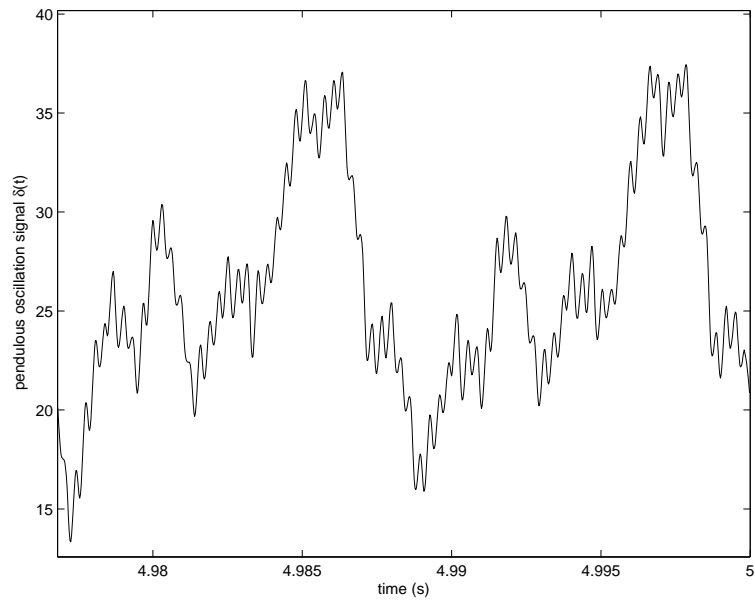


Figure 4.60: Pendulous oscillation signal of the IPM machine at 86.25 Hz, full-load, with no winding fault.

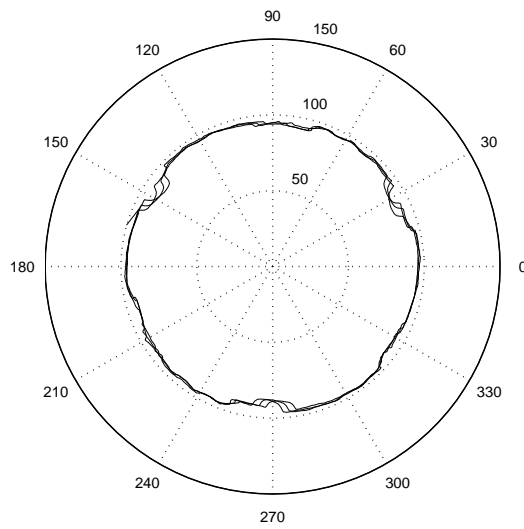


Figure 4.61: Voltage space-vector of the IPM machine at 86.25 Hz, half-load, with a 9.66Ω , 16.7% winding fault.

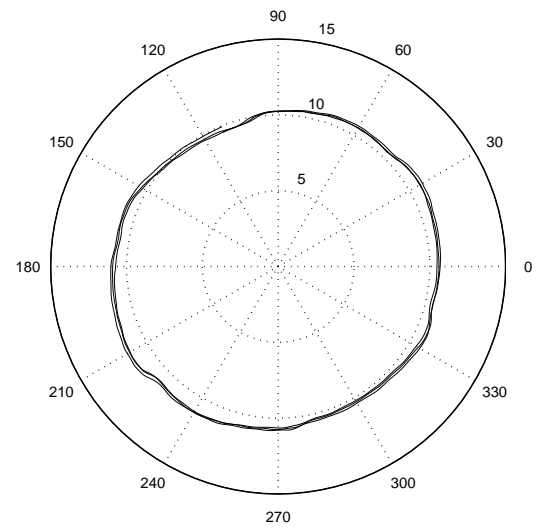


Figure 4.62: Current space-vector of the IPM machine at 86.25 Hz, half-load, with a 9.66Ω , 16.7% winding fault.

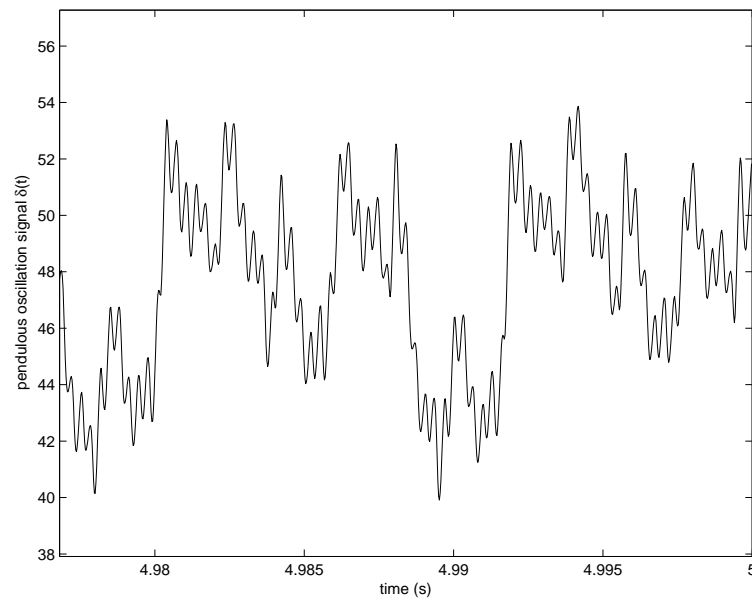


Figure 4.63: Pendulous oscillation signal of the IPM machine at 86.25 Hz, half-load, with a 9.66Ω , 16.7% winding fault.

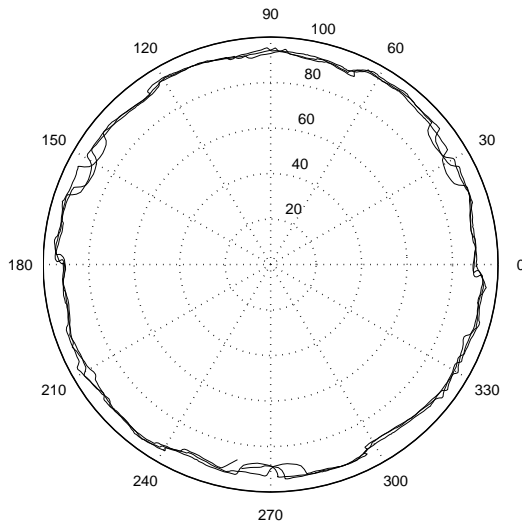


Figure 4.64: Voltage space-vector of the IPM machine at 86.25 Hz, three-quarter-load, with a $9.66\ \Omega$, 16.7% winding fault.

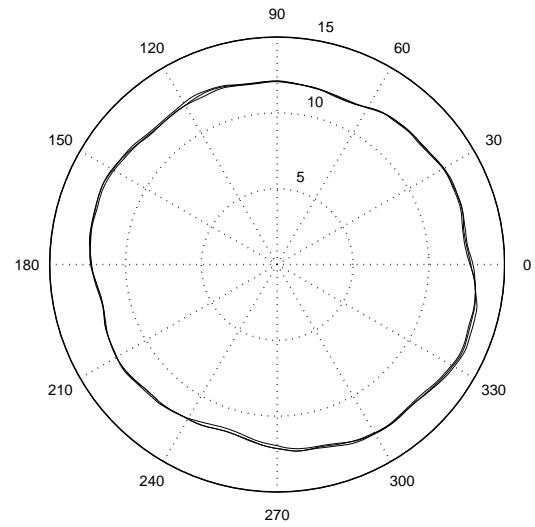


Figure 4.65: Current space-vector of the IPM machine at 86.25 Hz, three-quarter-load, with a $9.66\ \Omega$, 16.7% winding fault.

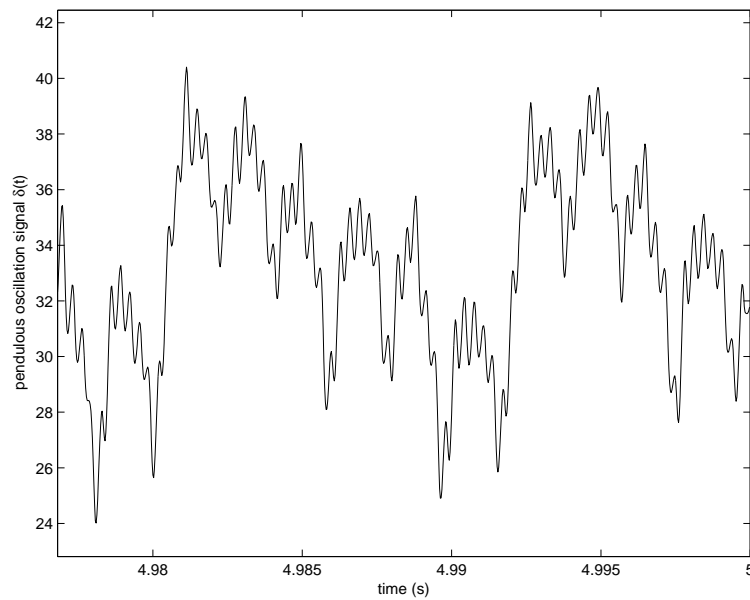


Figure 4.66: Pendulous oscillation signal of the IPM machine at 86.25 Hz, three-quarter-load, with a $9.66\ \Omega$, 16.7% winding fault.

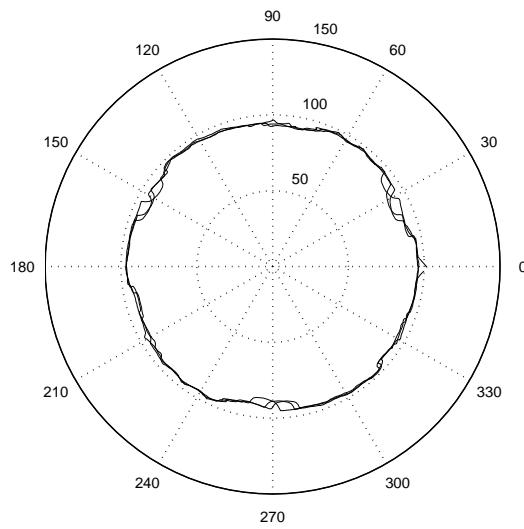


Figure 4.67: Voltage space-vector of the IPM machine at 86.25 Hz, half-load, with a 7.25Ω , 16.7% winding fault.

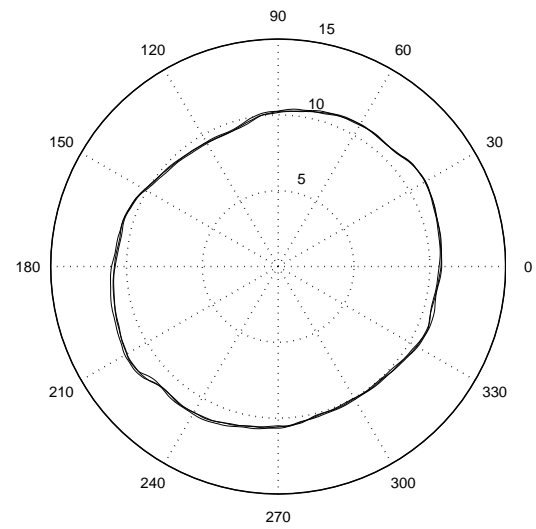


Figure 4.68: Current space-vector of the IPM machine at 86.25 Hz, half-load, with a 7.25Ω , 16.7% winding fault.

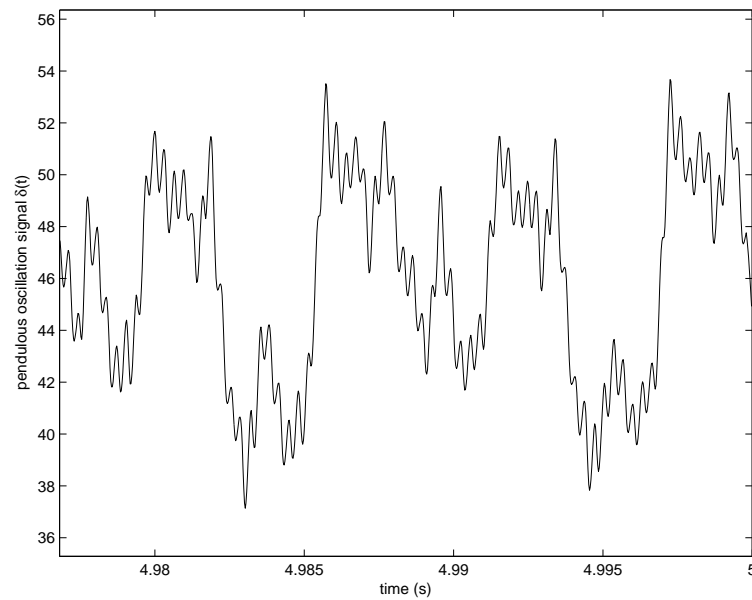


Figure 4.69: Pendulous oscillation signal of the IPM machine at 86.25 Hz, half-load, with a 7.25Ω , 16.7% winding fault.

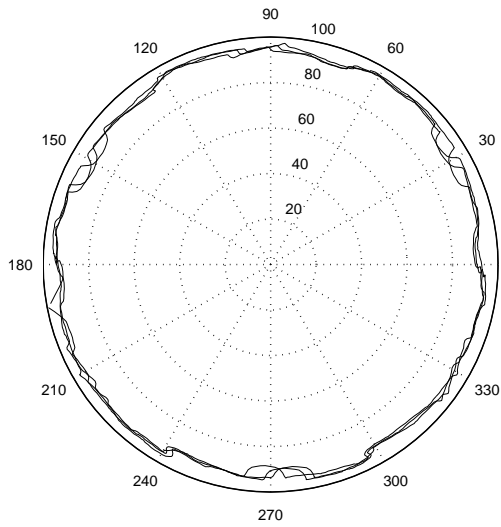


Figure 4.70: Voltage space-vector of the IPM machine at 86.25 Hz, three-quarter-load, with a $7.25\ \Omega$, 16.7% winding fault.

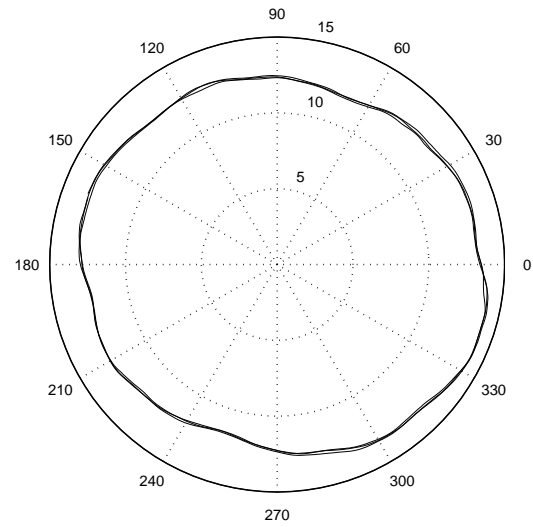


Figure 4.71: Current space-vector of the IPM machine at 86.25 Hz, three-quarter-load, with a $7.25\ \Omega$, 16.7% winding fault.

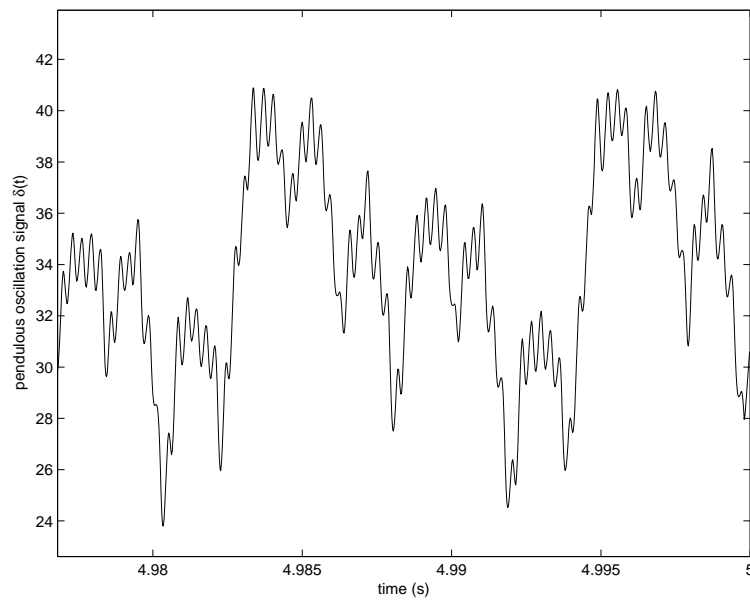


Figure 4.72: Pendulous oscillation signal of the IPM machine at 86.25 Hz, three-quarter-load, with a $7.25\ \Omega$, 16.7% winding fault.

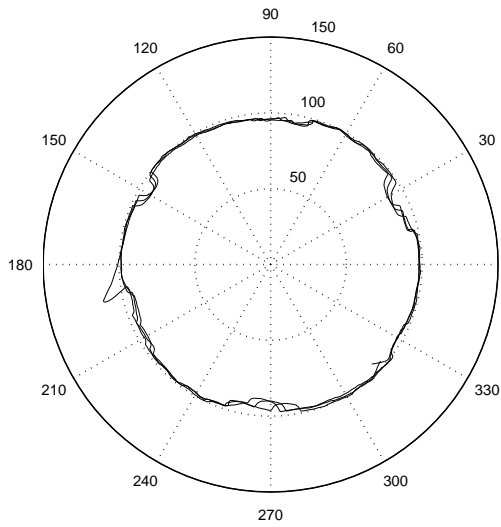


Figure 4.73: Voltage space-vector of the IPM machine at 86.25 Hz, half-load, with a $4.85\ \Omega$, 16.7% winding fault.

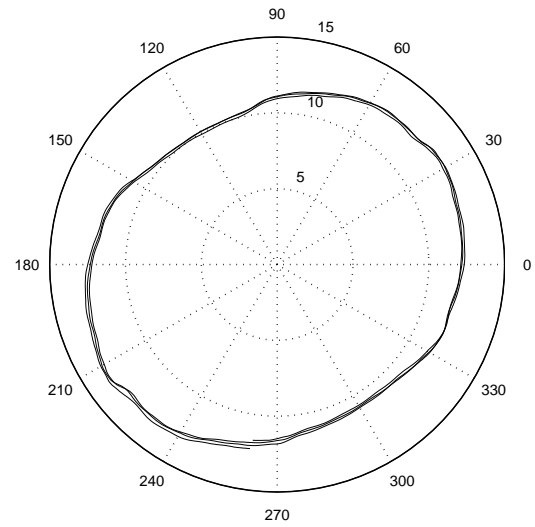


Figure 4.74: Current space-vector of the IPM machine at 86.25 Hz, half-load, with a $4.85\ \Omega$, 16.7% winding fault.

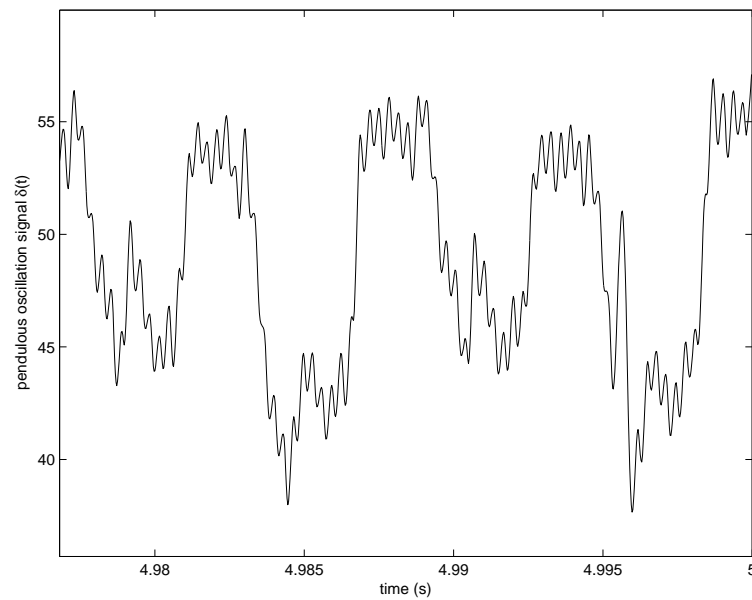


Figure 4.75: Pendulous oscillation signal of the IPM machine at 86.25 Hz, half-load, with a $4.85\ \Omega$, 16.7% winding fault.

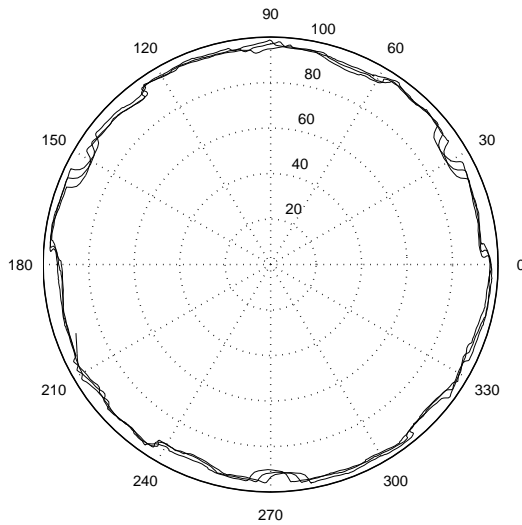


Figure 4.76: Voltage space-vector of the IPM machine at 86.25 Hz, three-quarter-load, with a $4.85\ \Omega$, 16.7% winding fault.

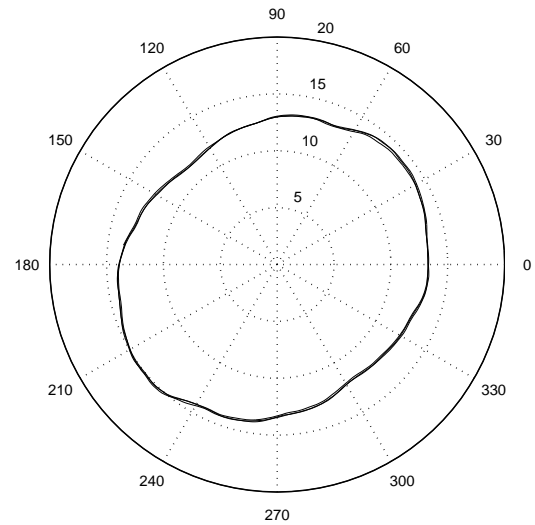


Figure 4.77: Current space-vector of the IPM machine at 86.25 Hz, three-quarter-load, with a $4.85\ \Omega$, 16.7% winding fault.

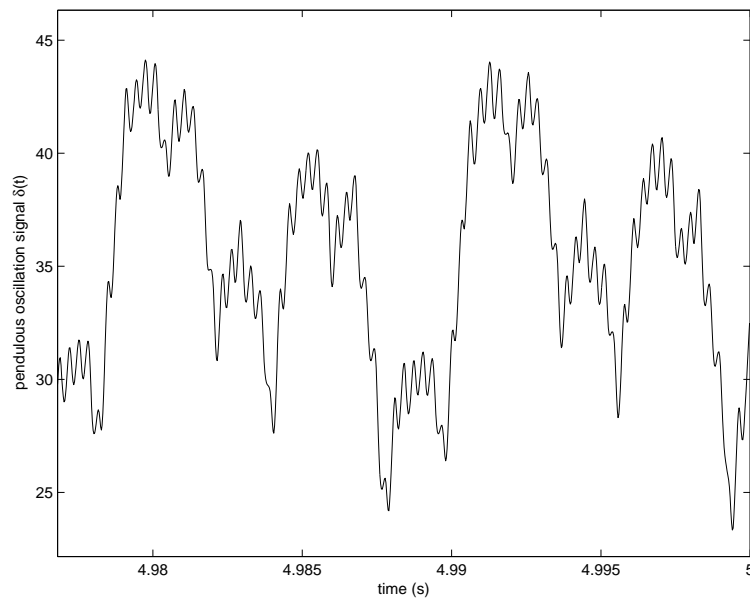


Figure 4.78: Pendulous oscillation signal of the IPM machine at 86.25 Hz, three-quarter-load, with a $4.85\ \Omega$, 16.7% winding fault.

4.5 Analysis and Discussion of Results

Diagnosis and prognostication of winding short-circuit faults is a very difficult engineering task. Not only must the fault index being used change during faulty operation as compared to healthy operation in order to diagnose the fault, but to prognosticate the deterioration of the fault the fault index must vary monotonically with the deteriorating fault resistance. Furthermore, a robust fault index diagnoses a fault without necessarily having a baseline for the healthy machine's characteristics or a baseline for the value of the fault index for healthy machine operation. Meeting the conditions of: a fault index which varies with fault severity for diagnosis, a fault index which varies monotonically with fault severity for prognostication, and meeting both of these conditions without a baseline for the healthy machine's characteristics is a very difficult task to accomplish. To further complicate matters, the use of machines which possess some degree of inherent fault tolerance in their winding topology, such as multiple parallel paths per phase which permits current redistribution in the winding, as well as the use of state-of-the-art ac drives with advanced control algorithms, may further mask the existence of a machine winding fault.

The healthy machine voltage and current waveforms have a slight imbalance as shown in Figure 4.1 through Figure 4.6. As the short-circuit fault becomes more severe, the time-domain voltage appears to remain mostly balanced, while the time-domain phase current magnitudes become increasingly imbalanced. However, the

current waveforms maintain their sinusoidal nature. The lack of observable PWM switching in the voltage waveforms is the result of the low bandwidth of the data acquisition system. The bandwidth of the data acquisition system was not large enough to avoid aliasing the PWM switching waveforms. “Smoothing” the voltage waveforms eliminated the aliased PWM pulses and permitted the computation of voltage space-vectors uncluttered by aliased PWM pulses.

The results from applying MCSA to the experimental data reveal a lack of significantly changing 3rd, 9th, and 27th harmonics as compared to the fundamental components of the phase current. Rather than conclude that the existence of a winding short-circuit fault does not increase the 3rd harmonic components in the phase currents it is more likely that, given the sensorless ac drive excitation, the existence of the fault increases the 3rd harmonic components in the phase currents for which compensation is performed by the ac drive. It is likely that the advanced ac drive control maintains a nearly sinusoidal current even through imbalanced operating conditions in the presence of a winding short-circuit fault. The lack of a clear trend in the harmonic magnitudes makes the use of MCSA for the diagnosis and prognostication of winding short-circuit faults inconclusive in this IPM machine excited as motor, and indicates that additional knowledge about the ac drive is necessary for successful fault diagnosis.

However, the imbalance shown in the time-domain phase current waveforms is

resolved by the symmetrical components transformation into increasing negative sequence phasor magnitudes as the fault resistance decreases, indicating an increasingly severe winding fault. The magnitudes of the positive sequence phasors also increase, indicating that the ac drive is sourcing more current as the fault becomes more severe. Furthermore, except for the one test point of 75% load with a $9.66\ \Omega$ fault resistance, Table 4.4 also shows an increasing negative sequence component for increasing fault severity. Even though the magnitude of the negative sequence component phasor for the 75% load and $9.66\ \Omega$ fault resistance test condition is slightly smaller than the healthy case, a fault of $9.66\ \Omega$ is not a very severe fault since that fault resistance is nearly twenty times the phase resistance. The winding with an applied fault resistance of $9.66\ \Omega$ is essentially a healthy winding, and it may be concluded that the negative sequence components method would serve reasonably well to prognosticate the fault.

The use of voltage and current space-vectors to diagnose and prognosticate a winding fault in this experimental IPM machine was inconclusive. In fact, either because of the IPM machine's characteristics or because of the influence of the ac drive control, the progression of the swing angle as a fault index varied in opposition to the trend that made it a successful fault index for induction machines. Instead of the swing angle increasing in value as the fault deteriorated, for this experimental IPM machine the maximum swing angle was found to occur for healthy operation, and the smallest swing angle was for operation with a $9.66\ \Omega$ fault resistance. Even though the

swing angle did vary with the fault resistance, the variation observed is not useful for fault diagnosis and prognostication. This space-vector pendulous oscillation method has been successfully applied and verified for induction machine, but has been rarely applied to permanent-magnet machines as is done in this work, and the inconclusive nature of these results points to the necessity of further investigation into the effects the ac drive is having on the fault diagnosis.

To summarize, two of the three fault diagnosis methods delivered inconclusive results regarding the diagnosis and prognostication of the stator winding short-circuit fault when the experimental IPM machine was operated as a motor with a sensorless ac drive.

Chapter 5

Experimental IPM Machine Results - Generating Operation

In this chapter the experimental results from various winding short-circuit tests performed with IPM machine driven as a generator are presented. Furthermore, the application of the three winding short-circuit fault diagnosis methods to the experimental data and the analysis of the results is also presented. In this context the three methods are applied as “off-line” diagnostics methods for the IPM machine.

The following experimental results demonstrate the effect various short-circuit winding fault resistances across various percentages of the machine phase winding as shown in Figure 3.3 through Figure 3.6 for 20 Hz, 30 Hz, and 40 Hz operation. The experiments were performed with the IPM machine driven as a generator at low speed because of the current limitations of the IPM machine winding. The low rotor test speeds ensured that the induced voltage would not create a phase or fault current that would exceed the rated current of the machine winding. The IPM machine fed a nominal $30\ \Omega$ wye-connected resistive load with the measured resistances being $28\ \Omega$, $29\ \Omega$, and $30\ \Omega$, unless the figure captions specify an open-circuit test condition.

5.1 Time-Domain Phase Voltages and Phase Currents

Figure 5.1 and Figure 5.2 show the healthy IPM machine line-to-neutral voltages and phase currents when driven as a generator at a speed of 400 r/min, which is a frequency of 20 Hz. The three-phase voltages are balanced, but there is a slight bias in the current sensors as indicated by the slight imbalance in the current waveforms. Figure 5.3 through Figure 5.7 show the open-circuit line-to-neutral voltages for the healthy case and the $5\ \Omega$ faulted case, to demonstrate the imbalances which occur among the line-to-neutral voltages for partial winding fault conditions while the machine terminals are in an open-circuit configuration.

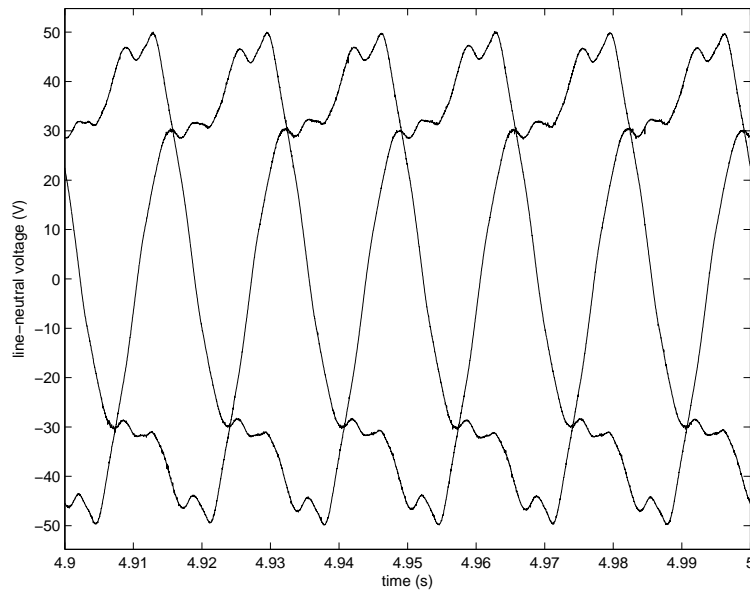


Figure 5.1: Line-to-neutral voltage of the IPM machine at 20 Hz with no winding fault.

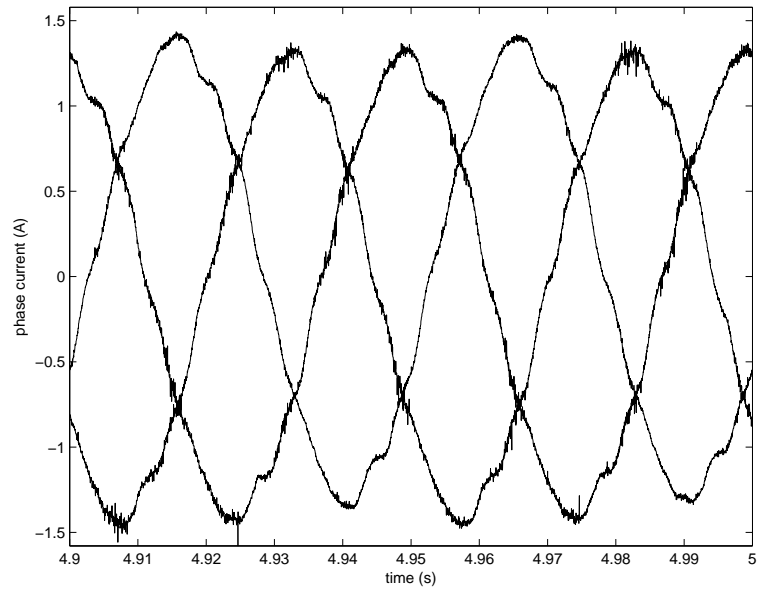


Figure 5.2: Phase current of the IPM machine at 20 Hz with no winding fault.

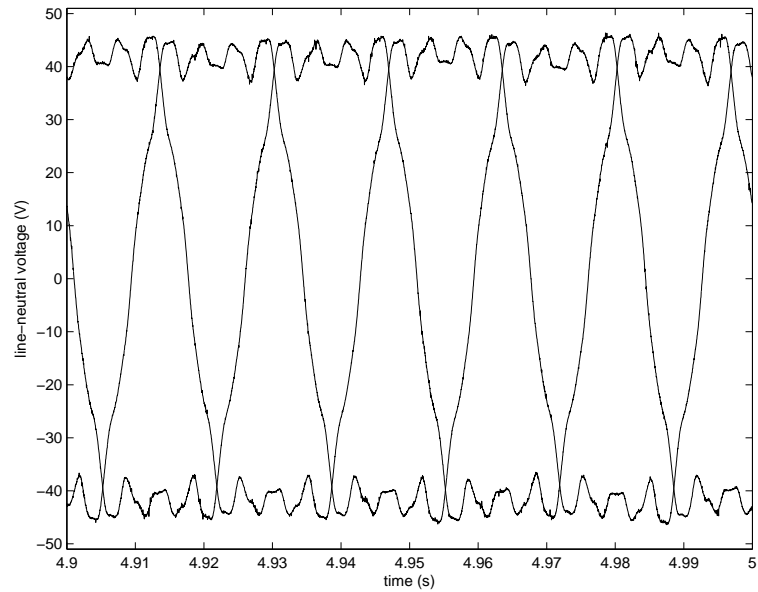


Figure 5.3: Open-circuit line-to-neutral voltage of the IPM machine at 20 Hz with no winding fault.

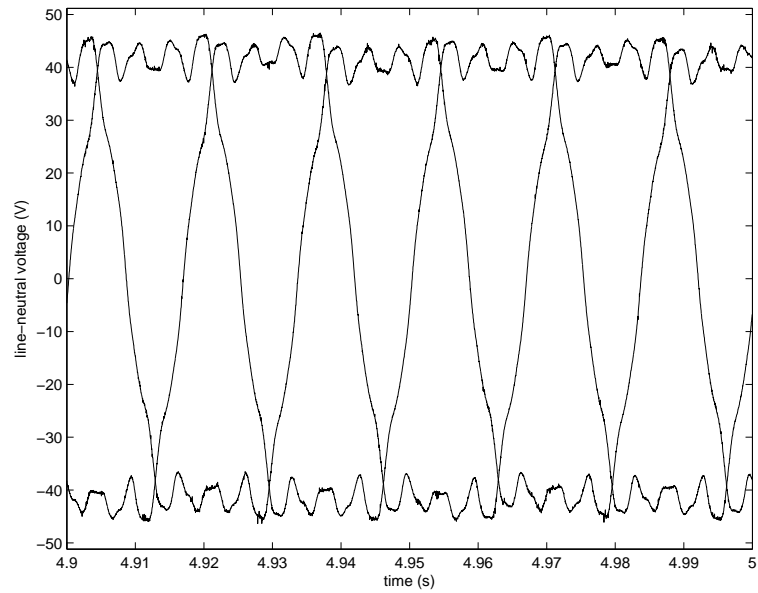


Figure 5.4: Open-circuit line-to-neutral voltage of the IPM machine at 20 Hz with a $5\ \Omega$, 16.7% winding fault.

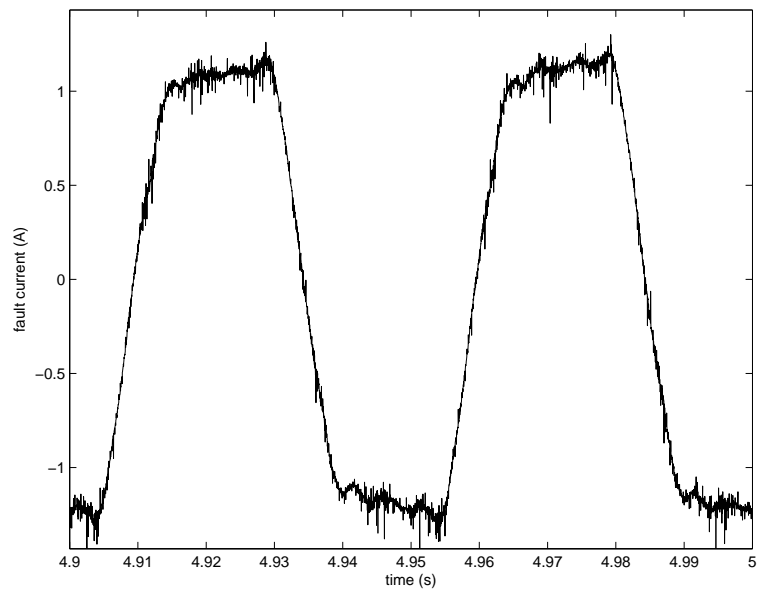


Figure 5.5: Circulating fault current of the IPM machine at 20 Hz with a $5\ \Omega$, 16.7% winding fault, with an open-circuit terminal configuration.

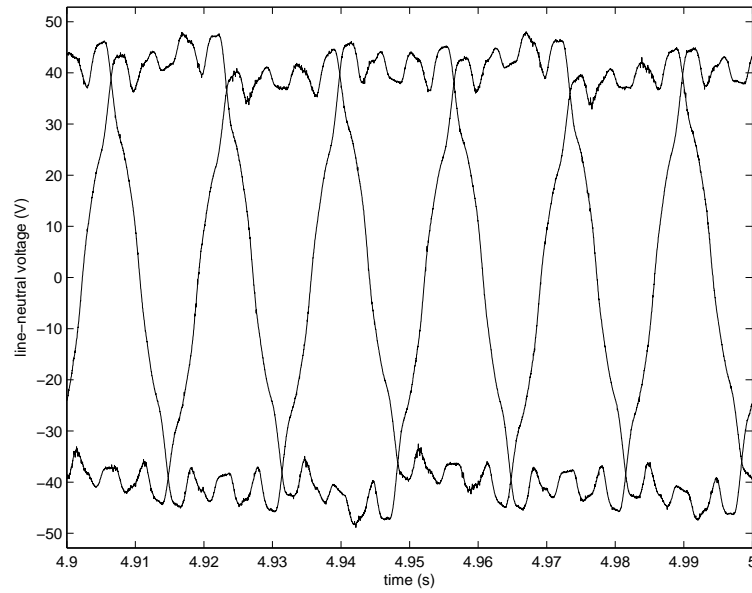


Figure 5.6: Open-circuit line-to-neutral voltage of the IPM machine at 20 Hz with a $5\ \Omega$, 33.3% winding fault.

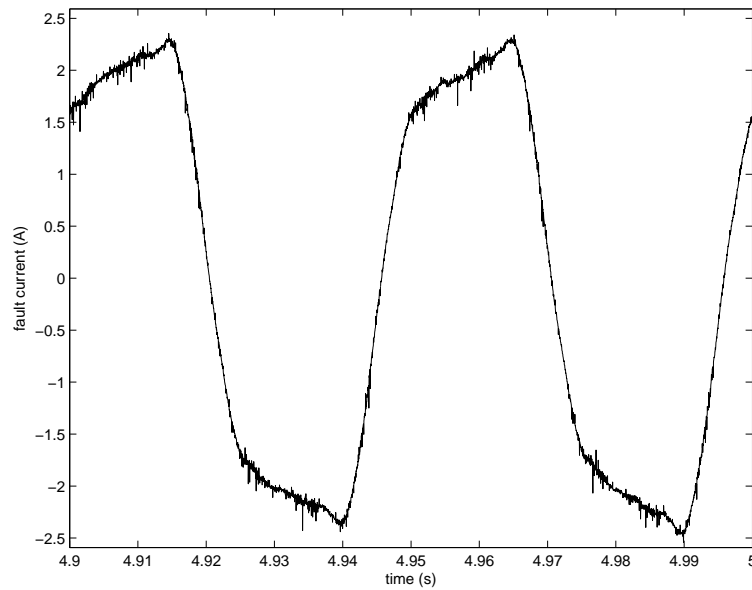


Figure 5.7: Circulating fault current of the IPM machine at 20 Hz with a $5\ \Omega$, 33.3% winding fault, with an open-circuit terminal configuration.

The experimental results for increasing fault severity/decreasing fault resistance are shown in Figure 5.8 through Figure 5.52. As the fault becomes more severe, both the magnitude of the time-domain voltages and the magnitude of the time-domain currents become increasingly imbalanced.

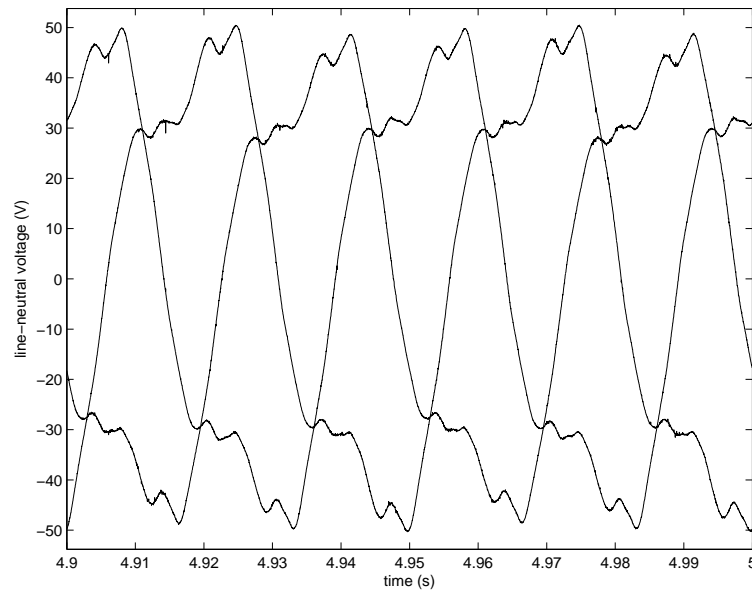


Figure 5.8: Line-to-neutral voltage of the IPM machine at 20 Hz with a $9.7\ \Omega$, 33.3% winding fault.

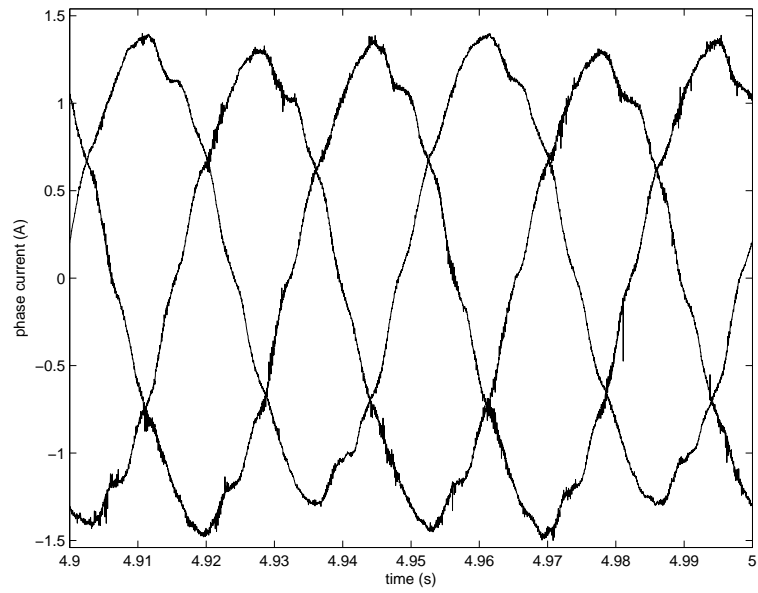


Figure 5.9: Phase current of the IPM machine at 20 Hz with a $9.7\ \Omega$, 33.3% winding fault.

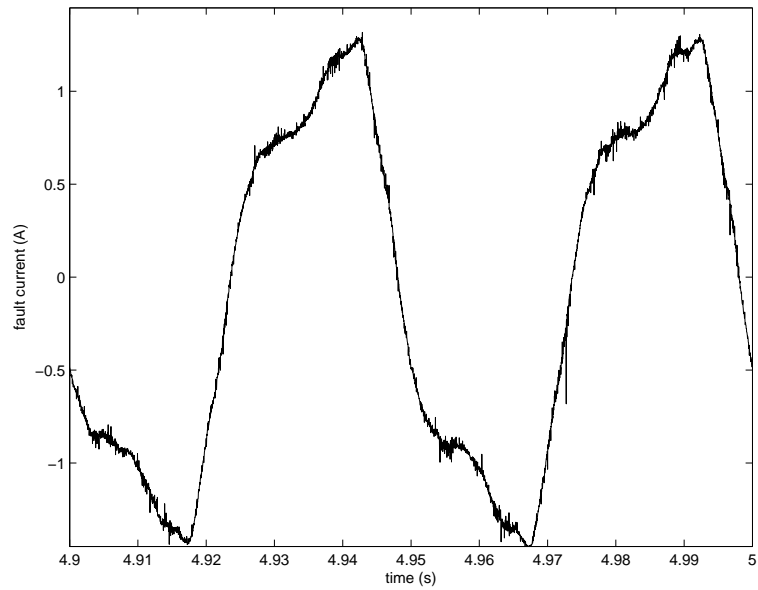


Figure 5.10: Fault current of the IPM machine at 20 Hz with a $9.7\ \Omega$, 33.3% winding fault.

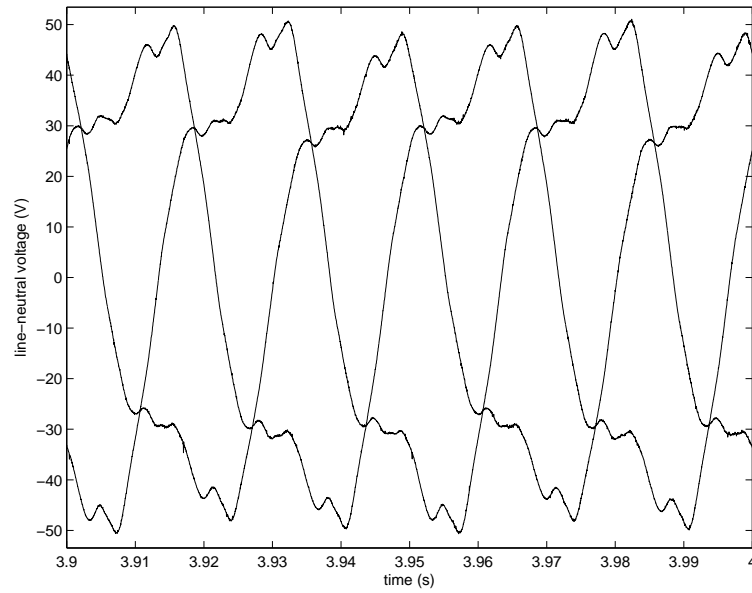


Figure 5.11: Line-to-neutral voltage of the IPM machine at 20 Hz with a 6.6Ω , 33.3% winding fault.

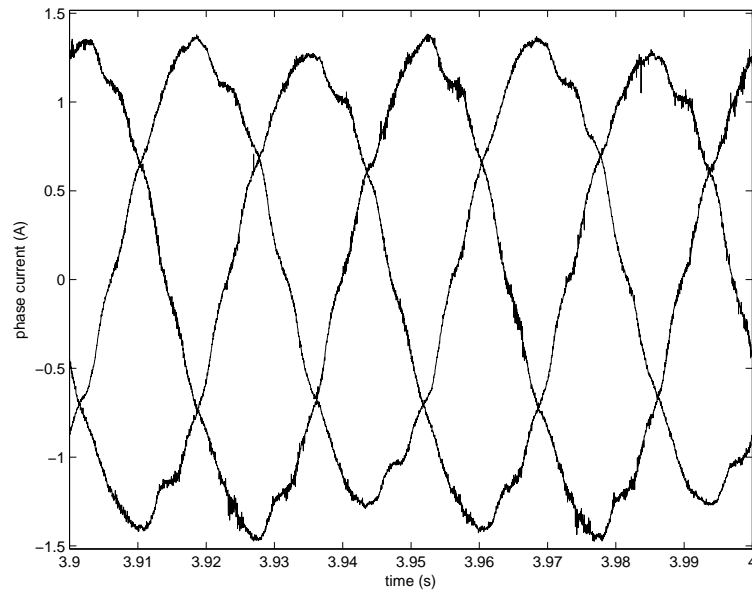


Figure 5.12: Phase current of the IPM machine at 20 Hz with a 6.6Ω , 33.3% winding fault.

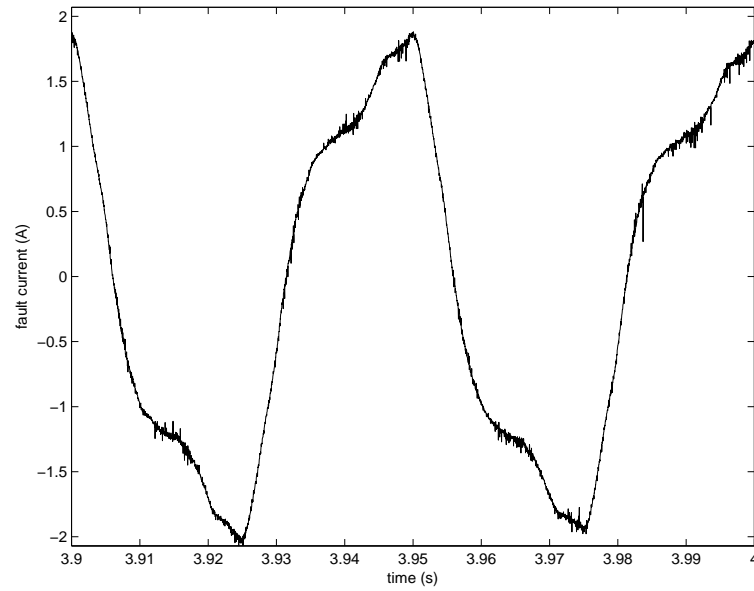


Figure 5.13: Fault current of the IPM machine at 20 Hz with a 6.6Ω , 33.3% winding fault.

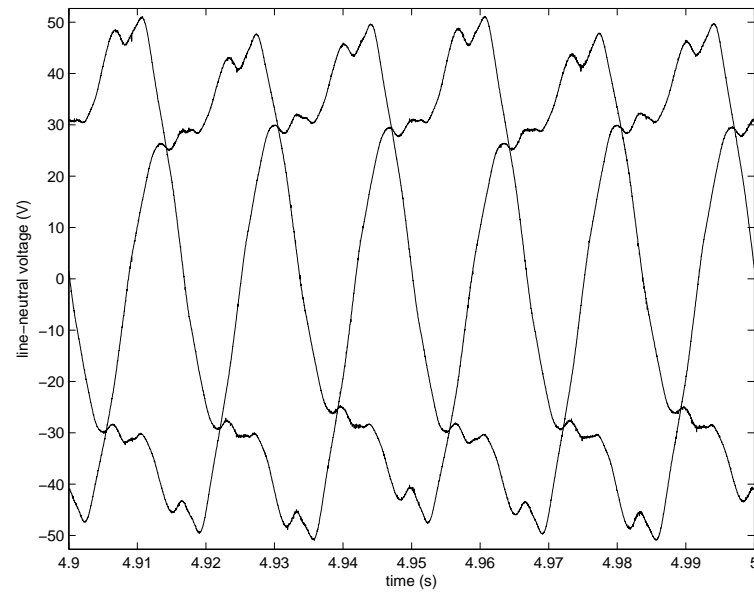


Figure 5.14: Line-to-neutral voltage of the IPM machine at 20 Hz with a 4.9Ω , 33.3% winding fault.

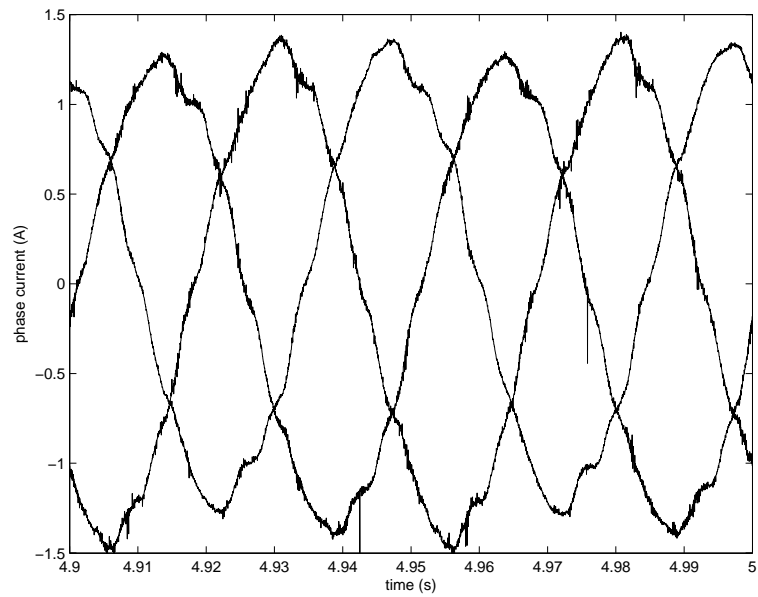


Figure 5.15: Phase current of the IPM machine at 20 Hz with a $4.9\ \Omega$, 33.3% winding fault.

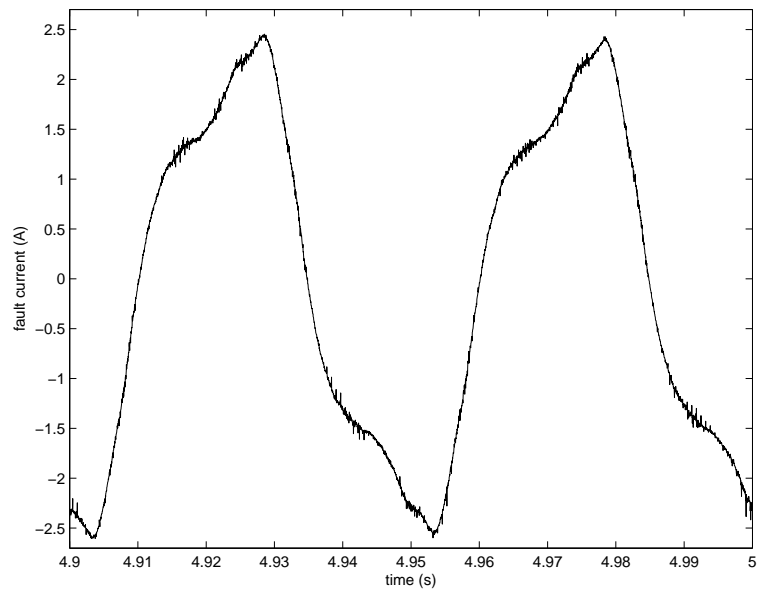


Figure 5.16: Fault current of the IPM machine at 20 Hz with a $4.9\ \Omega$, 33.3% winding fault.

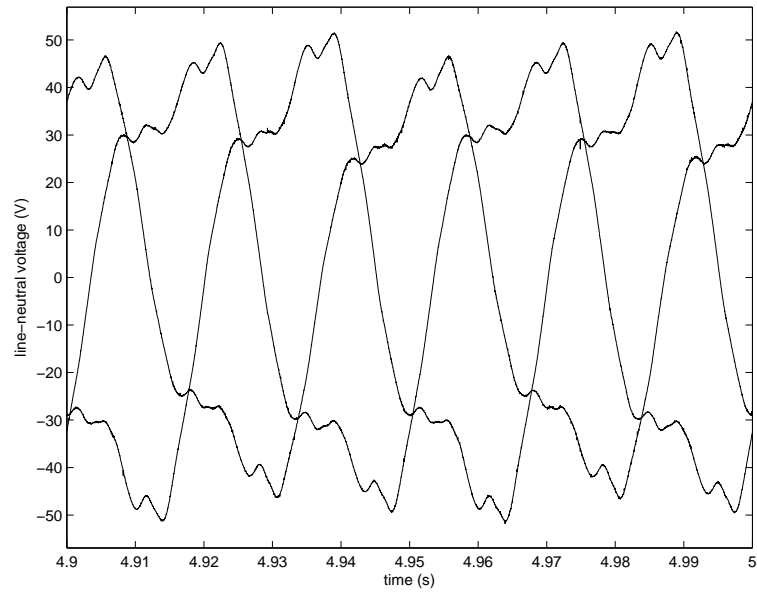


Figure 5.17: Line-to-neutral voltage of the IPM machine at 20 Hz with a 3.3Ω , 33.3% winding fault.

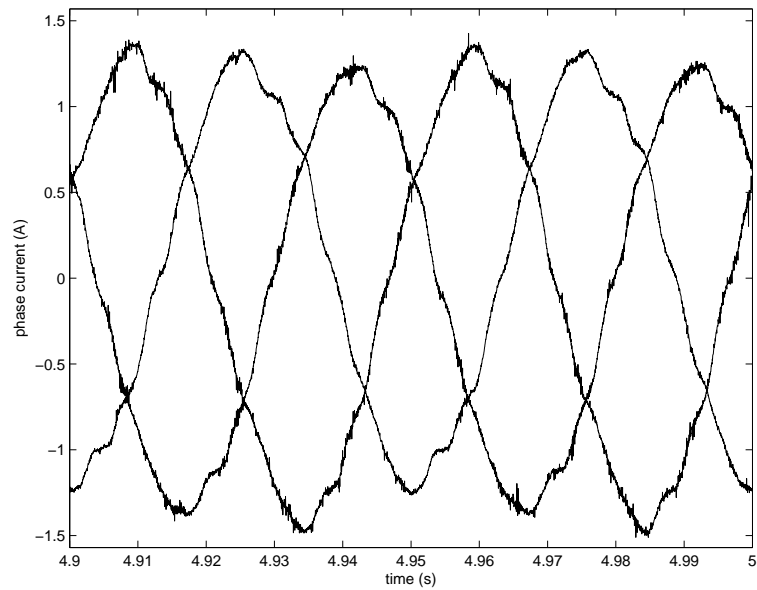


Figure 5.18: Phase current of the IPM machine at 20 Hz with a 3.3Ω , 33.3% winding fault.

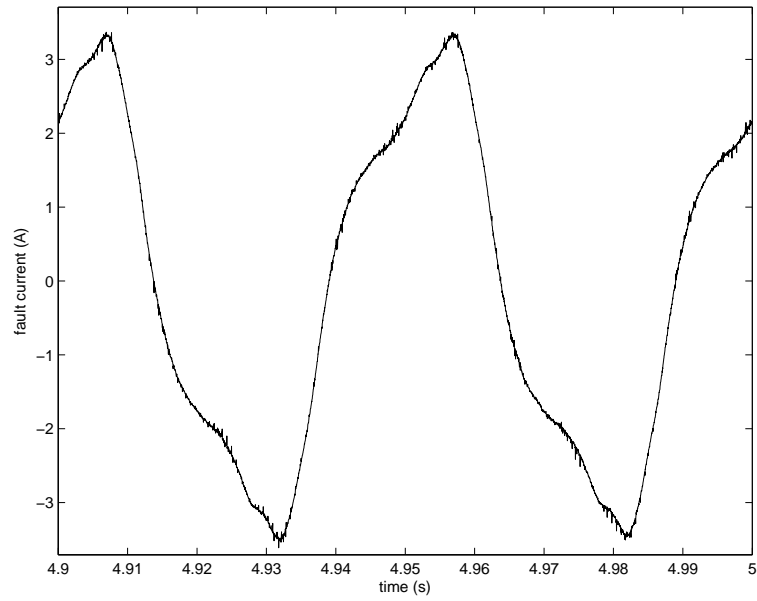


Figure 5.19: Fault current of the IPM machine at 20 Hz with a $3.3\ \Omega$, 33.3% winding fault.

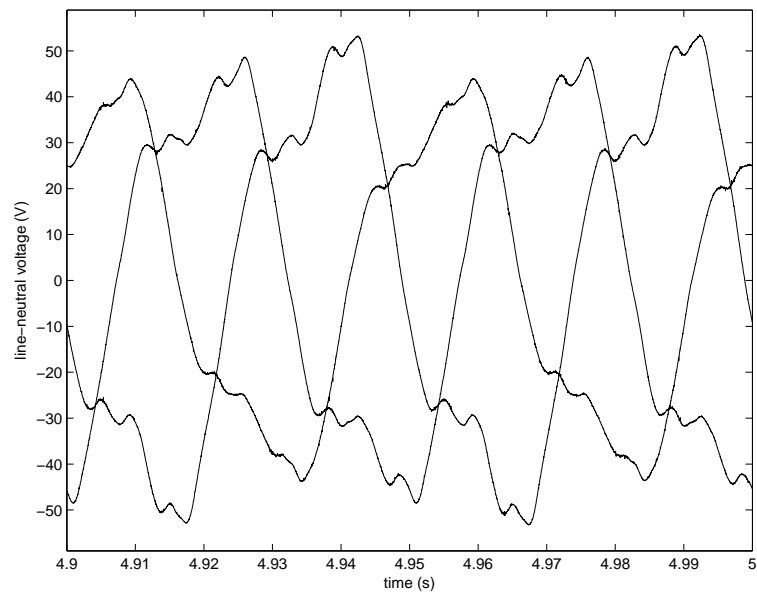


Figure 5.20: Line-to-neutral voltage of the IPM machine at 20 Hz with a $9.6\ \Omega$, 66.7% winding fault.

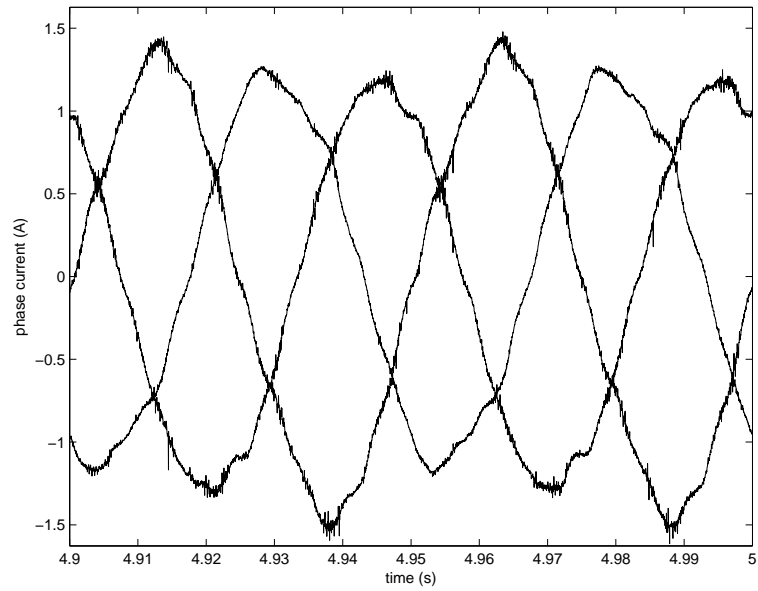


Figure 5.21: Phase current of the IPM machine at 20 Hz with a $9.6\ \Omega$, 66.7% winding fault.

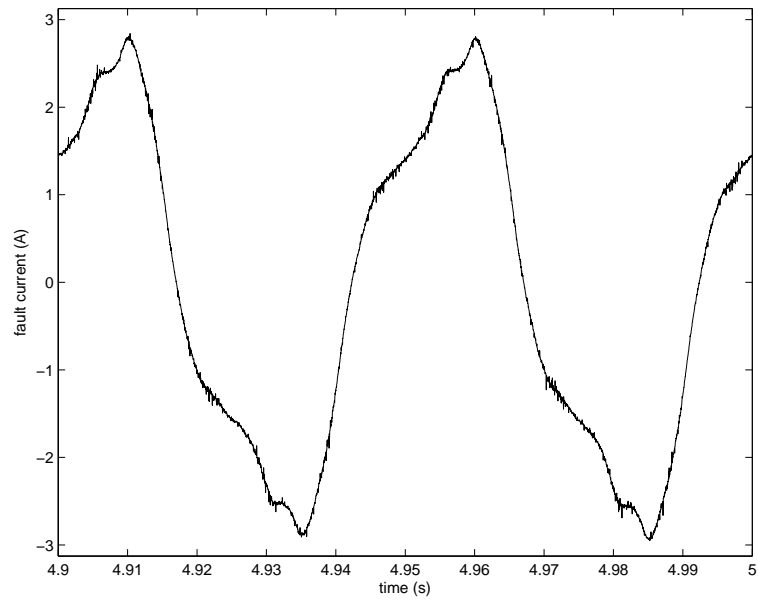


Figure 5.22: Fault current of the IPM machine at 20 Hz with a $9.6\ \Omega$, 66.7% winding fault.

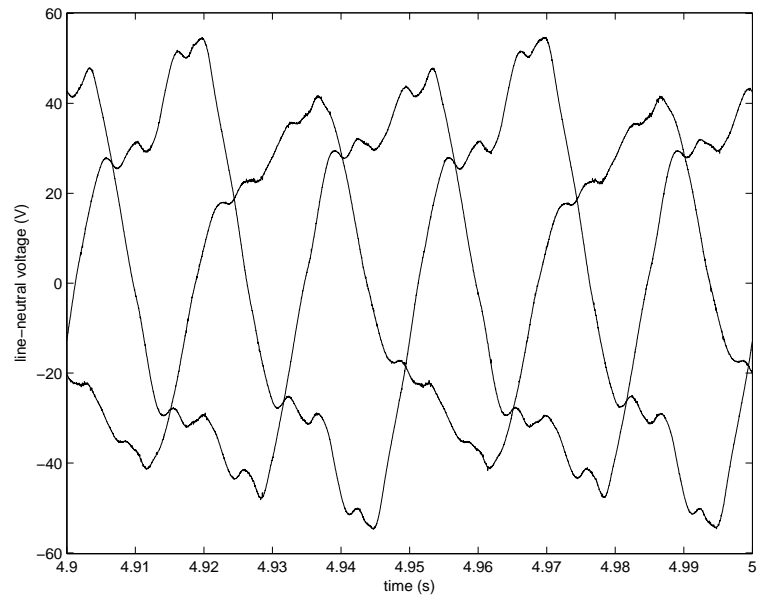


Figure 5.23: Line-to-neutral voltage of the IPM machine at 20 Hz with a 6.6Ω , 66.7% winding fault.

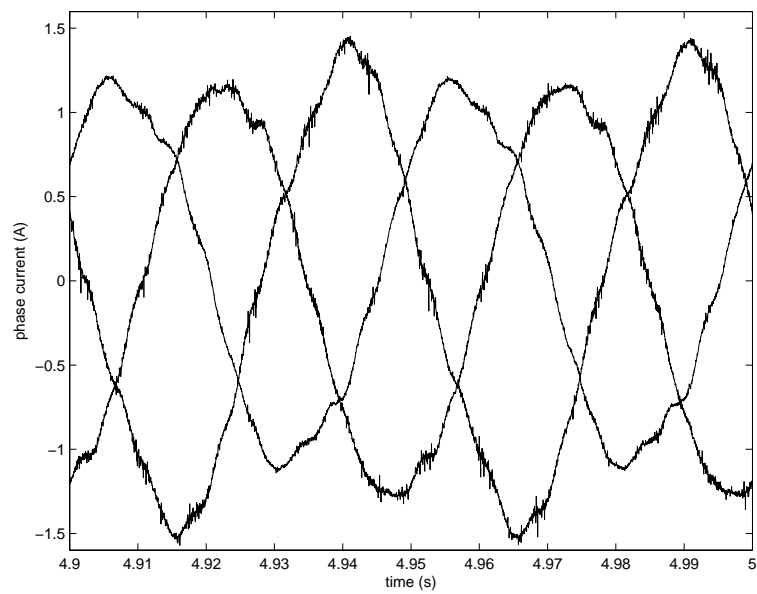


Figure 5.24: Phase current of the IPM machine at 20 Hz with a 6.6Ω , 66.7% winding fault.

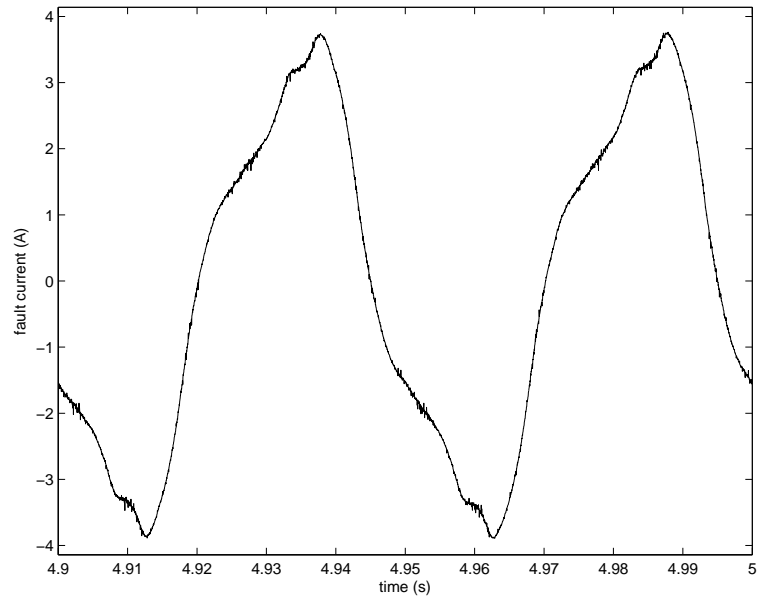


Figure 5.25: Fault current of the IPM machine at 20 Hz with a 6.6Ω , 66.7% winding fault.

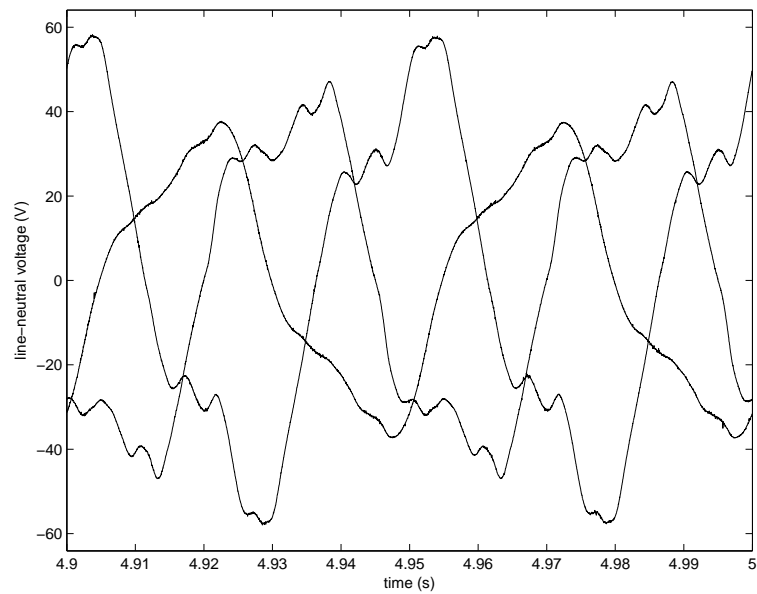


Figure 5.26: Line-to-neutral voltage of the IPM machine at 20 Hz with a 10Ω , 100% winding fault.

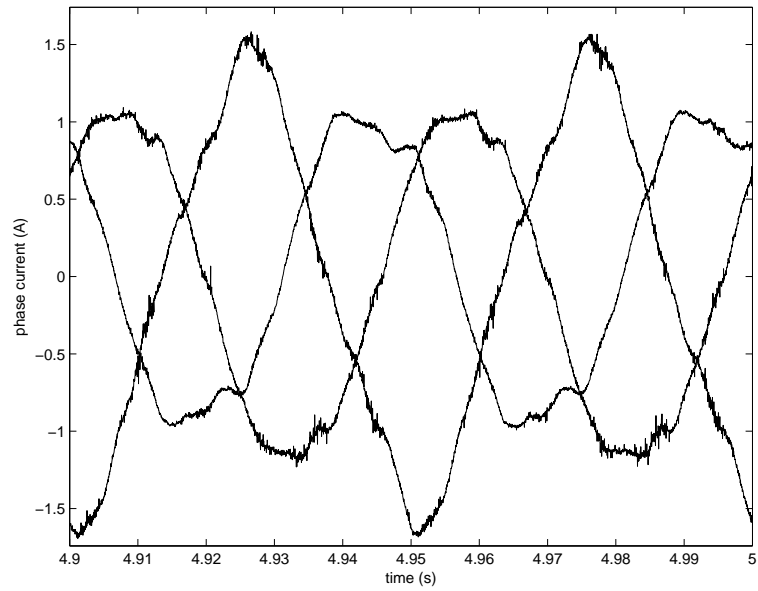


Figure 5.27: Phase current of the IPM machine at 20 Hz with a $10\ \Omega$, 100% winding fault.

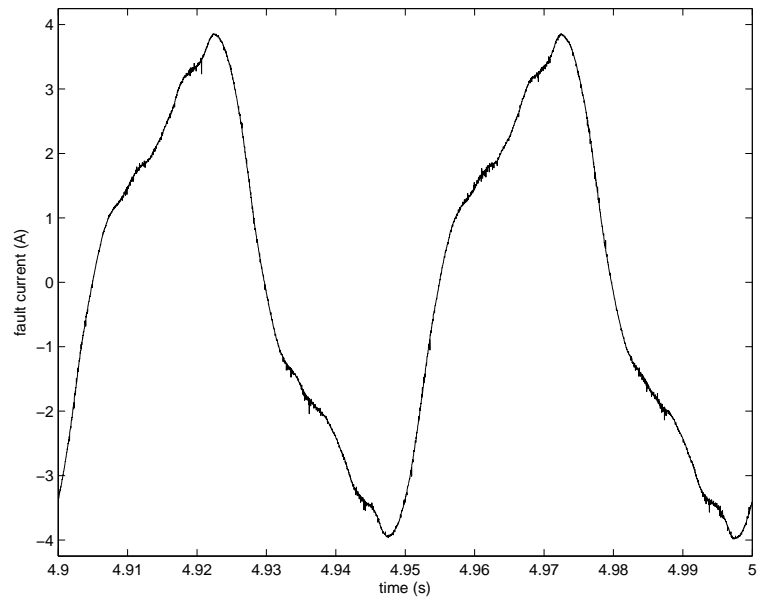


Figure 5.28: Fault current of the IPM machine at 20 Hz with a $10\ \Omega$, 100% winding fault.

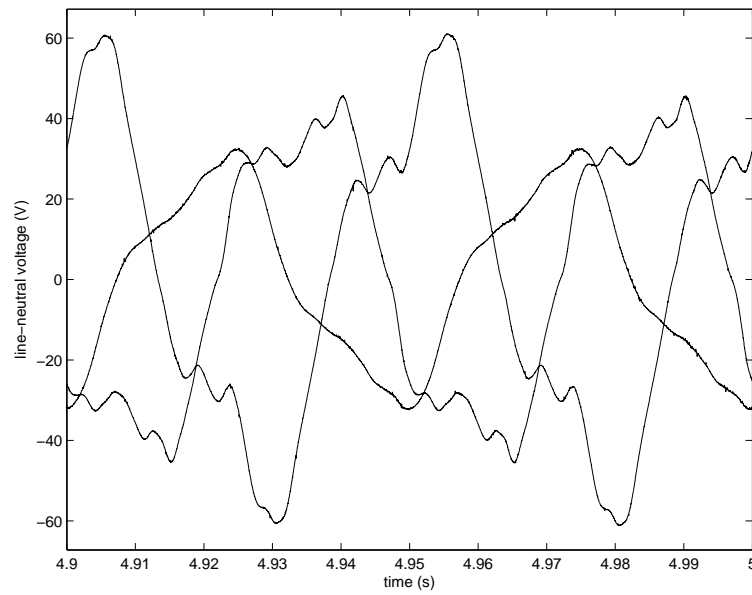


Figure 5.29: Line-to-neutral voltage of the IPM machine at 20 Hz with a 6.5Ω , 100% winding fault.

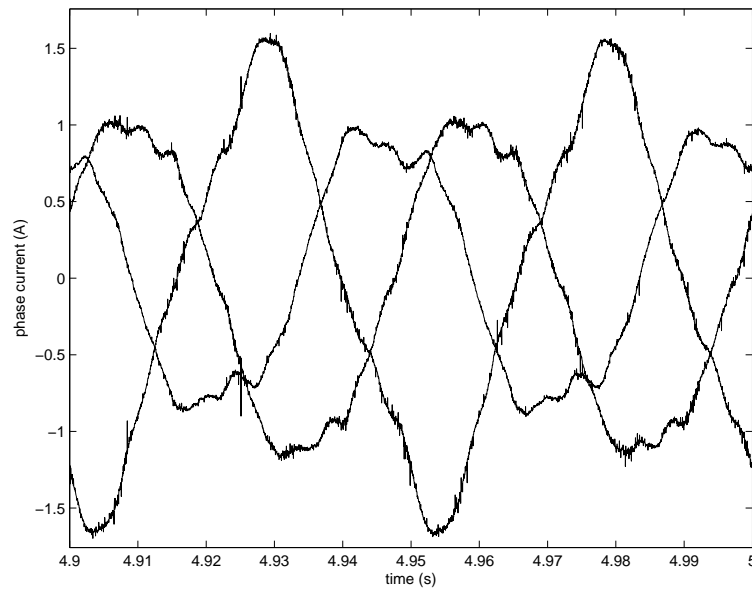


Figure 5.30: Phase current of the IPM machine at 20 Hz with a 6.5Ω , 100% winding fault.

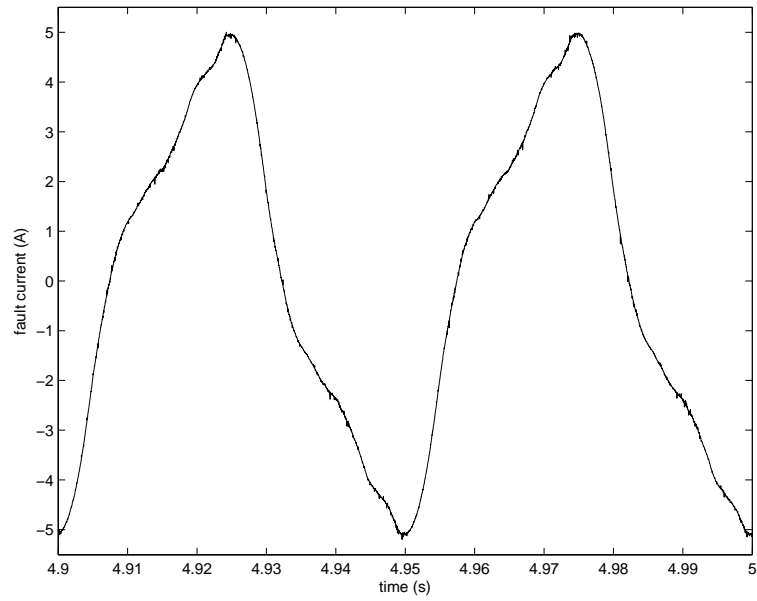


Figure 5.31: Fault current of the IPM machine at 20 Hz with a 6.5Ω , 100% winding fault.

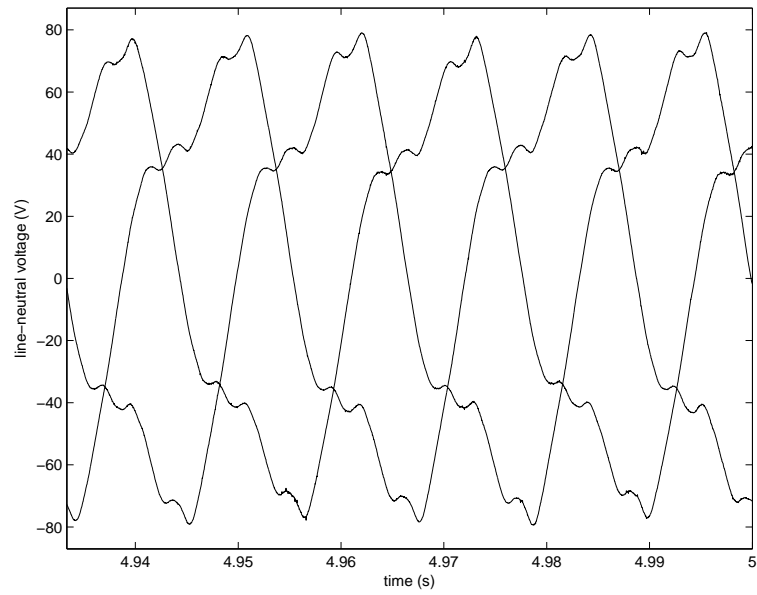


Figure 5.32: Line-to-neutral voltage of the IPM machine at 30 Hz with a 5.0Ω , 16.7% winding fault.

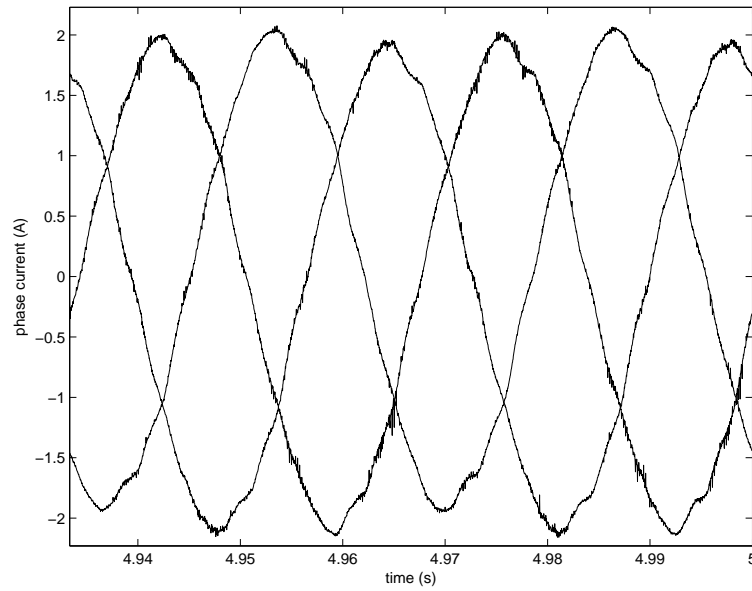


Figure 5.33: Phase current of the IPM machine at 30 Hz with a $5.0\ \Omega$, 16.7% winding fault.

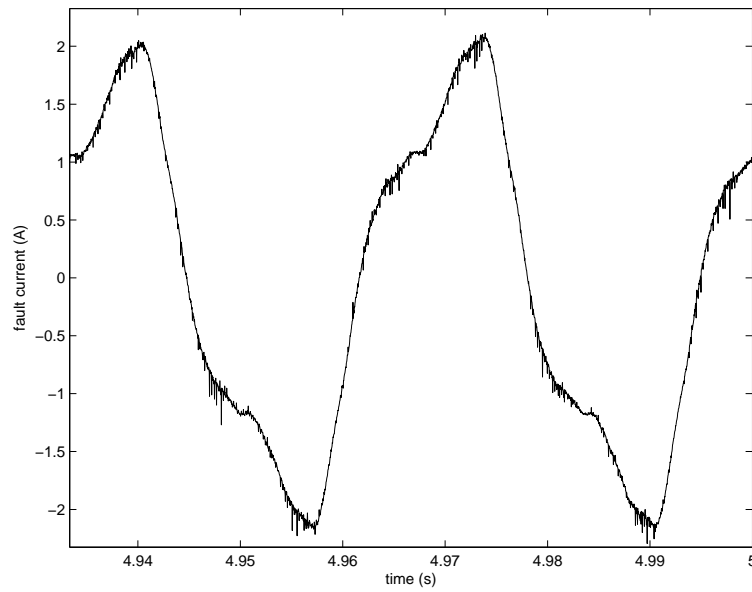


Figure 5.34: Fault current of the IPM machine at 30 Hz with a $5.0\ \Omega$, 16.7% winding fault.

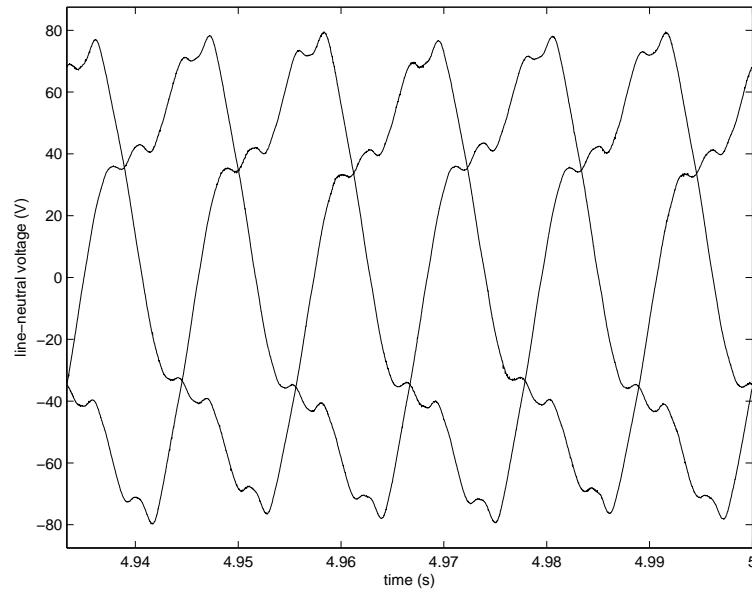


Figure 5.35: Line-to-neutral voltage of the IPM machine at 30 Hz with a 3.3Ω , 16.7% winding fault.

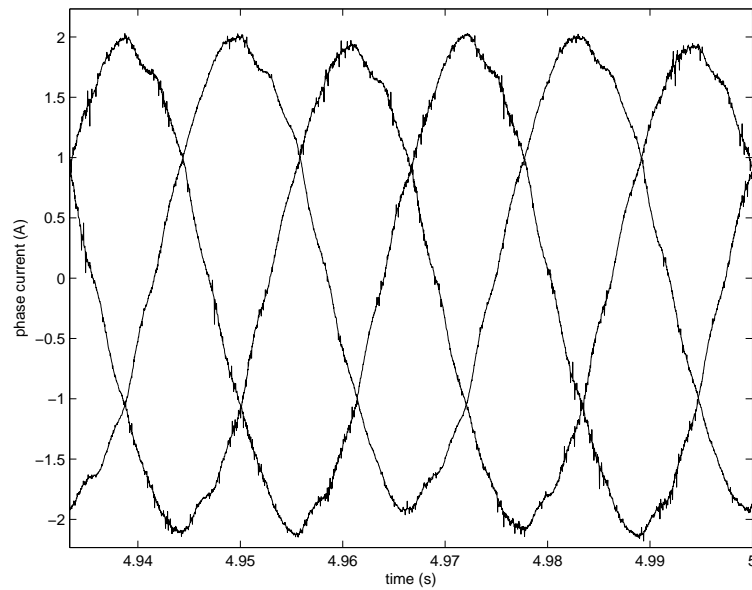


Figure 5.36: Phase current of the IPM machine at 30 Hz with a 3.3Ω , 16.7% winding fault.

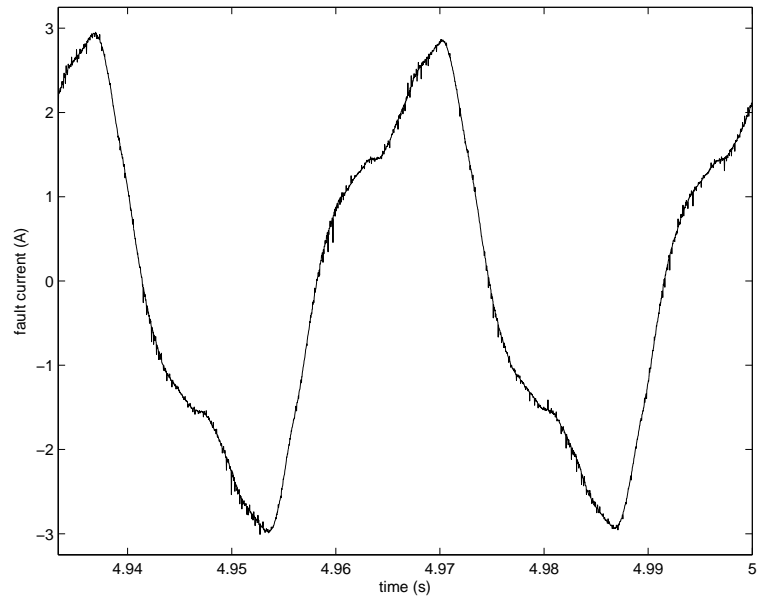


Figure 5.37: Fault current of the IPM machine at 30 Hz with a $3.3\ \Omega$, 16.7% winding fault.

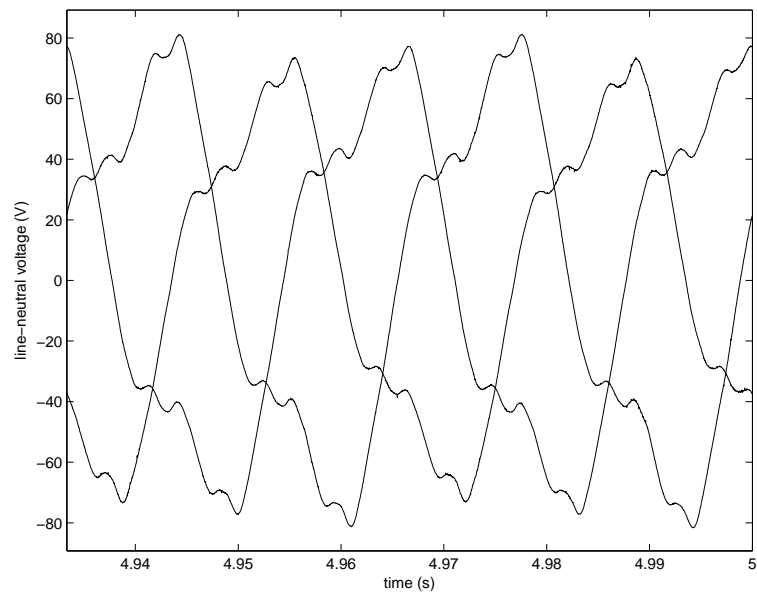


Figure 5.38: Line-to-neutral voltage of the IPM machine at 30 Hz with a $5.0\ \Omega$, 33.3% winding fault.

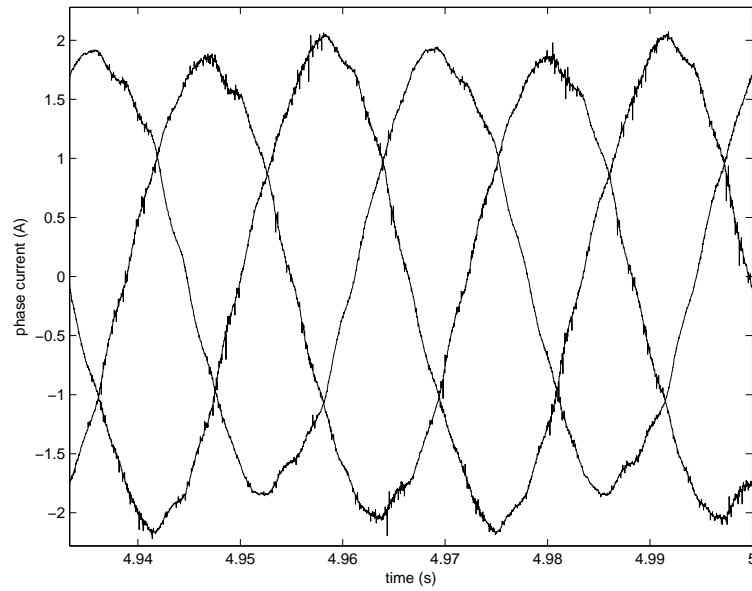


Figure 5.39: Phase current of the IPM machine at 30 Hz with a $5.0\ \Omega$, 33.3% winding fault.

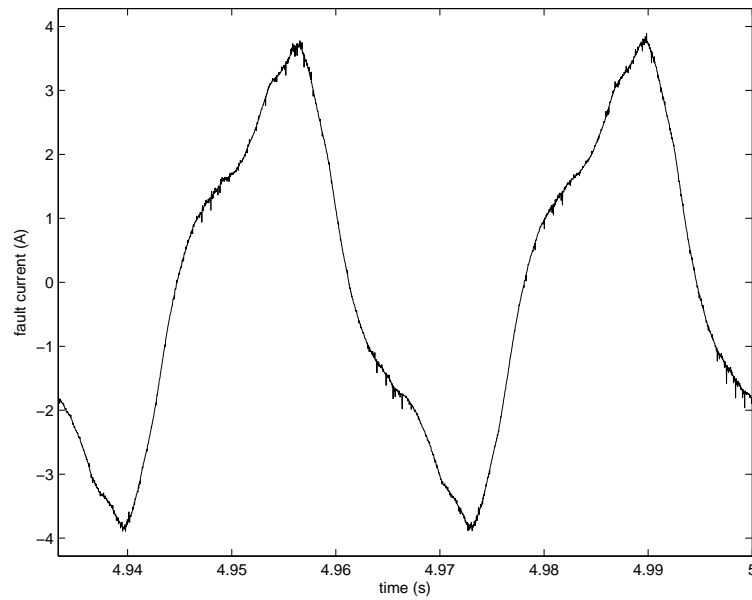


Figure 5.40: Fault current of the IPM machine at 30 Hz with a $5.0\ \Omega$, 33.3% winding fault.

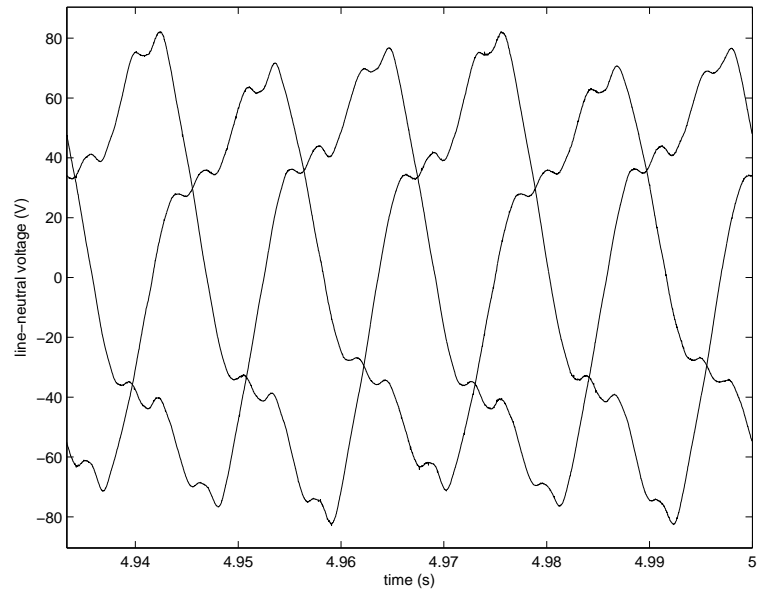


Figure 5.41: Line-to-neutral voltage of the IPM machine at 30 Hz with a 3.3Ω , 33.3% winding fault.

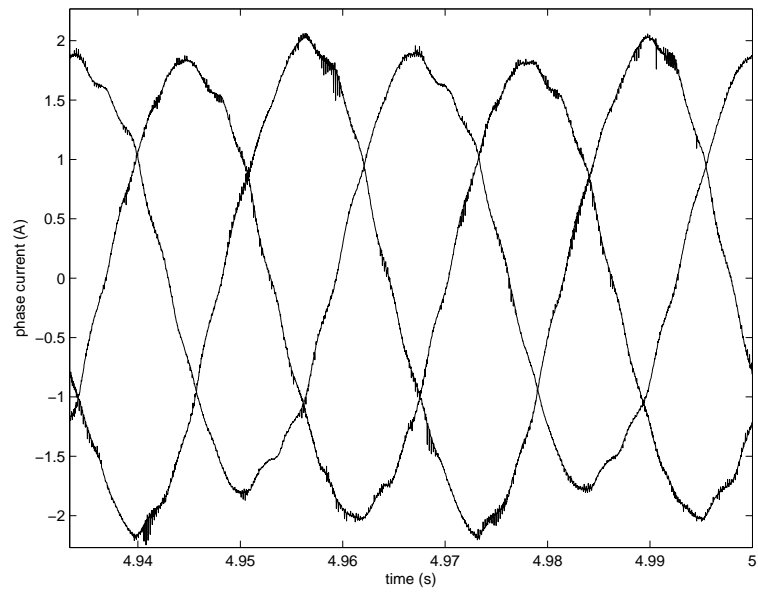


Figure 5.42: Phase current of the IPM machine at 30 Hz with a 3.3Ω , 33.3% winding fault.

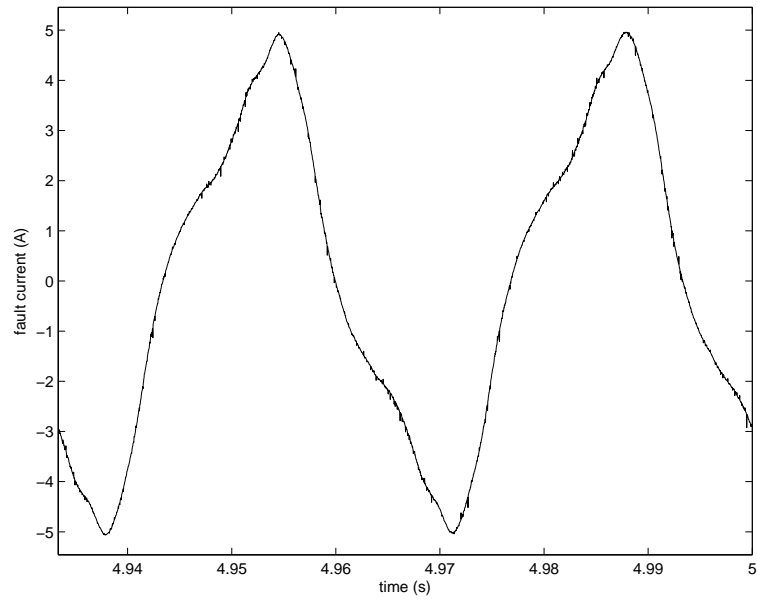


Figure 5.43: Fault current of the IPM machine at 30 Hz with a $3.3\ \Omega$, 33.3% winding fault.

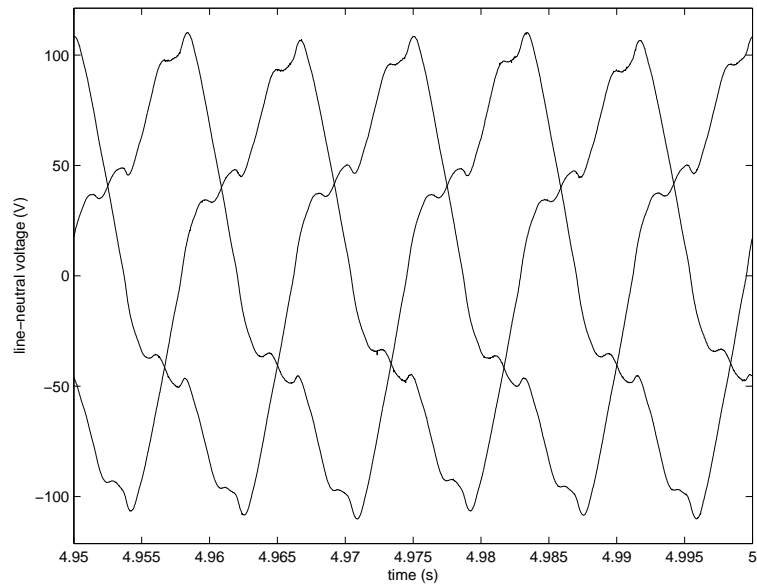


Figure 5.44: Line-to-neutral voltage of the IPM machine at 40 Hz with a $5.0\ \Omega$, 16.7% winding fault.

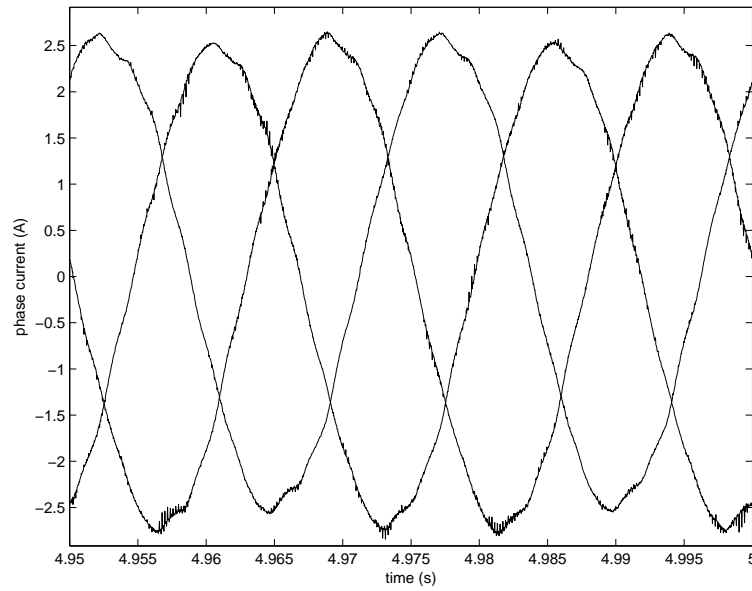


Figure 5.45: Phase current of the IPM machine at 40 Hz with a $5.0\ \Omega$, 16.7% winding fault.

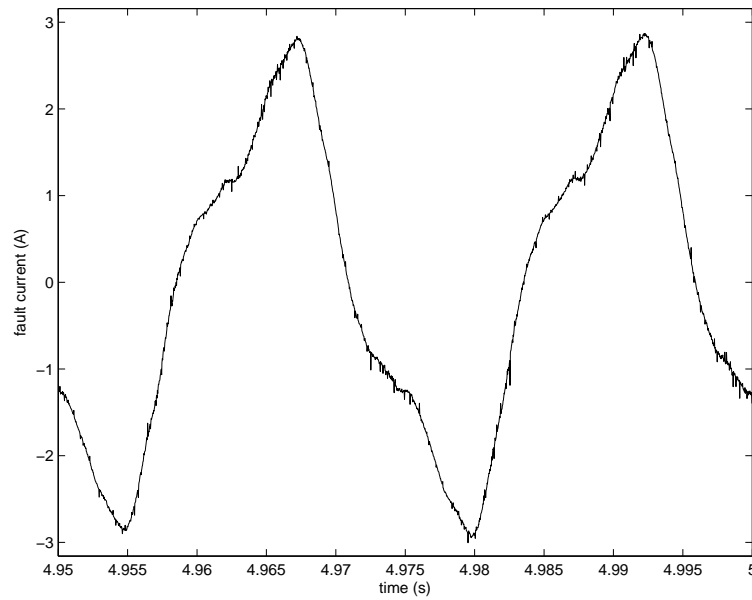


Figure 5.46: Fault current of the IPM machine at 40 Hz with a $5.0\ \Omega$, 16.7% winding fault.

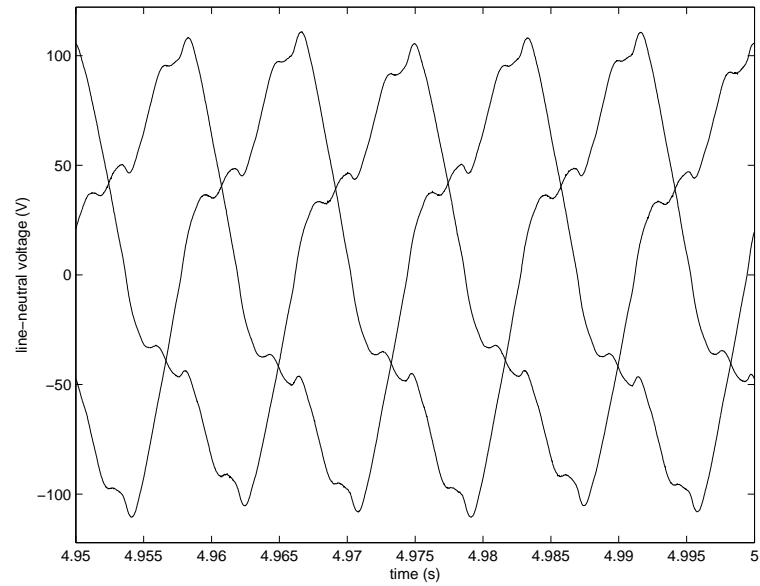


Figure 5.47: Line-to-neutral voltage of the IPM machine at 40 Hz with a 3.3Ω , 16.7% winding fault.

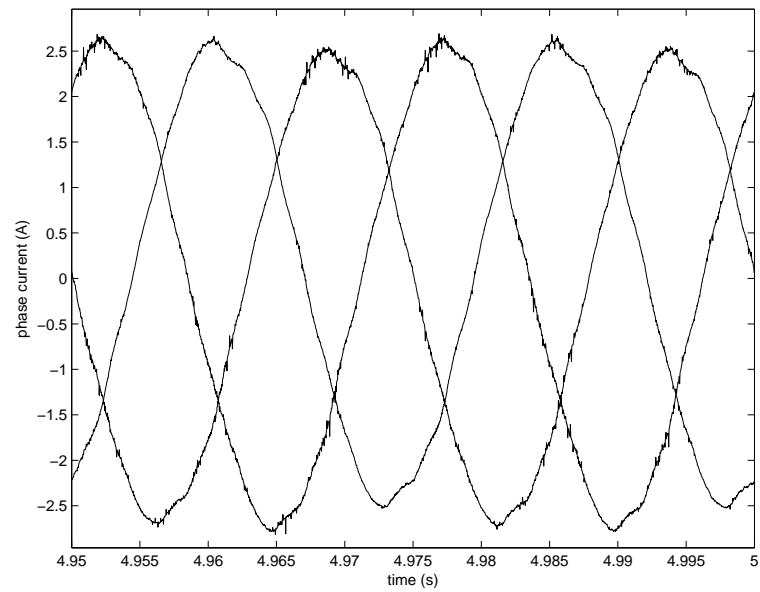


Figure 5.48: Phase current of the IPM machine at 40 Hz with a 3.3Ω , 16.7% winding fault.

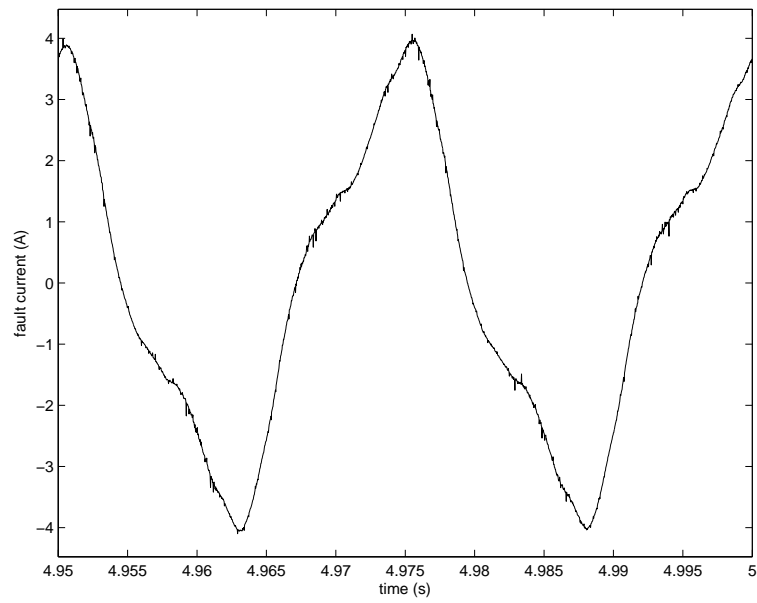


Figure 5.49: Fault current of the IPM machine at 40 Hz with a $3.3\ \Omega$, 16.7% winding fault.

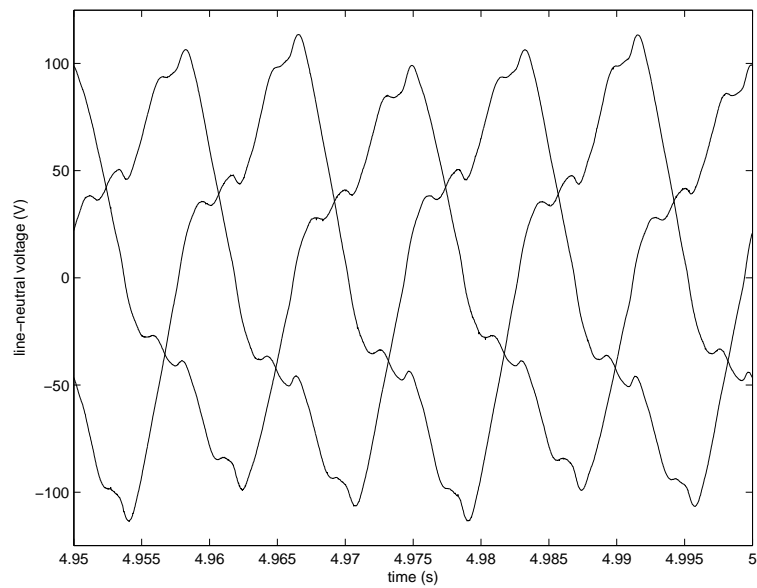


Figure 5.50: Line-to-neutral voltage of the IPM machine at 40 Hz with a $5.0\ \Omega$, 33.3% winding fault.

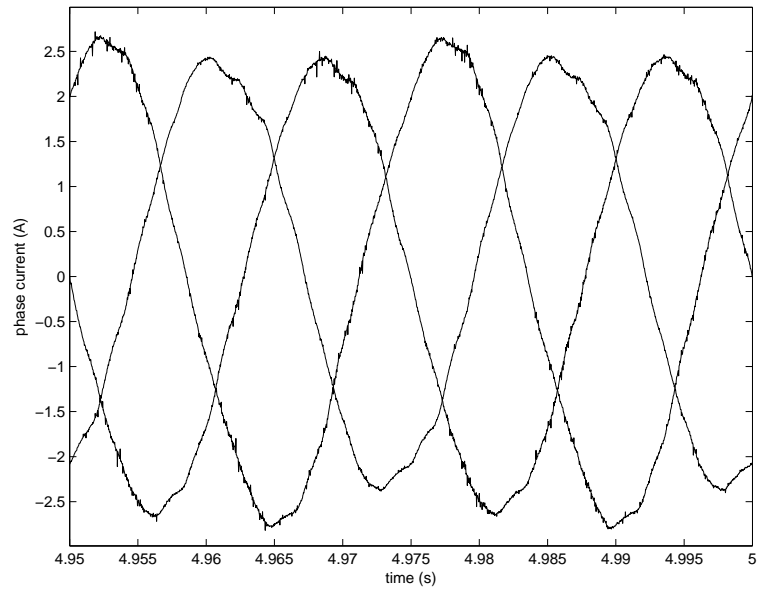


Figure 5.51: Phase current of the IPM machine at 40 Hz with a $5.0\ \Omega$, 33.3% winding fault.

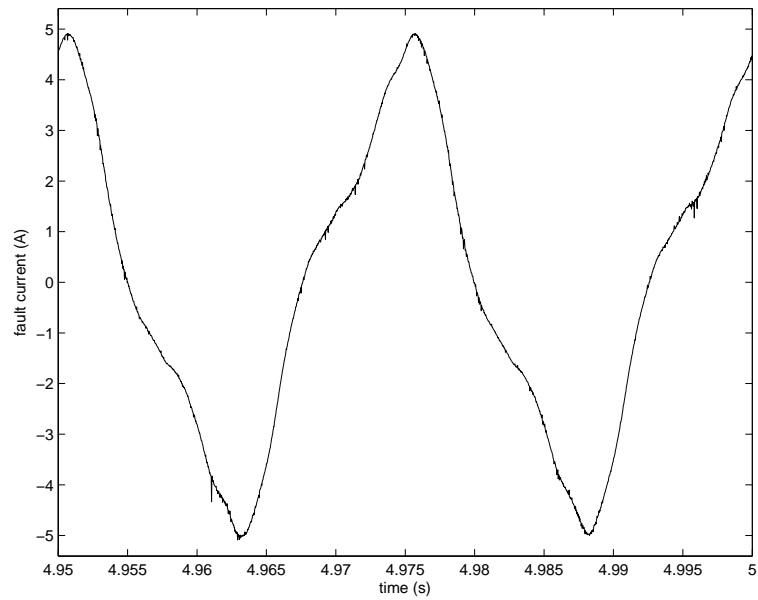


Figure 5.52: Fault current of the IPM machine at 40 Hz with a $5.0\ \Omega$, 33.3% winding fault.

5.2 Results of Motor Current Spectrum Analysis

The frequency spectra for the experimental phase currents of the IPM machine at different speed and torque test points and for increasing fault severity/decreasing fault resistances are shown in Figure 5.53 through Figure 5.100. As seen in Figure 5.53 through Figure 5.55, this IPM machine's phase currents contain a significant 5th, 7th, 11th, and 13th harmonic. Introducing a short-circuit fault to the winding leads to the appearance of a significant 3rd and 9th harmonic in the phase currents as seen in Figure 5.56 through Figure 5.100.

Table 5.1 through Table 5.9 contain the magnitudes of the harmonic components of the phase currents that appear under fault conditions. Note that as the fault becomes more severe, the magnitudes of the 3rd and 9th harmonic components significantly increase.

Table 5.1: 3rd harmonic components of the IPM machine faulted phase current when operated at 20 Hz.

<i>Winding fault %</i>	<i>Fault resistance</i>	<i>Phase A (dB)</i>	<i>Phase B (dB)</i>	<i>Phase C (dB)</i>
0 %	Inf.	-59.9	-52.1	-53.2
33.3 %	9.7 Ω	-37.3	-49.6	-39.2
33.3 %	6.6 Ω	-35.2	-45.8	-36.2
33.3 %	4.9 Ω	-33.7	-42.3	-34.2
33.3 %	3.3 Ω	-31.9	-32.1	-38.4
66.7 %	9.6 Ω	-26.2	-26.4	-34.9
66.7 %	6.6 Ω	-23.9	-24.3	-31.7
100 %	10 Ω	-19.3	-19.0	-26.6
100 %	6.5 Ω	-17.5	-16.5	-23.9

Table 5.2: 9rd harmonic components of the IPM machine faulted phase current when operated at 20 Hz.

<i>Winding fault %</i>	<i>Fault resistance</i>	<i>Phase A (dB)</i>	<i>Phase B (dB)</i>	<i>Phase C (dB)</i>
0 %	Inf.	-54.1	-62.2	-63.2
33.3 %	9.7 Ω	-48.6	-60.2	-59.2
33.3 %	6.6 Ω	-47.0	-55.8	-57.0
33.3 %	4.9 Ω	-47.2	-53.2	-59.1
33.3 %	3.3 Ω	-63.4	-46.9	-56.9
66.7 %	9.6 Ω	-44.0	-36.4	-42.2
66.7 %	6.6 Ω	-42.8	-35.3	-40.6
100 %	10 Ω	-37.3	-29.4	-36.5
100 %	6.5 Ω	-36.8	-28.0	-35.2

Table 5.3: 27rd harmonic components of the IPM machine faulted phase current when operated at 20 Hz.

<i>Winding fault %</i>	<i>Fault resistance</i>	<i>Phase A (dB)</i>	<i>Phase B (dB)</i>	<i>Phase C (dB)</i>
0 %	Inf.	-81.9	-77.1	-72.8
33.3 %	9.7 Ω	-85.0	-68.8	-83.2
33.3 %	6.6 Ω	-82.5	-66.8	-75.2
33.3 %	4.9 Ω	-77.6	-72.7	-75.5
33.3 %	3.3 Ω	-70.1	-73.7	-72.9
66.7 %	9.6 Ω	-67.1	-64.5	-60.8
66.7 %	6.6 Ω	-71.1	-64.2	-61.9
100 %	10 Ω	-71.0	-53.4	-56.5
100 %	6.5 Ω	-70.6	-53.6	-57.8

Table 5.4: 3rd harmonic components of the IPM machine faulted phase current when operated at 30 Hz.

<i>Winding fault %</i>	<i>Fault resistance</i>	<i>Phase A (dB)</i>	<i>Phase B (dB)</i>	<i>Phase C (dB)</i>
16.7 %	5.0 Ω	-42.7	-41.3	-63.4
16.7 %	3.3 Ω	-39.9	-39.7	-58.7
33.3 %	5.0 Ω	-32.3	-31.6	-45.9
33.3 %	3.3 Ω	-30.4	-30.6	-43.4

Table 5.5: 9th harmonic components of the IPM machine faulted phase current when operated at 30 Hz.

<i>Winding fault %</i>	<i>Fault resistance</i>	<i>Phase A (dB)</i>	<i>Phase B (dB)</i>	<i>Phase C (dB)</i>
16.7 %	5.0 Ω	-63.8	-55.1	-71.3
16.7 %	3.3 Ω	-66.3	-54.6	-68.8
33.3 %	5.0 Ω	-60.8	-49.0	-57.1
33.3 %	3.3 Ω	-64.2	-50.4	-52.9

Table 5.6: 27th harmonic components of the IPM machine faulted phase current when operated at 30 Hz.

<i>Winding fault %</i>	<i>Fault resistance</i>	<i>Phase A (dB)</i>	<i>Phase B (dB)</i>	<i>Phase C (dB)</i>
16.7 %	5.0 Ω	-70.7	-72.2	-87.1
16.7 %	3.3 Ω	-79.2	-81.5	-76.2
33.3 %	5.0 Ω	-76.3	-87.1	-92.5
33.3 %	3.3 Ω	-92.0	-96.5	-74.6

Table 5.7: 3rd harmonic components of the IPM machine faulted phase current when operated at 40 Hz.

<i>Winding fault %</i>	<i>Fault resistance</i>	<i>Phase A (dB)</i>	<i>Phase B (dB)</i>	<i>Phase C (dB)</i>
16.7 %	5.0 Ω	-40.2	-38.8	-57.8
16.7 %	3.3 Ω	-38.0	-37.1	-58.5
33.3 %	5.0 Ω	-30.6	-29.4	-55.9

Table 5.8: 9th harmonic components of the IPM machine faulted phase current when operated at 40 Hz.

<i>Winding fault %</i>	<i>Fault resistance</i>	<i>Phase A (dB)</i>	<i>Phase B (dB)</i>	<i>Phase C (dB)</i>
16.7 %	5.0 Ω	-66.0	-55.4	-66.6
16.7 %	3.3 Ω	-67.1	-55.1	-68.7
33.3 %	5.0 Ω	-58.4	-50.0	-54.1

Table 5.9: 27th harmonic components of the IPM machine faulted phase current when operated at 40 Hz.

<i>Winding fault %</i>	<i>Fault resistance</i>	<i>Phase A (dB)</i>	<i>Phase B (dB)</i>	<i>Phase C (dB)</i>
16.7 %	5.0 Ω	-79.9	-81.0	-81.4
16.7 %	3.3 Ω	-77.3	-89.2	-84.2
33.3 %	5.0 Ω	-87.8	-78.8	-74.5

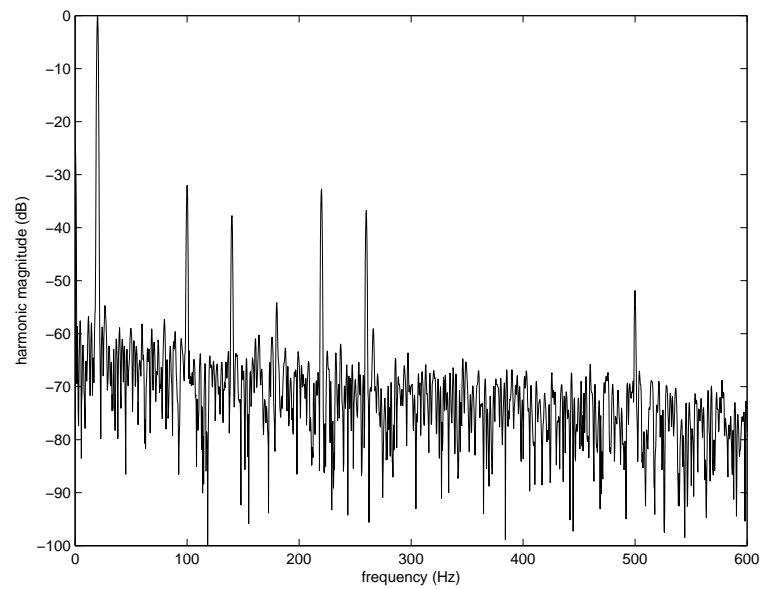


Figure 5.53: FFT of the IPM machine phase A current at 20 Hz with no winding fault.

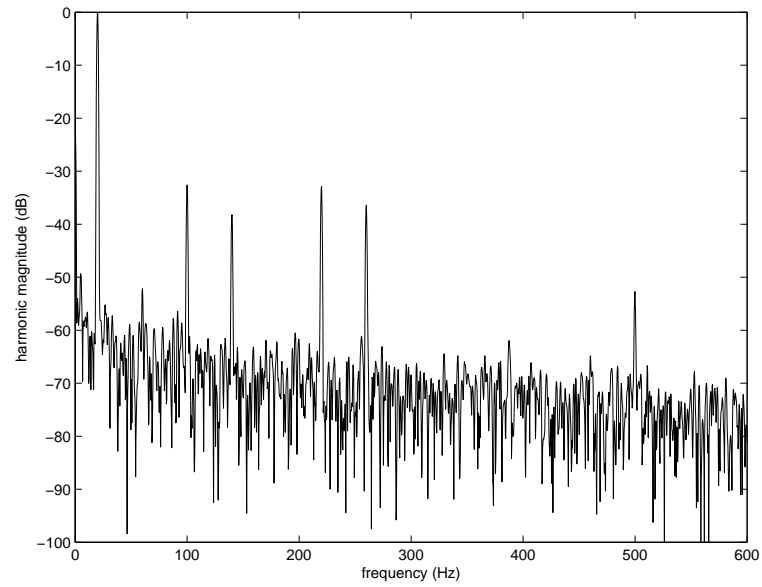


Figure 5.54: FFT of the IPM machine phase B current at 20 Hz with no winding fault.

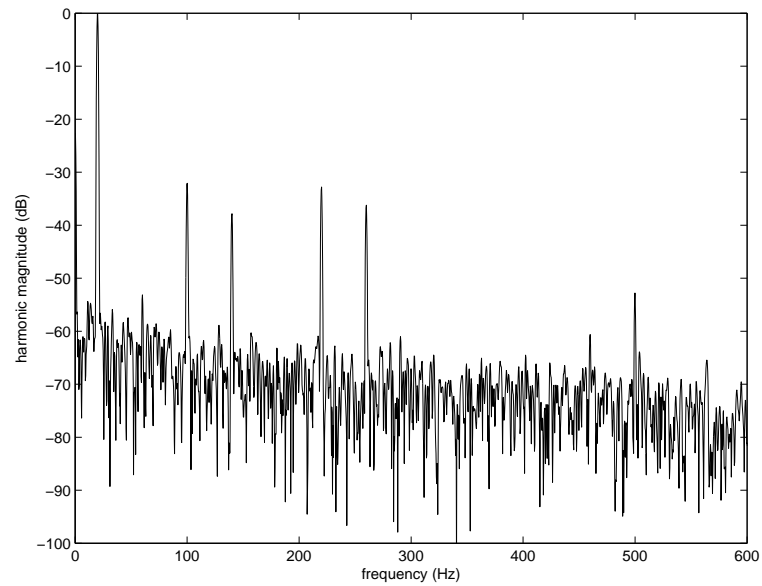


Figure 5.55: FFT of the IPM machine phase C current at 20 Hz with no winding fault.

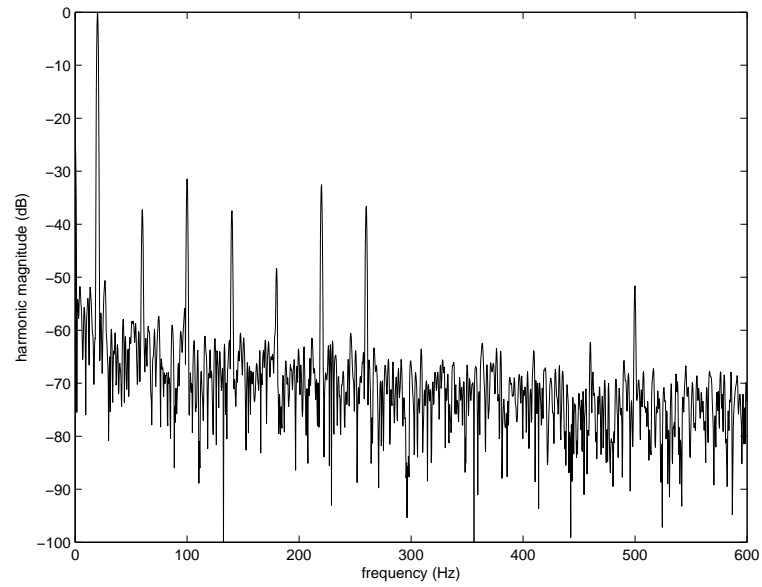


Figure 5.56: FFT of the IPM machine faulted phase current at 20 Hz with a 9.7Ω , 33.3% winding fault.

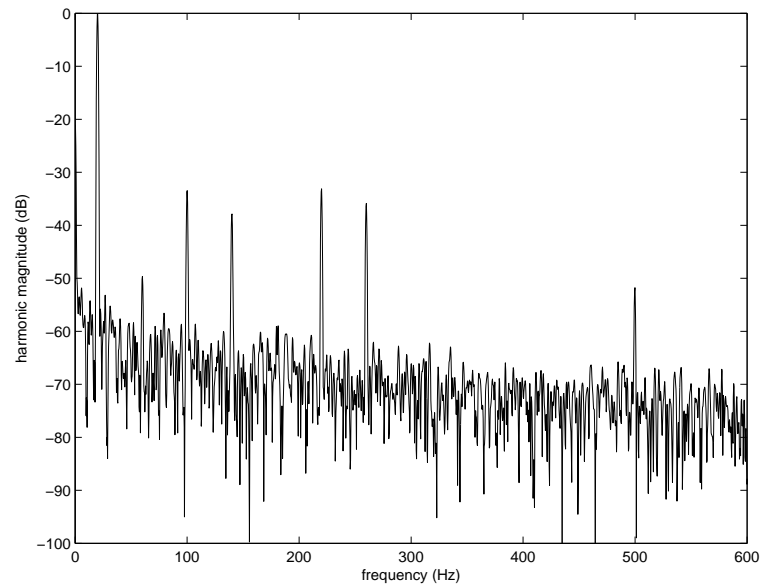


Figure 5.57: FFT of the IPM machine phase B current at 20 Hz with a 9.7Ω , 33.3% winding fault.

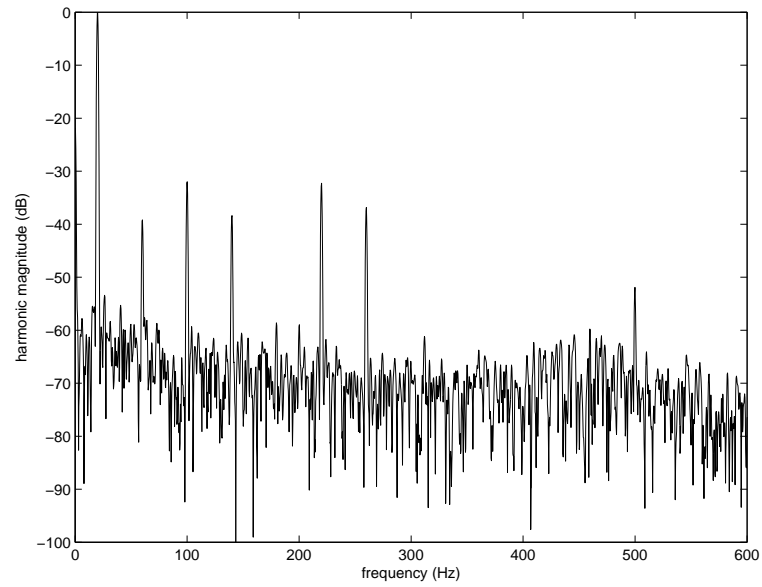


Figure 5.58: FFT of the IPM machine phase C current at 20 Hz with a 9.7Ω , 33.3% winding fault.

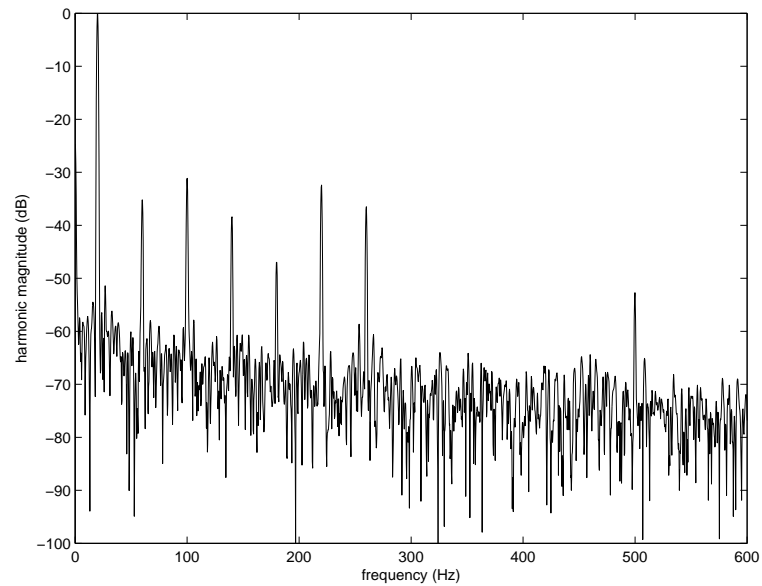


Figure 5.59: FFT of the IPM machine faulted phase current at 20 Hz with a 6.6Ω , 33.3% winding fault.

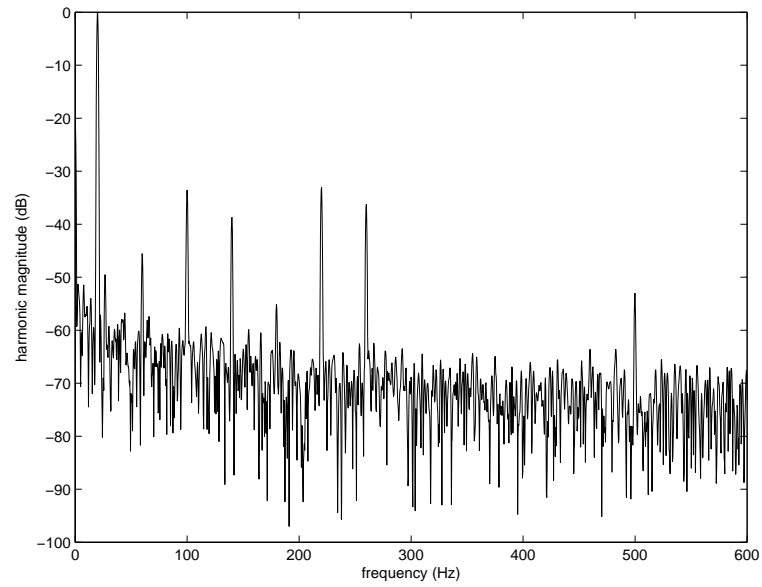


Figure 5.60: FFT of the IPM machine phase B current at 20 Hz with a 6.6Ω , 33.3% winding fault.

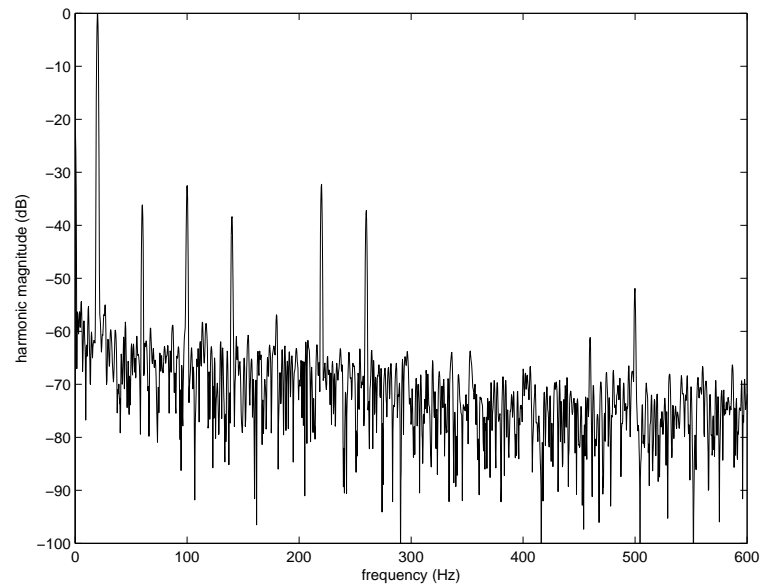


Figure 5.61: FFT of the IPM machine phase C current at 20 Hz with a 6.6Ω , 33.3% winding fault.

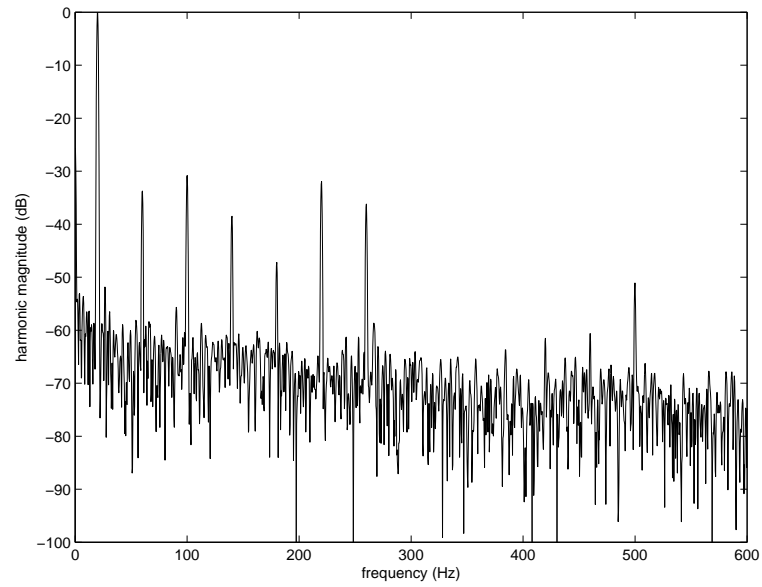


Figure 5.62: FFT of the IPM machine faulted phase current at 20 Hz with a 4.9Ω , 33.3% winding fault.

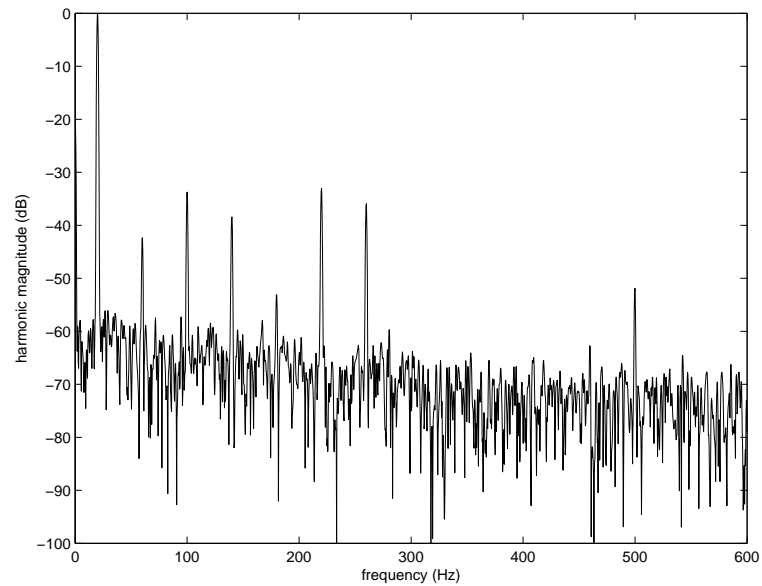


Figure 5.63: FFT of the IPM machine phase B current at 20 Hz with a 4.9Ω , 33.3% winding fault.

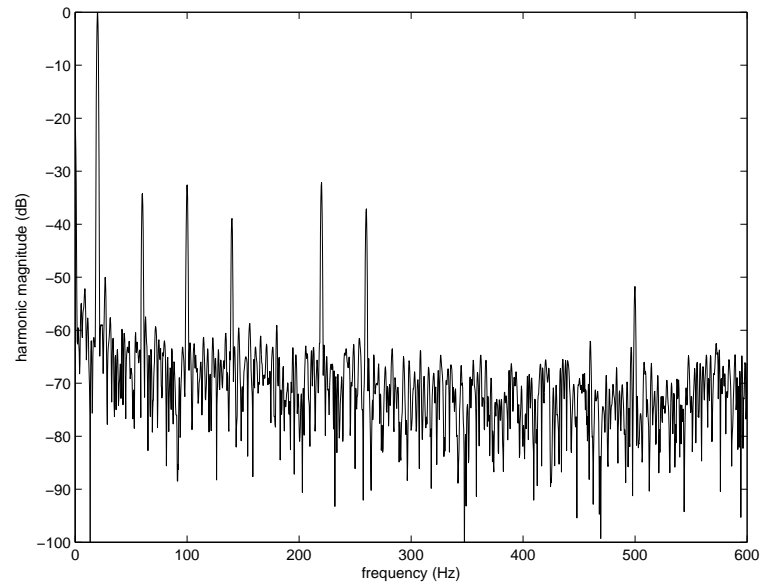


Figure 5.64: FFT of the IPM machine phase C current at 20 Hz with a 4.9Ω , 33.3% winding fault.

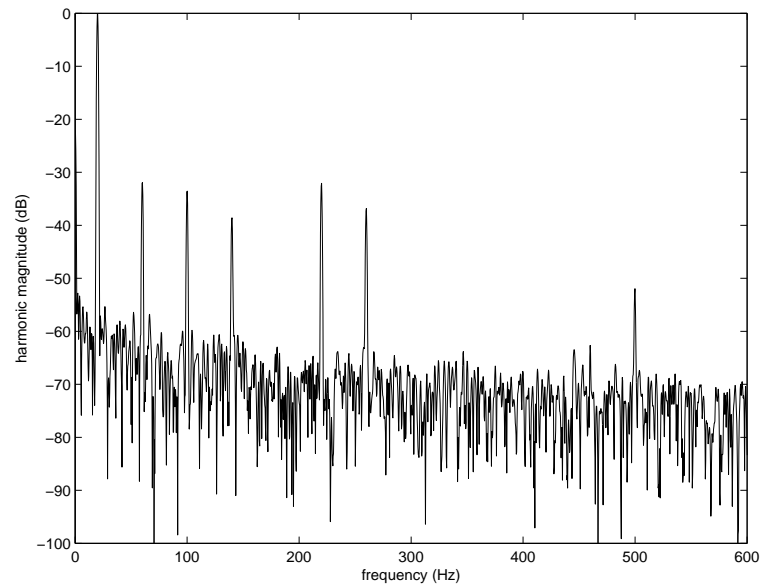


Figure 5.65: FFT of the IPM machine faulted phase current at 20 Hz with a 3.3Ω , 33.3% winding fault.

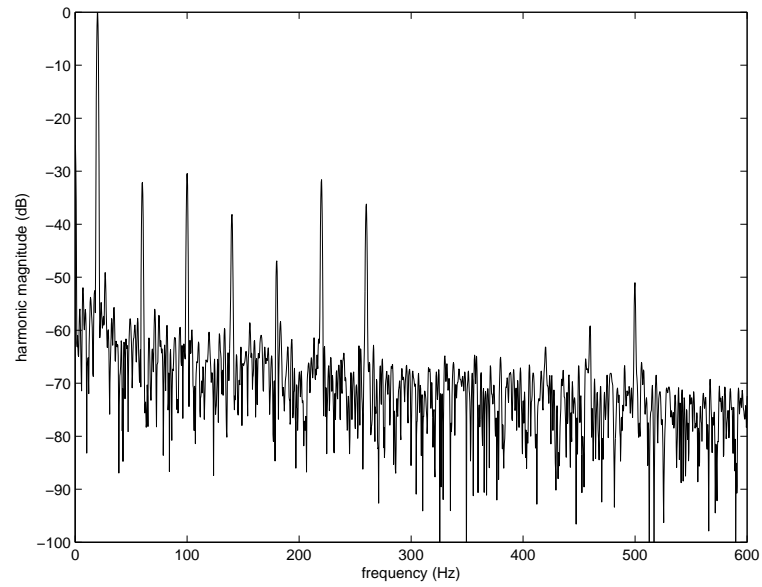


Figure 5.66: FFT of the IPM machine phase B current at 20 Hz with a 3.3Ω , 33.3% winding fault.

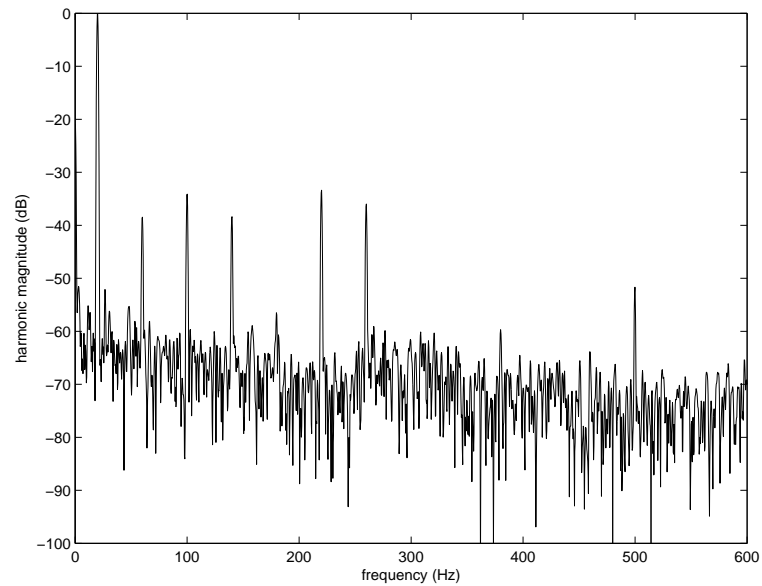


Figure 5.67: FFT of the IPM machine phase C current at 20 Hz with a 3.3Ω , 33.3% winding fault.

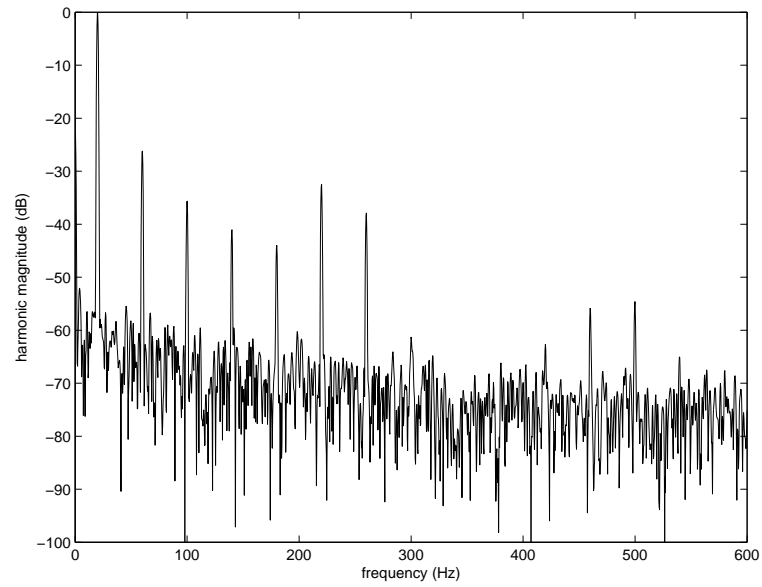


Figure 5.68: FFT of the IPM machine faulted phase current at 20 Hz with a 9.6Ω , 66.7% winding fault.

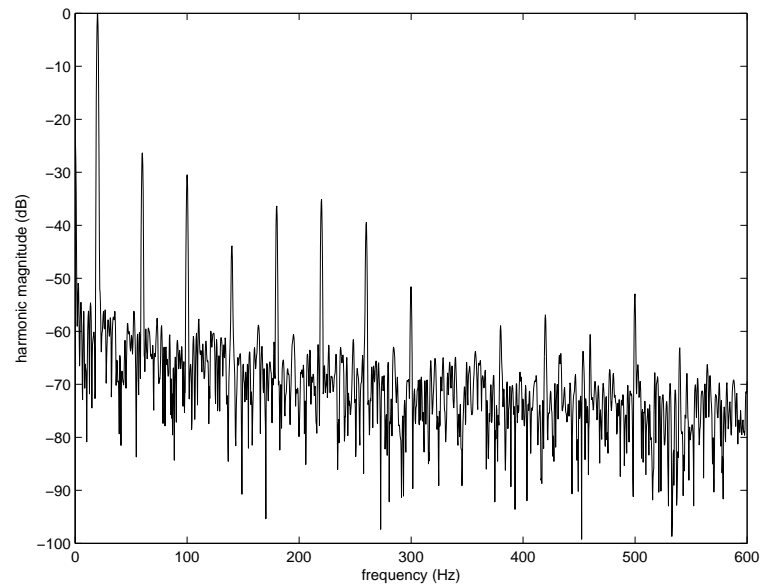


Figure 5.69: FFT of the IPM machine phase B current at 20 Hz with a 9.6Ω , 66.7% winding fault.

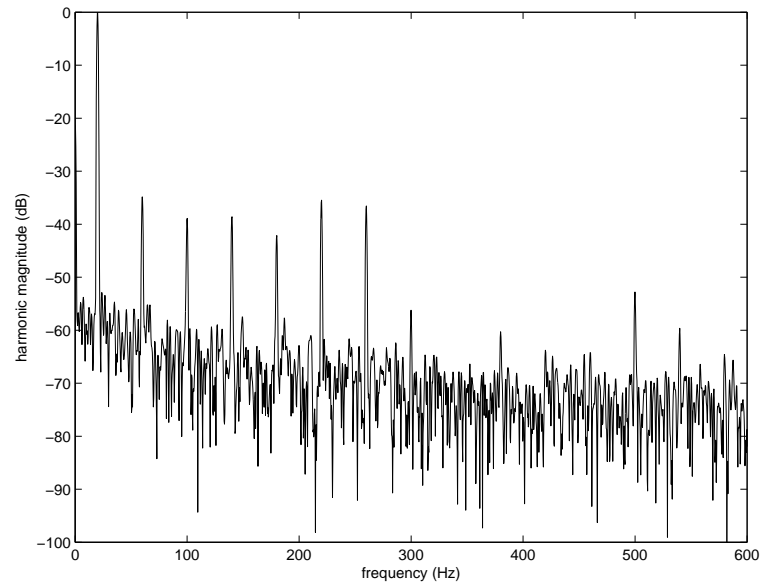


Figure 5.70: FFT of the IPM machine phase C current at 20 Hz with a 9.6Ω , 66.7% winding fault.

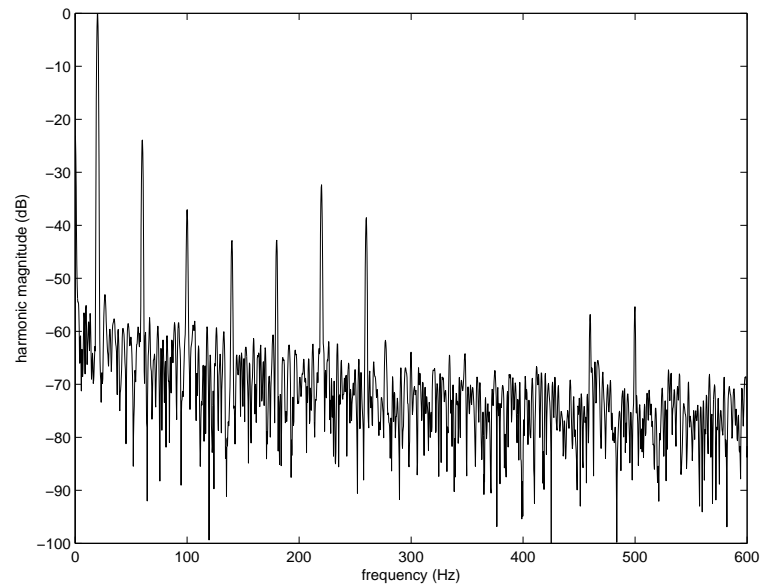


Figure 5.71: FFT of the IPM machine faulted phase current at 20 Hz with a 6.6Ω , 66.7% winding fault.

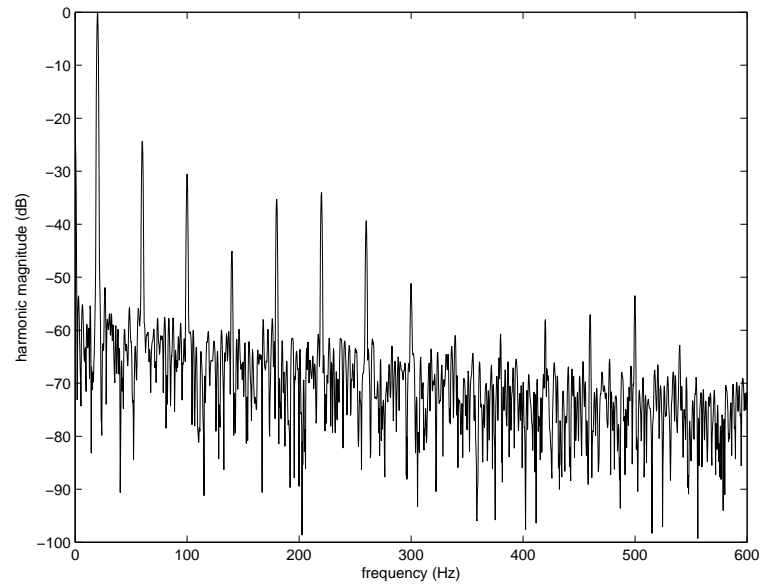


Figure 5.72: FFT of the IPM machine phase B current at 20 Hz with a 6.6Ω , 66.7% winding fault.

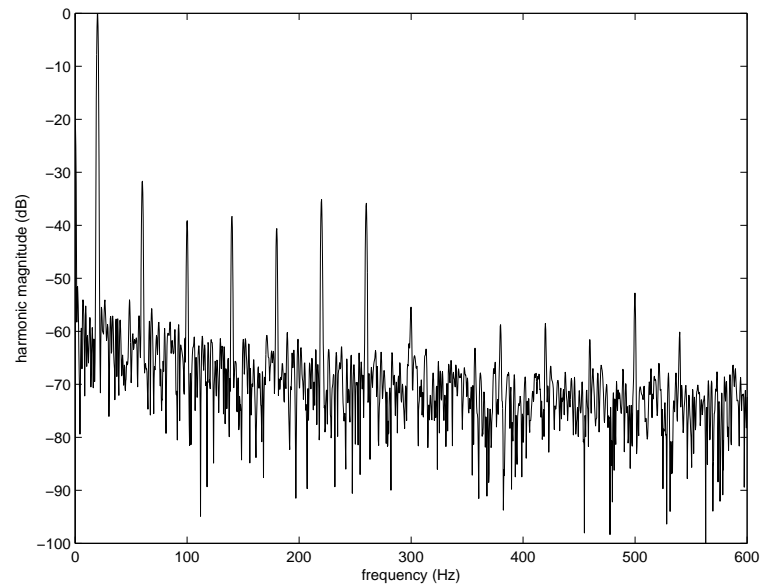


Figure 5.73: FFT of the IPM machine phase C current at 20 Hz with a 6.6Ω , 66.7% winding fault.

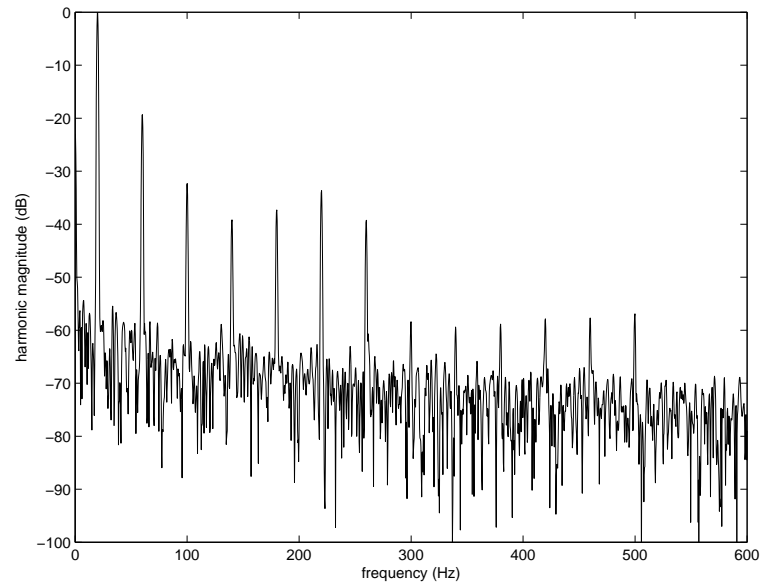


Figure 5.74: FFT of the IPM machine faulted phase current at 20 Hz with a $10\ \Omega$, 100% winding fault.

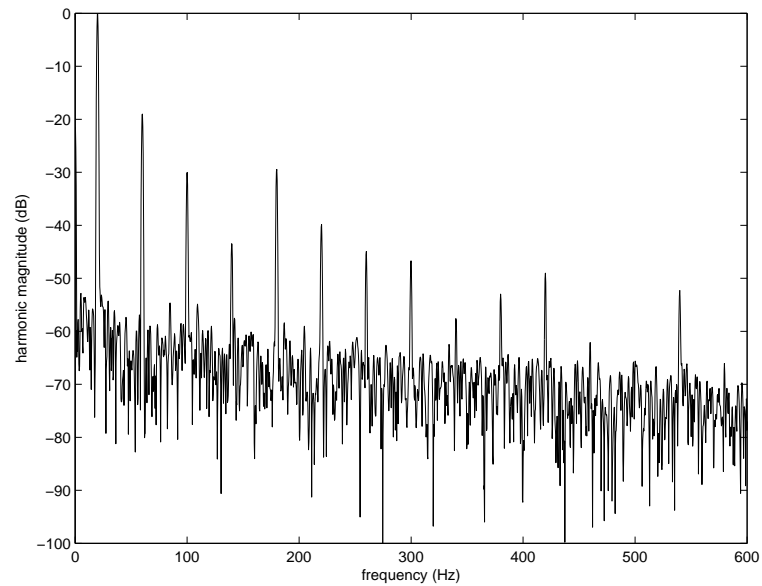


Figure 5.75: FFT of the IPM machine phase B current at 20 Hz with a $10\ \Omega$, 100% winding fault.

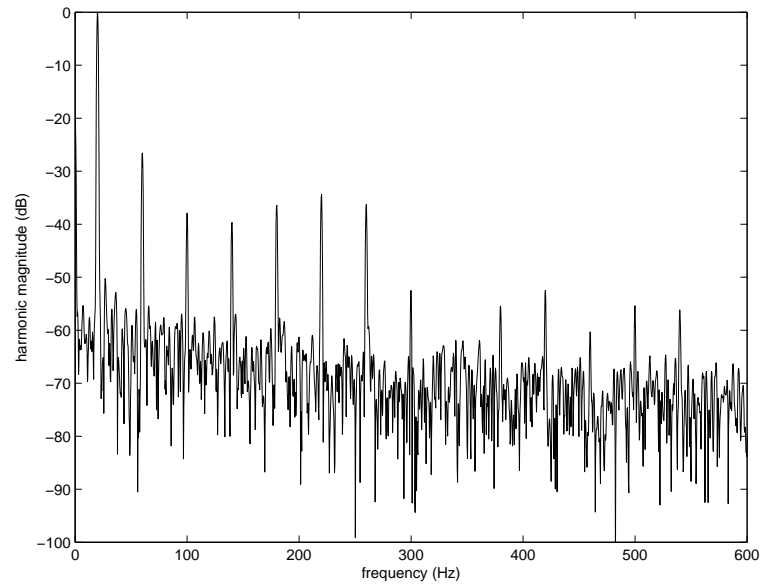


Figure 5.76: FFT of the IPM machine phase C current at 20 Hz with a $10\ \Omega$, 100% winding fault.

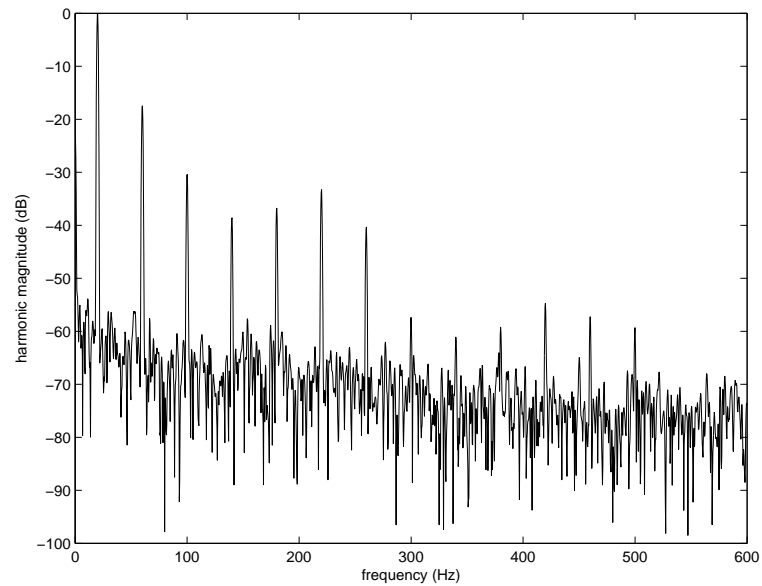


Figure 5.77: FFT of the IPM machine faulted phase current at 20 Hz with a $6.5\ \Omega$, 100% winding fault.

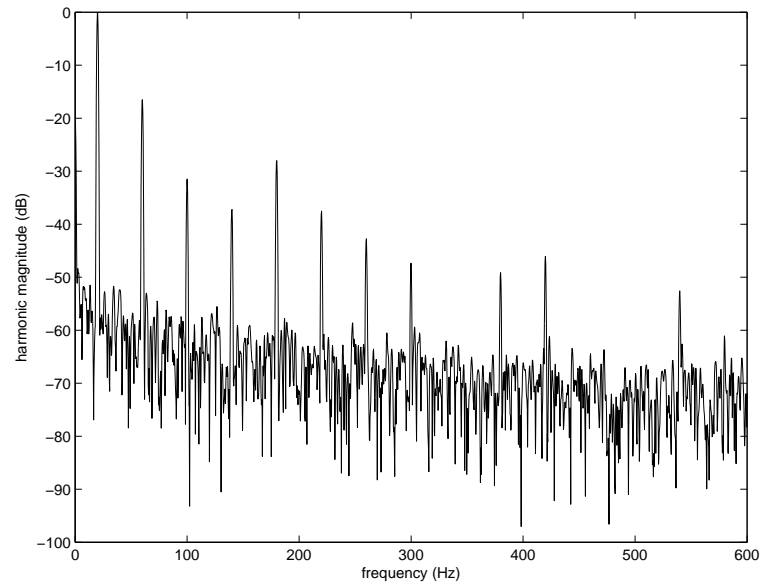


Figure 5.78: FFT of the IPM machine phase B current at 20 Hz with a 6.5Ω , 100% winding fault.

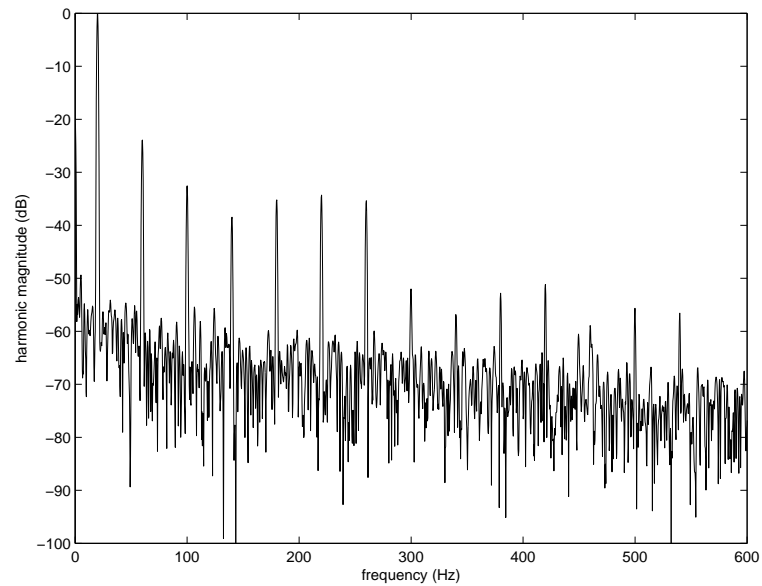


Figure 5.79: FFT of the IPM machine phase C current at 20 Hz with a 6.5Ω , 100% winding fault.

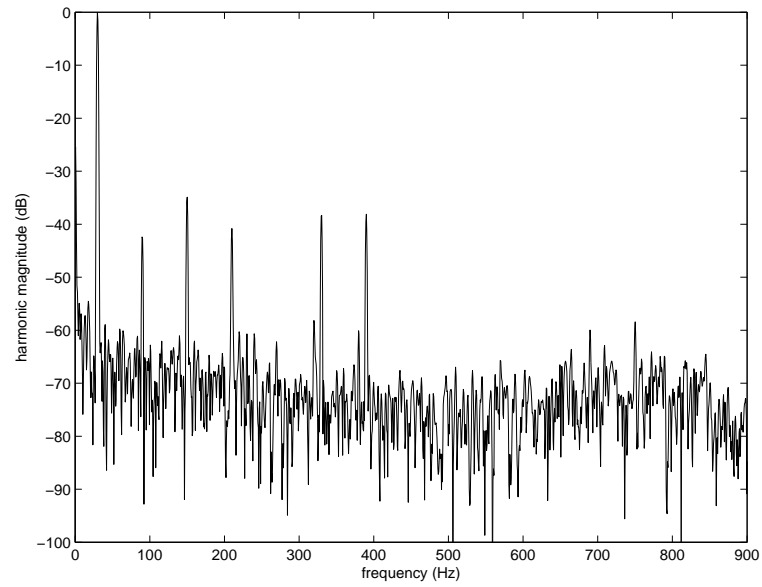


Figure 5.80: FFT of the IPM machine faulted phase current at 30 Hz with a 5.0Ω , 16.7% winding fault.

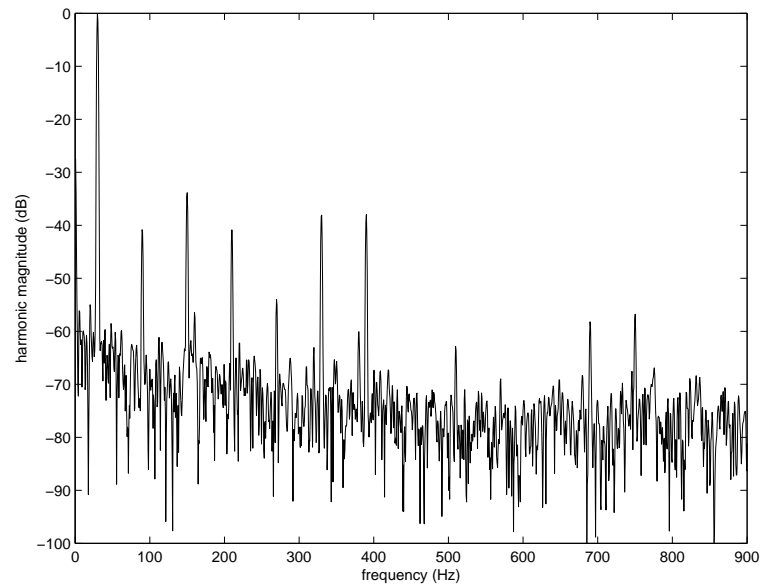


Figure 5.81: FFT of the IPM machine phase B current at 30 Hz with a 5.0Ω , 16.7% winding fault.

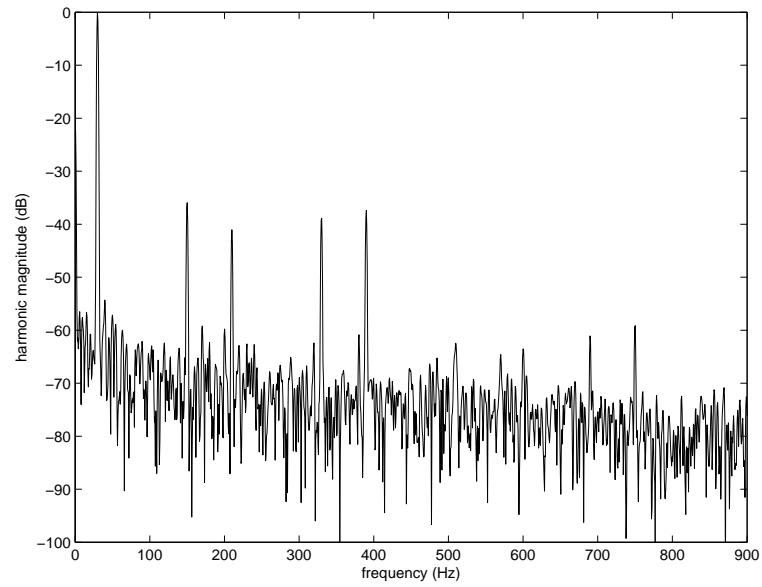


Figure 5.82: FFT of the IPM machine phase C current at 30 Hz with a 5.0Ω , 16.7% winding fault.

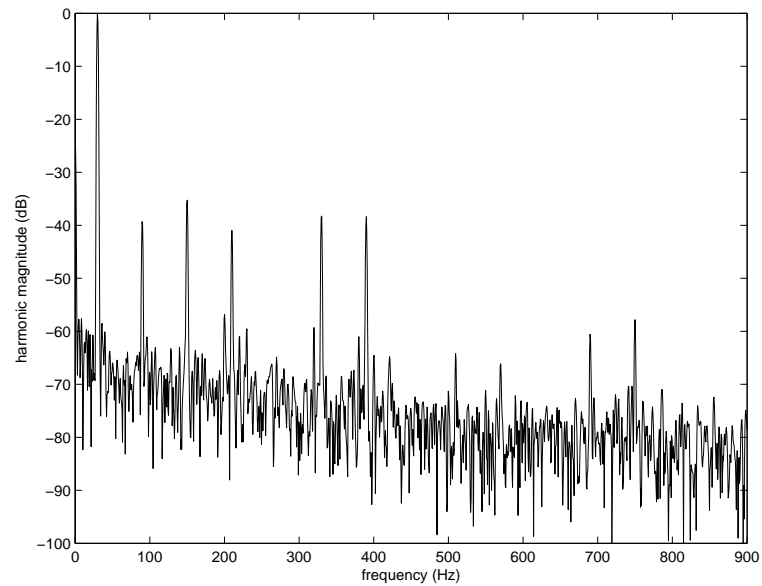


Figure 5.83: FFT of the IPM machine faulted phase current at 30 Hz with a 3.3Ω , 16.7% winding fault.

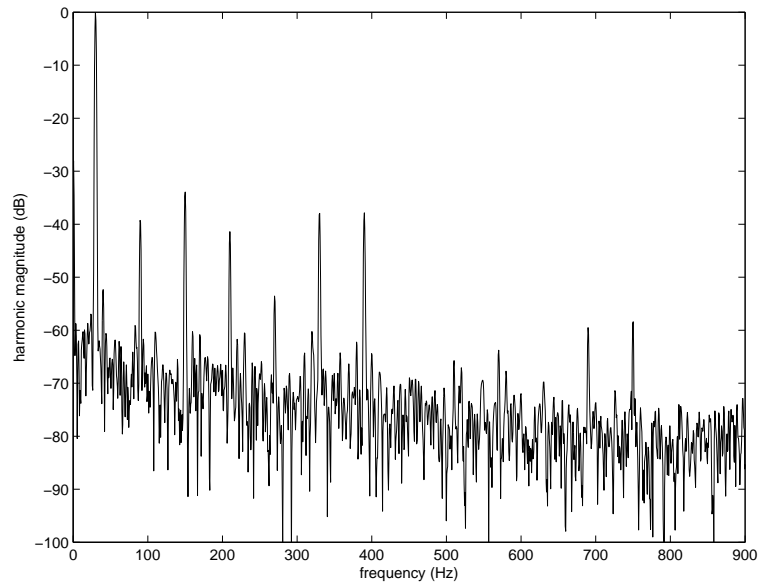


Figure 5.84: FFT of the IPM machine phase B current at 30 Hz with a 3.3Ω , 16.7% winding fault.

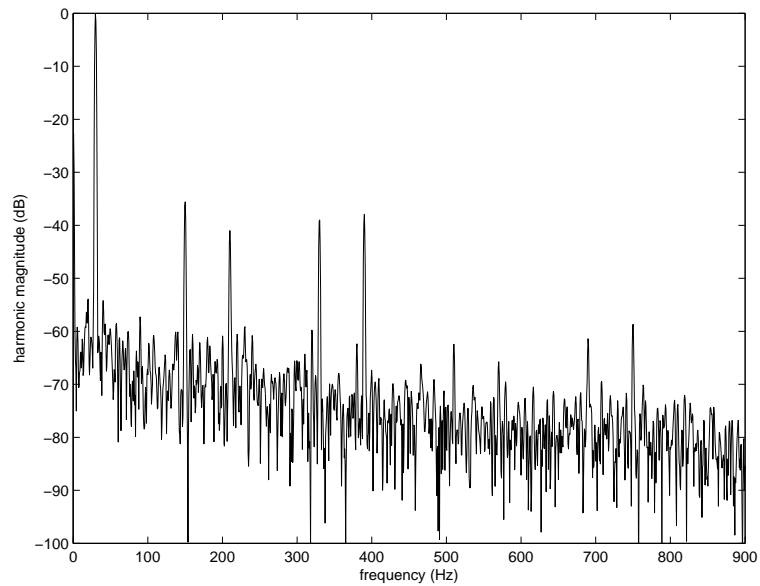


Figure 5.85: FFT of the IPM machine phase C current at 30 Hz with a 3.3Ω , 16.7% winding fault.

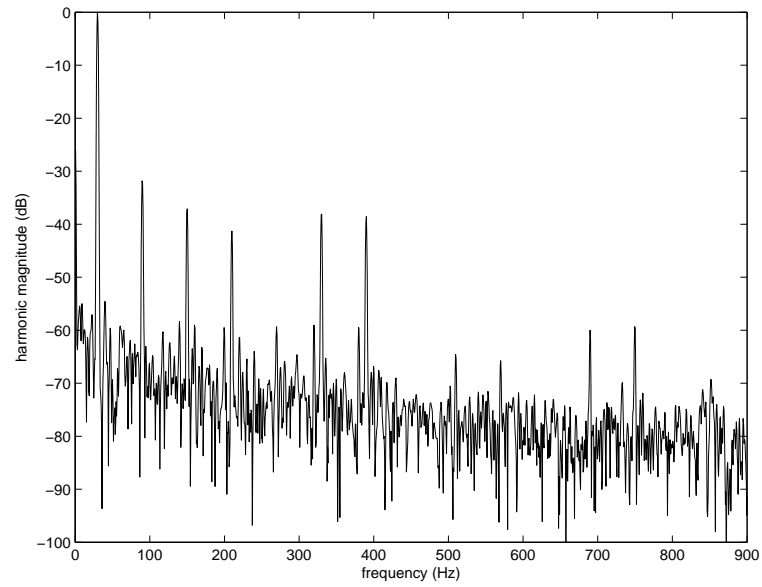


Figure 5.86: FFT of the IPM machine faulted phase current at 30 Hz with a 5.0Ω , 33.3% winding fault.

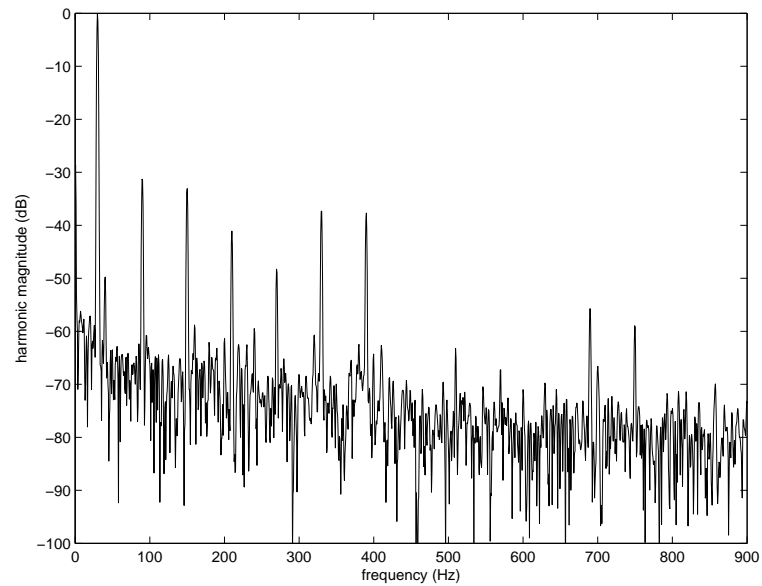


Figure 5.87: FFT of the IPM machine phase B current at 30 Hz with a 5.0Ω , 33.3% winding fault.

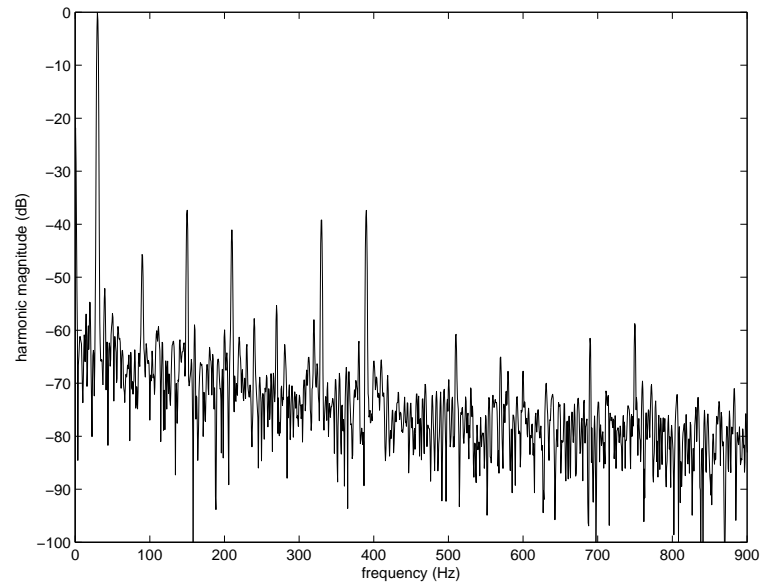


Figure 5.88: FFT of the IPM machine phase C current at 30 Hz with a 5.0Ω , 33.3% winding fault.

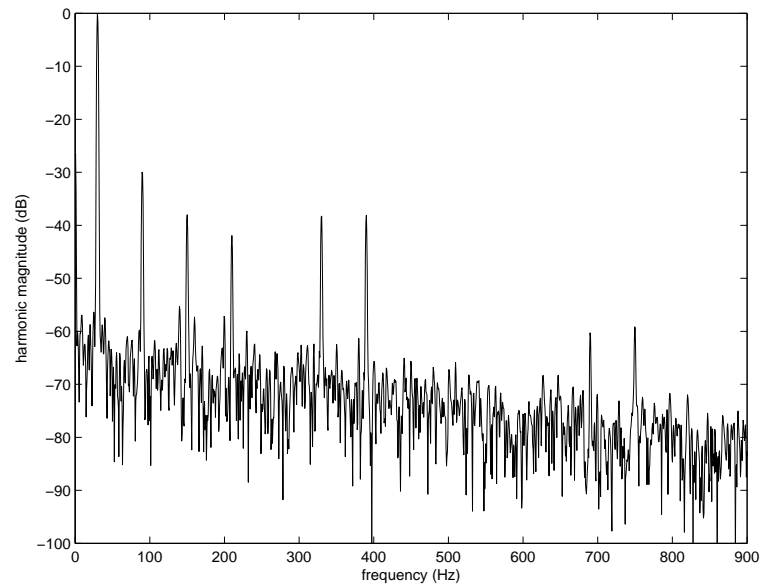


Figure 5.89: FFT of the IPM machine faulted phase current at 30 Hz with a 3.3Ω , 33.3% winding fault.

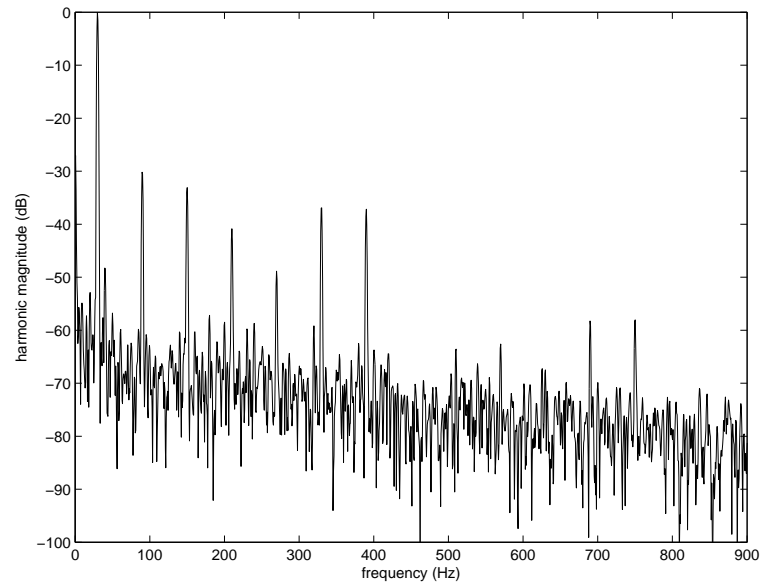


Figure 5.90: FFT of the IPM machine phase B current at 30 Hz with a 3.3Ω , 33.3% winding fault.

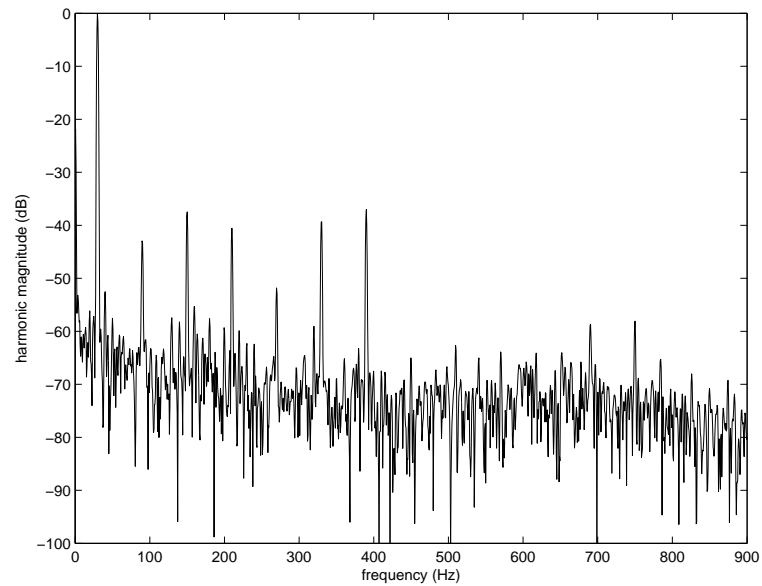


Figure 5.91: FFT of the IPM machine phase C current at 30 Hz with a 3.3Ω , 33.3% winding fault.

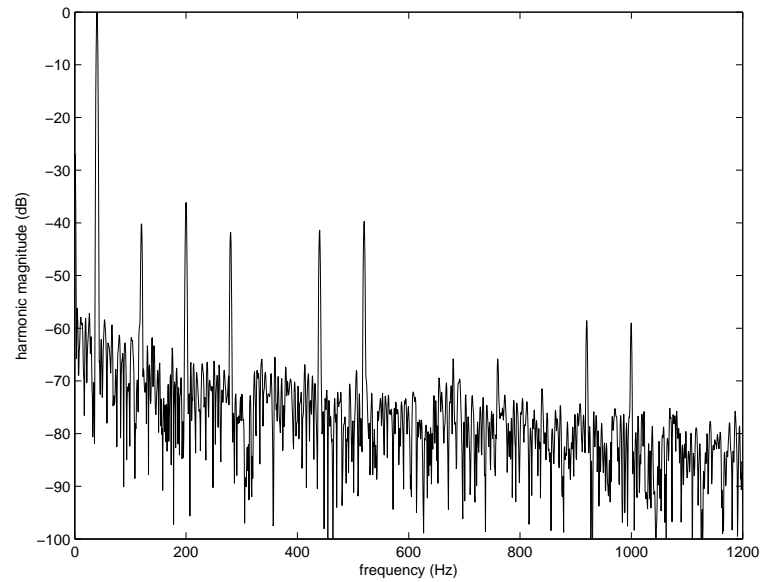


Figure 5.92: FFT of the IPM machine faulted phase current at 40 Hz with a 5.0Ω , 16.7% winding fault.

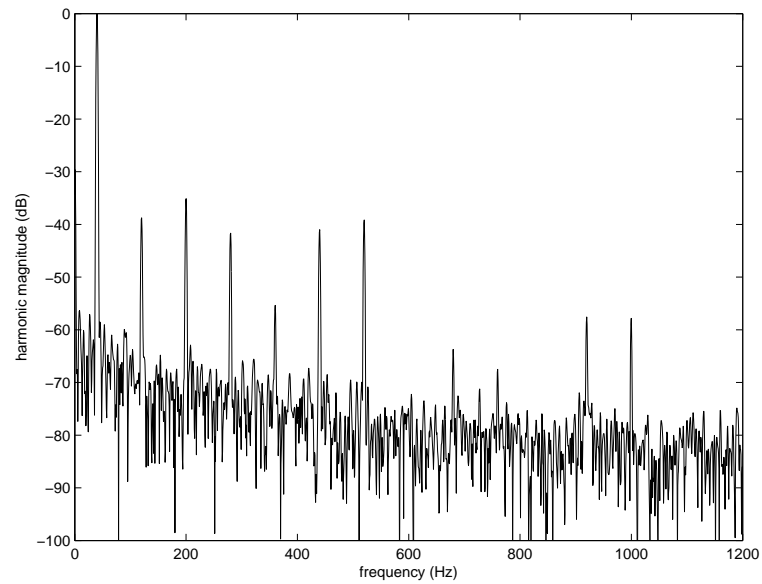


Figure 5.93: FFT of the IPM machine phase B current at 40 Hz with a 5.0Ω , 16.7% winding fault.

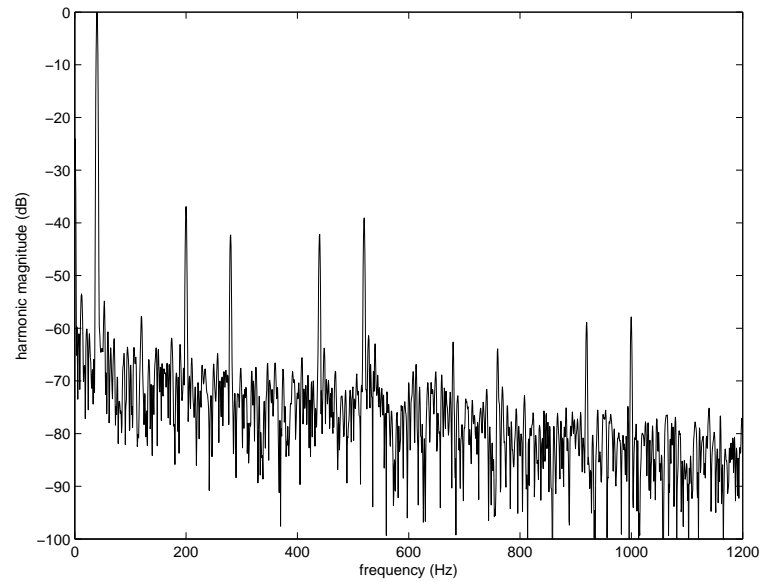


Figure 5.94: FFT of the IPM machine phase C current at 40 Hz with a $5.0\ \Omega$, 16.7% winding fault.

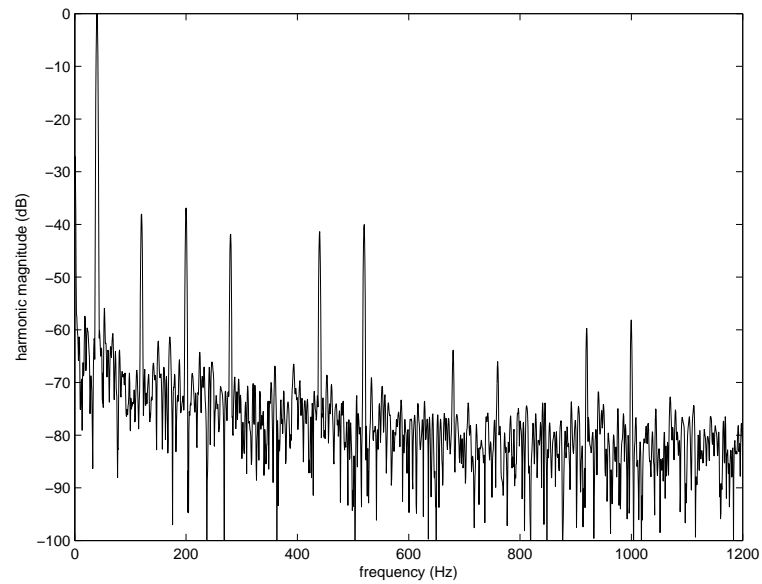


Figure 5.95: FFT of the IPM machine faulted phase current at 40 Hz with a $3.3\ \Omega$, 16.7% winding fault.

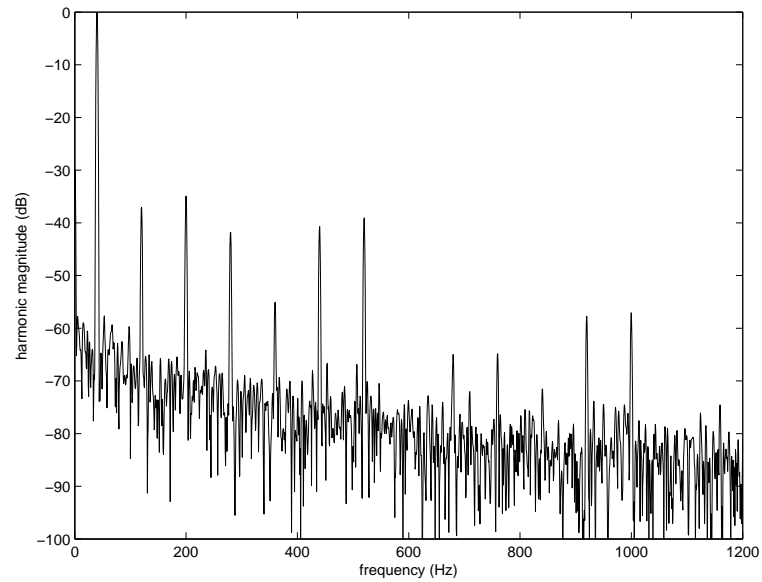


Figure 5.96: FFT of the IPM machine phase B current at 40 Hz with a 3.3Ω , 16.7% winding fault.

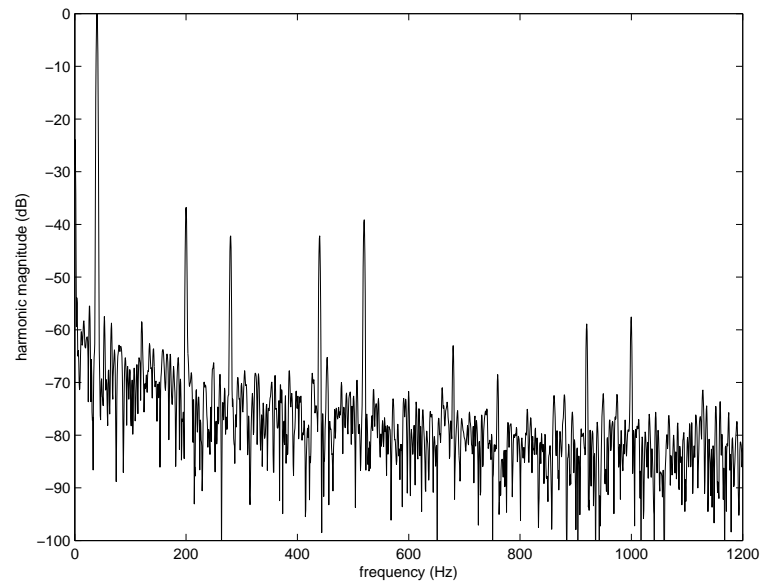


Figure 5.97: FFT of the IPM machine phase C current at 40 Hz with a 3.3Ω , 16.7% winding fault.

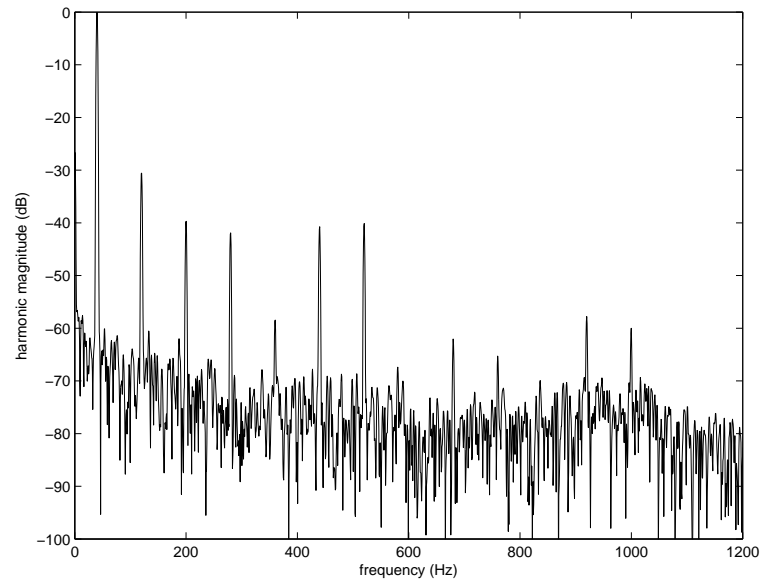


Figure 5.98: FFT of the IPM machine faulted phase current at 40 Hz with a 5.0Ω , 33.3% winding fault.

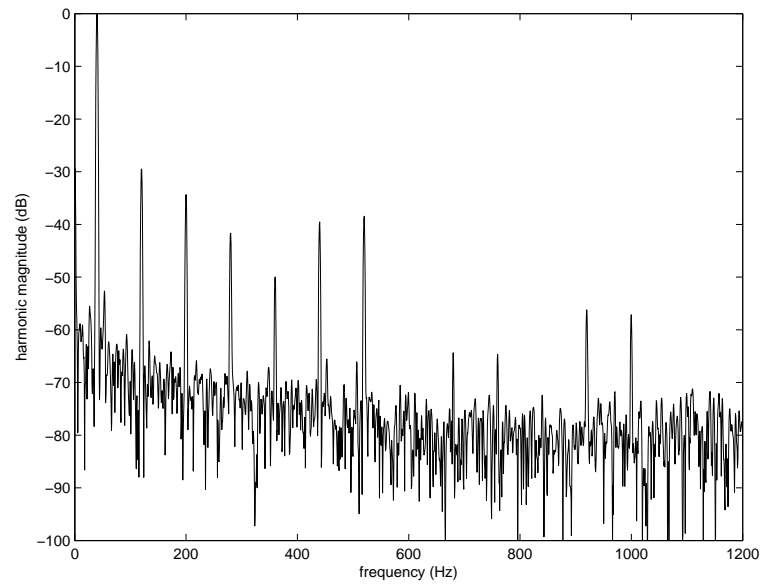


Figure 5.99: FFT of the IPM machine phase B current at 40 Hz with a 5.0Ω , 33.3% winding fault.

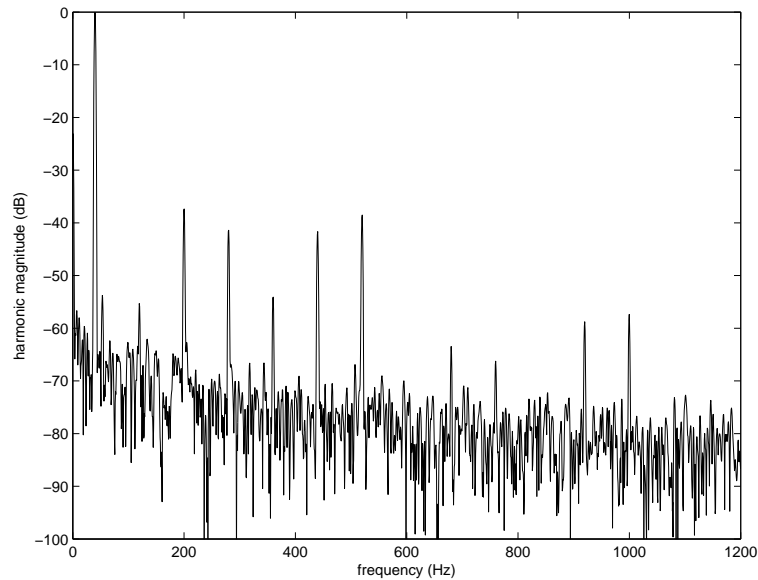


Figure 5.100: FFT of the IPM machine phase C current at 40 Hz with a 5.0Ω , 33.3% winding fault.

5.3 Results of Negative Sequence Components Analysis

The results of the negative sequence components method applied to the experimental phase currents of the IPM machine at different speed and torque test points and for increasing fault severity/decreasing fault resistances are shown in Table 5.10 through Table 5.12. For increasing fault severity/decreasing fault resistance there is a noticeable, monotonic change in the magnitude of the negative sequence component of the phase current.

Table 5.10: Magnitude of the symmetrical component phasors of the IPM machine when operated at 20 Hz.

<i>Winding fault %</i>	<i>Fault resistance</i>	<i>Positive</i>	<i>Negative</i>	<i>Zero</i>
0 %	Inf.	1.152	0.005	0.004
33.3 %	9.7 Ω	1.139	0.023	0.003
33.3 %	6.6 Ω	1.132	0.033	0.004
33.3 %	4.9 Ω	1.126	0.038	0.004
33.3 %	3.3 Ω	1.114	0.050	0.003
66.7 %	9.6 Ω	1.090	0.090	0.003
66.7 %	6.6 Ω	1.064	0.119	0.004
100 %	10 Ω	1.026	0.196	0.004
100 %	6.5 Ω	0.977	0.245	0.005

Table 5.11: Magnitude of the symmetrical component phasors of the IPM machine when operated at 30 Hz.

<i>Winding fault %</i>	<i>Fault resistance</i>	<i>Positive</i>	<i>Negative</i>	<i>Zero</i>
16.7 %	5.0 Ω	1.934	0.028	0.006
16.7 %	3.3 Ω	1.928	0.037	0.007
33.3 %	5.0 Ω	1.889	0.092	0.006
33.3 %	3.3 Ω	1.866	0.118	0.006

Table 5.12: Magnitude of the symmetrical component phasors of the IPM machine when operated at 40 Hz.

<i>Winding fault %</i>	<i>Fault resistance</i>	<i>Positive</i>	<i>Negative</i>	<i>Zero</i>
16.7 %	5.0 Ω	2.243	0.030	0.007
16.7 %	3.3 Ω	2.233	0.049	0.006
33.3 %	5.0 Ω	2.172	0.121	0.006

5.4 Results of Space-Vector Pendulous Oscillation Method Analysis

The results from applying the space-vector pendulous oscillation method to the experimental phase currents of the IPM machine at different speed and torque test points and for increasing fault severity/decreasing fault resistances are shown in

Figure 5.101 through Figure 5.148. The slightly distorted circle of the current space-vectors for the healthy machine operation shown in Figure 5.102 again indicate that there is a slight bias in the current sensors.

The voltage space-vectors, current space-vectors, and pendulous oscillation signals for the various fault conditions are shown in Figure 5.104 through Figure 5.148. The tabulation of the swing angle of the pendulous oscillation signal for the various test conditions is shown in Table 5.13, Table 5.14, and Table 5.15. For this IPM machine the swing angle is not a reliable indicator of the fault, as indicated by the non-monotonic nature of the progression of the swing angle versus the fault severity.

Table 5.13: Swing angle of the IPM machine when operated at 20 Hz.

<i>Winding fault %</i>	<i>Fault resistance</i>	<i>Swing angle</i>
0 %	Inf.	6.96 deg.
33.3 %	9.7 Ω	8.12 deg.
33.3 %	6.6 Ω	7.38 deg.
33.3 %	4.9 Ω	7.08 deg.
33.3 %	3.3 Ω	7.55 deg.
66.7 %	9.6 Ω	7.44 deg.
66.7 %	6.6 Ω	7.45 deg.
100 %	10 Ω	8.77 deg.
100 %	6.5 Ω	9.39 deg.

Table 5.14: Swing angle of the IPM machine when operated at 30 Hz.

<i>Winding fault %</i>	<i>Fault resistance</i>	<i>Swing angle</i>
16.7 %	5.0 Ω	6.01 deg.
16.7 %	3.3 Ω	6.25 deg.
33.3 %	5.0 Ω	5.75 deg.
33.3 %	3.3 Ω	6.25 deg.

Table 5.15: Swing angle of the IPM machine when operated at 40 Hz.

<i>Winding fault %</i>	<i>Fault resistance</i>	<i>Swing angle</i>
16.7 %	5.0 Ω	4.63 deg.
16.7 %	3.3 Ω	4.77 deg.
33.3 %	5.0 Ω	4.29 deg.

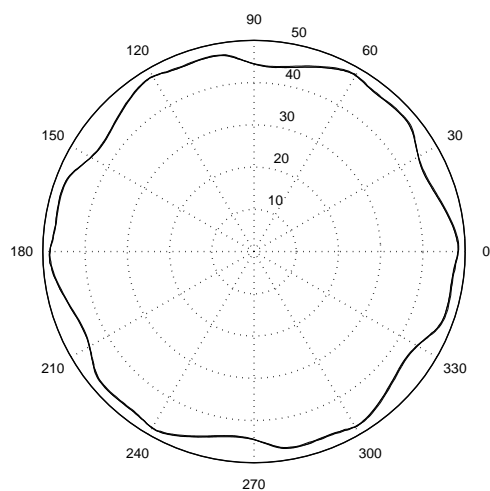


Figure 5.101: Voltage space-vector of the IPM machine at 20 Hz with no winding fault.

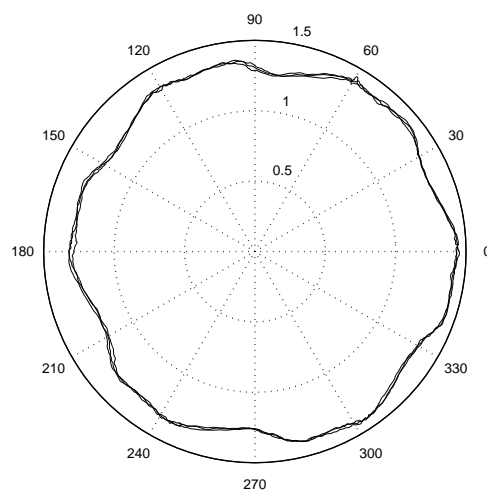


Figure 5.102: Current space-vector of the IPM machine at 20 Hz with no winding fault.

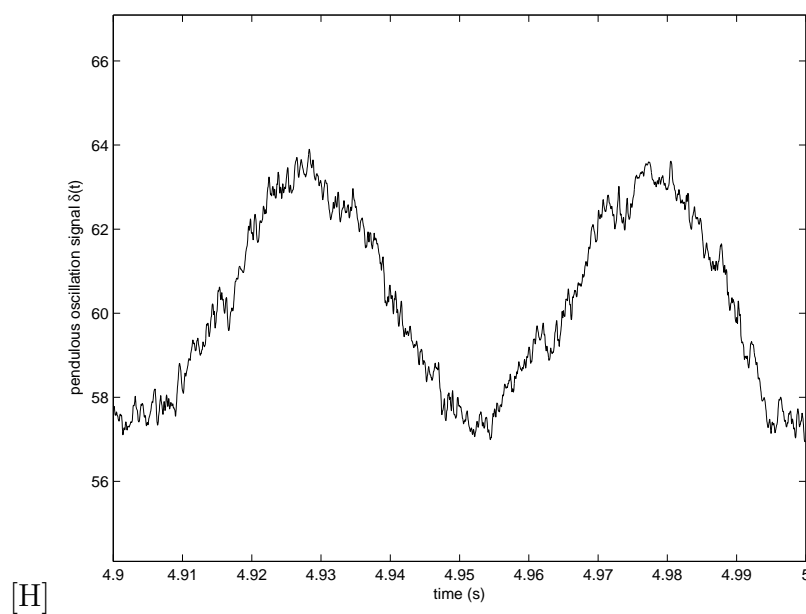


Figure 5.103: Pendulous oscillation signal of the IPM machine at 20 Hz with no winding fault.

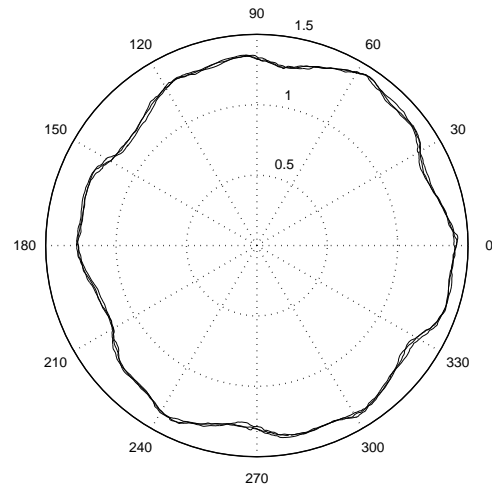
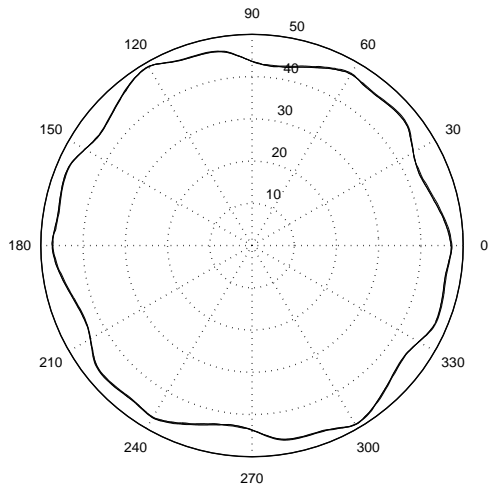


Figure 5.104: Voltage space-vector of the IPM machine at 20 Hz with a $9.7\ \Omega$, 33.3% winding fault.

Figure 5.105: Current space-vector of the IPM machine at 20 Hz with a $9.7\ \Omega$, 33.3% winding fault.

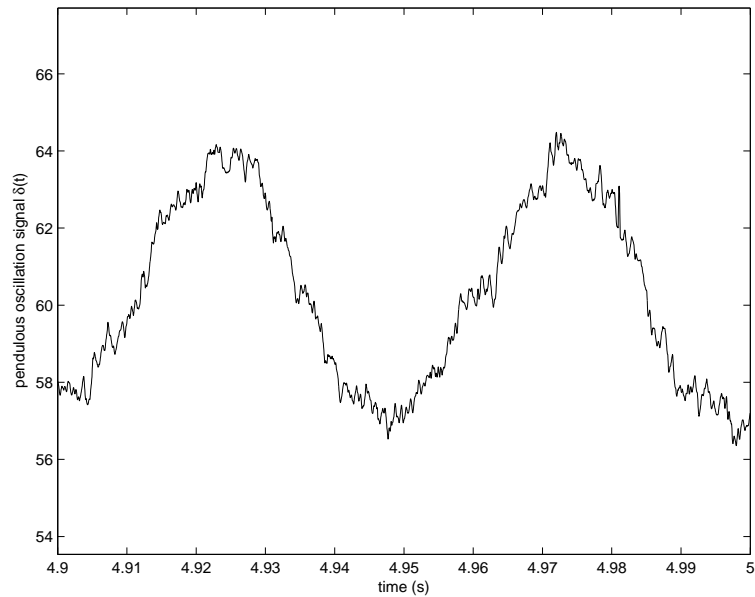


Figure 5.106: Pendulous oscillation signal of the IPM machine at 20 Hz with a $9.7\ \Omega$, 33.3% winding fault.

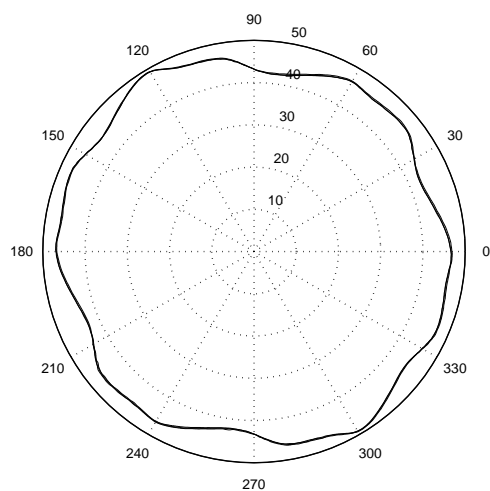


Figure 5.107: Voltage space-vector of the IPM machine at 20 Hz with a 6.6Ω , 33.3% winding fault.

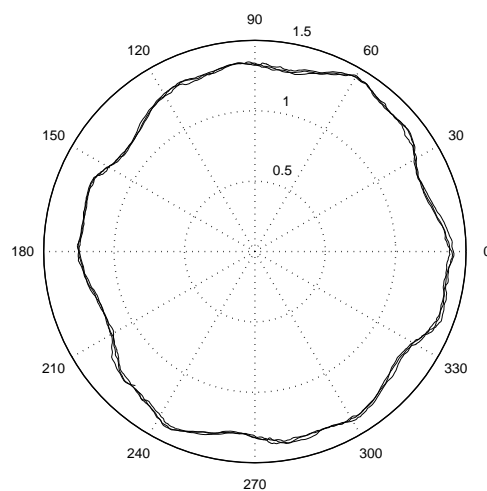


Figure 5.108: Current space-vector of the IPM machine at 20 Hz with a 6.6Ω , 33.3% winding fault.

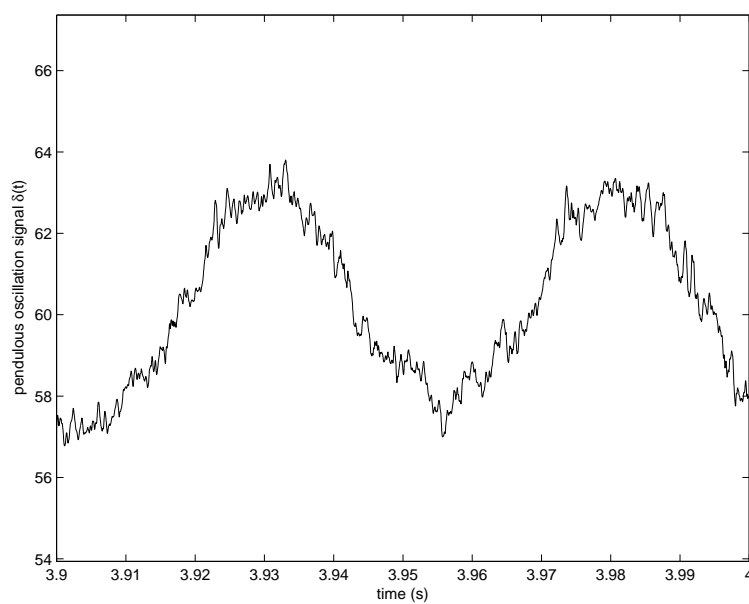


Figure 5.109: Pendulous oscillation signal of the IPM machine at 20 Hz with a 6.6Ω , 33.3% winding fault.

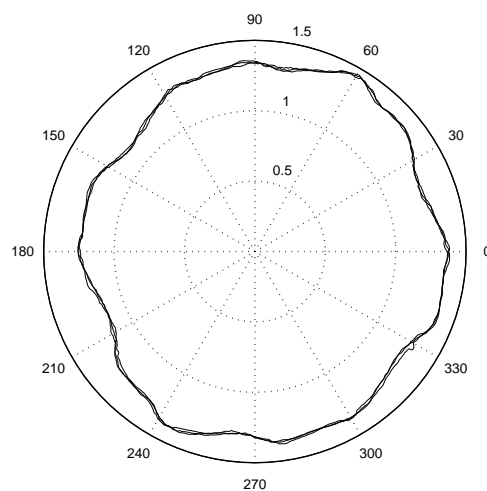
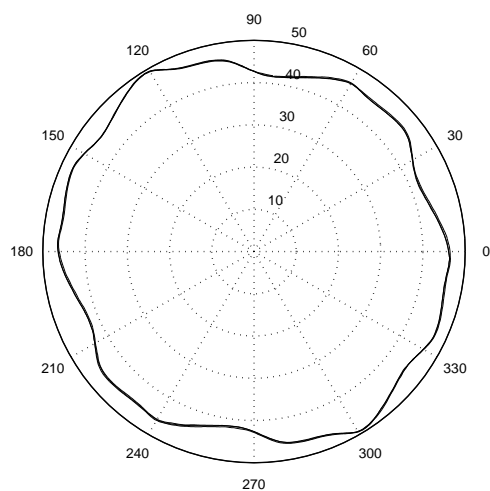


Figure 5.110: Voltage space-vector of the IPM machine at 20 Hz with a $4.9\ \Omega$, 33.3% winding fault.

Figure 5.111: Current space-vector of the IPM machine at 20 Hz with a $4.9\ \Omega$, 33.3% winding fault.

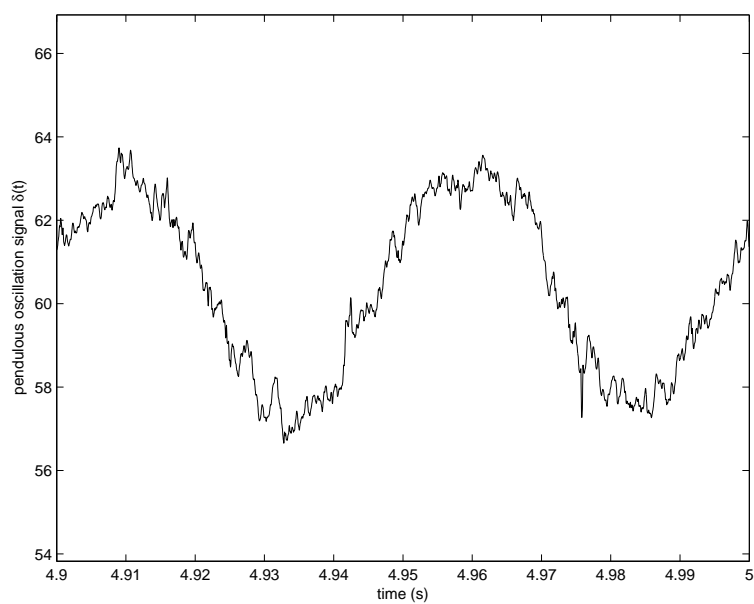


Figure 5.112: Pendulous oscillation signal of the IPM machine at 20 Hz with a $4.9\ \Omega$, 33.3% winding fault.

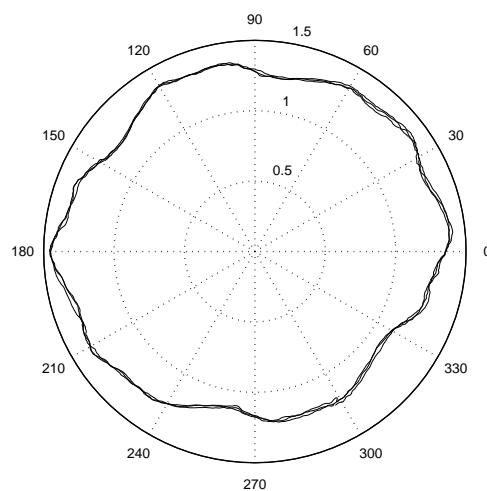
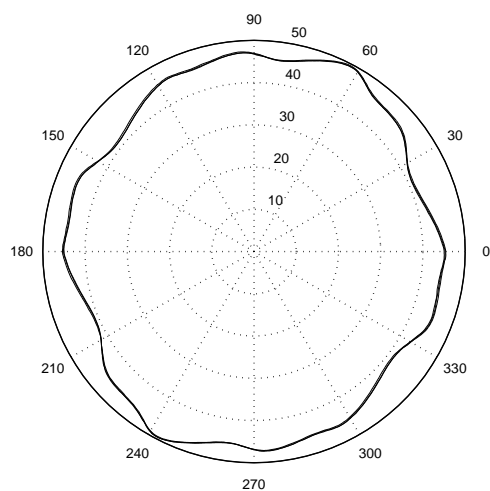


Figure 5.113: Voltage space-vector of the IPM machine at 20 Hz with a $3.3\ \Omega$, 33.3% winding fault.

Figure 5.114: Current space-vector of the IPM machine at 20 Hz with a $3.3\ \Omega$, 33.3% winding fault.

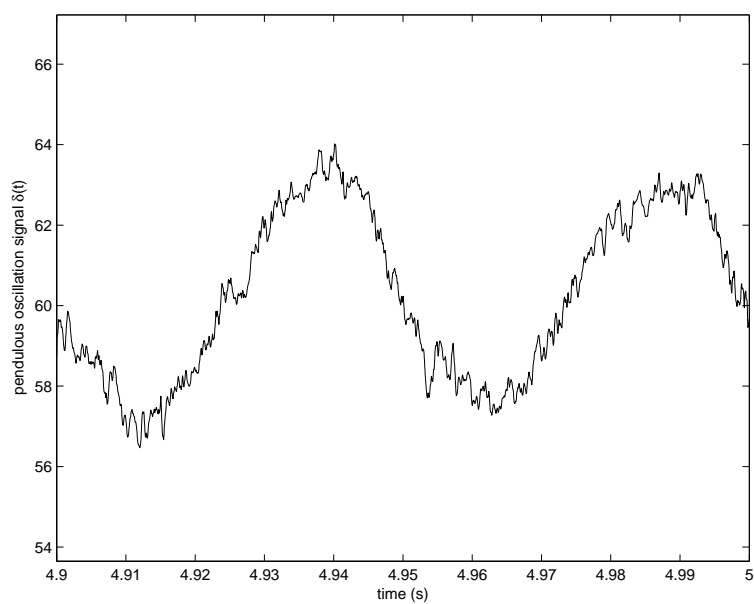


Figure 5.115: Pendulous oscillation signal of the IPM machine at 20 Hz with a $3.3\ \Omega$, 33.3% winding fault.

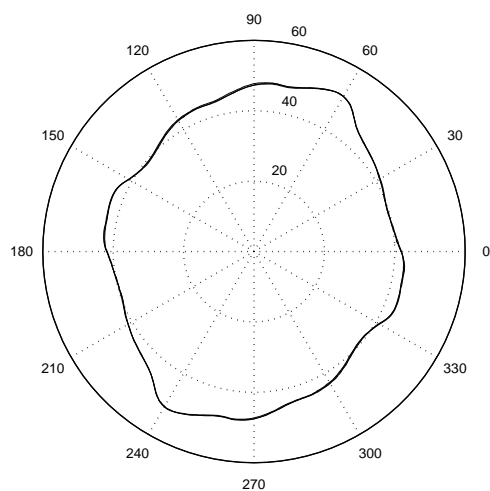


Figure 5.116: Voltage space-vector of the IPM machine at 20 Hz with a 9.6Ω , 66.7% winding fault.

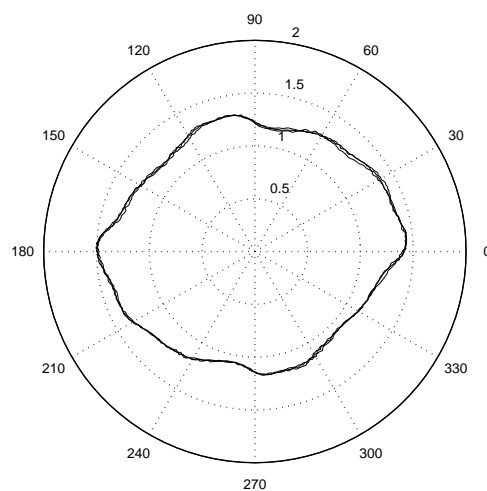


Figure 5.117: Current space-vector of the IPM machine at 20 Hz with a 9.6Ω , 66.7% winding fault.

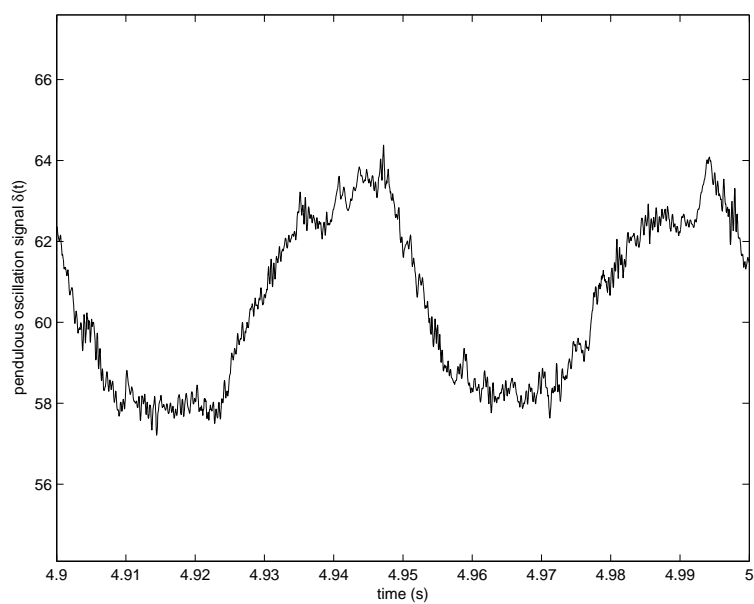


Figure 5.118: Pendulous oscillation signal of the IPM machine at 20 Hz with a 9.6Ω , 66.7% winding fault.

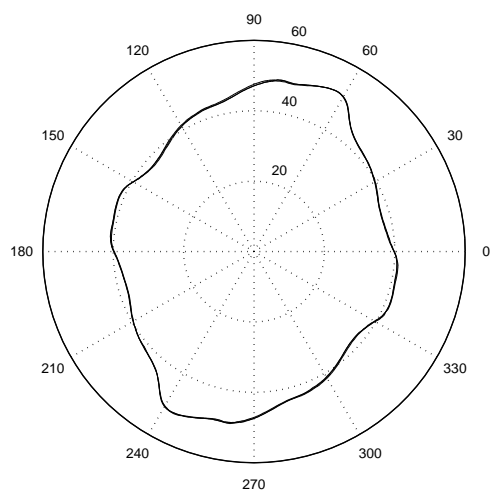


Figure 5.119: Voltage space-vector of the IPM machine at 20 Hz with a 6.6Ω , 66.7% winding fault.

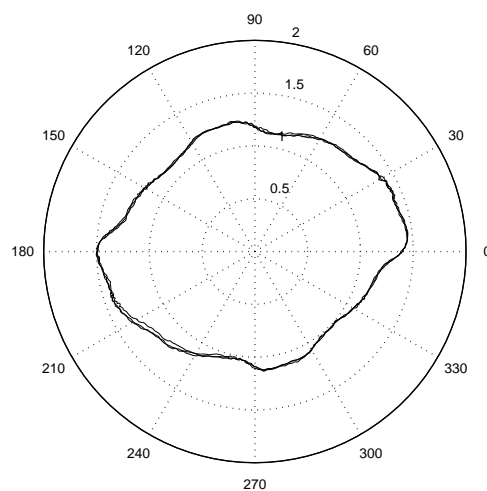


Figure 5.120: Current space-vector of the IPM machine at 20 Hz with a 6.6Ω , 66.7% winding fault.

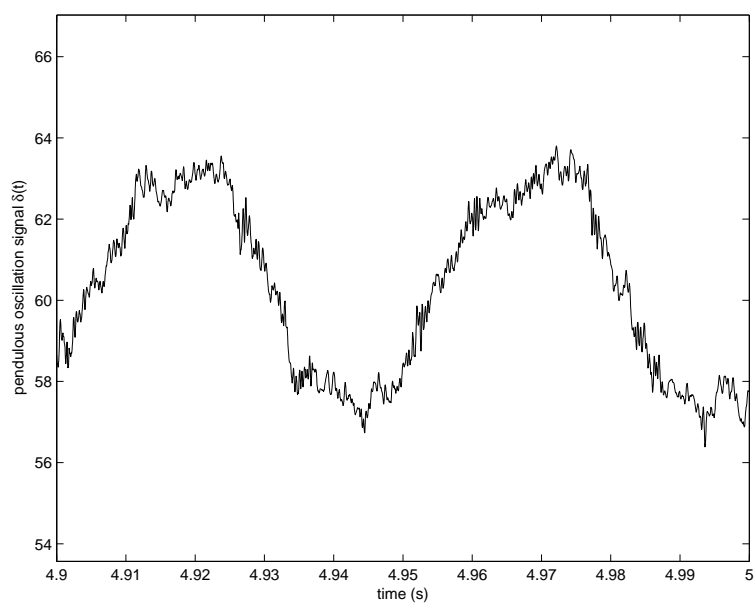


Figure 5.121: Pendulous oscillation signal of the IPM machine at 20 Hz with a 6.6Ω , 66.7% winding fault.

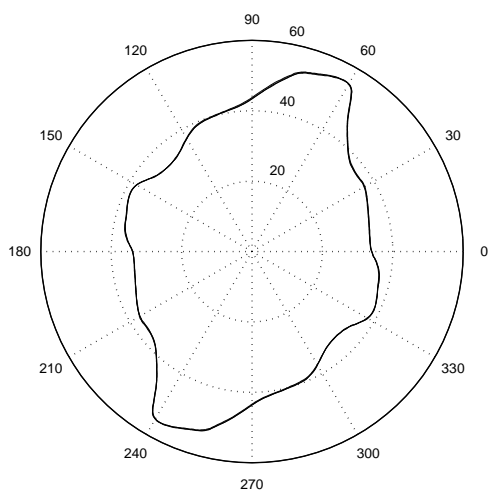


Figure 5.122: Voltage space-vector of the IPM machine at 20 Hz with a $10\ \Omega$, 100% winding fault.

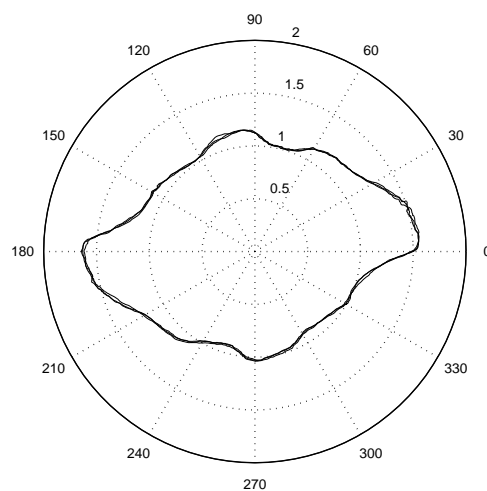


Figure 5.123: Current space-vector of the IPM machine at 20 Hz with a $10\ \Omega$, 100% winding fault.

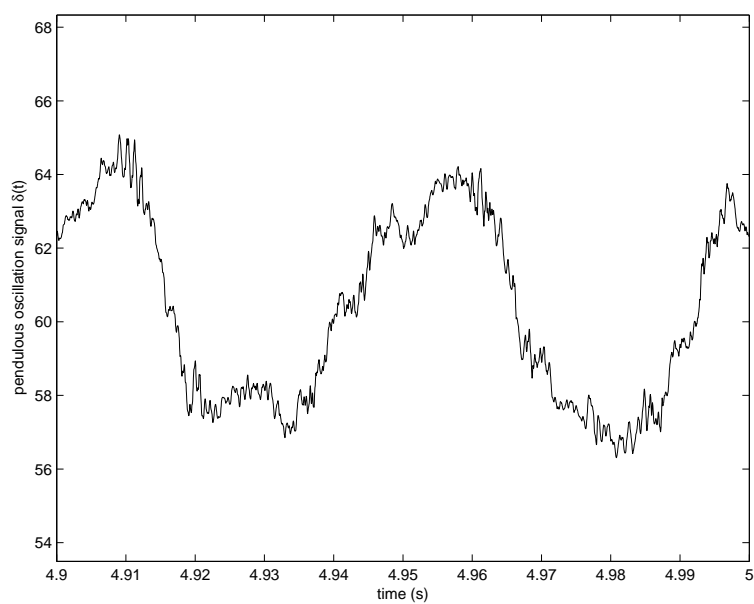


Figure 5.124: Pendulous oscillation signal of the IPM machine at 20 Hz with a $10\ \Omega$, 100% winding fault.

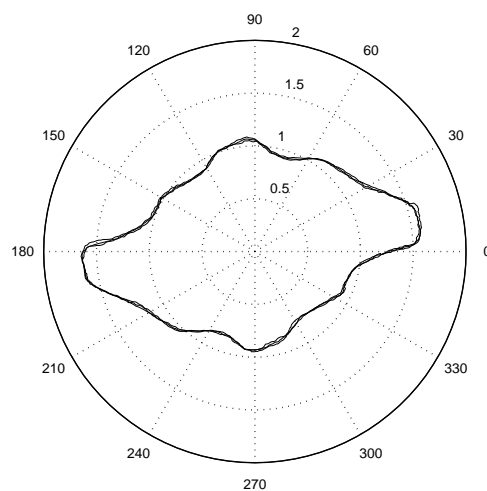
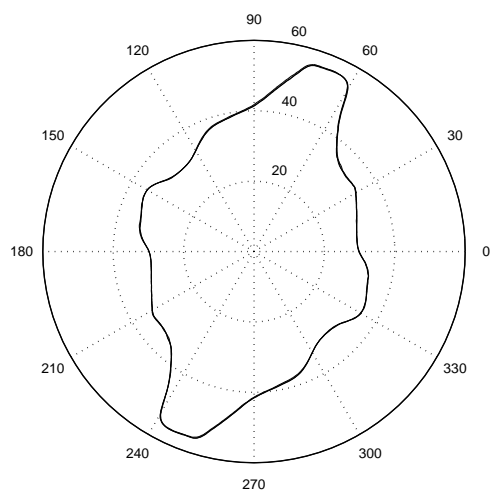


Figure 5.125: Voltage space-vector of the IPM machine at 20 Hz with a 6.5Ω , 100% winding fault.

Figure 5.126: Current space-vector of the IPM machine at 20 Hz with a 6.5Ω , 100% winding fault.

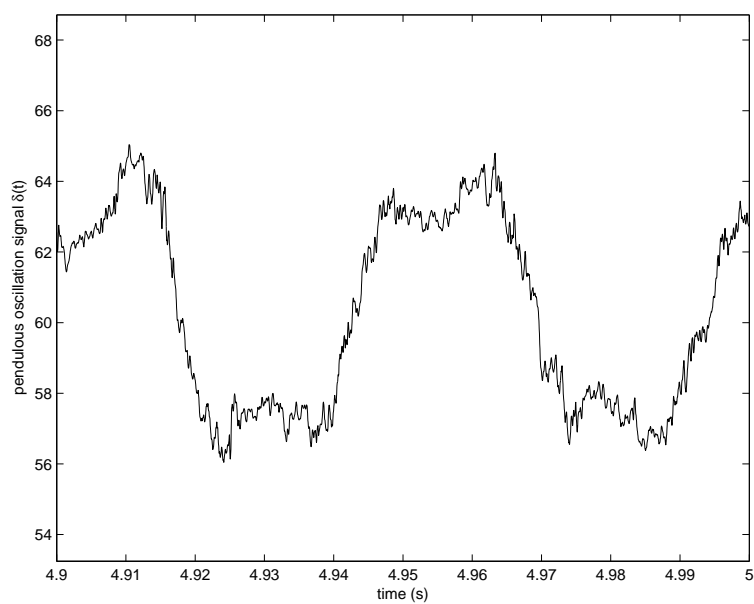


Figure 5.127: Pendulous oscillation signal of the IPM machine at 20 Hz with a 6.5Ω , 100% winding fault.

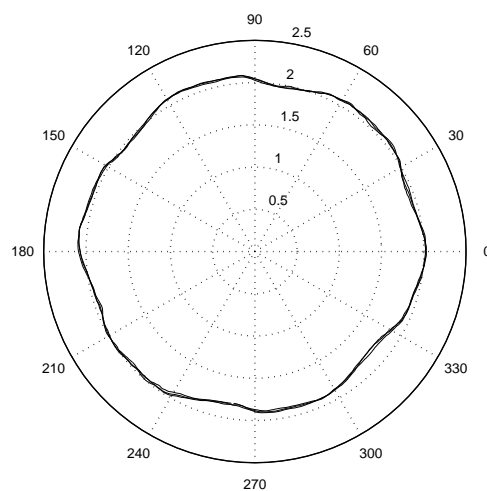
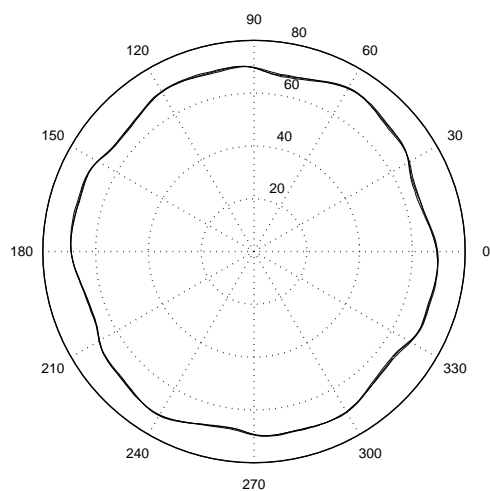


Figure 5.128: Voltage space-vector of the IPM machine at 30 Hz with a 5.0Ω , 16.7% winding fault.

Figure 5.129: Current space-vector of the IPM machine at 30 Hz with a 5.0Ω , 16.7% winding fault.

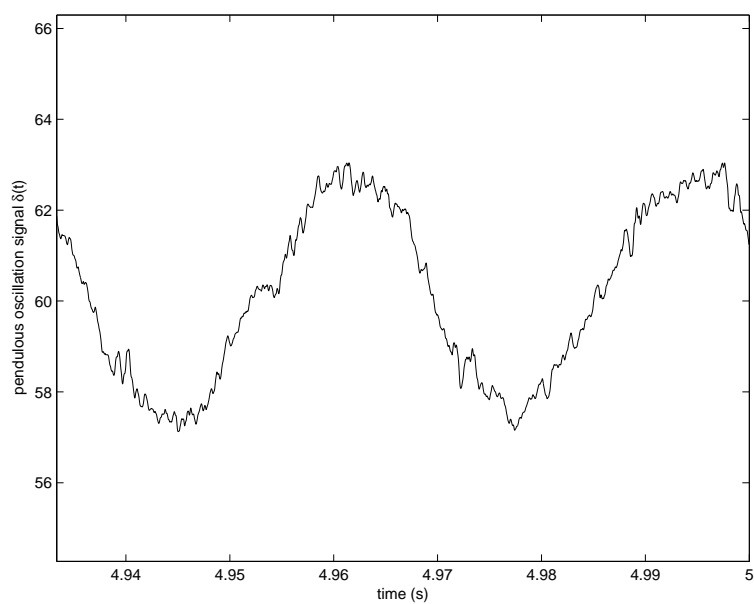


Figure 5.130: Pendulous oscillation signal of the IPM machine at 30 Hz with a 5.0Ω , 16.7% winding fault.

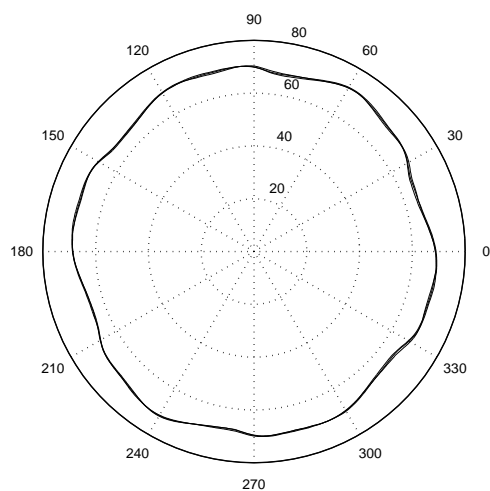


Figure 5.131: Voltage space-vector of the IPM machine at 30 Hz with a $3.3\ \Omega$, 16.7% winding fault.

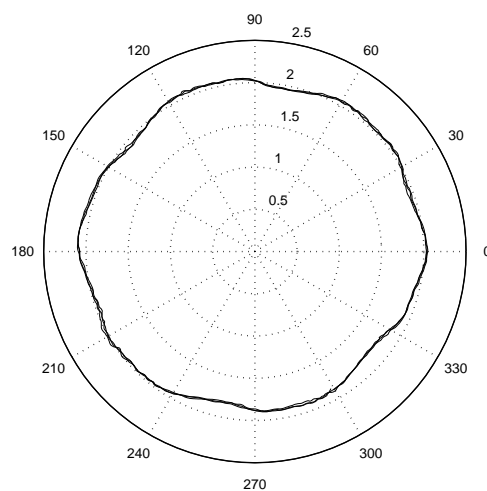


Figure 5.132: Current space-vector of the IPM machine at 30 Hz with a $3.3\ \Omega$, 16.7% winding fault.

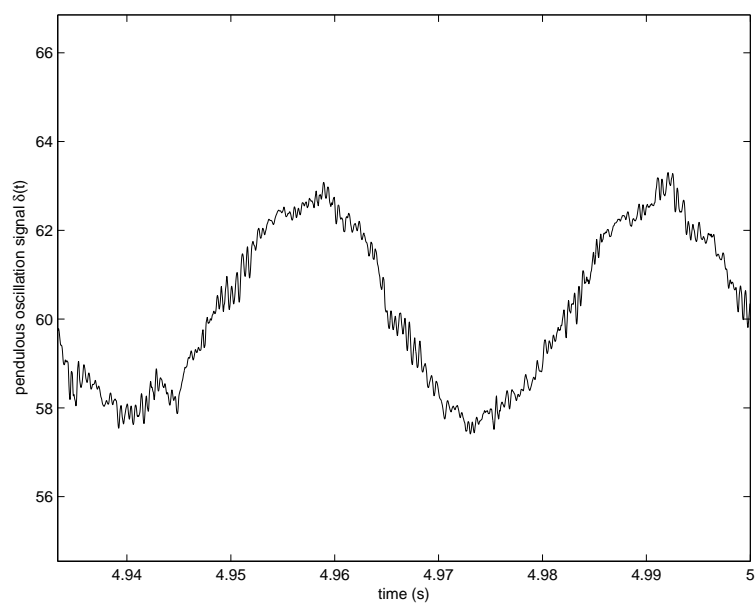


Figure 5.133: Pendulous oscillation signal of the IPM machine at 30 Hz with a $3.3\ \Omega$, 16.7% winding fault.

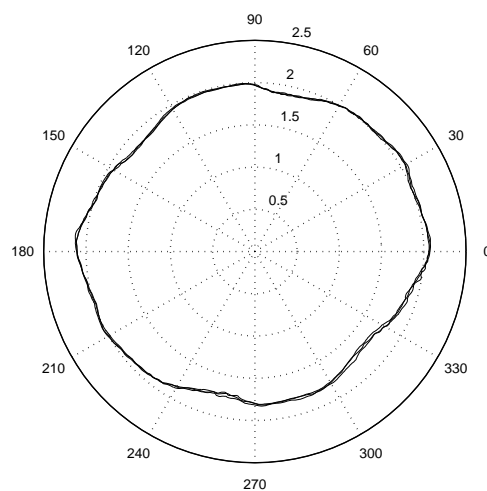
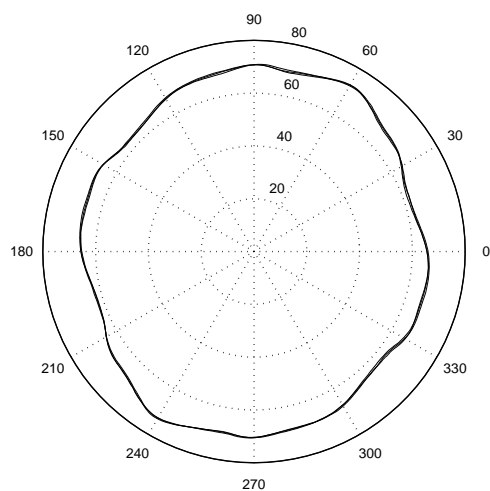


Figure 5.134: Voltage space-vector of the IPM machine at 30 Hz with a 5.0Ω , 33.3% winding fault.

Figure 5.135: Current space-vector of the IPM machine at 30 Hz with a 5.0Ω , 33.3% winding fault.

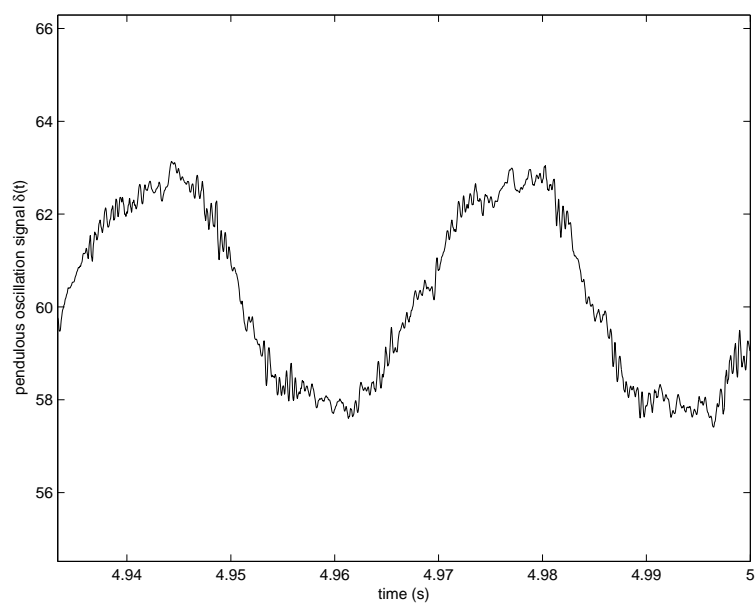


Figure 5.136: Pendulous oscillation signal of the IPM machine at 30 Hz with a 5.0Ω , 33.3% winding fault.

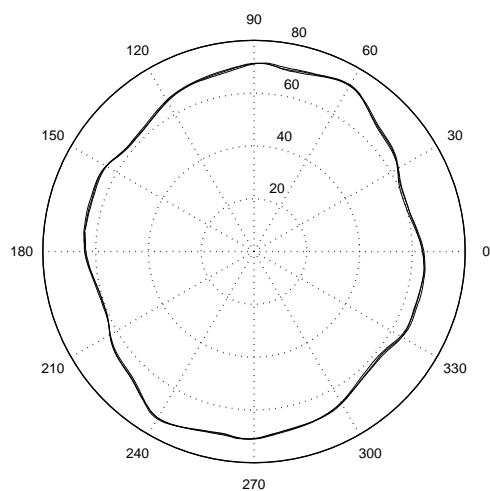


Figure 5.137: Voltage space-vector of the IPM machine at 30 Hz with a $3.3\ \Omega$, 33.3% winding fault.

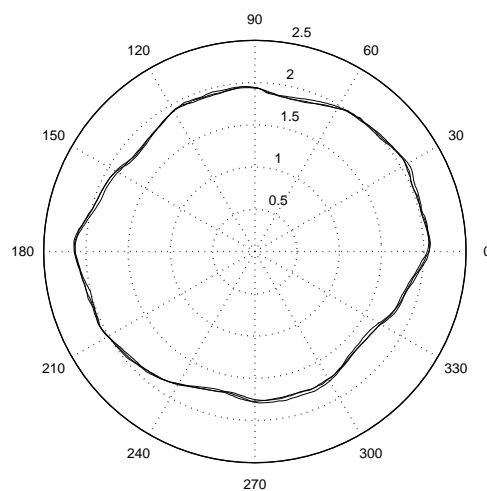


Figure 5.138: Current space-vector of the IPM machine at 30 Hz with a $3.3\ \Omega$, 33.3% winding fault.

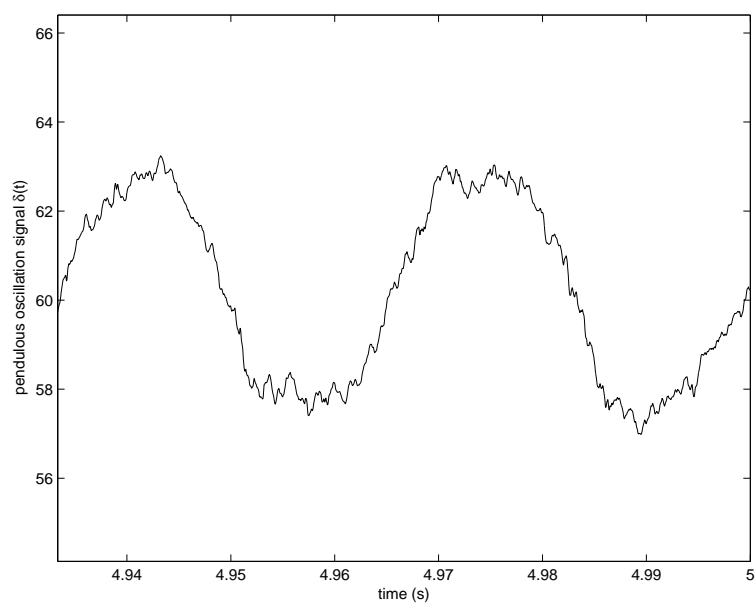


Figure 5.139: Pendulous oscillation signal of the IPM machine at 30 Hz with a $3.3\ \Omega$, 33.3% winding fault.

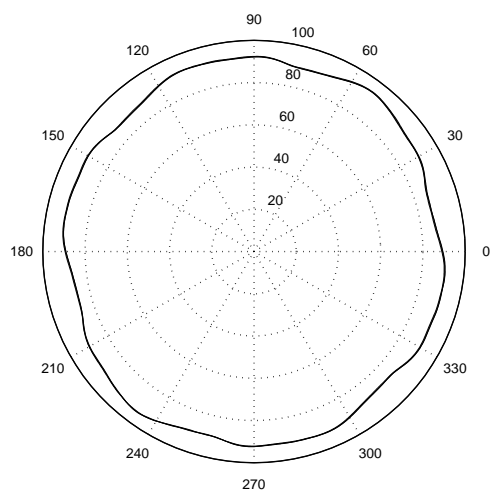


Figure 5.140: Voltage space-vector of the IPM machine at 40 Hz with a $5.0\ \Omega$, 16.7% winding fault.

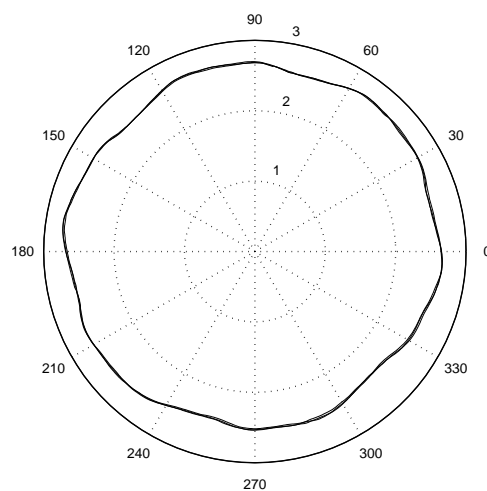


Figure 5.141: Current space-vector of the IPM machine at 40 Hz with a $5.0\ \Omega$, 16.7% winding fault.

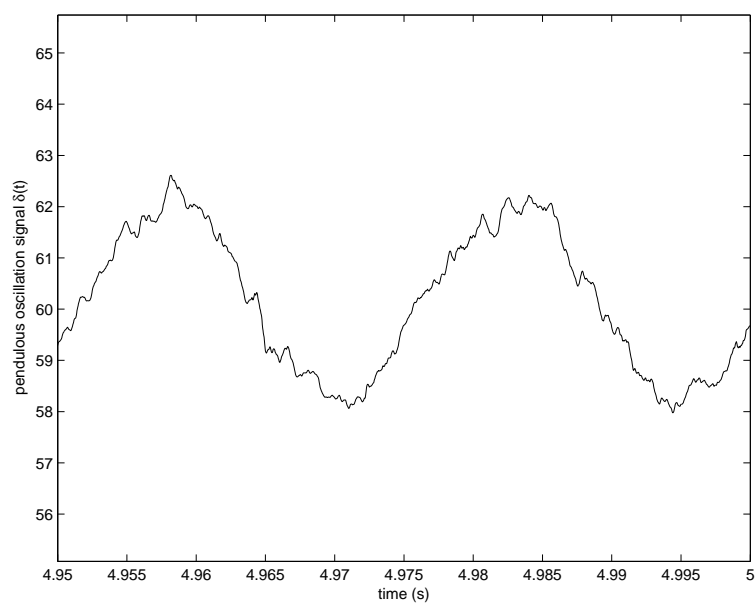


Figure 5.142: Pendulous oscillation signal of the IPM machine at 40 Hz with a $5.0\ \Omega$, 16.7% winding fault.

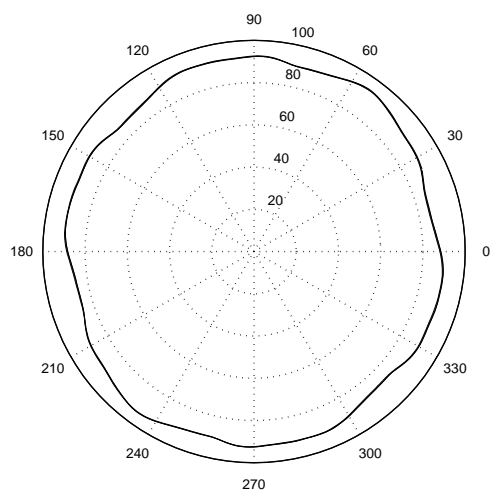


Figure 5.143: Voltage space-vector of the IPM machine at 40 Hz with a 3.3Ω , 16.7% winding fault.

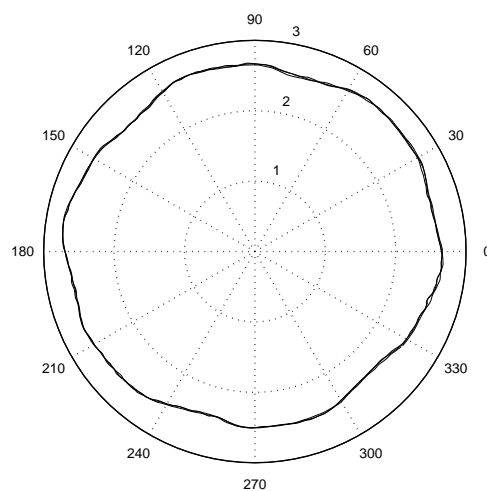


Figure 5.144: Current space-vector of the IPM machine at 40 Hz with a 3.3Ω , 16.7% winding fault.

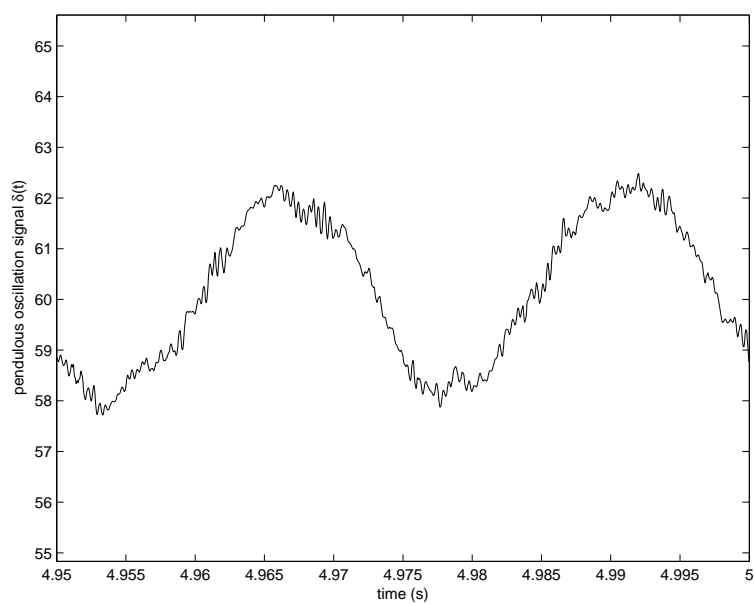


Figure 5.145: Pendulous oscillation signal of the IPM machine at 40 Hz with a 3.3Ω , 16.7% winding fault.

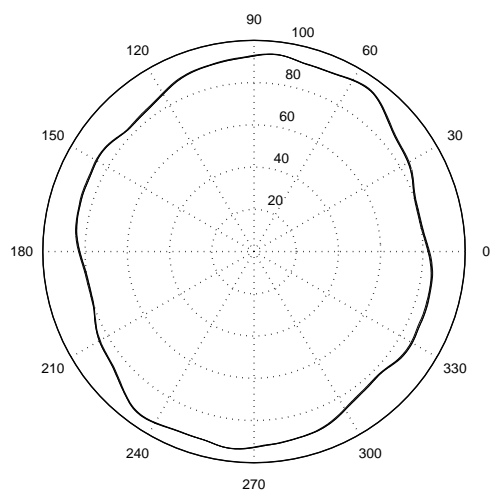


Figure 5.146: Voltage space-vector of the IPM machine at 40 Hz with a $5.0\ \Omega$, 33.3% winding fault.

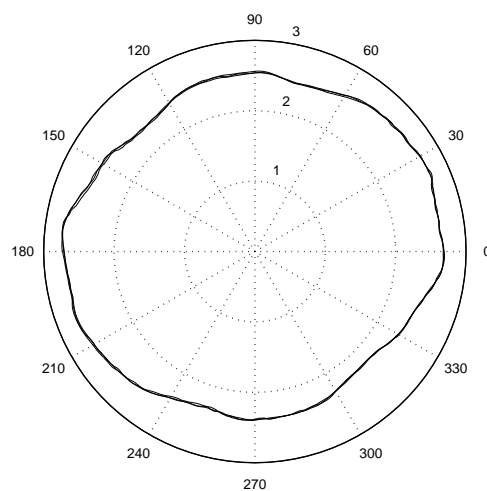


Figure 5.147: Current space-vector of the IPM machine at 40 Hz with a $5.0\ \Omega$, 33.3% winding fault.

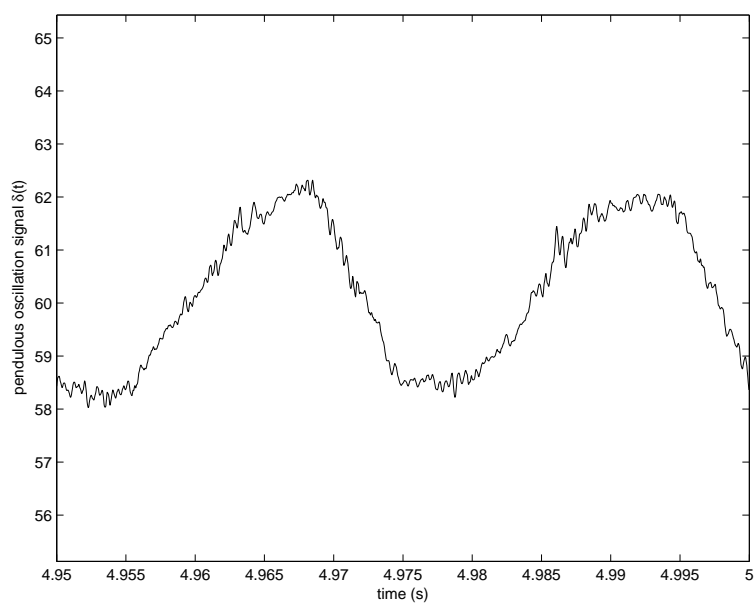


Figure 5.148: Pendulous oscillation signal of the IPM machine at 40 Hz with a $5.0\ \Omega$, 33.3% winding fault.

5.5 Analysis and Discussion of Results

Regarding the experiments of the case-study IPM machine operated as a generator the winding was reconfigured into one path per phase with the six coils connected in series, as shown in Figure 3.3 through Figure 3.6. Not only does operation as a generator eliminate any potential masking of fault indices through the effects of the ac drive control on the imposed machine excitation, but the re-configuration of the winding into one path per phase eliminates any potential “fault-tolerant” characteristics of multiple parallel path phase winding configurations. The time-domain phase voltage and current results seen in Figure 5.1 through Figure 5.52 demonstrate the changes that occur to the time-domain waveforms under various fault conditions. As the winding short-circuit fault becomes more severe, either through decreased fault resistance, increased percentage of the winding faulted, or higher rotor speed, both the line-to-neutral voltage waveforms as well as the phase current waveforms become increasingly imbalanced.

The application of MCSA to the IPM driven as a generator resulted in an increasing third harmonic in the current spectrum as the short-circuit fault increases in severity, demonstrating that MCSA is successful in diagnosing the winding fault in this IPM machine operated as a generator. Furthermore, for the current spectrum of the faulted phase, Phase A, the magnitude of the third harmonic component as compared to the fundamental increases monotonically, demonstrating that MCSA is

also successful for prognosticating the fault in this case-study machine.

The application of negative sequence components analysis to this IPM machine driven as a generator resulted in a monotonically increasing magnitude of the negative sequence current phasors as the short-circuit fault increases in severity, and a monotonically decreasing magnitude of the positive sequence current phasors as the short-circuit fault increases in severity. Both of these monotonic variations, but especially the increasing negative sequence component, make the negative sequence components analysis applicable to diagnosing and prognosticating the winding fault in this case-study IPM machine.

The use of voltage and current space-vectors to diagnose and prognosticate a winding fault in this experimental IPM machine driven as a generator was again inconclusive. As seen in Table 5.13 through Table 5.15 the swing angle did not vary significantly nor monotonically with the severity of the winding short-circuit fault.

The success of two of the three presented fault diagnosis methods in diagnosing the winding fault in this case-study experimental IPM machine indicates that either MCSA or the negative sequence components method could be successfully applied as an off-line diagnostic tool for diagnosing stator winding short-circuit faults. The strong generation of a 3rd harmonic component in the phase current further points to the possibility that the control algorithms in the ac drive during motoring operation may be compensating and masking the existence of the winding fault. For the pendulous oscillation method the strong magnetomotive force (MMF) generated by

the permanent-magnets in the rotor may be interfering with the use of swing angle as a fault index since, unlike the induction machine case [37], the rotor MMF does not vary with the operating conditions or the stator fault test conditions.

Chapter 6

Conclusions and Future Work

6.1 Conclusions

In this thesis the application of three stator winding short-circuit fault diagnosis methods to experimental data collected from a case-study IPM machine has been presented and analyzed. The case-study experimental IPM machine was operated as both a motor and a generator in order to comprehensively analyze the ability of the presented methods to diagnose and prognosticate winding short-circuit faults. While it was not possible in this work to embed these fault detection methods into the control algorithms of the commercial ac drive used in these experiments, the intent of applying these fault detection methods to this IPM machine operated as a motor is to analyze the possible success of the fault detection methods if they were to be included in an ac drive for on-line fault diagnosis. The intent of applying these fault detection methods to this IPM machine operated as a generator is to analyze the applicability of these fault detection methods without interference from the control systems of the ac drive. While these fault detection methods have been shown in the literature to be quite successful in diagnosing and prognosticating winding short-circuit faults in

induction machines, analyzing experimental test data from a case-study IPM machine demonstrates that these methods are not directly extensible to all machines, and not directly extensible to all possible operating conditions and designs of IPM machines.

The analysis of the experimental data from the IPM machine operated as a motor revealed that both MCSA and the space-vector pendulous oscillation method results were inconclusive in diagnosing the winding short-circuit fault. On the other hand, negative sequence components analysis of the experimental results for different fault conditions demonstrates a clear diagnosis of the winding fault, and if the unlikely high fault resistance test point is omitted, negative sequence components analysis was shown to successfully prognosticate the fault as well.

The analysis of the experimental data from the IPM machine operated as a generator revealed that both MCSA and negative sequence components analysis were successfully applied in diagnosing the winding short-circuit fault, while the space-vector pendulous oscillation method was inconclusive in diagnosing the fault. Motor current spectrum analysis successfully diagnosed the fault, while on the other hand, negative sequence components analysis both successfully diagnosed and prognosticated the winding fault.

What appears to significantly influence the success of diagnosing the winding fault is the degree of imbalance in the magnitudes of the fundamental frequency components of the phase currents under faulty conditions. The imbalance leads to a

successful fault diagnosis when using negative sequence components analysis. A monotonic relationship between the magnitude of the negative sequence current phasor and the fault resistance indicates that the magnitudes of the fundamental frequency components of the three phase currents become monotonically and increasingly imbalanced as the fault becomes more severe.

As indicated by this experimental case-study, both MCSA and negative sequence components analysis would be immediately successful in diagnosing the stator winding short-circuit fault when applied as an off-line test to this machine operated as a generator with a resistive load. If the machine terminals were in an open-circuit configuration for the off-line test the imbalance in the voltage waveforms also indicates a winding fault. However, as indicated by this same case-study, the application of MCSA and the pendulous oscillation methods as an on-line test of this machine operated as a motor would require additional verification that either method would be successful in diagnosing a winding fault. The lack of conclusive fault indices given in this case-study underlines the importance of not assuming without verification that a particular fault diagnosis/prognosis method is extensible to a particular machine or category of machines.

6.2 Future Work

The application and verification of the diagnostic and prognostic ability of MCSA, negative sequence components analysis, and the space-vector pendulous oscillation method could be further extended to additional test configurations and operating conditions such as various increased and decreased load resistances for generator operation, resulting in increased and decreased phase currents based on the applied resistive load. Further detailed study of the magnetic circuit of the IPM machine under fault conditions could also be explored. If access to an ac drive which permits manipulation and observation of the PWM control can be obtained, as well as access to a data acquisition system of sufficient bandwidth to observe PWM voltage pulses, the effects of the drive control on the output voltage as the ac drive compensates for the machine fault should also be investigated.

The influence of the strong permanent-magnet MMF on fault detection using these three methods could possibly be investigated through the use of a field-wound synchronous machine, which would permit control of the rotor MMF through the applied field current. Finally, consideration should be given to possibly developing a new, robust short-circuit fault detection method for IPM machines and experimentally verifying this new method through a compressive set of case-studies utilizing finite-element analysis and experimental results.

Bibliography

- [1] A. E. Fitzgerald, C. Kingsley, and S. Umans, *Electric Machinery*. McGraw-Hill Companies, Incorporated, 2003.
- [2] N. Tesla, “Electro magnetic motor,” U.S. Patent 381,968, 1888.
- [3] —, “Electro magnetic motor,” U.S. Patent 381,968, 1888.
- [4] W. Thomson and M. Fenger, “Current signature analysis to detect induction motor faults,” *Industry Applications Magazine, IEEE*, vol. 7, no. 4, pp. 26–34, 2001.
- [5] B. Mirafzal and N. A. O. Demerdash, “On innovative methods of induction motor interturn and broken-bar fault diagnostics,” *Industry Applications, IEEE Transactions on*, vol. 42, no. 2, pp. 405–414, 2006.
- [6] “Report of large motor reliability survey of industrial and commercial installations, part i,” *Industry Applications, IEEE Transactions on*, vol. IA-21, no. 4, pp. 853–864, 1985.
- [7] “Report of large motor reliability survey of industrial and commercial installations, part ii,” *Industry Applications, IEEE Transactions on*, vol. IA-21, no. 4, pp. 865–872, 1985.
- [8] P. F. Albrecht, J. C. Appiarius, R. M. McCoy, E. Owen, and D. K. Sharma, “Assessment of the reliability of motors in utility applications - updated,” *Energy Conversion, IEEE Transactions on*, vol. EC-1, no. 1, pp. 39–46, 1986.
- [9] P. Zhang, K. Younsi, and P. Neti, “A novel online stator ground-wall insulation monitoring scheme for inverter-fed ac motors,” in *Energy Conversion Congress and Exposition (ECCE), 2013 IEEE*, 2013, pp. 3541–3547.
- [10] W. Thomson, “On-line mcsa to diagnose shorted turns in low voltage stator windings of 3-phase induction motors prior to failure,” in *Electric Machines and Drives Conference, 2001. IEMDC 2001. IEEE International*, 2001, pp. 891–898.

- [11] A. Bonnett and G. Soukup, "Cause and analysis of stator and rotor failures in three-phase squirrel-cage induction motors," *Industry Applications, IEEE Transactions on*, vol. 28, no. 4, pp. 921–937, 1992.
- [12] S. Grubic, J. Aller, B. Lu, and T. Habetler, "A survey on testing and monitoring methods for stator insulation systems of low-voltage induction machines focusing on turn insulation problems," *Industrial Electronics, IEEE Transactions on*, vol. 55, no. 12, pp. 4127–4136, 2008.
- [13] M. Fenger, S. Campbell, and J. Pedersen, "Motor winding problems caused by inverter drives," *Industry Applications Magazine, IEEE*, vol. 9, no. 4, pp. 22–31, 2003.
- [14] M. Melfi, A. Sung, S. Bell, and G. Skibinski, "Effect of surge voltage risetime on the insulation of low-voltage machines fed by pwm converters," *Industry Applications, IEEE Transactions on*, vol. 34, no. 4, pp. 766–775, 1998.
- [15] G. Stone and J. Kapler, "Stator winding monitoring," *Industry Applications Magazine, IEEE*, vol. 4, no. 5, pp. 15–20, 1998.
- [16] B. Vaseghi, B. Nahid-Mobarakeh, N. Takorabet, and F. Meibody-Tabar, "Experimentally validated dynamic fault model for pmsm with stator winding inter-turn fault," in *Industry Applications Society Annual Meeting, 2008. IAS '08. IEEE*, 2008, pp. 1–5.
- [17] B. Vaseghi, N. Takorabet, F. Meibody-Tabar, A. Djerdir, J. Farooq, and A. Miraoui, "Modeling and characterizing the inter-turn short circuit fault in pmsm," in *Electric Machines Drives Conference (IEMDC), 2011 IEEE International*, 2011, pp. 551–556.
- [18] B. Vaseghi, B. Nahid-Mobarakeh, N. Takorabet, and F. Meibody-Tabar, "Modeling of non-salient pm synchronous machines under stator winding inter-turn fault condition: Dynamic model - fem model," in *Vehicle Power and Propulsion Conference, 2007. VPPC 2007. IEEE*, 2007, pp. 635–640.
- [19] B. Vaseghi, N. Takorabet, and F. Meibody-Tabar, "Fault analysis and parameter identification of permanent-magnet motors by the finite-element method," *Magnetics, IEEE Transactions on*, vol. 45, no. 9, pp. 3290–3295, 2009.
- [20] C. Rojas, M. Melero, M. F. Cabanas, J. Cano, G. Orcajo, and F. Pedrayes, "Finite element model for the study of inter-turn short circuits in induction motors," in *Diagnostics for Electric Machines, Power Electronics and Drives, 2007. SDEMPED 2007. IEEE International Symposium on*, 2007, pp. 415–419.

- [21] E. Wiedenbrug, G. Frey, and J. Wilson, "Early intervention," *Industry Applications Magazine, IEEE*, vol. 10, no. 5, pp. 34–40, 2004.
- [22] A. Gandhi, T. Corrigan, and L. Parsa, "Recent advances in modeling and online detection of stator interturn faults in electrical motors," *Industrial Electronics, IEEE Transactions on*, vol. 58, no. 5, pp. 1564–1575, 2011.
- [23] J. Sottile, J. and J. Kohler, "An on-line method to detect incipient failure of turn insulation in random-wound motors," *Energy Conversion, IEEE Transactions on*, vol. 8, no. 4, pp. 762–768, 1993.
- [24] E. Wiedenbrug, G. Frey, and J. Wilson, "Impulse testing and turn insulation deterioration in electric motors," in *Pulp and Paper Industry Technical Conference, 2003. Conference Record of the 2003 Annual*, 2003, pp. 50–55.
- [25] S.-B. Lee, R. Tallam, and T. Habetler, "A robust, on-line turn-fault detection technique for induction machines based on monitoring the sequence component impedance matrix," *Power Electronics, IEEE Transactions on*, vol. 18, no. 3, pp. 865–872, 2003.
- [26] M. Benbouzid and G. Kliman, "What stator current processing-based technique to use for induction motor rotor faults diagnosis?" *Energy Conversion, IEEE Transactions on*, vol. 18, no. 2, pp. 238–244, 2003.
- [27] J. Penman, H. Sedding, B. Lloyd, and W. T. Fink, "Detection and location of interturn short circuits in the stator windings of operating motors," *Energy Conversion, IEEE Transactions on*, vol. 9, no. 4, pp. 652–658, 1994.
- [28] N. Leboeuf, T. Boileau, B. Nahid-Mobarakeh, G. Clerc, and F. Meibody-Tabar, "Real-time detection of interturn faults in pm drives using back-emf estimation and residual analysis," *Industry Applications, IEEE Transactions on*, vol. 47, no. 6, pp. 2402–2412, 2011.
- [29] M. Awadallah and M. Morcos, "Application of ai tools in fault diagnosis of electrical machines and drives-an overview," *Energy Conversion, IEEE Transactions on*, vol. 18, no. 2, pp. 245–251, 2003.
- [30] C. Fortescue, "Method of symmetrical co-ordinates applied to the solution of polyphase networks," *American Institute of Electrical Engineers, Transactions of the*, vol. XXXVII, no. 2, pp. 1027–1140, 1918.
- [31] B. Mirafzal and N. A. O. Demerdash, "On innovative methods of induction motor inter-turn and broken-bar fault diagnostics," in *Electric Machines and Drives, 2005 IEEE International Conference on*, 2005, pp. 762–769.

- [32] S. M. A. Cruz and A. J. M. Cardoso, "Diagnosis of stator inter-turn short circuits in dtc induction motor drives," *Industry Applications, IEEE Transactions on*, vol. 40, no. 5, pp. 1349–1360, 2004.
- [33] G. Joksimovic and J. Penman, "The detection of inter-turn short circuits in the stator windings of operating motors," *Industrial Electronics, IEEE Transactions on*, vol. 47, no. 5, pp. 1078–1084, 2000.
- [34] B. Mirafzal and N. A. O. Demerdash, "Effects of load magnitude on diagnosing broken bar faults in induction motors using the pendulous oscillation of the rotor magnetic field orientation," *Industry Applications, IEEE Transactions on*, vol. 41, no. 3, pp. 771–783, 2005.
- [35] F. Harris, "On the use of windows for harmonic analysis with the discrete fourier transform," *Proceedings of the IEEE*, vol. 66, no. 1, pp. 51–83, 1978.
- [36] W. Duesterhoeft, M. W. Schulz, and E. Clarke, "Determination of instantaneous currents and voltages by means of alpha, beta, and zero components," *American Institute of Electrical Engineers, Transactions of the*, vol. 70, no. 2, pp. 1248–1255, 1951.
- [37] B. Mirafzal, R. Povinelli, and N. A. O. Demerdash, "Interturn fault diagnosis in induction motors using the pendulous oscillation phenomenon," *Energy Conversion, IEEE Transactions on*, vol. 21, no. 4, pp. 871–882, 2006.
- [38] S. Nandi and H. Toliyat, "Novel frequency-domain-based technique to detect stator interturn faults in induction machines using stator-induced voltages after switch-off," *Industry Applications, IEEE Transactions on*, vol. 38, no. 1, pp. 101–109, 2002.
- [39] A. Sayed-Ahmed, C.-C. Yeh, N. A. O. Demerdash, and B. Mirafzal, "Analysis of stator winding inter-turn short-circuit faults in induction machines for identification of the faulty phase," in *Industry Applications Conference, 2006. 41st IAS Annual Meeting. Conference Record of the 2006 IEEE*, vol. 3, 2006, pp. 1519–1524.
- [40] P. Neti and S. Nandi, "Stator inter-turn fault detection of synchronous machines using field current signature analysis," in *Industry Applications Conference, 2006. 41st IAS Annual Meeting. Conference Record of the 2006 IEEE*, vol. 5, 2006, pp. 2360–2367.
- [41] H. Toliyat and T. Lipo, "Transient analysis of cage induction machines under stator, rotor bar and end ring faults," *Energy Conversion, IEEE Transactions on*, vol. 10, no. 2, pp. 241–247, 1995.

- [42] M. Benbouzid, M. Vieira, and C. Theys, "Induction motors' faults detection and localization using stator current advanced signal processing techniques," *Power Electronics, IEEE Transactions on*, vol. 14, no. 1, pp. 14–22, 1999.
- [43] R. Tallam, S.-B. Lee, G. Stone, G. Kliman, J.-Y. Yoo, T. Habetler, and R. Harley, "A survey of methods for detection of stator-related faults in induction machines," *Industry Applications, IEEE Transactions on*, vol. 43, no. 4, pp. 920–933, 2007.
- [44] I. Brown, D. Ionel, and D. Dorrell, "Influence of parallel paths on current-regulated sine-wave interior-permanent-magnet machines with rotor eccentricity," *Industry Applications, IEEE Transactions on*, vol. 48, no. 2, pp. 642–652, 2012.
- [45] N. Leboeuf, T. Boileau, B. Nahid-Mobarakeh, N. Takorabet, F. Meibody-Tabar, and G. Clerc, "Estimating permanent-magnet motor parameters under inter-turn fault conditions," *Magnetics, IEEE Transactions on*, vol. 48, no. 2, pp. 963–966, 2012.
- [46] A. Sayed-Ahmed and N. A. O. Demerdash, "Fault-tolerant operation of delta-connected scalar- and vector-controlled ac motor drives," *Power Electronics, IEEE Transactions on*, vol. 27, no. 6, pp. 3041–3049, 2012.
- [47] B. Vaseghi, B. Nahid-mobarakh, N. Takorabet, and F. Meibody-Tabar, "Inductance identification and study of pm motor with winding turn short circuit fault," *Magnetics, IEEE Transactions on*, vol. 47, no. 5, pp. 978–981, 2011.
- [48] A. Mahyob, P. Reghem, and G. Barakat, "Permeance network modeling of the stator winding faults in electrical machines," *Magnetics, IEEE Transactions on*, vol. 45, no. 3, pp. 1820–1823, 2009.
- [49] A. Sayed-Ahmed, B. Mirafzal, and N. A. O. Demerdash, "Fault-tolerant technique for Δ -connected ac-motor drives," *Energy Conversion, IEEE Transactions on*, vol. 26, no. 2, pp. 646–653, 2011.
- [50] T. Nehl, N. Demerdash, and F. Fouad, "Impact of winding inductances and other parameters on the design and performance of brushless dc motors," *Power Apparatus and Systems, IEEE Transactions on*, vol. PAS-104, no. 8, pp. 2206–2213, 1985.
- [51] T. A. Nyamusa and N. Demerdash, "Transient analysis of partial armature short circuit in an electronically commutated permanent magnet motor system using an integrated nonlinear magnetic field-network model," *Energy Conversion, IEEE Transactions on*, vol. EC-2, no. 1, pp. 86–92, 1987.

- [52] Q. Wu and S. Nandi, "Fast single-turn sensitive stator interturn fault detection of induction machines based on positive- and negative-sequence third harmonic components of line currents," *Industry Applications, IEEE Transactions on*, vol. 46, no. 3, pp. 974–983, 2010.
- [53] M. Arkan, D. Perovic, and P. Unsworth, "Online stator fault diagnosis in induction motors," *Electric Power Applications, IEE Proceedings -*, vol. 148, no. 6, pp. 537–547, 2001.
- [54] A. Stavrou, H. Sedding, and J. Penman, "Current monitoring for detecting interturn short circuits in induction motors," *Energy Conversion, IEEE Transactions on*, vol. 16, no. 1, pp. 32–37, 2001.
- [55] S. Williamson and K. Mirzoian, "Analysis of cage induction motors with stator winding faults," *Power Apparatus and Systems, IEEE Transactions on*, vol. PAS-104, no. 7, pp. 1838–1842, 1985.
- [56] B. Mirafzal and N. A. O. Demerdash, "Induction machine broken-bar fault diagnosis using the rotor magnetic field space-vector orientation," *Industry Applications, IEEE Transactions on*, vol. 40, no. 2, pp. 534–542, 2004.
- [57] G. Sizov, A. Sayed-Ahmed, C.-C. Yeh, and N. A. O. Demerdash, "Analysis and diagnostics of adjacent and nonadjacent broken-rotor-bar faults in squirrel-cage induction machines," *Industrial Electronics, IEEE Transactions on*, vol. 56, no. 11, pp. 4627–4641, 2009.
- [58] P. Vas, *Parameter Estimation, Condition Monitoring, and Diagnosis of Electrical Machines (Monographs in Electrical and Electronic Engineering)*. London, UK: Oxford Univ. Press, 1993.
- [59] A. Sayed-Ahmed, G. Sizov, and N. A. O. Demerdash, "Diagnosis of inter-turn short circuit for a polyphase induction motor in closed-loop vector-controlled drives," in *Industry Applications Conference, 2007. 42nd IAS Annual Meeting. Conference Record of the 2007 IEEE*, 2007, pp. 2262–2268.
- [60] I. Brown, D. Ionel, and D. Dorrell, "Unbalanced operation of current regulated sine-wave interior permanent magnet machines," in *Energy Conversion Congress and Exposition (ECCE), 2010 IEEE*, 2010, pp. 4123–4130.
- [61] J. Tapia, F. Leonardi, and T. Lipo, "A design procedure for a pm machine with extended field weakening capability," in *Industry Applications Conference, 2002. 37th IAS Annual Meeting. Conference Record of the*, vol. 3, 2002, pp. 1928–1935 vol.3.

- [62] Q. Wu and S. Nandi, "Fast single-turn sensitive stator inter-turn fault detection of induction machines based on positive and negative sequence third harmonic components of line currents," in *Industry Applications Society Annual Meeting, 2008. IAS '08. IEEE*, 2008, pp. 1–8.
- [63] J. Kang, "General purpose permanent magnet motor drive without speed and position sensor," *Yaskawa Electric Corp., Japan, Yaskawa Application Note WP. AFD*, 2009.
- [64] N. Demerdash, R. Miller, T. Nehl, and T. Nyamusa, "Improved transistor-controlled and commutated brushless dc motors for electric vehicle propulsion," Virginia Polytechnic Institute and State University, Tech. Rep., 1983.
- [65] T. M. K. Hijazi, "Finite element - network graph theory modeling techniques for design and analysis of permanent magnet electronically commutated brushless dc motors including rotor damping effects," Ph.D. dissertation, Clarkson University, 1988.
- [66] G. Y. Sizov, "Analysis, modeling, and diagnostics of adjacent and nonadjacent broken rotor bars in squirrel-cage induction machines," Master's thesis, Marquette University, 2007.
- [67] A. M. S. Ahmed, "Control of pwm ac motor-drive systems under faulty conditions," Ph.D. dissertation, Marquette University, 2009.
- [68] J. F. Bangura, "A time-stepping coupled finite element-state space modeling of sinusoidal- and inverter-fed induction motor drives," Master's thesis, Marquette University, 1996.
- [69] G. Strang, *Computational Science and Engineering*. Wellesley-Cambridge Press, 2007.
- [70] N. A. O. Demerdash, "Design and analysis of electric motors in adjustable speed drives," *class notes for EECE 5210, Marquette University, Milwaukee, Wisconsin, Fall 2011*, Fall 2011.
- [71] —, "Advanced concepts in analysis and design of electric machines and drives," *class notes for EECE 6220, Marquette University, Milwaukee, Wisconsin*, Spring 2012.
- [72] —, "Advanced electrical machines and drives," *class notes for EECE 6210, Marquette University, Milwaukee, Wisconsin*, Spring 2011.
- [73] —, "Electrical transients and surges in power systems and devices," *class notes for EECE 4250/5250, Marquette University, Milwaukee, Wisconsin*, Fall 2010.